

Sheffield Hallam University

Liquid crystal films confined between patterned substrates.

ANQUETIL-DECK, Candy.

Available from the Sheffield Hallam University Research Archive (SHURA) at:

<http://shura.shu.ac.uk/19280/>

A Sheffield Hallam University thesis

This thesis is protected by copyright which belongs to the author.

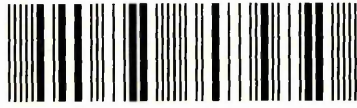
The content must not be changed in any way or sold commercially in any format or medium without the formal permission of the author.

When referring to this work, full bibliographic details including the author, title, awarding institution and date of the thesis must be given.

Please visit <http://shura.shu.ac.uk/19280/> and <http://shura.shu.ac.uk/information.html> for further details about copyright and re-use permissions.

Adsetts Centre City Campus
Sheffield S1 1WB

101 895 512 7



Sheffield Hallam University
Learning and IT Services
Adsetts Centre City Campus
Sheffield S1 1WB

REFERENCE

urn

ProQuest Number: 10694160

All rights reserved

INFORMATION TO ALL USERS

The quality of this reproduction is dependent upon the quality of the copy submitted.

In the unlikely event that the author did not send a complete manuscript and there are missing pages, these will be noted. Also, if material had to be removed, a note will indicate the deletion.



ProQuest 10694160

Published by ProQuest LLC (2017). Copyright of the Dissertation is held by the Author.

All rights reserved.

This work is protected against unauthorized copying under Title 17, United States Code
Microform Edition © ProQuest LLC.

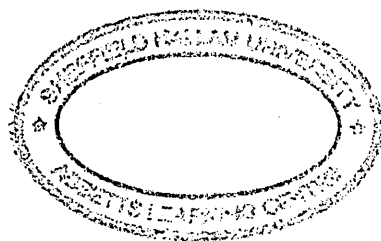
ProQuest LLC.
789 East Eisenhower Parkway
P.O. Box 1346
Ann Arbor, MI 48106 – 1346

Liquid Crystal Films Confined between Patterned Substrates

Candy Anquetil-Deck

A thesis submitted in partial fulfilment of the requirements of
Sheffield Hallam University for the degree of Doctor of Philosophy

March 2008



Abstract

In this thesis, systems of nematic liquid crystals confined between patterned substrates have been studied using molecular computer simulation. The aim of this work, done in parallel with experimentalists in Leeds, has been to investigate the use of chemical patterning as a novel method for controlling liquid crystal alignment.

In the first part of this thesis, the study of confined systems of liquid crystalline particles has been addressed. Using the hard needle wall and hard gaussian overlap potentials, homeotropic and planar alignment of model molecules on the substrates has been induced. We have then extended the study of confined liquid crystals systems from the use of unpatterned symmetric substrates systems to hybrid anchored systems and, finally, to a system involving one patterned substrate. The results from this initial study show that surface anchoring can be controlled by changing the surface interaction parameter and that, by varying the surface interaction parameter across a model substrate, a pattern can be imposed on the confining surfaces.

In the second part of this thesis, the substrate model developed in our initial stripe systems is used to simulate liquid crystal films confined between two identical patterned substrates. This is achieved through a comprehensive investigation of stripe patterned systems. In this, we show that, by varying key parameters like the stripe width, the surface interaction parameters and the film thickness, surface patterning can be used to control the polar anchoring angle and set the azimuthal anchoring. Our results show that a full range of tilt angles can be obtained by changing these key parameters.

Following this work on striped systems, we extend our study to 2D patterned substrates (i.e. square and rectangle patterns). Here, the results show that by changing two key parameters, the surface interaction parameter and the shape of the pattern, it is possible to gain more complete control of the bulk tilt angle as the latter varies

monotonically as the key parameters are changed.

We close the thesis with brief descriptions of some other substrate patternings that have been considered in this thesis work. These include circle and displaced/rotated stripe systems. We then draw some conclusions and comment on possible directions for future work.

A la mémoire de mon père,

A mon époux,

A ma famille...

*Whoso loveth instruction loveth knowledge :
but he that hateth reproof is brutish.*

Proverbs 12 : 1, The Bible

Acknowledgments

First of all I would like to thank my supervisors Dr. Douglas J. Cleaver and Pr. Christopher M. Care for giving me the opportunity of taking this PhD and their guidance and help throughout this project. Thank you to Jon, Steve and Jim, our collaborators in Leeds for helpful discussions. I would like also to thank EPSRC for funding.

A big *diolch un fawr* to Paul, Anne and Peter for their hospitality and for accepting me as a part of their family during these four years that I spent in Sheffield. Thanks for your love and care. You've been like a mum and dad to me!

Ta muchely to Trevor and Ruth who looked after my husband to be and took care of us.

It also gives me pleasure to thank all of my friends and colleagues whom I have worked with over the past three or so years. So thanks to Fatima, David, Richard, Sergei, Adam, Mich, Tim and Lawrence.

Last but not least, I wish to acknowledge my family, especially my mum, for her love and support and my beloved Ludwig for your love, your support and your encouragement.

Advanced studies

- July 2004 : Collaborative Computational Project 5 (CCP5) Molecular Simulation Summer School, Poster Presentation "*Anchoring of liquid crystals on self-assembled monolayers (SAMs)*". Cardiff University.
- February 2005 : Course : Soft condensed matter and advanced colloid science, Utrecht University, Netherland.
- May 2005 : Oral Presentation "*Anchoring of liquid crystals on self-assembled monolayers (SAMs)*". Materials Research Institute, Sheffield Hallam University.
- August 2005 : Poster Presentation "*Anchoring of liquid crystals on self-assembled monolayers (SAMs)*". CCP5 annual meeting, "Computational techniques and applications for materials modelling". Keele University.
- November 2005 : Oral Presentation "*Anchoring of liquid crystals on self-assembled monolayers (SAMs)*". Materials Research Institute, Sheffield Hallam University.
- April 2006 : Poster Presentation "*Anchoring of liquid crystals on self-assembled monolayers (SAMs)*". British Liquid Crystal Society (BLCS) workshop. University of York.
- June 2006 : Oral Presentation "*Anchoring of liquid crystals on patterned self assembled monolayers-a simulation study*". Second year postgraduate student research presentations day, Sheffield Hallam University.
- July 2006 : Oral Presentation "*Anchoring of liquid crystals on patterned self assembled monolayers*". International school of liquid crystals, "Colloids, interfaces and liquid crystals", Erice, Italy.

- July 2006 : Poster Presentation “*Anchoring of liquid crystals on patterned self assembled monolayers*”. International school of liquid crystals, “Colloids, interfaces and liquid crystals”, Erice, Italy.
- September 2006 : Oral Presentation “*Anchoring of liquid crystals on patterned self assembled monolayers*”. CCP5 annual meeting, “Phase behaviour from molecular simulation”, Bradford University.
- May 2007 : Oral Presentation “*Nematic liquid crystals on patterned substrates*”. Material and Engineering Research Institute, Sheffield Hallam University.

Contents

1	Introduction	1
1.1	Aim	2
1.2	Organisation of the thesis	2
2	The influence of surfaces on liquid crystal systems	4
2.1	Liquid crystalline phase	4
2.1.1	Description of ordering in LC systems	6
2.1.2	Types of LCs	6
2.1.3	LC Phases	8
2.2	Applications	11
2.2.1	LC technology : Liquid Crystal Displays (LCDs)	11
2.2.2	Other applications	12
2.3	Surface effects and anchoring of LCs	13
2.4	Techniques of surface alignment	15
2.4.1	Rubbing	15
2.4.2	Photoalignment	16
2.5	New technique : Self-Assembled Monolayers (SAMs)	20
2.5.1	Historical development of SAMs	20
2.5.2	Liquid crystal alignment on SAM	21
2.5.3	Patterning SAMs	22
2.6	Liquid crystals on patterned substrates	24
2.7	Results from our collaborators	26
2.7.1	Stamps	26
2.7.2	Circle patterns	26
2.7.3	Stripe patterns	27

2.7.4	Checkerboard	28
3	Liquid crystal simulations	32
3.1	Simulation of LCs	32
3.1.1	The Monte-Carlo (MC) Method	32
3.1.2	Practical aspects	36
3.2	Molecular modelling of bulk LC behaviour	39
3.2.1	Lattice models	39
3.2.2	Off lattice model	40
3.2.3	Hard particles	40
3.2.4	Soft particles	44
3.2.5	All-atom models	50
3.3	Molecules in contact with interfaces	51
3.3.1	Hard rod-like particles	52
3.3.2	Soft particles	55
3.3.3	All-atom models	58
3.4	Conclusions	59
4	Simulation of confined systems	61
4.1	Confined systems and anchoring phenomena	61
4.2	Simulation details	62
4.3	Symmetric anchored systems	63
4.3.1	Homeotropic anchoring	65
4.3.2	Planar anchoring	66
4.3.3	Competing anchoring	68
4.3.4	Other Systems: moderate planar and homeotropic anchoring	69
4.4	Hybrid anchored systems	70
4.4.1	$k_{st}=3; k_{sb}=0$	71
4.4.2	$k_{st}=3; k_{sb}=1.5$	74
4.4.3	$k_{st}=0; k_{sb}=1.5$	75
4.5	Systems with one striped substrate	77
4.5.1	Comparison homeotropic region	80
4.5.2	Comparison hybrid region	81

4.6	Conclusions	82
5	Nematic liquid crystals on stripe patterned substrates	83
5.1	Initial system	84
5.1.1	Homeotropic confinement region	89
5.1.2	Planar confinement region	91
5.1.3	Preliminary conclusions	91
5.1.4	Comparison between the symmetric and the stripe patterned systems	94
5.1.5	Conclusion	96
5.2	Influence of the proportion %homeotropic %planar	96
5.2.1	Homeotropic alignment region(H region)	99
5.2.2	Planar alignment region(P region)	100
5.2.3	Conclusion	104
5.3	Influence of the k_s values for a system with 40% H 60% P	106
5.3.1	Conclusion	114
5.4	Influence of the thickness of the simulation box	114
5.4.1	Homeotropic surface region	117
5.4.2	Planar surface region	118
5.4.3	Conclusion	122
5.5	Influence of the k_s values for a system with 40% H 60% P, $L_z=8\kappa\sigma_0$	122
5.5.1	Conclusion	129
5.6	Smooth transitions	130
5.6.1	Conclusion	134
5.7	Conclusions	135
6	Nematic liquid crystals on rectangle patterned substrates	137
6.1	Square patterned substrates	137
6.1.1	Sharp transitions	138
6.1.2	Azimuthal angle	143
6.1.3	Smooth transitions	144
6.1.4	Conclusion	145
6.2	Rectangle patterned substrates	147

6.2.1	Influence of the k_s values	148
6.2.2	Conclusions	154
6.2.3	Influence of the ratio L_x/Ly	157
6.3	Conclusions	167
7	Conclusions and future work	168
7.1	Other directions	168
7.1.1	Circle patterns	168
7.1.2	Striped substrates : out of phase	176
7.1.3	Striped substrates rotated at 90 degrees to each other	176
7.2	Conclusions	178
7.3	Future work	180

Chapter 1

Introduction

Conventional liquid crystal (LC) devices rely on the control of the LC molecules at a surface to control the orientation of the LC molecules in the bulk of the device. This is usually achieved by chemical and mechanical treatments of a substrate. There are a number of reasons why being able to pattern the alignment of LCs is advantageous. Firstly there are a number of technological applications that have been devised. For example, bistable systems, which can exhibit two or more stable optical states and only require power to switch between them, resulting in devices with improved battery life. Secondly, a number of theory papers have been published which suggest a large range of potential new behaviours for these systems, but these still need to be tested experimentally.

Currently there are a number of techniques for producing patterned alignment in LC devices. Multirubbing, Photoalignment and patterned Self-Assembled monolayers (SAMs). All of these methods have advantages and disadvantages, but SAMs are arguably the most flexible since the interactions between the LC molecules and the substrates can be readily studied by changing the functional SAM end groups. Also the technique of microcontact printing of SAMs can produce patterns on a nanometre scale, which is not accessible to the mechanical and optical alignment techniques. The alignment of LCs on the nanoscale is unexplored at present.

Chemical patterning has potential to create new alignment conditions for nematic LCs and, thus, new functions of LCDs can be envisaged. In this thesis, we investi-

gate, by Monte-Carlo simulation, the effect of novel substrate chemical patterning on LC anchoring. For this, the hard gaussian overlap (HGO) model is used to simulate the LC molecules and we explore their behaviour when confined between various patterned substrates.

1.1 Aim

The work presented in this thesis addresses the study of confined liquid crystal by means of molecular simulations. The aims of this study were initially defined as follows:

- To investigate, by computer simulation, the use of novel substrate patterning approaches in the control of liquid crystal anchoring.
- To develop a model able to retrieve the behaviour of real systems
- To study, in detail, the effect of different parameters on the system
- To investigate how the written pattern penetrates the LC
- To see if a tilt can be induced and controlled using patterning
- To check if the polar and azimuthal anchoring coefficients can be controlled independently using patterning.
- To compare the results obtained from our simulations with the experimental results obtained by our collaborators at Leeds

1.2 Organisation of the thesis

The remainder of this thesis is arranged as follows.

In chapter 2, some background information about LCs is given. Specifically, we briefly describe the different types of LCs and the different phases they can form. This chapter also contains a short description of some applications followed by a more detailed literature review regarding the influence of surfaces on LC systems. Finally, this chapter ends with summary of key results obtained by our collaborators.

Chapter 3 comprises a description of the relevant Monte Carlo (MC) simulation techniques used in this thesis and a comprehensive literature review of simulations performed on LC systems. This includes bulk and confined behaviour, studied with models ranging from atomistic resolution to mesoscopic descriptions.

Chapter 4 combines a detailed description of the proposed model for simulating confined LC films with some preliminary results obtained with this initial model. Specifically, the behaviour of unpatterned confined systems (symmetric and hybrid systems) is investigated. Finally, initial results on a one-patterned-surface system are given.

Chapter 5 presents series of sets of results obtained for nematic LC systems confined between two stripe patterned substrates. The effects of key systems parameters on the system behaviour are thus analysed and discussed.

In chapter 6, results for nematic LC systems confined between rectangle patterned substrates are presented. The effect of the surface interaction parameter and the rectangle shape ratio L_x/L_y are investigated. Here, comparisons with stripe patterned systems and square patterned systems are provided in order to provide a comprehensive picture of the effect of this class of patterning on LC film alignment.

Finally, chapter 7 brings together the main results and conclusions of this thesis, suggestions for future areas of work are considered and some other patterned systems considered in our thesis work are listed.

Chapter 2

The influence of surfaces on liquid crystal systems

Why do certain surfaces align LCs and others not ? Work on surface-induced alignment has been performed by numerous researchers, having been pioneered by Lehmann, Grandjean, Mauguin, Chatelain and others. This chapter gives an overview of this topic, starting with an account of the advantages and drawbacks of different methods and techniques of surface alignment. Following this, we concentrate on methods based on self-assembled monolayers (SAMs). This chapter ends with a summary of results from Jonathan Bramble of Leeds University who has been undertaking an experimental PhD into the area of patterned SAMs to control LC alignment.

2.1 Liquid crystalline phase

We usually distinguish three states of matter : solid, liquid and gas, probably because they are part of our everyday life. Nevertheless, a fourth one, named “liquid crystal” also exists which may not be as well known but is very useful for a number of different applications. Liquid crystals (Fliessende Krystalle) were first named by Lehmann in 1889 [1]. In his original article, Lehmann described liquid crystals (LCs) as being solid bodies (but non-crystalline) which are able to flow like liquids (but not as easily). The first recognition of LC phase is usually attributed to Reinitzer (1888) [1, 2], who detected a substance (cholesteryl benzoate) which

was weakly fluid but had crystalline properties. The term LC is actually used to denote a number of different states of matter in which the degree of order varies from being almost perfect (long range positional and orientational order found in crystals) to almost disordered (isotropic phase). A number of alternative terms are sometimes used to talk about LCs including mesomorphic phase [3], mesophase or paracrystalline phase [2].

Starting from the most disordered phase (isotropic phase) and either compressing or cooling the system into the most ordered phase (crystal), a typical LC will form an initial intermediate phase with orientational order (nematic phase) and then, by compressing more, a phase with partial positional order (smectic phase). To illustrate this further, it is useful to consider the phase behaviour of the substance cholesteryl myristate [4]. This substance exhibits its solid phase at room temperature. On heating to 71°C , a phase transition occurs: the solid melts and a liquid is obtained. Nevertheless, this liquid phase is quite cloudy. If the temperature is raised further to 85°C , the previously cloudy liquid becomes clear like water. The cloudy liquid represents a state between the solid and the conventional liquid phase and is, in fact, LC (Fig. 2.1). It is a fluid and so takes the shape of its container, but the fact that it is cloudy indicates that it differs from an isotropic liquid.

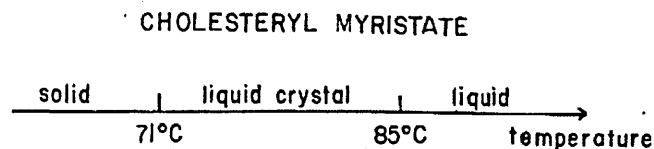


Figure 2.1: Phase diagram of cholesteryl myristate. A gas phase is not shown because the molecule decomposes at high temperature [4].

The molecules in the solid state are constrained to be in a certain position. We can say that the crystalline solid phase possesses long range *positional order*. In this phase, the molecules also often orient themselves with respect to each other. We say, then, that the solid phase also possesses long range *orientational order* [4]. If we increase the temperature and the solid melts to give an isotropic liquid, both of these types of order are lost simultaneously. However, if the solid melts to give an LC phase, the positional order might be lost but the orientational order is main-

tained: the molecules in the liquid crystal phase are then able to move, like those in a conventional liquid, but they remain aligned in a certain direction (Fig. 2.2).

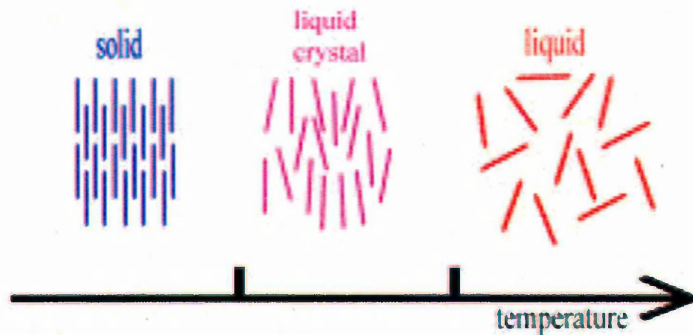


Figure 2.2: Schematic illustration of the solid, liquid crystal, and liquid phases. The slender "sticks" represent molecules.

2.1.1 Description of ordering in LC systems

How can we describe the orientational order in an LC? The bulk can be characterized by two parameters. The *director* \hat{n} which gives the average orientation of the molecules (Fig. 2.3)(each molecule is oriented at some angle θ relative to the director) and the *nematic order parameter* S , which characterises the distribution of the molecular orientations. The most useful (and commonly used) formulation for this employs the average of P_2 , the second order Legendre polynomial [5]:

$$S = \langle P_2(\cos\theta) \rangle = \left\langle \frac{3}{2}\cos^2(\theta) - \frac{1}{2} \right\rangle \quad (2.1)$$

In an isotropic liquid, the average of the $\cos^2\theta$ terms is $\frac{1}{3}$ so S goes to zero. In the nematic phase, the order parameter increases as the temperature decreases (Fig. 2.4).

2.1.2 Types of LCs

There are two main categories of LC, known as *thermotropic LCs* and *lyotropic LCs*. We can distinguish them by the mechanisms that drive their self-organisation. If the phase transitions are induced by a change in temperature, the molecules are designated as thermotropic [5]. In some cases, however, such temperature effects

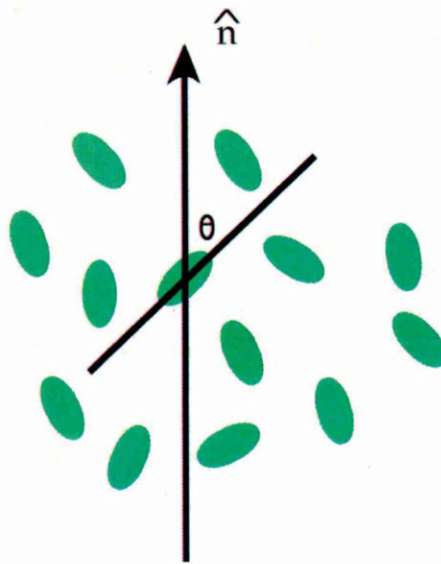


Figure 2.3: Schematic showing molecular order and the director in a nematic liquid crystal.

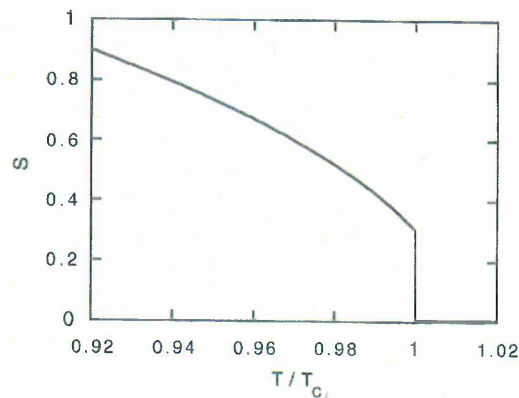


Figure 2.4: Typical temperature dependence of the order parameter S . T_C is the temperature of the nematic liquid crystal to isotropic liquid phase transition [6].

are difficult to control (molecules in a solution). In such systems, mesophase phase transitions are instead induced by adjusting the concentration of molecules in the solution. Such systems are termed lyotropic.

A range of different molecule types can form thermotropic mesophases, but all of these show a significant degree of shape anisotropy. The most common type of these

are rod-shape molecules (Fig. 2.5), also known as *calamitic* LCs, which are able to manifest many different phases. The other well-known type of mesogen is discotic LC phases [4, 6]: Typical discotic, nematic and smectic mesogens are represented in Fig. 2.6.

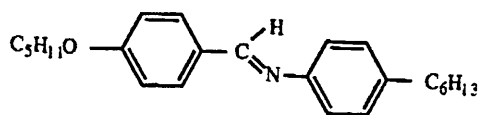


Figure 2.5: Typical calamitic liquid crystal molecule [6].

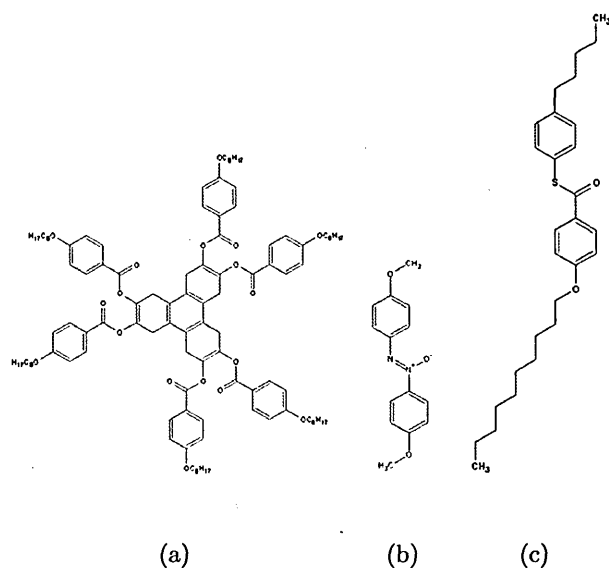


Figure 2.6: Mesogen leading to a (a)discotic (b)nematic or (c)smectic phases [7].

2.1.3 LC Phases

The simplest LC phase is the *nematic* phase (Fig. 2.7 a, Fig. 2.8). The simplest type of object which can exhibit a nematic phase is the rigid rod [5] Two other common phases formed by calamitic LCs are the *smectic A* and *smectic C* phases (Fig. 2.7 b, Fig. 2.9). As shown in Fig. 2.7, these phases not only have orientational order but also some positional order. In the smectic A, the layering is normal to the director, whereas, in the smectic C, the molecules are tilted in the

layers. If the molecules that form a LC phase are chiral (lack inversion symmetry), then, chiral phases can also be found (see Fig. 2.11). In the case of calamitic LCs, the nematic phase can then be replaced by a chiral nematic phase, in which the director rotates around an axis perpendicular to the director but with a pitch much greater than molecular dimensions (Fig. 2.10) [6].

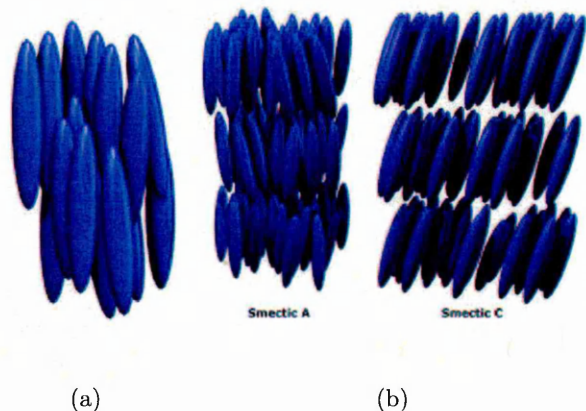


Figure 2.7: Schematic illustration of the nematic, smectic A and smectic C phases [7].

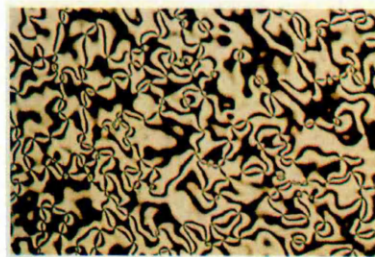


Figure 2.8: Nematic liquid crystal viewed between crossed polarizers. The LC appears dark where the director points along one of the polarizer axes. [4].

Nematic phase

Here, we concentrate on the simplest LC phase, the nematic phase. A nematic phase usually occurs below the isotropic phase, when the temperature is decreased. As we said before, this phase can be thought of as a liquid which has long range

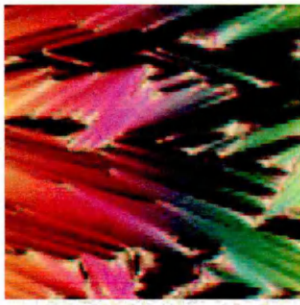


Photo courtesy of
Dr. Mary Neuber, ICI-KSU

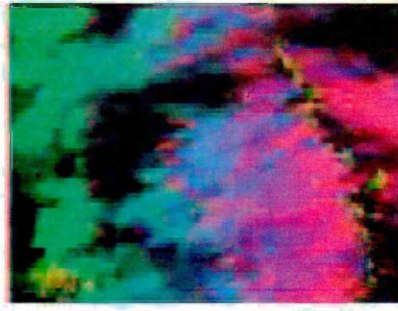


Photo courtesy Dr. Mary Neuber, ICI-KSU

(a) Photo of the smectic A phase.

(b) Photo of the smectic C phase.

Figure 2.9: Smectic liquid crystal [8].

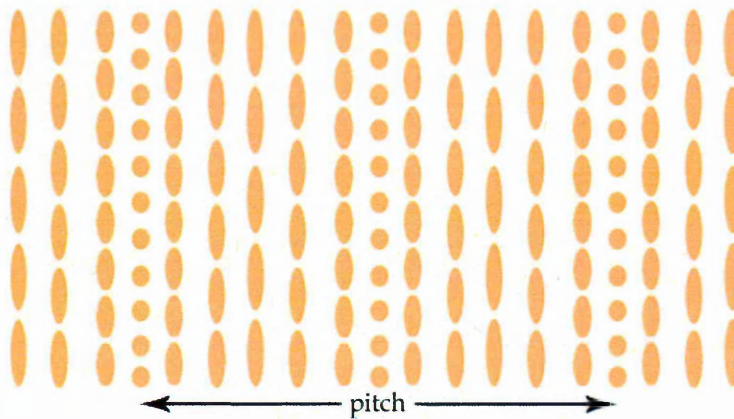


Figure 2.10: Structure of the chiral nematic phase.

orientational order, but lacks long range positional order. There are two types of nematic : *uniaxial* and *biaxial*. The uniaxial nematic is characterized by [9,10]:

- no positional order but the molecules maintain a preferred orientational direction
- the state \mathbf{n} and $-\mathbf{n}$ are indistinguishable
- the direction of the vector director is arbitrary, but can be imposed by an external force such as an applied field.

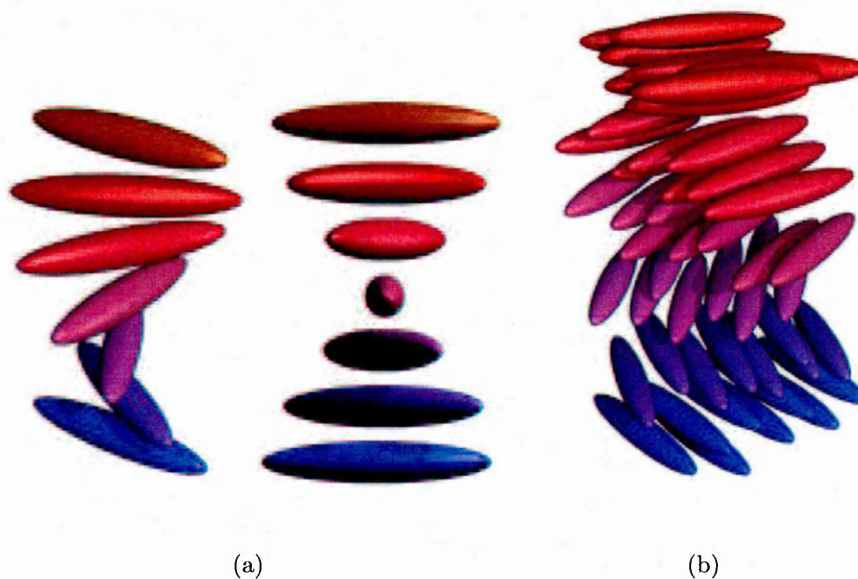


Figure 2.11: (a) A more idealized view of the nematic twisting of the cholesteric phase (viewed both on-angle and head-on). Clearly the cholesteric phase is chiral, with a very specific handedness. This chiral structure can be observed using optical techniques (for instance, by viewing the phases through crossed polarizers). (b) Structure of the twisting nematic layers. The different nematic layers have been coloured differently so as to differentiate them. The twisting of the nematic director from layer to layer is clear [7].

2.2 Applications

2.2.1 LC technology : Liquid Crystal Displays (LCDs)

We live in an age where new technologies are developed with great speed. Today, the amount of information travelling from one computer to another is huge. Nevertheless, to be able access this information, the user needs a display. It is not surprising then, that developments in display technology have accompanied those made in computer technology. In recent years LCDs have become a dominant features in laptop and now, desktop computers and it appears that they are destined to play a major role in the future. Displays function by using their ability to control light. There are two different ways to achieve this. Each area can be able to

generate light : this is called an *active display*, the most common example being the Light-Emitting Diode (LED). The second approach does not generate light, but controls the amount of light that passes through or is reflected by the display. This is called a *passive display* [4]. The most important passive display is the LCD. Passive and active displays need electrical power to work. Nevertheless, because passive displays are able to use the ambient light, they can have lower power requirements. This is one of the main advantages of these devices.

Twisted Nematic mode (TN)

The most popular LCD is the twisted nematic device, which was developed in 1971 by Schadt and Helfrich. The TN LCD consists of a layer of LC material sandwiched between two glass plates. The inner glass surfaces are treated so as to make the LC material lie nearly parallel to the surfaces. Nevertheless, the LC material at one surface is made to lie perpendicular to the other : the director of the nematic LC twists through an angle of 90° . On the outer surfaces of the glass plates are placed polarisers with orthogonal orientations. In the “off state”, the incoming light is therefore linearly polarised before entering the cell. This polarisation is then rotated by the twisted optic axis of the LC, allowing the light to pass through the second polariser. In the “on state”, when the LC material is aligned by an applied electric field, the twisted director arrangement is disrupted. Consequently, the light transmitted through the first polarizer is not rotated and so is extinguished by the second polariser (Fig. 2.12). Fig. 2.13 shows the transmission of an LCD as a function of applied voltage. This shows that the transmission level remains constant until a threshold voltage V_{th} is reached. Then, the transmission decreases monotonically to zero.

2.2.2 Other applications

Other application of LCs include their use in polymer display liquid crystals, where small droplets of LC are formed in a polymer film. Polymer dispersed liquid crystal sheets can be formed into big panels which, upon application of an electric field, can be made opaque or transparent (see Fig. 2.14). Chiral nematic materials are of great technological importance because of their ability to selectively reflect light of

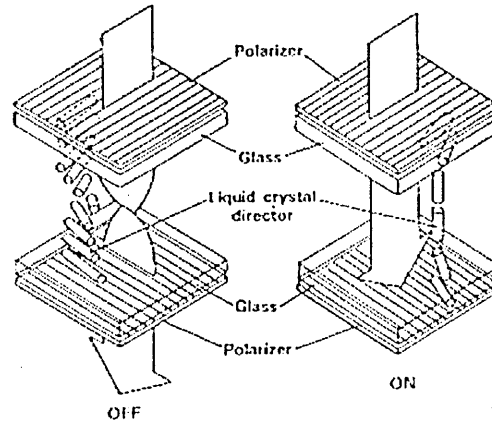


Figure 2.12: Typical Twisted nematic LDC (Normally White Mode) [11].

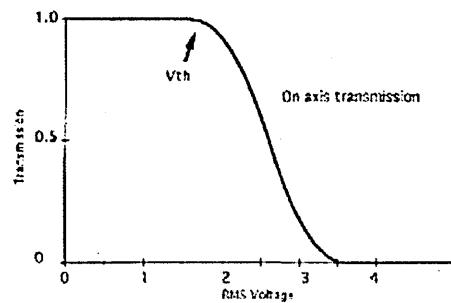


Figure 2.13: LCD transmission (brightness) as a function of applied voltage [11].

a wavelength equal to that of the pitch length. As a consequence, the chiral nematic materials can be used as thermometers which reflect different colours at different temperatures, if the pitch is suitable. LCs are now also being used for applications in photonics and organic electronics. These uses exploit the LCs ability to adopt complex dielectric structures which can either be switched able or locked in place (using photopolymerisation).

2.3 Surface effects and anchoring of LCs

The interaction between LC fluids and solid surfaces has attracted much interest. If LCs are confined between surfaces, a range of different phenomena can be observed. The most obvious of these relate to perturbations to the liquid crystalline structure close to the surface (i.e for $z \leq \xi$, where ξ is a surface correlation length). Beyond



(a)



(b)

Figure 2.14: Polymer dispersed liquid crystal sheet [12].

this region (i.e for $z > \xi$), the bulk liquid crystalline structure is recovered with an orientation which, in the absence of other applied fields, is fixed by the surfaces. This phenomenon of LC orientation by its confining substrates is called anchoring [13] and is essential for all LC cell applications, such as displays (LCDs). This macroscopic effect results from the microscopic level orientational and positional packing of the LC molecules located at and near the confining surface. Anchoring has mainly been studied using LCs in their nematic phase because, first of all, it is a relatively simple phase (no long range positional order) and secondly because the nematic phase is used in most LCD applications.

2.4 Techniques of surface alignment

2.4.1 Rubbing

This technique is the most conventional and widely used method of achieving surface alignment. This process consists of rubbing a thin organic film, such as polyimide (PI), polyvinyl alcohol (PVA), nylon, by moving a cloth on the substrate (Fig. 2.15). PI is usually chosen because its heat resistance assures the stability of the rubbed surface even at elevated temperatures [14,15].

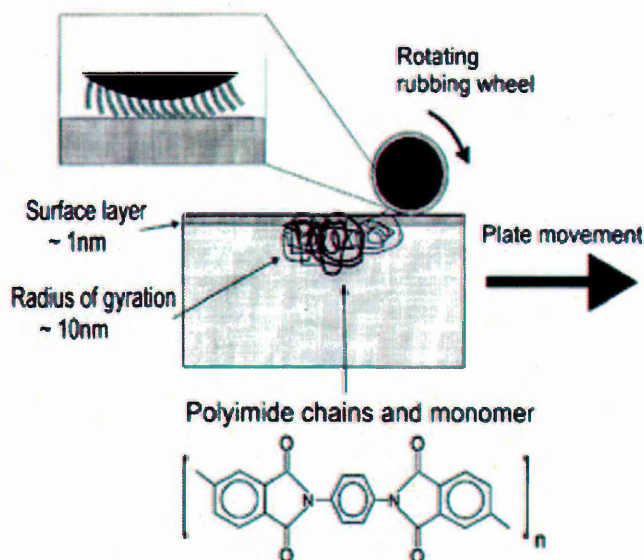


Figure 2.15: Illustration of the rubbing process.

[16].

If a nematic LC is placed on a rubbed surface, the molecules can adopt preferred alignment in terms of both their in-plane and their out-of-plane orientations. Usually, the molecules align along the rubbing direction [16,17] and the LC molecules point up from the surface by a small pretilt angle [16] (Fig. 2.16).

Alternatively, it has been found that for some thin organic films (polystyrene), the LCs tend to align in plane but perpendicular to the rubbing direction [16] (Fig. 2.16). The value of any pretilt angle depends on the surface structure of the polymer [16,18] and is very important in the sense that if it is zero, there is an

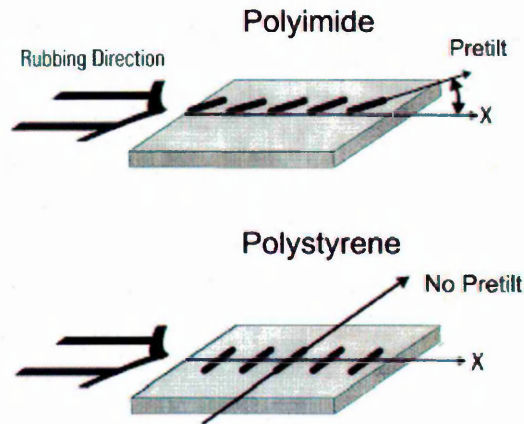


Figure 2.16: LC orientation and pretilt angle in rubbed polyimides and in polystyrene.

[16].

ambiguity in the twisting of the LC helix in a twisted nematic device [16,19] which significantly increases switching speed. Increasing the pretilt angle in LCDs is one of the most important routes to achieving high optical contrast.

Twisted nematic(TN) LCDs have been fabricated using mechanical rubbing to align the LCs. The main disadvantage of this technique is that dust and static electricity are generated [15,17,20,21]. In the production of LCDs, a washing process is used to remove the dust and the electrostatic charges generated by rubbing [15]. Even though this washing process is very useful in removing these drawbacks, it is not without consequences. For example, this process can influence the pretilt angle generation, the polar anchoring energy and the surface order parameter [15].

Finally, even though the rubbing technique is widely used, the detailed microscopic mechanisms by which it operates are not well understood.

2.4.2 Photoalignment

One of the more attractive alternatives to rubbing is the generation of a surface anisotropy in the alignment film by photochemical means [19]. As the name indicates, this alignment technique involves exposure to light. An advantage of this method is that it allows production of multi-domain displays much more readily than does the rubbing method. [14,21].

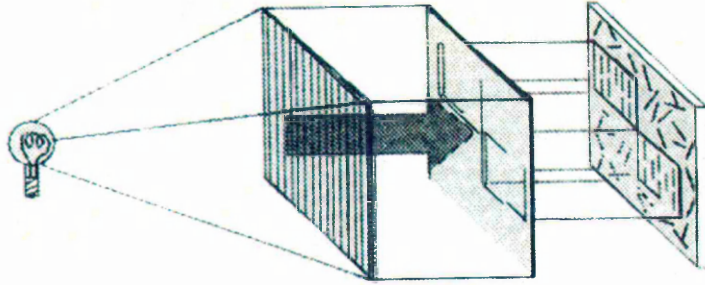


Figure 2.17: Principle of photoalignment [20].

Cis/trans isomerisation

This mechanism is typical of materials such as azo dyes (molecules containing two adjacent nitrogen atoms between carbon atoms). Azo dyes exist in two isomeric configurations : the *trans* isomer ((E)-isomer) and the *cis* isomer ((Z)-isomer). Isomer refers to a molecule for which different locally stable configurations have generally different properties. The *trans* isomer, referred as the rod-like isomer, generally favours homeotropic alignment whereas the *cis* isomer, referred as the bent-shaped configuration, induces planar alignment of LCs [19]. Under UV light, the molecules with their transition moments parallel to the polarization direction absorb light and transform into this *cis*-isomer. As this configuration is unstable, the molecules relax to the *trans*- isomer (Fig. 2.18). By repeating this process, the number of molecules with transition moments perpendicular to the polarization direction increases, so giving rise to a preferred alignment on the surface [19,20].

Crosslinking

Under UV light, some polymers undergo crosslinking. Crosslinking (Fig. 2.19) is the process of chemically joining two or more molecules by a covalent bond. Such behaviour is common in, e.g., derivatives of polyvinylcinnamate (PVC). It has been proved that PVC film, when exposed to UV radiation, gives homogeneous LC alignment perpendicular to the polarization direction of the light. More generally, depending on the polymer used, parallel or perpendicular aligning directions can be

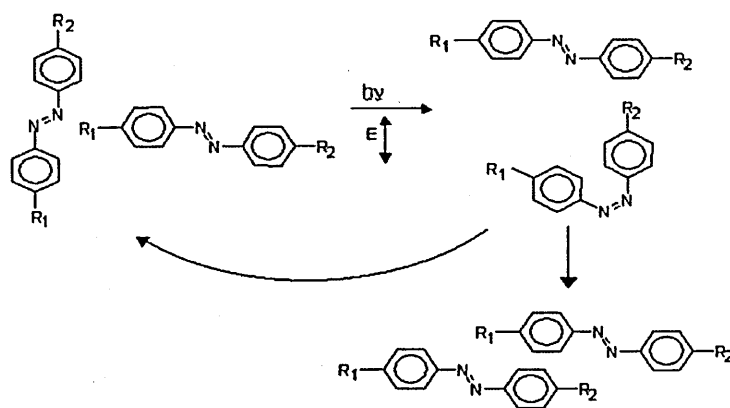


Figure 2.18: Example of the isomerisation of an azobenzene.

[20].

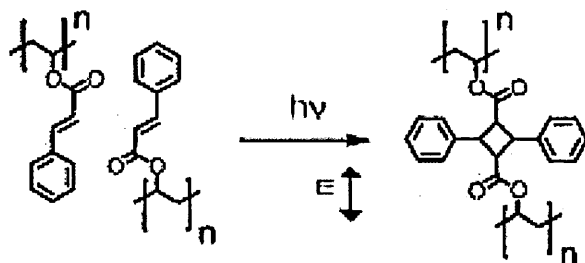


Figure 2.19: [2+2]-cycloaddition reaction of a cinnamate moiety.

[20].

obtained. The best crosslinkable material reported so far is the coumarin side-chain polymer [19].

Photodegradation

This third technique by which polarized light can be used to produce LC-aligning substrates, is centred on selective degradation of PI type of polymers. In this case, UV light degrades the molecules that are aligned along the polarization direction (Fig. 2.20). Consequently, after the exposure, the chains of the polymer are not isotropically distributed anymore, tending instead to align in a preferred direction. This technique suffers from some disadvantages such as the creation of electric charges during the photochemical reaction. More significantly, if the material is

over exposed, the bonds that are directed in the preferred direction can break due to an “overdose” [19, 20]. The use of substrates made using this technique also

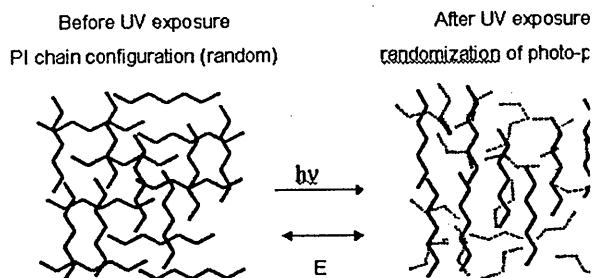


Figure 2.20: Schematic mechanism of polyimide degradation.

[20].

seems to affect the performance of LCDs. For example, it has been found that the polar anchoring energy is 10 times lower than that of rubbed PI [19].

Discussion

To summarise, three different techniques can be used to give photoalignment : *trans/cis* isomerization, crosslinking (or dimerization process) and photodegradation. The long term stability of azo-containing alignment material is poor because of its photochemical sensitivity to visible light. The anisotropic degradation of PI shows poor thermal stability. The polar anchoring of PI has also been found to be affected by this decomposition.

On the other hand, PI has been developed to give a full range of pretilt angles from 0° to 90° and the photosensitivity of the material can be changed by molecular design. As mentioned before, the best crosslinkable material is the coumarin side-chain polymer. This material is extremely photosensitive to polarized UV but shows excellent thermal and photochemical stability after alignment.

2.5 New technique : Self-Assembled Monolayers (SAMs)

SAMs are used in a number of different applications such as corrosion prevention, lithographic resists and biomolecular recognition. Patterned SAMs are SAMs which have a specific spatial distribution. When used appropriately as substrates for LC adsorption, this can lead to different preferred anchoring arrangements in neighbouring substrate regions. The interaction between a SAM-coated substrate and the adsorbed molecules depends on the chemical natures of both species.

2.5.1 Historical development of SAMs

At the end of the 19th century, people started to study organic films. In the 1890s, Pockels [22] studied monolayers at the air water interface and in the 1920s Langmuir [23] made monolayers of amphiphilic molecules on water. In the 1930s, Blodgett [24] studied the deposition of long chained carboxylic acids on solid surfaces and in 1946, the first SAM was observed. Zisman reported the spontaneous absorption of alkyamine on a platinum substrate. In 1983, Nuzzo and Allara [25] worked on the thiol/gold SAM formation.

There are many ways to form monolayers on surfaces. SAMs are obtained by immersing a surface in a solution whose molecules have strong chemical affinity with that surface [26]. The most studied SAMs are those formed at metal surfaces by surfactants with electron-rich head groups and n-alkyl tails. A typical SAM system (Fig. 2.21) can be obtained by immersing a gold-covered substrate into an alkanethiol solution. The molecules used to form SAMs are commonly composed of three parts :

- A group binding with the surface. There are different systems used for the binding: thiol/semiconductor; carboxylic acid/oxide; but the most widely used is thiol/Au. The binding is achieved by chemisorption (in which the enthalpies of interaction are high: greater than 10 kcal/mol) or physisorption (in which the enthalpies of interaction are low) [26].

- A central chain of chosen length.

- An end group which determines most of the behaviour of the SAM.

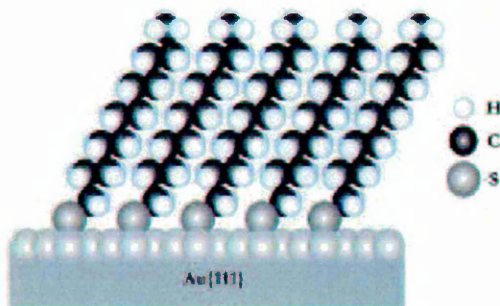


Figure 2.21: Schematic of an n-dodecanethiolate monolayer self-assembled on an atomically smooth gold substrate. The assembly is established by the bonds between the sulphur headgroups and the gold surface as well as van der Waals interactions between neighbouring hydrocarbon chains [26]

2.5.2 Liquid crystal alignment on SAM

Drawhorn and Abbott [27] reported, in 1995, the use of SAMs formed from alkanethiol on gold to study the anchoring of LCs on surfaces. In this work, they reported that mixed SAMs, formed from n-alkanethiol with long and short aliphatic chains, were able to homeotropically align nematic phases of MBBA or 5CB (Fig. 2.22). In comparison, single-component SAMs : $HS - (CH_2)_n - (CH_3)$ (with $2 < n < 15$) lead to random planar or tilted alignment. Drawhorn and Abbott also demonstrated patterning of LCs through the use of a polydimethylsiloxane (PDMS) stamps (Fig. 2.23). In 1996, Evans and co-workers subsequently showed that func-



Figure 2.22: Chemical structures of MBBA and 5CB

[27].

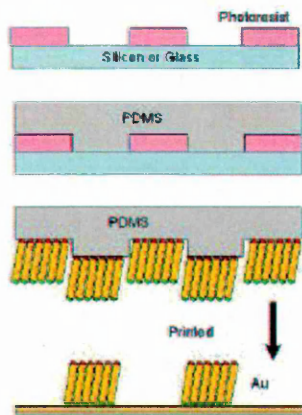


Figure 2.23: PDMS printing scheme

[25].

tionalised SAMs can be used to control the anchoring of LCs [28]. It was found that low-energy CF_3 surfaces gave homeotropic anchoring for $8CB$ but an anchoring transition for $5CB$. High-energy $COOH$ and OH surfaces gave planar alignment for $5CB$ and for $8CB$. In 1996, Gupta and Abbott [29] published the first results using SAMs formed from alkanethiols on the surface of obliquely deposited films of gold. They reported that SAMs supported on obliquely deposited films of gold permit uniform, planar, or tilted anchoring of nematic LCs. In 1999, Alkhairalla *et al.* [30] published a more complete study of the anchoring of nCB materials on SAMs. Evanescent wave ellipsometry was used to determine the orientational wetting of various $nCBs$ ($n=5-9$) at the interface with a series of SAMs. From this it was shown that OH and $COOH$ -terminated monolayers give planar alignment for all the nCB LCs ((Fig. 2.24)).

2.5.3 Patterning SAMs

Printing approaches gained attention when, in 1993, Kumar and Whitesides [31] discovered that a polymer inked with an alkanethiol solution and brought into contact with gold can lead to formation of a monolayer of the adsorbing molecules in the area of contact. Microcontact printing involves the use of soft lithography to pattern SAMs in a high resolution, low cost, easy to use approach. This technique

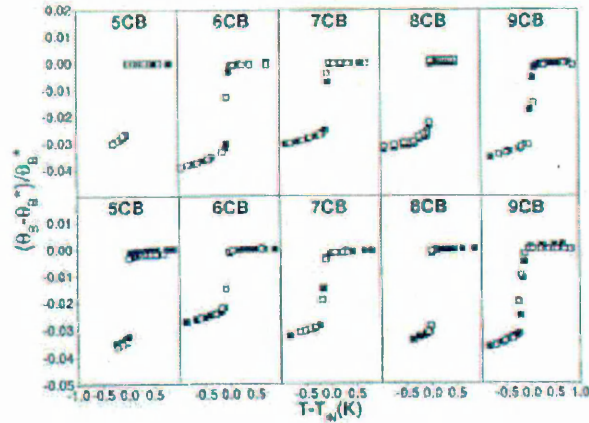


Figure 2.24: Orientational wetting and anchoring data for nCB liquids on $COOH$ (top set) and OH monolayers (bottom set). For temperatures above the isotropic-nematic bulk transition temperature (T_{IN}), the ordinate is a direct measure of the amount of nematic film adsorbed at the substrate-isotropic interface. Below T_{IN} , the ordinate measures the strength of alignment in the mesoscopic region of the nematic phase probed by the evanescent field. The reduction in the Brewster angle indicates planar anchoring. [30].

is called soft lithography because the key element used to transfer the pattern to the substrate is an elastomeric stamp and not a rigid inorganic material of the sort usually used for the fabrication of microelectronic systems [32]. Soft lithography relies on a patterned stamp formed from a master. The masters used in soft lithography are made from silicon with a vertical inverse of the desired pattern. For features greater than $1 \mu m$, photo lithography is used to fabricate the master. Otherwise, electron-beam lithography is used. Stamps are created by pouring liquid polydimethylsiloxane (PDMS) onto the masters, and then curing at a temperature between 20 and 80 degrees C for up to 48 hours (Fig. 2.25). The PDMS is then removed from the master and used to directly print the SAM on to the substrate [32].

PDMS is well known to be able to produce high quality SAM patterns. There are several advantages in using PDMS. PDMS is an elastomer which is deformable enough to properly coat the substrate even if the surface is nonplanar. Also, because it is a durable elastomer, it is possible to use the same stamp about 100 times.

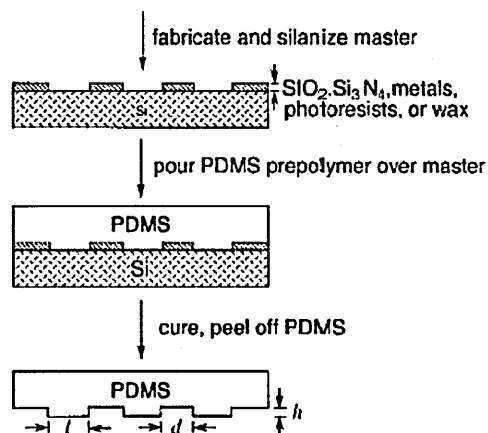


Figure 2.25: Schematic illustration of the procedure for casting PDMS replicas from a master having relief structures on its surface. [32].

Nevertheless, this technique suffers some problems due to deformation or distortion of the microstructure of the PDMS surface. These deformations are known as pairing, sagging and shrinking (Fig. 2.26). To overcome some of these problems, stiffer materials have been developed. These materials are also based on PDMS but are harder and result in more accurate patterning, but they introduce new problems like non-conformal contact with the substrate. To solve these problems, hybrid stamps have been created, in which a thin hard PDMS (hPDMS) layer is covered with a soft PDMS layer followed by a hard back plate [33].

When generating a patterned SAM, the stamp is initially inked with the first alkanethiol solution and dried before being put into contact with the substrate. The thiol diffuses out of the PDMS and forms a SAM in the areas of contact. On submerging the partially coated substrate in a second alkanethiol solution, the thiol of this second solution forms another SAM in the regions that were not in contact with the stamp. This is known as “backfilling”.

2.6 Liquid crystals on patterned substrates

Patterning substrates on the micron-scale is now routine surface science. Some of these methods present no major obstacles to significantly reducing the features

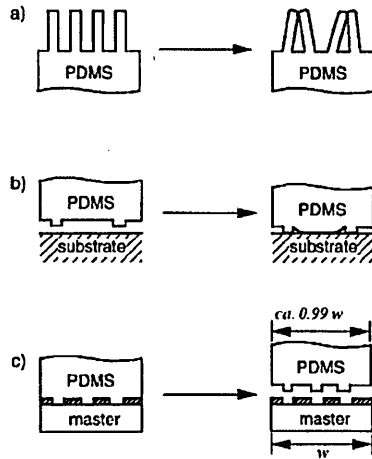


Figure 2.26: Schematic illustration of possible deformations and distortions of microstructures in the surfaces of PDMS stamps. a) Pairing, b) sagging, c) shrinking [32].

towards the nano-scale. However, for obvious reasons, almost nothing is known experimentally about liquid crystal (LC) anchoring on patterned substrates when the pattern scale falls below the wavelength of light. Whereas conventional uniaxial alignment is sufficient for many applications, more sophisticated, patterned alignment offers the prospect of improving the optical performance of devices, for instance with respect to the viewing angle. Patterned LC alignment raises various questions, such as “Can tilt be induced and controlled using patterning?”; and “Can patterning give independent control over the two anchoring coefficients?”. Kumar *et al.* [34] showed that substrate morphology at sub- μm scales is of great importance in determining LC alignment. Specifically, they concluded that anisotropy in surface morphology of a substrate on a submicron length scale can play a defining role in determining the resulting anchoring behaviour.

Some displays being developed for the hand-held device market require two optically-distinct stable states (i.e. bistability). The ZBD (Zenithal Bistable Device) [35] achieves this by using a blazed grating which has stable “continuous” and “defect” states. In recent years, much attention has been given to using patterns to achieve bistable switching in LC devices, due to its potential to combine high display resolution with significantly decreased power consumption. Kim *et*

al. [36–38] presented a general approach to establishing in-plane alignment bistability by exploiting the orientational frustration induced by a checkerboard pattern. Lee *et al.* [39] subsequently demonstrated a continuous variation in LC pretilt using a checkerboard pattern comprising regions with orthogonally etched grooves. Bechtold and Oliveira [40] also experimentally investigated the equilibrium configuration of the director for a submicron patterned substrate. Here, alternating homeotropic and random planar stripes were generated by selectively irradiating a SAM with UV. James *et al.* [41,42] also studied striped patterns in their modelling of an LCOS (Liquid Crystal on Silicon) device. Here, the patterning was achieved using high-resolution linear electrodes with rewritable input voltages. It is apparent, then, that a range of patterning approaches-topological, electrical, chemical, ...- are now being considered for achieving bistability in LCD applications.

2.7 Results from our collaborators

The simulation results presented in the later chapters of this thesis were generated as part of a collaboration project with J. Bramble, S. Evans and J. Henderson of Leeds University. Here, we show typical examples of the experimental results obtained by our collaborators for nematic LCs confined between one patterned SAM and one uniform SAM homeotropic substrates.

2.7.1 Stamps

Fig. 2.27 shows a selection of the stamps used by our collaborators in Leeds. These stamps are immersed in an ethanol solution 12 hours prior to use to prevent contamination of the printed surface by short chained PDMS.

2.7.2 Circle patterns

Arrays of circles were formed by printing a CF_3 SAM to leave circular voids which were backfilled with a $COOH$ SAM. The sizes of the circles determine the nature of the LC disclinations that form as a result of the patterned surface. If the circles are $20\mu\text{m}$ in diameter, it is possible for multiple domains to form within each circle

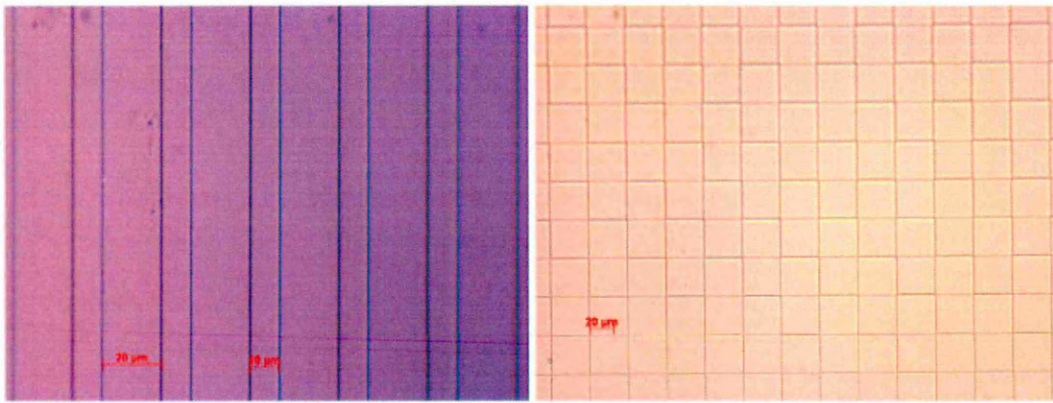


Figure 2.27: Optical images of PDMS stamps

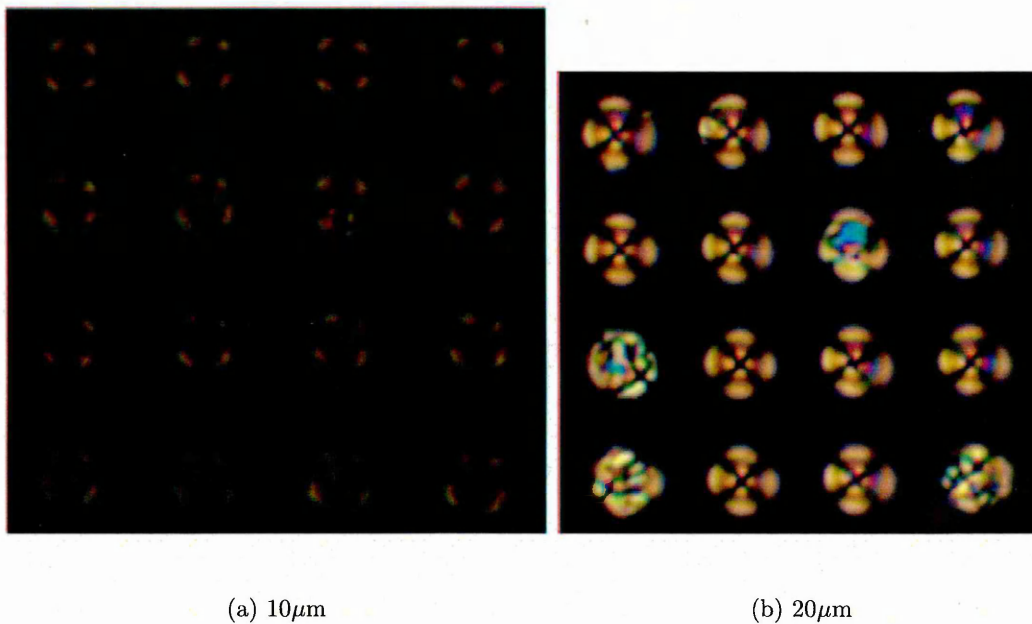


Figure 2.28: Nematic *9CB* aligned on circular SAM patterns and visualised through crossed polarisers

(Fig. 2.28(b)). Decreasing the sizes of the circles to 10 μ m (Fig.2.28(a)), leads to the formation of a single domain in each circle.

2.7.3 Stripe patterns

Stripes of different widths have been examined in Leeds by our collaborators. They started with 50 μ m stripes and saw that the alignment is oriented down the stripes

rather than being random planar. This implies that the line defects along the stripe boundaries tend to twist rather than splay. We deduce this from the splay defects seen in Fig. 2.29. Fig. 2.30 shows a schematic diagram of the LC structure in the stripe region and around one of these splay defects. The splay defects occur due to the degeneracy of the director along the stripes. Fig. 2.31 shows a polarising microscopy image of 9CB aligned on a multi-stripe substrate. Here, the alignment of the LC along the stripes is very uniform, as indicated by the consistent colour of the striped regions.

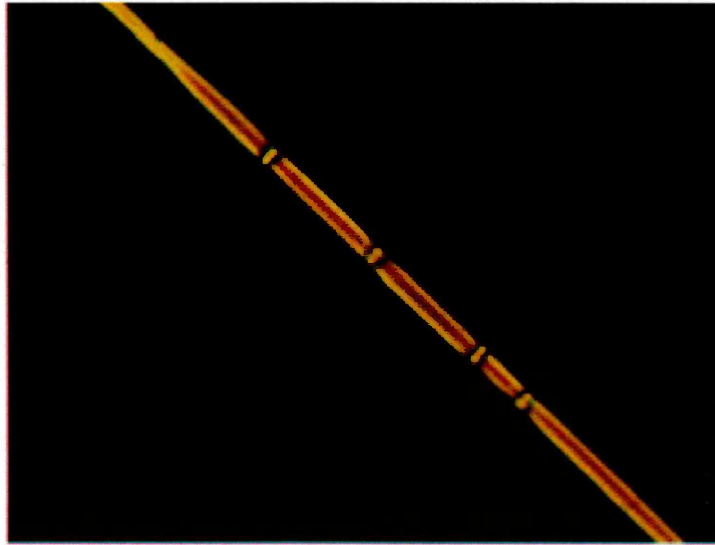


Figure 2.29: Nematic 9CB aligned on $10\mu\text{m}$ stripe

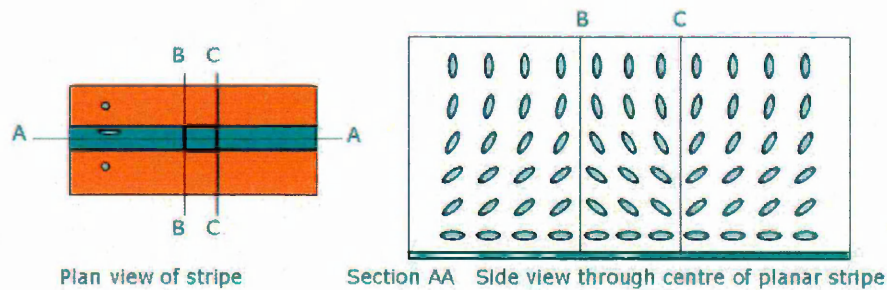


Figure 2.30: Structure of the LC aligned on stripes of $10\mu\text{m}$

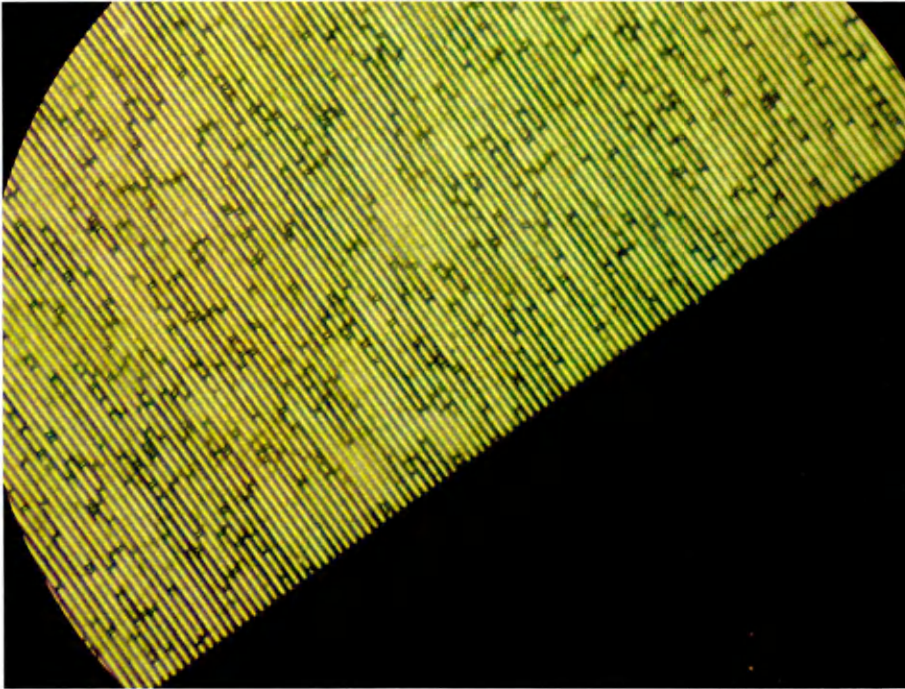


Figure 2.31: Nematic 9CB on $2\mu\text{m}$ stripes of COOH and CF_3 in a $23\mu\text{m}$ cell, visualisation through crossed polarisers.

2.7.4 Checkerboard

A checkerboard pattern of CF_3 and COOH SAMs was printed with $8\mu\text{m}$ squares. The patterned surface was constructed into a cell and filled with the LC 9CB. It was noted by our collaborators that the thickness of the samples determined the texture seen. In the case of thin samples ($13\mu\text{m}$), the homeotropic-homeotropic (H-H) regions were black. If the cell thickness was increased ($23\mu\text{m}$), these regions appeared light, indicating a splay in the bulk. Fig. 2.32 shows a microscopy image of a thick sample. From this image, we can deduce that the director points diagonally across the squares. There are two different degenerate states where the director points along two opposite diagonals. These degenerate states are optically identical, but the splay and twist in the HH regions indicate where their boundaries lie. The HH regions are splayed and twisted in the bulk of the cell due to their proximity to the splayed state above the planar-homeotropic (PH) regions. When a HH region is surrounded by four PH regions of the same hybrid aligned nematic (HAN) configuration, the director points in the same direction across the diagonal.

However, when it is surrounded by PH regions with different HAN configurations, the director is not able to match the orientation of the director at each boundary. This can be seen optically as darker HH squares. As these regions are caused by having different neighbouring PH regions, they form a border around each of the degenerate states. Fig. 2.33 shows a schematic example of these different states and how they relate to Fig. 2.32.

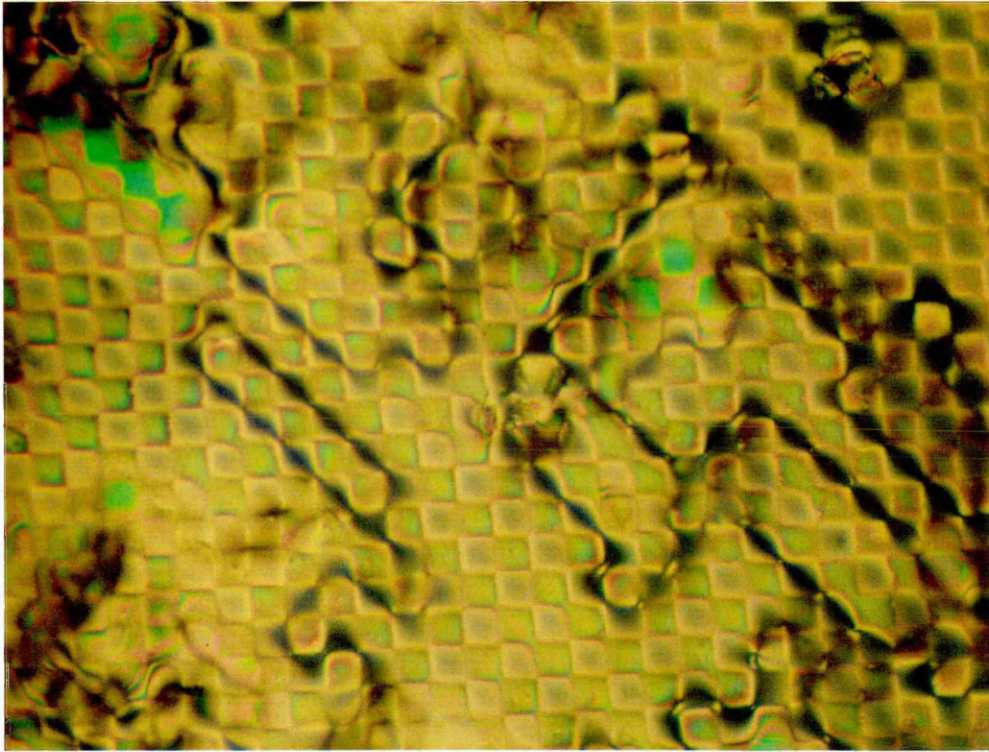


Figure 2.32: Nematic LC aligned on $8\mu\text{m}$ squares. Visualisation through crossed polarisers

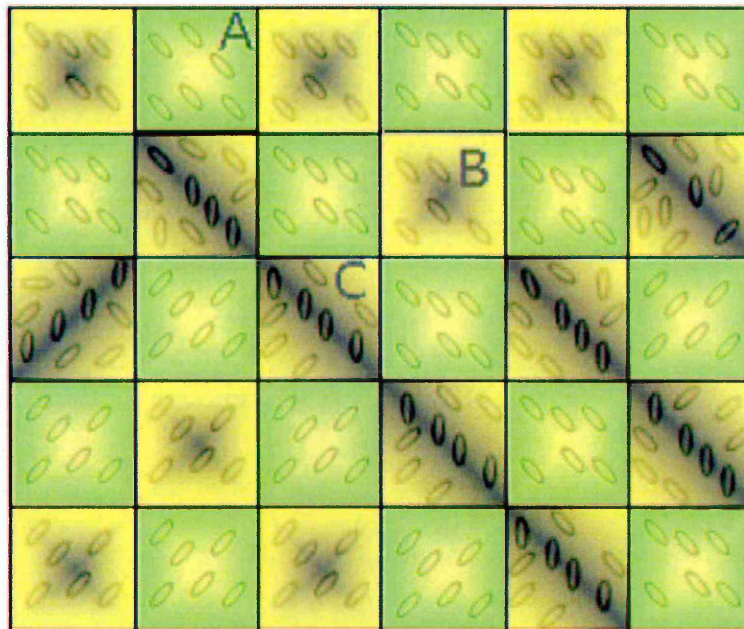


Figure 2.33: Schematic showing the bulk director orientation on a square-patterned substrate. A - PH region, B - HH region with identical neighbours, C - HH region with different neighbouring PH regions. Note the direction of the LC director in an HH region tries to match that of its neighbours

Chapter 3

Liquid crystal simulations

This chapter contains an overview of the modelling method used to simulate liquid crystals. First of all, we present studies of bulk ordering and then studies of confined systems. There are two main types of model, generic LC lattice models and off lattice models. The latter can be split into two main types, hard and soft particle models. These two main model types have been studied extensively. We present in this chapter a review of the work done with off lattice model, from early results to more recent studies.

3.1 Simulation of LCs

Computer simulations of many-body systems can be used to gain insight into the microscopic behaviour of real liquids and solids. There are two distinct but nevertheless complementary approaches for this which are in common use. On one hand, realistic molecular models can be used in order to assist the interpretation of real experiment. On the other hand, idealized models can be adopted in order to make close comparison with theoretical concepts. In the case of LCs, comparison between experiment and simulation is difficult because such simulations are very time consuming.

3.1.1 The Monte-Carlo (MC) Method

The Monte Carlo method is used to find the solution of mathematical problems using a probabilistic approach; it has been applied to a wide variety of different

problems. In the molecular physics of LCs, the term MC usually refers to the use of a specific sampling method as proposed by Metropolis [43]. The original Metropolis algorithm was proposed to simulate the evolution of a system at a defined temperature T towards thermal equilibrium. Let us imagine that the system, initially in the state a of energy E_a , evolves into a new state b of energy E_b . If E_b is lower than E_a , state b becomes adopted as the new state because the lower the energy is, the more stable the state is. Otherwise, the state b is accepted with the probability : $A_{ab}(T) = e^{-\frac{(E_b-E_a)}{kT}}$. Let us consider a system of N particles in the canonical (constant NVT) ensemble and let us assume that the particles are interacting in a pairwise fashion. The total potential ν is then given by :

$$\nu = \sum_{i < j}^N U(\mathbf{X}(i), \mathbf{X}(j)) \quad i, j \in [1 \dots N]$$

where \mathbf{X} is the complete set of positions and orientations of the system. In this canonical ensemble, a time independent configurational property can be obtained from :

$$\langle A \rangle_{real} = \int \rho_{NVT}(\mathbf{X}) A(\mathbf{X}) d\mathbf{X}^N \quad (3.1)$$

with :

$$\rho_{NVT} = \frac{e^{-\beta\nu}}{Q_{NVT}} \quad (3.2)$$

Q_{NVT} being the partition function for the canonical ensemble. If the system is ergodic, $\langle A \rangle_{real}$ can be obtained by averaging its instantaneous values over a sufficient number of uncorrelated state points, Γ_i , provided that they appear with a probability density appropriate to the considered ensemble. Therefore :

$$\langle A \rangle_{real} = \frac{1}{M} \sum_{i=1}^M A_i \quad (3.3)$$

Metropolis *et al.* designed a stochastic process for creating such a sequence of state points in the canonical ensemble where each configuration, Γ_i , appeared with a probability $e^{-\beta\nu}$. This sequence corresponds to a discrete Markov chain, that is a stochastic sequence of states within each step of which, memory extends only to the preceding state. A Markov chain is a sequence of trials that satisfies two conditions [44] :

1. The outcome of each trial belongs to a finite set of outcomes, $\{\Gamma_1, \Gamma_2, \dots, \Gamma_m, \Gamma_n, \dots\}$, called the state space.

2. The outcome of each trial depends only on the outcome of the trial that immediately precedes it.

π is defined as the transition matrix, with the element π_{mn} being the probability of moving from state m to state n (see Fig. 3.1). The probability that a system is in a particular state is given by a state vector $\mathbf{p} = \{p_1, p_2, \dots, p_m, p_n, \dots\}$. What is required is a transition matrix such that the limiting distribution of the chain,

$$p = \lim_{\Gamma \rightarrow \infty} p^1 \pi^\Gamma$$

is equal to the desired distribution, p_{NVT} . The limiting distribution must satisfy the eigenvalue equation

$$p\pi = p \quad (3.4)$$

$$\sum_m p_m \pi_{mn} = p_n$$

with eigenvalue unity. This can be achieved by satisfying microscopic reversibility. The condition of microscopic reversibility requires that the probability of going from state b to a is equal to that of the reverse transition and, therefore :

$$p_a \pi_{ab} = p_b \pi_{ba} \quad (3.5)$$

The transition matrix for the system under consideration is not directly available, however the limiting distribution p_∞ is known to be the probability density of the canonical ensemble (ρ_{NVT}), that is :

$$p_\infty = p_{NVT}(\Gamma_\infty) \quad (3.6)$$

$$= \frac{1}{Q_{NVT}} e^{-\beta\nu(\Gamma)} \quad (3.7)$$

In this most basic form, the Metropolis method considers a two dimensional system of circular particles. Let us imagine a system of N particles. One particle i is chosen at random. This particle is moved at random. A new position is assigned to this particle. $\delta\nu_{ab}$ is the difference of energy between the two states,

$$\delta\nu_{ab} = \nu_b - \nu_a \quad (3.8)$$

The move is accepted if $\delta\nu_{ab} \leq 0$. However, if $\delta\nu_{ab} > 0$, the move is accepted with a probability $e^{-\beta\delta\nu_{ab}}$. To achieve this, a random number $\zeta \in [0, 1]$ is generated, the

move being accepted if $\zeta \leq e^{-\beta\delta\nu_{ab}}$ and rejected otherwise. The method can be extended to three dimensional systems of non spherical and even non rigid molecules. In this case, one particle i is chosen at random and is translated and rotated at random. Consequently, a new position and a new orientation are assigned to this molecule. The attempted move is then accepted or rejected using the same energy change criterion described previously.

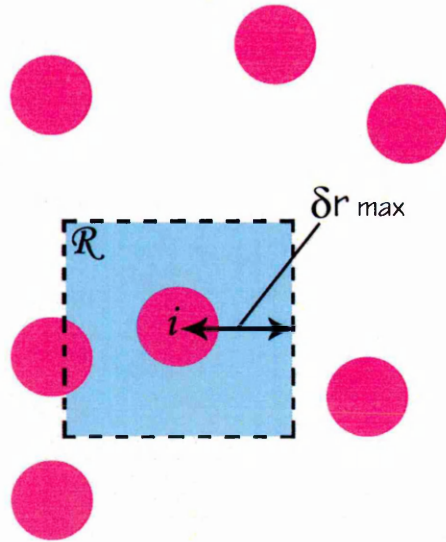


Figure 3.1: In a system of 2D State n is obtained from state m by moving atom i with a uniform probability to any point in the blue region R

MC algorithm

1. A particle i is chosen at random
2. New random position (and orientation) are calculated
3. if $(\delta\nu_{ab} \leq 0)$ or $(\zeta \leq e^{-\beta\delta\nu_{ab}})$
 Move accepted
 else
 Move rejected
4. Instantaneous observable are calculated and stored
5. Return to step 1 until n_{step} performed

6. Observable averages are computed

3.1.2 Practical aspects

Periodic boundary conditions [45]

Commonly, molecular simulations are used to shed light on macroscopic behavior and obtain information that is not easily determined from experiments. Typical computer simulations employ 10^2 to 10^6 particles, the limit on the system size being due to computational time. These numbers are still far below the real sizes of most systems. The behaviour at the system boundaries is, therefore, a major issue. The states of particles near the boundaries are different from those of particles more fully surrounded by other particles, because the particles surrounded by boundaries have deficient bonds. In order to model a macroscopic system in terms of a finite simulation system of N particles, the concept of periodic boundary conditions is often employed. Within this, periodic images of the basic simulation configuration are replicated in one, two or three dimensions (Fig. 3.2). If a particle leaves the system through one side, it then re-enters on the opposite side (molecule represented in green on Fig. 3.2), thus keeping the number of particles constant.

Minimum image convention [44]

The central box in Fig. 3.3 contains eleven molecules. The dashed box constructed with molecule 1 at its centre also contains eleven molecules. The dashed circle represents a potential cutoff beyond which the molecule's interaction strength is zero. In such a system, the interaction between particles is readily computed according to the minimum image convention. A particle interacts with its nearest neighbours or images from the neighbouring boxes. Implementation of a cutoff distance r_c (see Fig. 3.4), for short range potentials allows for neglect of weak interactions on distances exceeding a few molecular lengths. If L is a side of a cubic simulation box, the requirement $L > 2r_c$ has to be satisfied. Using a cutoff creates discontinuities in the potential energy and any force functions which can affect the results by providing energy sinks. The discontinuity in energy can be removed, though, by imposing an appropriate shift on the potential so that it is exactly zero at the

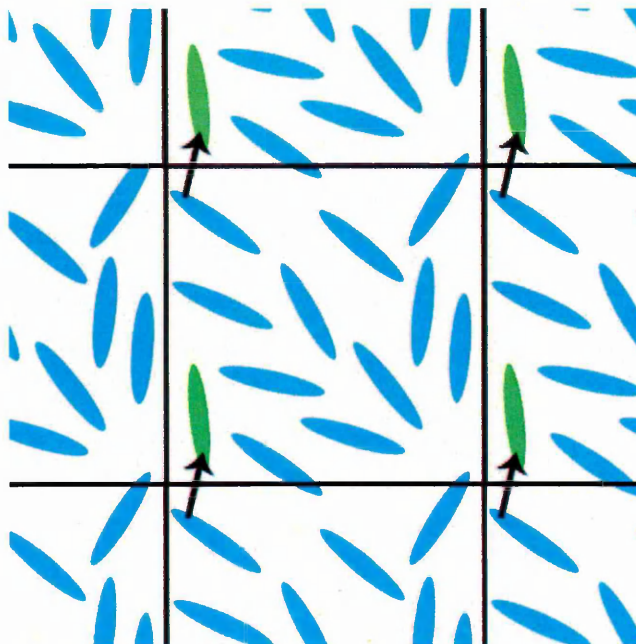


Figure 3.2: Two dimensional periodic system. The molecules can enter and leave each box across each of the four edges.

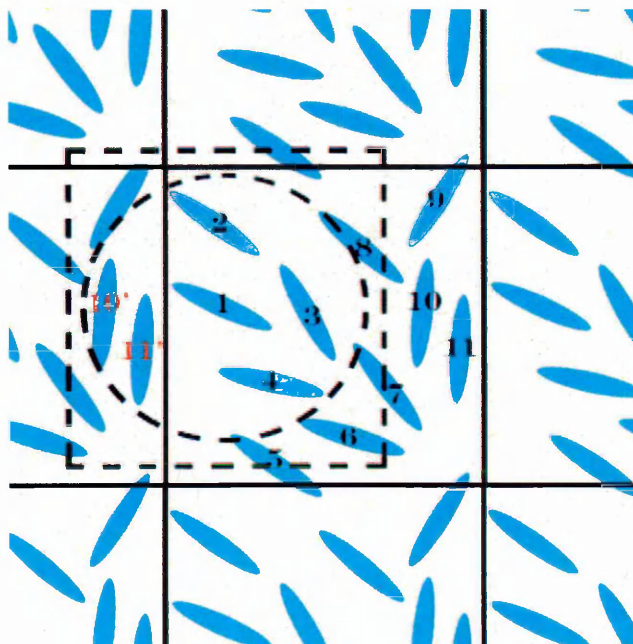


Figure 3.3: The minimum image convention in a two-dimensional system.

cutoff distance.

Verlet Neighbour list

When a potential function has a spatial cutoff, particles at a large separation from each other do not interact. The Verlet neighbour list is an algorithm for utilising this property. The neighbour list contains all of the particles which are within or nearly within an outer cutoff radius r_c of each particle. This is shown in Fig. 3.4 where r_c is the cutoff in the potential and r_l is the cutoff in the Verlet neighbour list. When determining a particles interactions, only the subset of particles initially found to be within r_c are considered as possible contributions. As the simulation proceeds, particles translate, making it necessary, from time to time, to update the list of particles. If $r_l - r_c$ is too small then the array will need to be updated too frequently, if it is too large then, at every function evaluation, an unnecessary number of calculations will be performed. Typically an $r_l - r_c$ value of $0.1 r_c$ is found to be the best compromise between these two competing factors. Fig. 3.4 shows the cutoff and its skin around molecule 1. Molecules 2, 3, 4 and 5 are on the list of molecule 1. Molecule 6 is not. Only molecules 3, 4 and 5 are within the range of the potential at the time the list is constructed. At some later time, particle 6 has translated to location 6'. If the list update criterion is validated, this particle will join the list even though it is not yet interacting with the central particle.

Reduced units [44]

In computer simulation, instead of using the real units of length, time, energy, etc, we use what we call reduced units. In the case where the system has got some characteristic length, for example it is sensible to use it as a unit of length.

In our models, there is a characteristic length and (for some systems) a characteristic energy, σ_0 and ϵ_0 respectively. consequently, all distances have been measured in units of σ_0 and all energies in units of ϵ_0 . The unit of density then becomes $1/\sigma_0^3$ and the unit of the force becomes ϵ_0/σ_0 .

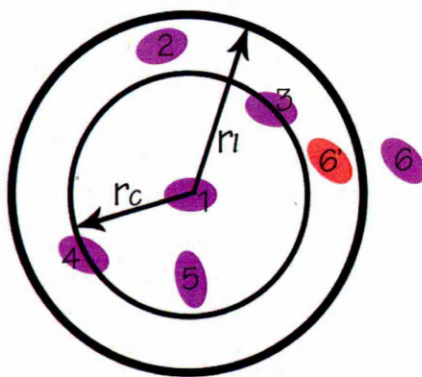


Figure 3.4: The interaction cutoff r_c , and neighbour list cutoff r_l , around a molecule 1.

3.2 Molecular modelling of bulk LC behaviour

3.2.1 Lattice models

The simplest generic LC model is the lattice-based Lebwohl-Lasher model [46]. In this, the LC is represented by spins located on a simple-cubic lattice with periodic boundary conditions, each spin interacting only with their nearest neighbours. On cooling, this model undergoes a first order phase transition when the spin orientations become aligned with one another.

In 1986, Fabbri and Zannoni [47] investigated the Lebwohl-Lasher model to determine if this model is detailed enough to display the important characteristics of the I-N transition. They performed MC simulations of a cubic lattice system with periodic boundary conditions. According to their simulation results, the Lebwohl-Lasher model exhibits many of the features seen experimentally at the I-N phase transition.

Some variants of the Lebwohl-Lasher model have been used to investigate the behaviour of lattice system of biaxial particles [48] and the phase diagrams have been

determined. Other variants have been used to study the phase behaviour of thin uniaxial liquid crystal films with competing surface fields [49].

3.2.2 Off lattice model

We now consider LC models in which freely-translating particles are used to represent individual molecules. The earliest work in this area concentrated on the effects of particle shape on the interactions of colloidal particles. In 1949, Onsager considered rigid and hard anisotropic particles [50]. In his approach, Onsager made assumptions that the rods are not able to intersect each other (i.e. they interact through steric repulsion), the volume fraction is much less than one and the rods are very long. He then showed that such a system can exhibit a density-driven I-N transition and so, that attractive forces are not necessary to drive orientational order in such system. However, because of its assumptions, this theory cannot be applied to systems where the particle elongation is less than 5.

3.2.3 Hard particles

We know that hard repulsive forces have a dominant effect on the structure of dense fluid systems. This is why interest in studies of hard bodies has been stimulated. In such systems, the repulsive forces are modelled in a simple way and the attractive forces are totally neglected. Because these systems are relatively easily simulated, they have frequently been used as first testing systems for theory [51].

Hard Ellipsoid of Revolution(HER)

In 1972, Vieillard-Baron [52], was the first to study (by Monte-Carlo simulation) the properties of a two-dimensional system of long hard ellipses, introducing the notion of a “contact function”. Due to limitation in computer power, Vieillard-Baron was not able to perform a three-dimension study of this system. He showed that, for sufficient long ellipsoids, the two-dimensional system can exhibit two first-order phase transitions : a solid-nematic transition and a nematic-liquid transition. He concluded stating that a study of a three-dimensional system would be of interest.

A systematic investigation of ellipsoidal fluids was difficult to perform because of

the problem of finding a suitable contact function for deciding whether or not two ellipsoids were overlapping. This was overcome when Perram and co-workers [53,54] defined a new contact function which was used by Frenkel *et al.* [55,56] to establish the first phase diagram of a system of hard ellipsoids of revolution (HER) for a range of length-to-breadth ratios. They found a remarkable symmetry between systems with inverse length-to-breadth ratios. Specifically, they found that the phase diagram for HER is virtually symmetrical not only at low density but also at high density where there is a high degree of orientational order. The authors clearly identified four different phases : isotropic fluid, nematic fluid, ordered solid and plastic solid. However, they found nematic phases only for length-to-breadth ratios greater than 2.75 (and length-to-breadth ratios lower than $1/2.75$ for a system of oblate particles). They presented results as well for hard-sphere and hard-platelet systems. Using a similar model of HER, Allen and Frenkel [57] have been the first to concentrate on pretransitional phenomena associated with the I-N phase transition. They reported the observation of the divergence of the collective rotation time in the isotropic phase approaching the I-N transition. They emphasized, just like in [56], that the isotropic-nematic transition is first order. Then, Allen and Frenkel [58] concentrated on the nematic phase itself and presented the first results, by computer simulation, of the Frank elastic constants of a LC composed of freely translating and rotating molecules. They modelled a HER system in the nematic region and also a hard spherocylinder system at three different densities. They found that the elastic constants are of the correct order of magnitude and in the expected ratios with $K_3(\text{bend}) > K_1(\text{splay}) > K_2(\text{twist})$. Even if their results were encouraging, they were limited, because of the capacity of the supercomputer, in system size and running simulation time.

Later, studies of systems with length-to-breadth ratios $L/D=1/10, 1/5, 1/3, 3, 5$ and 10 were performed. In all cases, a spontaneous nematic phase developed. In reviewing this work, Allen and Wilson underlined, like Frenkel *et al.*, the fact that there are similarities between prolate and oblate systems [59]. However, they showed that there are, also, systematic differences : systems of oblate particles are slightly more aligned at a given density than those of prolate particles.

Hard spherocylinders (HSC)

Another model used to simulate calamitic LC behaviour is the hard spherocylinder. A spherocylinder is a cylinder of length L , diameter D , terminated by two hemispherical caps so that k , the elongation of this object is : $k = 1 + L/D$. The first simulation on HSCs was performed by Vieillard-Baron [60] using elongation $k=2$ and $k=3$. In this study, he did not find any LC phases. In fact, these phases are only stable for $k > 4.1$. Vieillard-Baron did try to investigate a HSC system for $k=6$ but, because of the lack of computational resources, this attempt was aborted.

Over a decade later, Stroobants *et al.* [61] presented results on systems of parallel spherocylinders with length to breadth ratios $0.25 \leq L/D \leq 5$. As these particles were always perfectly aligned, the low density phase was the nematic phase. They found that for $L/D > 0.5$, a stable smectic phase is formed. However, because the orientations of the particles were fixed, this model was not suitable as a reference system for real smectics. The transition from the nematic to the smectic phase seemed to be continuous. A year later, other studies revealed the existence of a columnar phase as well as the smectic phase [62]. However, this columnar phase was only observed for $L/D > 3$ at densities intermediate between the smectic and crystalline phases. The transition between the smectic and the columnar phase was reported to be first order if $L/D \leq 5$. This transition became continuous in the limit $L/D \rightarrow \infty$.

Frenkel [63, 64] performed 3D simulations of hard spherocylinders with length-to-breadth ratio $L/D=5$ and full translational and orientational freedom because he wanted to establish whether or not the smectic order persisted if the molecular orientations were left free. He found that this system exhibited four stable phases : isotropic liquid, nematic liquid crystal, crystalline solid and, indeed, a smectic A. In 1990, Veerman and Frenkel [65] revisited Vieillard-Baron's HSC systems [60] with full orientational freedom, and so obtained a phase diagram of hard spherocylinders for $L/D \leq 5$. They observed that for $L/D \leq 3$, the only stable phases are the isotropic and the solid phase. They expected the nematic and the smectic phases to be thermodynamically stable for $L/D > 3$. McGrother *et al.* [66] simulated

large systems of HSCs of elongation $L/D=3$ to 5. They proposed a more complete phase diagram and confirmed the simulation results of Frenkel [64] for the system $L/D \leq 5$ which exhibits isotropic, nematic, smectic A and solid phases. They showed that for $L/D=3.2$, by compressing the system from the isotropic phase, there is a clear first order transition to the smectic phase without passing through a nematic phase. They also demonstrated that for $L/D=4$, both the nematic and the smectic A phases are stable, the nematic phase being the first to be exhibited through compression from the isotropic phase.

Hard Gaussian Overlap (HGO) model

This model, based on the shape parameter of the Gay-Berne model (see further down) has attracted renewed interest. The first simulation paper based on this model was published in 1997 by Padilla and Velasco [67] who identified an isotropic-nematic transition. They used particles with length-to-breadth ratios $L/D=3$ and $L/D=5$. We can ask why it is useful to introduce the HGO model. The answer is that this model is quite convenient for both numerical work and computer simulation studies because it is based on a closed expression for the orientationally-dependent contact distance. The HGO model can be seen as equivalent to the well known Gay-Berne model, stripped from its attractive interaction. The potential resulting from this is:

$$U_{HGO}(\hat{\mathbf{r}}_{ij}\hat{\mathbf{u}}_i, \hat{\mathbf{u}}_j) = \begin{cases} 0 & \text{if } r_{ij} \geq \sigma(\hat{\mathbf{r}}_{ij}, \hat{\mathbf{u}}_i, \hat{\mathbf{u}}_j) \\ \infty & \text{if } r_{ij} < \sigma(\hat{\mathbf{r}}_{ij}, \hat{\mathbf{u}}_i, \hat{\mathbf{u}}_j) \end{cases}$$

where $\sigma(\hat{\mathbf{r}}_{ij}, \hat{\mathbf{u}}_i, \hat{\mathbf{u}}_j)$, the contact distance, is given by

$$\sigma(\hat{\mathbf{r}}_{ij}, \hat{\mathbf{u}}_i, \hat{\mathbf{u}}_j) = \sigma_0 \left[1 - \frac{\chi}{2} \left[\frac{(\hat{\mathbf{r}}_{ij} \cdot \hat{\mathbf{u}}_i + \hat{\mathbf{r}}_{ij} \cdot \hat{\mathbf{u}}_j)^2}{1 + \chi(\hat{\mathbf{u}}_i \cdot \hat{\mathbf{u}}_j)} + \frac{(\hat{\mathbf{r}}_{ij} \cdot \hat{\mathbf{u}}_i - \hat{\mathbf{r}}_{ij} \cdot \hat{\mathbf{u}}_j)^2}{1 - \chi(\hat{\mathbf{u}}_i \cdot \hat{\mathbf{u}}_j)} \right] \right]^{-1/2} \quad (3.9)$$

de Miguel and Martín del Rio [68] compared the simulation results they obtained for HGO fluids with the results obtained by Padilla and Velasco for a hard ellipsoid fluid. This comparison shown that the two models present qualitative similarities but quantitative differences, due to the larger volume excluded by a pair of HGO molecules compared to that of HER. However, there is a remarkable agreement between Frenkel and Mulder simulations [56] for the isotropic-nematic properties of

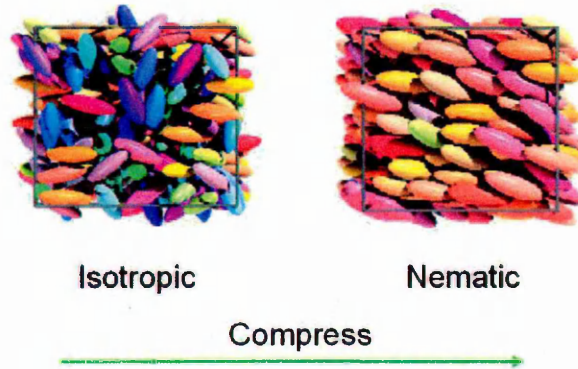


Figure 3.5: Phase behaviour of the HGO model.

the $L/D=3$ HER fluid.

Padilla and Velasco [67] showed that HGO and HER models present qualitative similarities for moderate elongation. Less than a decade before, Rigby [69] showed that this is not the case for highly non-spherical particles, for which the behaviour of the two models differs appreciably.

3.2.4 Soft particles

More realistic models use soft particles instead of hard particles. Unlike hard particles, they do not have an infinitely repulsive hard core, but rather an optional attractive well with a steeply rising potential at a certain distance, hence the term soft particle.

Lennard-Jones potential

Neutral atoms and molecules are subject to two distinct forces in the limit of large distance and short distance: an attractive force at long ranges (van der Waals force) and a repulsive force at short ranges (the result of overlapping electron orbitals). The Lennard-Jones potential is a simple mathematical model that represents this behaviour. It was proposed in 1931 by John Lennard-Jones. The Lennard-Jones potential (see Fig. 3.7) is:

$$U_{ij} = 4\epsilon_0 \left[\left(\frac{\sigma_0}{r_{ij}} \right)^{12} - \left(\frac{\sigma_0}{r_{ij}} \right)^6 \right]$$

Here ϵ_0 is the well depth (i.e. the strength of the strongest attractive interaction) and σ_0 is the collision diameter (i.e. the distance at which the potential between two particles is zero). $\left(\frac{\sigma_0}{r_{ij}}\right)^{12}$ is the repulsive term and $\left(\frac{\sigma_0}{r_{ij}}\right)^6$ is the attractive term. The equilibrium properties calculated from early simulations of spheres interacting through a two-body potential of the Lennard-Jones type [70] have been shown to agree very well with the corresponding properties of argon.



Figure 3.6: Lennard-Jones fluid

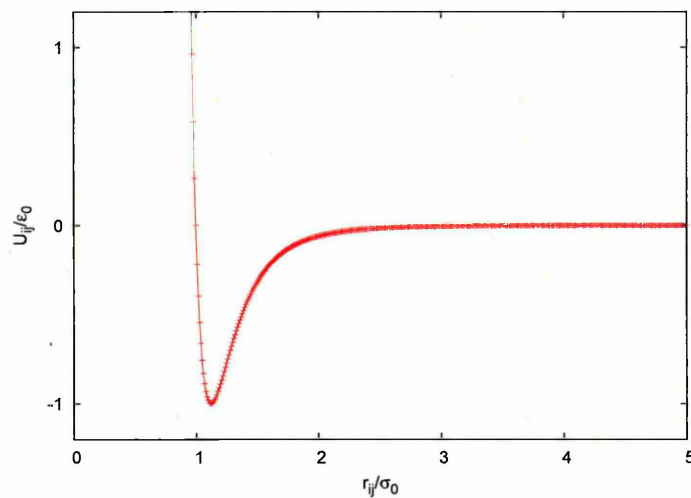


Figure 3.7: Lennard-Jones potential for $\sigma_0=1$ and $\epsilon_0=1$.

Berne-Pechukas potential

Realistic atom-atom potential models are computationally expensive to simulate for long periods. For this reason, idealized models have been developed, characterised

by key parameters : the shapes and the sizes of the molecules. Real liquid crystal molecules are only moderately complicated but long time and length scales are involved in LC phase behaviour. So, the internal degrees of freedom are often ignored in computer simulation models and a rigid molecule is introduced (Fig. 3.8). To model anisotropic molecules as single-site objects (instead of multi-site molecules

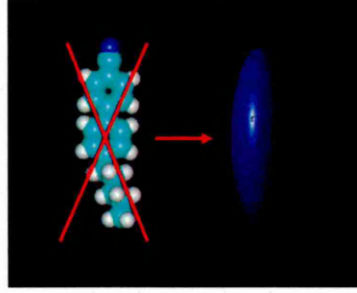


Figure 3.8: Coarse grained modelling of liquid crystals

represented by several Lennard-Jones particles), Berne and Pechukas [71] proposed a generalised form of the Lennard-Jones potential with the angular dependence of σ determined by the overlap of two ellipsoidal Gaussian functions. To simplify their model, Berne and Pechukas assumed each ellipsoid to be rotationally symmetric about a principal axis. Their problem, then, was to calculate the potential of interaction between two ellipsoids as a function of the vector between their centres and their respective orientations. They defined the potential as

$$U_{BP}(\hat{\mathbf{r}}_{ij}\hat{\mathbf{u}}_i, \hat{\mathbf{u}}_j) = \epsilon(\hat{\mathbf{u}}_i, \hat{\mathbf{u}}_j) \exp[-r_{ij}^2/\sigma^2(\hat{\mathbf{r}}_{ij}, \hat{\mathbf{u}}_i, \hat{\mathbf{u}}_j)] \quad (3.10)$$

where $\epsilon(\hat{\mathbf{u}}_i, \hat{\mathbf{u}}_j)$ and $\sigma(\hat{\mathbf{r}}_{ij}\hat{\mathbf{u}}_i, \hat{\mathbf{u}}_j)$ are angle dependent strength and range parameters, respectively. The ‘‘Gaussian overlap’’ (GO) shape parameter $\sigma(\hat{\mathbf{r}}_{ij}, \hat{\mathbf{u}}_i, \hat{\mathbf{u}}_j)$ was calculated to be that given in Eqn. 3.9 and $\epsilon(\hat{\mathbf{u}}_i, \hat{\mathbf{u}}_j)$ was assumed to take the form

$$\epsilon(\hat{\mathbf{u}}_i, \hat{\mathbf{u}}_j) = \epsilon_0[1 - \chi^2(\hat{\mathbf{u}}_i \cdot \hat{\mathbf{u}}_j)^2]^{-1/2} \quad (3.11)$$

where ϵ_0 , σ_0 are constants and χ is the anisotropy shape parameter. The parameter χ is determined by the length to breadth ratio σ_s/σ_e via

$$\chi = \frac{(\sigma_s/\sigma_e)^2 - 1}{(\sigma_s/\sigma_e)^2 + 1} \quad (3.12)$$

Gay-Berne potential

The original potential of Berne and Pechukas was not entirely satisfactory because the well depth ϵ was only dependent on the relative orientations of the particles. This meant that there was no difference between the side-side and the end-end interaction well depths whereas in reality, the well depths for these two configurations are significantly different [72]. Gay and Berne [73] subsequently defined a new strength parameter which included some dependence on $\hat{\mathbf{r}}_{ij}$. This new potential was

$$U_{GB}(\hat{\mathbf{r}}_{ij}, \hat{\mathbf{u}}_i, \hat{\mathbf{u}}_j) = 4\epsilon(\hat{\mathbf{r}}_{ij}, \hat{\mathbf{u}}_i, \hat{\mathbf{u}}_j) \left[\left(\frac{\sigma_0}{r_{ij} - \sigma(\hat{\mathbf{r}}_{ij}, \hat{\mathbf{u}}_i, \hat{\mathbf{u}}_j) + \sigma_0} \right)^{12} - \left(\frac{\sigma_0}{r_{ij} - \sigma(\hat{\mathbf{r}}_{ij}, \hat{\mathbf{u}}_i, \hat{\mathbf{u}}_j) + \sigma_0} \right)^6 \right] \quad (3.13)$$

the well depth anisotropy term now being

$$\epsilon(\hat{\mathbf{r}}_{ij}, \hat{\mathbf{u}}_i, \hat{\mathbf{u}}_j) = \epsilon_0 \epsilon_1^\nu (\hat{\mathbf{u}}_i \cdot \hat{\mathbf{u}}_j) \epsilon_2^\mu (\hat{\mathbf{r}}_{ij}, \hat{\mathbf{u}}_i, \hat{\mathbf{u}}_j) \quad (3.14)$$

with

$$\epsilon_1(\hat{\mathbf{u}}_i, \hat{\mathbf{u}}_j) = [1 - \chi^2 (\hat{\mathbf{u}}_i \cdot \hat{\mathbf{u}}_j)^2]^{-1/2} \quad (3.15)$$

and

$$\epsilon_2(\hat{\mathbf{r}}_{ij}, \hat{\mathbf{u}}_i, \hat{\mathbf{u}}_j) = 1 - \frac{1}{2} \chi' \left[\frac{(\hat{\mathbf{r}}_{ij} \cdot \hat{\mathbf{u}}_i + \hat{\mathbf{r}}_{ij} \cdot \hat{\mathbf{u}}_j)^2}{1 + \chi'(\hat{\mathbf{u}}_i \cdot \hat{\mathbf{u}}_j)} + \frac{(\hat{\mathbf{r}}_{ij} \cdot \hat{\mathbf{u}}_i - \hat{\mathbf{r}}_{ij} \cdot \hat{\mathbf{u}}_j)^2}{1 - \chi'(\hat{\mathbf{u}}_i \cdot \hat{\mathbf{u}}_j)} \right]. \quad (3.16)$$

The parameter χ' is related to the associated well depth ratio ϵ_s/ϵ_e , through

$$\chi' = \frac{(\epsilon_s/\epsilon_e)^{1/\mu} - 1}{(\epsilon_s/\epsilon_e)^{1/\mu} + 1} \quad (3.17)$$

where ϵ_s and ϵ_e are the side by side well depth and the end to end well depth. If the exponents μ and ν are respectively fixed at 2 and 1, and if σ_e/σ_s and ϵ_s/ϵ_e are respectively fixed at 3 and 5, the potential Eqn. 3.13 gives a good fit to a linear four-site Lennard-Jones potential representation of an anisotropic molecule.

The standard Gay-Berne potential is represented in Fig. 3.9 and Fig. 3.10 show the resultant phase behaviour. As we can see, a GB system can exhibit three different liquid phases. The most disordered phase is the isotropic phase. If we compress such a system or if we cool it down, the GB system will then exhibit a nematic phase and finally, a smectic phase.

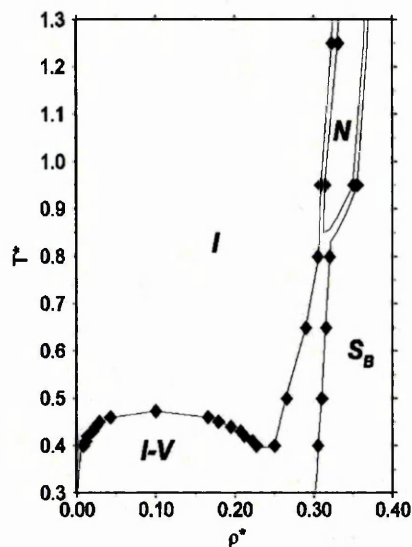


Figure 3.9: Phase diagram of the standard Gay-Berne model [74]

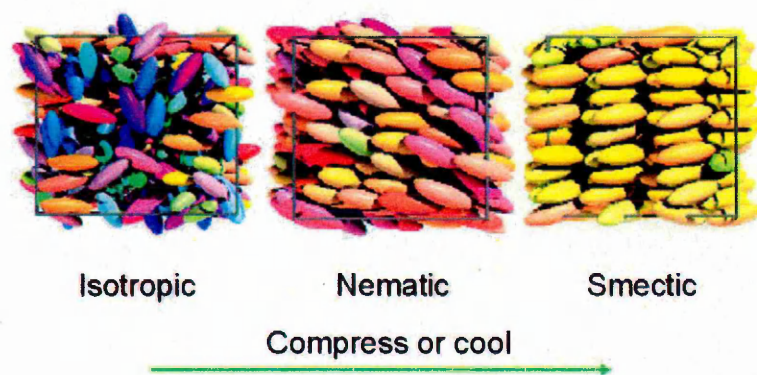


Figure 3.10: Phase behaviour of a Gay-Berne system

The behaviour of the GB model can be tuned through modification of the four parameters κ , κ' , μ and ν . The most studied parametrisation, $\text{GB}(\kappa, \kappa', \mu, \nu) = (3, 5^{-1}, 1, 2)$ was that put forward by Gay and Berne [73] from their fit to linear arrays of Lennard-Jones sites. The first simulation performed using this parametrisation was in 1987. Adams *et al.* [72] simulated a system of particles interacting via the GB potential in order to determine, for consistency, if this potential was useful for modelling nematic LCs and identifying the I-N transition temperature for a given density. They found that the system exhibits a spontaneous I-N transition at a scale density $\rho^* = 0.32$ and at temperature $1.7 \leq T^* \leq 1.8$.

Following this, an initial phase diagram was published by de Miguel *et al.* [75]. Two systematic studies of the Gay-Berne model were performed. The first of these investigated the effect of the anisotropic parameter κ' at fixed values of κ [76]. κ' can be considered as the parameter which controls the relative contribution of the attractive interactions for a range of different molecular configurations. For $\kappa' \geq 5$, it was demonstrated that the system shows a transition from isotropic to smectic A phase. A second observation concerning the parameter κ' is the fact that, as κ' increases, the density at the transition point decreases. By studying the case where $\kappa' \leq 2.5$, an isotropic-nematic transition was identified and the transition density decreased as κ' was increased. In this study, it was also shown that the GB fluid, for $\kappa=3$ and $\kappa'=1$ and 1.25, exhibits a triple point where the vapour, isotropic and nematic phases coexist simultaneously.

In the second of these studies, Brown *et al.* [74] investigated the effects of the elongation of the particles κ . By studying a range of length to breadth ratios $3 \leq \kappa \leq 4$ they found that, even for this small range of elongations, the phase diagram shows significant changes. The most surprising observation was probably the growth of a stable S_A "island", surrounded by a nematic phase and a smectic B phase. This study also looked at the stability of the nematic phase as κ is changed. With decreased κ , the I-N transition appeared at lower density and pressure. Subsequently, these systems were briefly reviewed by Allen *et al.* [77].

Even though the most commonly studied model employing soft particles is the Gay-Berne model, work has been investigating other models such as the soft repulsive spherocylinders (SRS) [78] in order to determine their phase diagrams. Reference [78] considered a system of SRS of aspect ratio $L/D=4$. For this aspect ratio, numerous simulations have been performed using HSC [63–66] and these studies showed that a nematic and a smectic phase form for this value of L/D . Earl *et al.* obtained these two phases as well and numerous conclusions from [63–66] were the conclusions as well in this study. One of the advantages over the well known Gay-Berne is the fact that it is 3-4 times faster.

3.2.5 All-atom models

Full atom-atom potentials have been employed increasingly in the simulation of LCs. This atom-atom approach uses a standard empirical force field to determine intermolecular contributions to the potential energy and, thus, the internal molecular structure [79]. However, this type of simulation is computationally expensive and the calculations are very time consuming. A number of different studies of the cyanobiphenyl family have been performed [80–82]. In 1989, Picken *et al.* studied a system containing 64 5CB molecules using a united-atom model (in this model, the hydrogen atoms were subsumed into the carbon atoms). They looked at the nematic phase of this system and, in particular, the effect of adding to the system partial atomic charges [80]. Cross and Fung, in 1994, performed simulations of 5CB using two methods : the first used atomic detail to model the molecules as accurately as possible and the second, defined as “pseudo-5CB” by the authors, used a simplified approach (Fig. 3.11). In the first method, the CH, CH₂ and CH₃ groups were represented as single units. In the second method, the rings were represented as single units, so the number of interaction sites dropped from 19 (first method) to 9 (second method) [81].

In 1994, Komolkin *et al.* performed simulations to compare a united-atom (UA) model and a full-atom (FA) model. In their simulations they used a system of 75 mesogens. In the UA simulation, the molecules contained 19 sites giving a total of 1425 interaction sites and for the FA simulation, the molecules contained 38 sites giving a total of 2850 interaction sites. They concluded that the extension from UA to FA model is very expensive and unnecessary and that the UA model can be improved more effectively by introducing an anisotropic UA model [82].

Cook and Wilson [83] performed the first thousand-molecule simulation of a mesogen at the fully atomistic level. In their study, instead of using a united atom model, where carbons and their associated hydrogen are considered as a single atom, they used the fully atomistic model. The advantage of keeping this full atomistic model is the fact that intramolecular and intermolecular interactions are accurate. When the carbon and the hydrogens are united, the flexibility of the molecule is not accu-

rate. In their study, Cook and Wilson compared their results with key experimental quantities such as the density and diffusion coefficient and found remarkable agreement between the two. They also found that there is a system size dependence. The results they obtained for the $N=1000$ system was in very good agreement with experiment and they showed a considerable improvement over the values they obtained for $N=125$. Berardi *et al.* [84] studied the odd-even effect, which corresponds to large alternation of phase properties for homologues containing an n -alkyl chain, as n varies from even to odd. They showed, for the first time, that the N-I transition temperatures can be well reproduced in a MD simulation. They found that the odd-even effect arises because the structure of the $n=1$ homologue leads to the terminal phenyl ring being unable to adopt a good alignment with the LC director, something which does not apply for the $n=0$ and $n=2$ homologues. However, very long run times were found necessary to fully equilibrate these systems. In a recent review [85], progress towards accurate atomistic modelling of nematics is discussed in detail, and in particular, the progress towards accurate prediction of material properties is exposed.

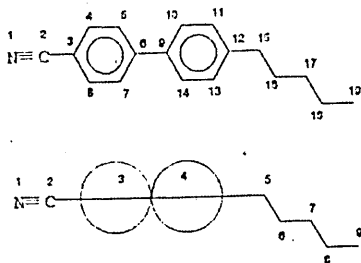


Figure 3.11: Schematic representations and numbering systems for the 5CB molecules in the two types of MD calculations [81]

3.3 Molecules in contact with interfaces

It is clear, from an experimental point of view, that confinement of LCs breaks the symmetry of the confined fluid by inducing two main effects : positional layering and orientational ordering through a mechanism called anchoring [13]. The first effect is a universal consequence of the confinement and the second is specific to

molecules with shape anisotropy.

3.3.1 Hard rod-like particles

The theory of hard particles in contact with hard wall predicts that the particles prefer parallel alignment close to the wall [86, 87]. An isotropic to nematic phase transition is also predicted in the near-wall region.

Mao *et al.* [88] studied a system of hard rod-like particles confined between two parallel plates. They presented density profiles and order parameter profiles for this system at isotropic bulk densities. Results were obtained by computer simulation for rods with $L/D=10$ and $L/D=20$, and from a self-consistent integral equation exact in the limit $L/D \rightarrow \infty$. They investigated the effects of the finite aspect ratio on both the depletion potential and the surface tension and found that these results are close to the predictions for infinite aspect ratio.

In 2000, Bates and Frenkel [89] studied a two-dimensional system of HSC confined to lie in a plane. They found that, depending on the length-to-breadth ratio of the molecules, different cases are observed. MC simulation of 2D systems of HSC were performed with $L/D=1, 2, 3, 4, 5, 7, 9$ and 15 . For a system of long rods ($L/D \geq 9$), at high pressure, the transition from solid to nematic occurs. The behaviour exhibited by short rods was found to be rather different. For ($L/D \leq 7$), the rod system does not exhibit a nematic phase but instead a first order transition from solid to isotropic phase.

The surface energy or anchoring energy f_s is commonly taken to be related to θ_s , the angle between the surface director and the natural anchoring angle, by [13, 90] :

$$f_s = \frac{1}{2} W_0 \sin^2(\theta_s) \quad (3.18)$$

where W_0 is the anchoring strength and measures the ease with which the director can deviate from the impose anchoring direction. Molecular simulations of a LC confined in slab geometry have been carried out [90]. In this paper, the anchoring strength at one of the walls is measured by applying an orienting perturbation at the opposite wall, which generates a director profile across the slab. Allen inves-

tigated how an homeotropically aligned liquid crystalline layer at a solid surface responded to this perturbation. He found good agreement between simulation and density functional theory in the Onsager approximation, for the density and order parameter profiles. He then compared the director angle θ_z profiles from simulation with the elastic theory and with the Onsager theory. To fit the profile obtained from the elastic theory to the simulation's profile, the author has to determine two parameters namely the extrapolation length λ and the elastic constant ratio κ . From the value of the first parameter, one can determine the nature of the anchoring strength [90, 91]. Then, Andrienko *et al.* [92] proposed a method for measuring the LC surface anchoring strength W by molecular simulation. They simulated a similar system as the one in [90]. The method is based on the study of the director fluctuations in the LC cell. Here, rather than measuring the fluctuation of the director, they measured the fluctuations of the second rank order tensor components. This method relates thermal order parameter fluctuations in a confined geometry to the zenithal anchoring coefficient. This approach contrasted with the more direct measurement of the anchoring strength performed previously by Allen [90].

Subsequently van Roij *et al.* [93–95] used hard spherocylinders confined between a hard smooth wall and an isotropic liquid crystal and observed surface induced wetting and planar ordering. These studies also showed that the planar arrangement is the natural state of a hard-rod nematic phase in contact with a flat surface when surface adsorption is not made possible.

In 2001, Chrzanowska *et al.* [96] looked at the structure of a system of HGO molecules confined between the two hard walls, from density-functional theory and MC simulations. Here, the interactions between the walls and the particles were modelled using the Hard Needle Wall (HNW) potential [97]. As they compared the results from theory and from simulation, they found rather different I-N transition densities and widths. Despite its simplicity, however, the density functional theory successfully predicted much of the structure seen in the confined liquid.

Downton and Allen [98] investigated the anchoring of hard spherocylinders confined between two hard walls onto which LC molecules had been perpendicularly grafted.

They varied the length of the LC molecules and the grafting density and observed quite a few different anchoring regimes : homeotropic, planar, tilted and decoupled planar. For a reasonable grafting ($\sigma=3.75\%$, σ being the surface coverage) and for chains with the same length as the LC, they found homeotropic anchoring of the LC. As they decreased the length of the chains, they found a similar behaviour for high grafting ($\sigma=10\%$). What they did not expect was to find LC aligning in the xy plane. This was observed for two cases : for chains with the same length as the LC and at high grafting ($\sigma\geq 5\%$). They also found some tilted cells which were comparable with the results obtained by Lange and Schmid who found tilted behaviour in simulation of rods confined between short polymer brushes [99, 100]. Later, Downton and Hanna [101] extended the study by considering atomistic simulations, in which the grafted chains are fully flexible. They studied this system to investigate if small concentrations of grafted chains on the surface may change the LC orientation from planar to homeotropic as seen in [98]. They found that as the density of grafted chains is increased, the extension of the smectic region, induced by the free surface (surface without grafted chains), increased as well in the bulk region. At the higher grafted density, the interaction between the chains and the LC force the latter to lie perpendicular to the surface (at low grafted density, the LC lie parallel to the surface). In their study, they did not observe a tilted phase as they did in [98]. Nevertheless, because of the size of the simulations, these results have to be treated with caution. In fact, the authors were not able to explain the behaviour of their system. The fact that increasing the grafted density promotes a transition from planar to homeotropic might be due to the fact that the planar anchoring (obtained for low grafting) becomes weaker and so increases the influence of the free surface on the bulk LC. As a conclusion, the homeotropic anchoring at the surface might be induced by the free surface rather than by the chains.

Barnes [102, 103] studied confined and flexoelectric liquid crystalline systems. In [102], an intensive study of confined systems of HGO particles was performed using different surface potentials, namely, the Hard Needle Wall (HNW) (see section 4.2) and two more realistic potentials, namely the rod-sphere (RSP) and the rod-surface (RSUP) potentials. He then focused on pear-shaped particles and presented a phase

diagram for different particle lengths. In [103], he focussed on the effects of confinement on a system of HGO particles interacting with the substrates via the HNW potential. He showed that homeotropic and planar arrangement can be obtained and the anchoring phase diagram showed regions of bistability which were explicitly examined through simulation. In his studies, he showed that the preferred particle alignment on the surface can be easily controlled by the parameter k_s , the needle length.

3.3.2 Soft particles

In 1996, Zhang *et al.* [104] studied a system of GB particles in the presence of surfaces. In this, they attempted to determine the dependence of the bulk orientation on the molecule-substrate interaction. The molecule-substrate potential used was in the spirit of the GB model. Using this potential, they tried to describe the effect of rubbed polymers on LCs. They demonstrated that the rubbing has an impact on the pretilt angle and that the greater the rubbing strength, the greater the pretilt angle, due to the increase in nematic order in the vicinity of the surface.

Stelzer *et al.* [105] studied a system of Gay-Berne nematic liquid crystal confined between smooth surfaces. They performed two independent simulation to investigate how the anisotropy of the molecule-surface interaction influences the anchoring strength. In both cases, they observed surface-induced smectic A layering. In the first simulation, the potential between the particles and the wall was similar to the Gay-Berne potential in the sense that it comprised a term ϵ which depended on \hat{r}_{ij} , \hat{u}_i and \hat{u}_j . They called this potential the “anisotropic surface potential”. In the second simulation, the parameter ϵ was made independent of the molecular orientation. This wall-molecule potential was called “isotropic surface potential”.

The same year, Stelzer *et al.* [106,107] also studied an uniaxial nematic liquid crystal in contact with a rough surface. They found that a smectic C phase was induced at the surface and, as the distance between the surface and the molecules increases, the smectic order disappears leaving a nematic structure within the bulk. The intermediate region between the smectic C and the nematic bulk was characterised

by a high degree of biaxiality. Correspondingly, the director orientation underwent a strong distortion close to the surface.

Wall and Cleaver [108] studied a system of GB particles confined between two substrates, at low and moderate particle-substrate coupling strengths. For both couplings, the onset of positional order in the central region appears to induce a pretilt transition in the surface region. By cooling the two systems, an ordered fluid is formed in the central region. The surface layers appear to be the major influence of the orientational order of the central region.

Palermo *et al.* [109] determined the alignment of GB particles near a graphite substrate. In their paper, they exposed the case where the behaviour of the first layer is totally different from the rest of the bulk. The first layer aligns parallel to the substrate, with the second layer perpendicular, penetrating the first monolayer with their ends to touch the graphite. The authors found that the structure of the first two adsorbed layers is not affected by different director orientations induced in the bulk liquid crystal but is totally determined by the surface potential.

Gruhn and Schoen [110,111] investigated a system of confined GB molecules. They studied very thin films of particles in a slab geometry confined between two plane parallel solid substrates composed of atoms (i.e. wall atoms); upon changing the thickness of the film, the orientation of bulk region particles was found to change regularly from planar to homeotropic.

Latham and Cleaver [112] studied a system of confined mixtures of GB particles. In these studies they altered the particle-substrate well-depth anisotropy term. They altered it so it has broken azimuthal symmetry.

Webster *et al.* [113] examined the formation, structure and relaxation of smectic chevrons. They found that, depending on the nature of the surfaces confining the system, tilted layers of bookshelf structure could be obtained. The system which formed the bookshelf structure had rough surfaces and the one that exhibited a chevron/tilted layer had smooth surfaces. They found that the coupling between the smectic layers and the surfaces was rather weak because the smectic domains

formed in the bulk rather than growing out from the surfaces.

Steuer *et al.* [114] investigated the effect of flat walls on the phase behaviour of LCs. In their study, they used two different kinds of substrates. The first one favoured homeotropic alignment whereas in the second, both walls preferred homogeneous planar alignment but with a 90 degree difference between the azimuthal angles at the two walls. The walls consisted of particles interacting with the fluid via a Lennard-Jones type potential. In both cases, a nematic phase formed. In the second case, where planar alignment was favoured on both surfaces, they found, in the nematic, that the director smoothly twisted from one surface to the other. They concluded, not surprisingly, by saying that the confinement of the bulk allows it to exhibit an isotropic-nematic transition at lower density than for the bulk system.

The effect of surface roughness on the LCs has been investigated. The roughness of the surface is commonly introduced by embedding molecules, with random position and orientation, in the wall. Cheung and Schmid [115] studied the effect of the rough surfaces on the structure of the isotropic and nematic confined fluid and, on the anchoring properties of the LC fluid. The surface anchoring coefficient was determined by the director fluctuation method [92]. The authors found that the effect of increasing the surface roughness has the same impact on the systems studied at different densities. They found that, by increasing the surface roughness, the local density and order near the wall, not surprisingly, decreases. The decrease in order is due to the fact that, because the embedded molecules have random orientation, this causes the molecules from the two first layers to be disordered as well. As the surface roughness is increased, a tilt angle appears and the greater is the surface roughness, the better the tilt angle propagates in the bulk. This is consistent with the behaviour observed previously by Downton and Allen [98]. The final remark regarding the impact of the surface roughness is that the anchoring strength is obviously decreased as the roughness is increased. This study has been extended and the effect of surface roughness on the I-N transition has been investigated [116]. The system used is the one introduced in [115]. Cheung and Schmid found that, the rougher the surface, the higher the pressure needed for the system to exhibit an I-N transition.

Kiyohara *et al.* [117] studied the mechanism of surface anchoring of rod-like molecules on substrates. They considered substrates with corrugated patterns at their surfaces. They used the GB model for molecular interactions. They found that the director of the molecules aligned along the grooves. They concluded that, as the grooves become thinner, the azimuthal anchoring becomes stronger.

3.3.3 All-atom models

Cleaver and Tildesley [118] performed energy minimisations on systems of 8CB molecules, represented by an assembly of 22 spherical sites, absorbed on either a smooth or graphite planar substrates. They found that strips of 50 molecules formed structures almost fully compatible with scanning tunneling microscopy (STM) observations.

Yoneya and Iwakabe [119] performed molecular dynamics simulations on systems of 8 molecules of 8CB anchored on graphite and initially arranged in the structures shown by the STM experiments. However, due to the small system size used and the lack of periodic boundary conditions, these arrangements proved to be unstable.

Yoneya and Iwakabe [120], also presented results of MD simulations of liquid crystal alignment on a polyimide monolayer. The LC molecule was 8CB and the polyimide oligomer was PMDA-PPD. Both the molecular models for 8CB and PMDA-PPD were detailed atomic models, except for the CH_2 and CH_3 groups, which were regarded as united atoms. They found that the stable LC alignment direction on the polyimide monolayer was roughly along the polyimide chain direction.

Cleaver *et al.* [121] studied periodic systems of monolayers of 8CB and 10CB molecules anchored on graphite using energy minimisation and molecular dynamics techniques. The findings of this study showed structures fully consistent with the STM observations.

A more systematic series of simulations was conducted by Binger and Hanna [122–124] who performed realistic molecular dynamics and molecular mechanics simulations of various liquid crystals molecules (e.g. 5CB, 8CB, MBF). Systems ranging

from single molecules up to two monolayers anchored on different polymeric substrates (e.g. PE, PVA, Nylon 6) were investigated. The authors found that for most substrates, the molecules adopt planar arrangements with specific favoured conformations.

Several simulation studies have explored interactions of *8CB* LCs with crystalline substrates [119, 120, 122, 124]. McDonald and Hanna [125, 126] have presented simulation studies of terraced wetting (which appears when a droplet completely wets a surface) of a LC fluid on a crystalline surface using atomistic molecular dynamics. The model *8CB* has been discussed in [122, 125] and consists of united atoms. They showed that, depending on the value of ϵ_{fs} , the fluid-surface interaction parameter, one can obtain partial or total wetting. They first studied isolated droplets of *8CB* because this gave insight into the phase structure of LC fluid. The droplets appeared to have a spherical shape (in order to minimize the free energy) and depending on the temperature, the droplets exhibited a smectic A phase or an isotropic phase. Then, they looked at the droplet structure during wetting. First of all, they observed layering of molecules parallel to the surface, just like the simple fluid system, the wetting being partial or complete. Depending on the temperature and on the value of ϵ_{fs} , a different number of layers was observed and, as a consequence, a partial or complete wetting was obtained. As they were looking at the structure of the adsorbed monolayers during spreading, they noticed that the shape of the wetting film is of interest because, the spreading droplet appears not to be completely radially symmetric but, instead, forms a diamond shaped monolayer as it spreads. They also noticed that at the fluid-vapour interface, the molecules adopt an homeotropic alignment, which was previously demonstrated in [101]. For partial wetting droplets in equilibrium with the bulk smectic state, a “hedgehog” structure was observed (this structure gave the minimum energy configuration with homeotropic alignment at the fluid-vapour interface and planar alignment at the fluid-surface interface).

3.4 Conclusions

A lot of progress has been made in computer simulation due to the rapid development of computer hardware. As we saw in sections 3.2.5 and 3.3.3, at the atomistic level, it is now possible to get a good description of the real systems and, because parallelisation techniques are improving, we will be soon able to simulate bigger systems. Coarse-grained models have shown very good agreement with real systems. Even if things like flexibility and intramolecular forces are neglected, coarse-grained models have been able to reproduce phase diagrams for example. We saw in section 3.3 that the interest in confined systems is growing, due to the research in new devices. Model systems have been developed for which it is possible to control the preferred alignment (surface roughness, HNW, rubbed polymers) of the LC on the substrates and to induce tilt in the cell. Nevertheless, the control of the anchoring tilt is still not an easy thing to achieve. In the field of devices today, we are looking at a way to be able to control independently the azimuthal and the polar coefficient. In the next chapters, we will be looking at patterning of substrates and we will investigate the effects of confining patterned substrates on a nematic LC. We will investigate if this patterning is sufficient to control the tilt angle and control independently the two anchoring coefficients (polar and azimuthal).

Chapter 4

Simulation of confined systems

The Gay-Berne model is well known and much used in the field of molecular simulation. This model is usually used to model a number of different liquid crystalline phases (isotropic, nematic, smectic). Nevertheless, if the nematic phase only is of interest, the Hard Gaussian Overlap (HGO) model is a viable alternative. In fact, because of the simplicity of the potential (no attractive interactions), it is computationally faster.

To complement the experimental work on the micron scale described in the previous section, we have undertaken a molecular simulation study of liquid crystal anchoring at nanoscale patterned substrates. In this, we have performed a series of Monte Carlo simulations of rod-shaped particles confined in slab geometry between two planar walls. Inter-particle interactions have been modelled through the HGO potential [67], and wall-particle interaction through the Hard Needle Wall (HNW) potential.

4.1 Confined systems and anchoring phenomena

The orientation of the nematic LCs is random in the absence of perturbations (external field, confinement) [5, 127]. Nevertheless, it can be easily oriented by surfaces [13]. When a liquid crystal is confined, several regions can be distinguished. First, at the substrate, the molecules are in direct interaction with the substrate. Their orientation is directly linked with the substrate. The direct interaction between the LCs and the substrate determines the microscopic anchoring

condition [128]. Then, there is an interfacial region where the order parameters and the nematic director evolve from that in the surface layer to that in the bulk. The structure of the interfacial region will determine the macroscopic anchoring. The orientation of the bulk director is, then, determined by, but not necessarily the same as that at, the surface. The anchoring direction refers to the director of the bulk in absence of deformation [127]. LC anchoring can be described by two parameters: the easy axis direction e and the anchoring coefficient W . These two parameters are critical design parameters for LC devices. Computer simulation is very useful here because experiment cannot investigate all details of the liquid crystalline structure.

4.2 Simulation details

Different ways to model surfaces by computer simulation have been proposed [104, 108]. However, some questions about the easy axis angle or the anchoring coefficient are still open. Here, particle-substrate interactions have been modelled using the hard needle-wall potential (HNW) [97]. In this, the particles do not interact directly with the surfaces. Rather the surface interaction is achieved by considering a hard axial needle of length $\sigma_0 k_s$ placed at the centre of each particle (see Fig. 4.1). This gives an interaction

$$v^{HNW} = \begin{cases} 0 & \text{if } |z_i - z_0| \geq \sigma_w(\hat{\mathbf{u}}_i) \\ \infty & \text{if } |z_i - z_0| < \sigma_w(\hat{\mathbf{u}}_i) \end{cases} .$$

where z_0 represents the location of a substrate and

$$\sigma_w(\hat{\mathbf{u}}_i) = \frac{1}{2} \sigma_0 k_s \cos(\theta_i) \quad (4.1)$$

The parameter k_s provides a molecular-level control on the surface anchoring properties. Physically, setting $0 < k_s < \kappa$ leads to a system in which molecules can embed their ends, but not their central cores into the substrate. $\theta_i = \arccos(u_{i,z})$ is the angle between the substrate normal and the particle's orientation vector, which also corresponds to the zenithal Euler angle. For small k_s , the homeotropic arrangement has been shown to be stable, whereas planar anchoring is favoured for long k_s [97]. The mechanism responsible for the change of surface alignment as a

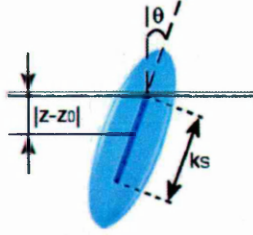
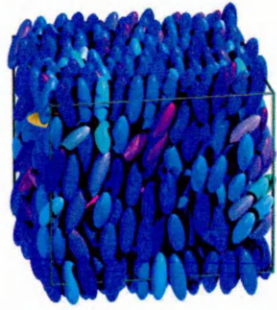


Figure 4.1: Schematic representation of the geometry used for the hard needle wall (HNW) particle–substrate interaction [97].

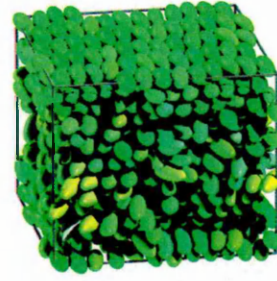
function of k_s is related to the varying amount of molecular volume that can be absorbed into the surface as the needle length is changed. Furthermore, despite its simplicity, the HNW potential has been found to exhibit qualitatively identical behaviour to more complex particle-substrate potentials [102]. Here, by making k_s different for different walls or allowing it to vary across one wall, we investigate the molecular-scale effects of substrate patterning.

4.3 Symmetric anchored systems

First of all, it is important to understand that the influence of the substrates on a system of HGO particles depends on two different parameters: the density and the needle length. All simulations were performed using $N=864$ HGO particles with a length to breadth ratio $\kappa=3$. The substrates were separated by a distance $L_z = 4\kappa\sigma_0$ and located at $z_0=\pm L_z/2$. The simulation box lengths in the other directions were determined, for each imposed value of the dimensionless number density ρ^* , by the relationship $L_x=L_y= \sqrt{N\sigma_0^3/(\rho^*L_z)}$. Typical run lengths at each state point were 0.5×10^6 Monte Carlo(MC) sweeps (where one sweep represents one attempted move per particle) of equilibration followed by a production run of 0.5×10^6 MC sweeps. Each system studied was compressed from the isotropic phase ($\rho^*=0.24$) into the nematic ($\rho^* \geq 0.3$) density range by increasing the number density by $\Delta\rho^*=0.01$ after each production run. Maximum translational and rotational move parameters were allowed to vary during the equilibration stage until they yielded acceptance ratios of approximately 50%. During the production stage, analysis was performed by dividing stored system configurations into 100 equidistant constant- z slices and



(a) $k_{st}=k_{sb}=0$



(b) $k_{st}=k_{sb}=3$

Figure 4.2: Snapshots of the symmetric systems

performing averages of relevant observables in each slice. This yielded profiles of quantities such as $\rho^*(z)$ from which structural changes could be assessed. The density profile provides information about the layering of the particles through the location, the number and the height of the peaks. Orientational order profiles were also measured, particularly

$$Q_{zz}(z) = \frac{1}{N(z)} \sum_{i=1}^{N(z)} \left(\frac{3}{2} u_{i,z}^2 - \frac{1}{2} \right) \quad (4.2)$$

which measures variation across the confined films of orientational order measured with respect to the substrate normal. Here $N(z)$ is the instantaneous occupancy of the relevant slice. For patterned systems, we have also further subdivided the system to assess lateral inhomogeneities induced by the patterning.

It is informative to consider, first, the two classes of anchoring behaviour exhibited by symmetrical systems (i.e., those with $k_{st}=k_{sb}=k_s$, i.e. the same value of k_s at both substrates). Previous work on related hard-particle models has established that for k_s equal or close to the particle length to breadth ratio, planar alignment will be favoured, whereas for $k_s \simeq 0$, orthogonal alignment is favoured [97]. This can be observed in Fig. 4.2(a) and Fig. 4.2(b)

As shown in Fig. 4.3, on entering the nematic phase, Q_{zz} adopts positive values (i.e., orthogonal anchoring) for $k_s=0$ and negative values (i.e., planar anchoring)

for $k_s = \kappa = 3$. The structural changes involved in these two scenarios are illustrated by the density profiles plotted in Fig. 4.4(b) and Fig. 4.5(b).

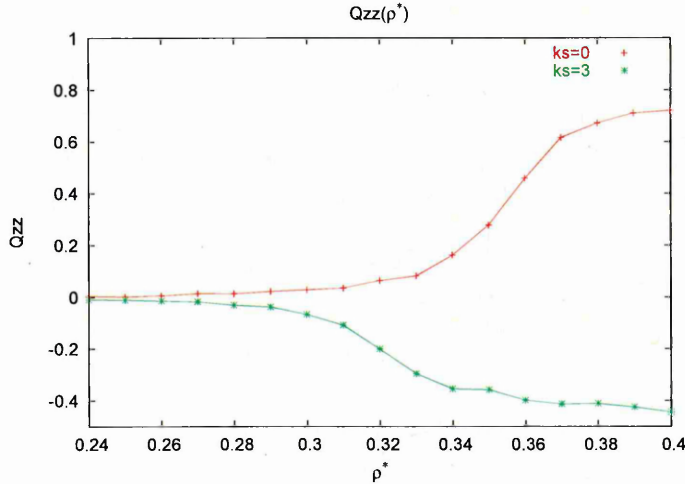
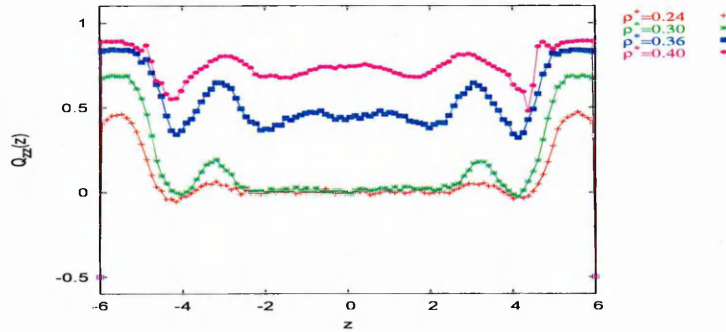


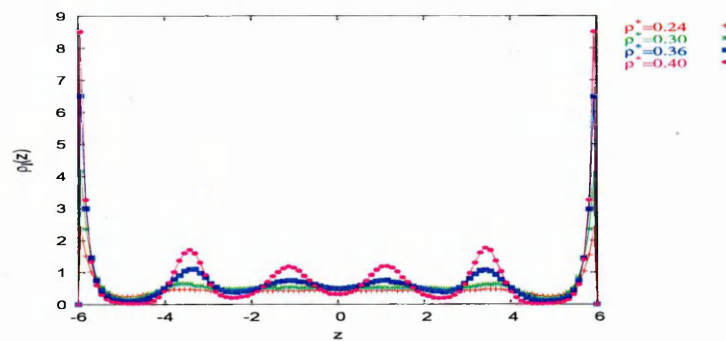
Figure 4.3: Nematic order parameter measured with respect to the substrate normal, $Q_{zz}(z)$, for symmetric systems. Here, data values were averaged over the central 50% of the film width.

4.3.1 Homeotropic anchoring

This anchoring corresponds to the configuration where the molecules are normal to the substrates ($\theta_z=0$, θ_z being the angle between the normal to the substrate and the molecular axis). This configuration develops when the needle length $k_s \simeq 0$. Typical Q_{zz} and density profiles are shown in Fig. 4.4. Looking at Fig. 4.4(b), we can notice that $\rho_l^*(z)$ is an oscillatory function. This function displays two main peaks at $|z - z_0| \sim 0$ which correspond to the first layer of particles. The peaks correspond to the locations of the centres of mass, so, in this case, the centres of mass of the molecules are located (in average) at the wall. If we start looking at the locations of the other peaks, we can see that there is an oscillatory wavelength of about κ , the molecule length. So, in this system, the molecules are arranged end to end. Because the two substrates are separated by a distance $L_z = 4\kappa\sigma_0$ and because the molecule length is equal to $\kappa\sigma_0$, we cannot have more than five peaks on the graph representing the density profile. If we look at Fig. 4.4(b), the peaks are situated at $z \sim [-6; -3; 0; 3; 6]$.



(a) Q_{zz} profile



(b) Density profile

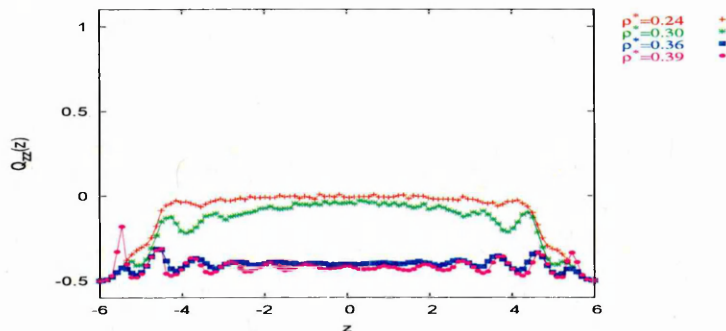
Figure 4.4: $Q_{zz}(z)$ and density profile of the symmetric system: $k_{st}=k_{sb}=0$

If we now concentrate on the Q_{zz} profile, the first noticeable thing is the fact that Q_{zz} increases monotonically with density for symmetric systems with homogeneous alignment (Fig. 4.4(a)). The homeotropic arrangement corresponds to the region where Q_{zz} is positive. Q_{zz} , just like the density profile, is an oscillatory function. We can notice that the maxima for the two profiles are usually in phase. This can be explained by the fact that, the higher the local density, the higher the order and, therefore, the better the ordering with respect to the wall.

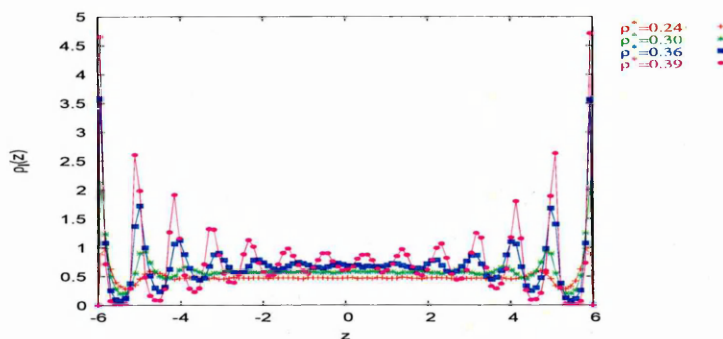
4.3.2 Planar anchoring

Planar anchoring corresponds to the configuration where the molecules lie parallel to the substrates ($\Delta\theta = \pi/2$). This configuration develops when the needle length

$k_s \sim \kappa$. Typical Q_{zz} and density profiles are shown in Fig. 4.5. By looking at these



(a) Q_{zz} profile



(b) Density profile

Figure 4.5: $Q_{zz}(z)$ and density profile of the symmetric system: $k_{st}=k_{sb}=3$

profiles, we can notice that the first peaks are situated at $|z - z_0| \sim 0$. Those peaks correspond to particles lying approximately parallel with the surfaces. Looking at the locations of the other peaks, we can see that there is an oscillation of about σ_0 , the molecule breadth. So, in this system, the molecules are arranged side to side. If we now concentrate on the Q_{zz} profile, the first noticeable thing is the fact that Q_{zz} decreases monotonically with density for symmetric systems with planar alignment (Fig. 4.5(a)). The planar arrangement corresponds to the situation where Q_{zz} is negative. Q_{zz} , just as the density profile, is an oscillatory function. We can notice that in this configuration, maxima in the density profile induce minima in the Q_{zz} profile. This can be explained by the fact that high planar order leads

to negative Q_{zz} . For a more detailed description of all 3 eigenvalues of the order tensor, see section 5.1.1.

4.3.3 Competing anchoring

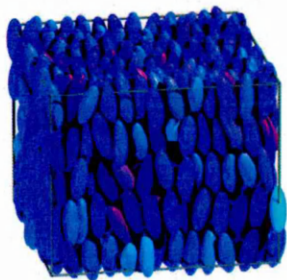
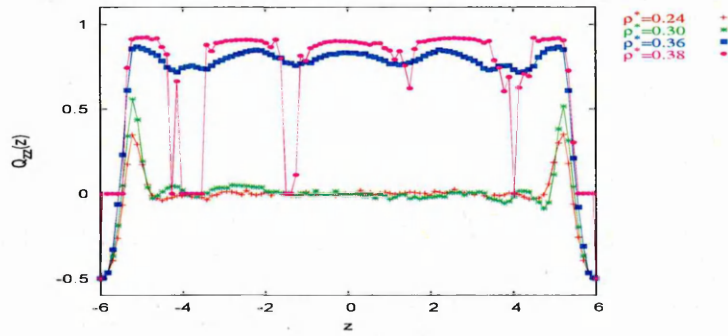
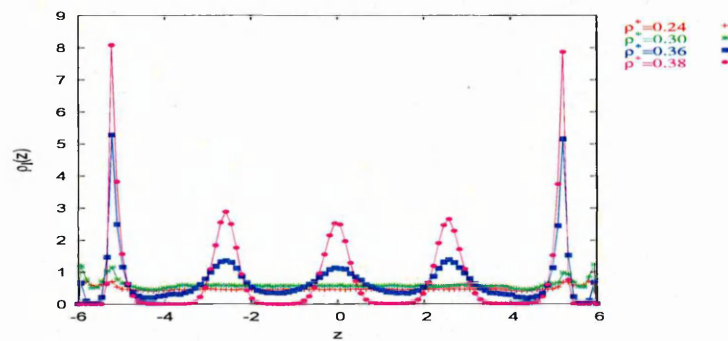


Figure 4.6: Snapshots of the symmetric systems: $k_{st}=k_{sb}=1.5$

This term “competing anchoring” corresponds to a situation where the planar and the homeotropic anchoring are of comparable strength. This situation takes place when the needle length $k_s \sim \kappa/2$. Usually, if we simulate a system where, on one of the substrates, the alignment of the molecules is strongly planar or homeotropic and on the other substrate, we choose the needle length $k_s \sim \kappa/2$, the behaviour of the molecules on that second substrate will depend on the nature of the first substrate (in the nematic phase). This is what we will demonstrate in the next section where we deal with hybrid systems. If we use a symmetric system with $k_s=\kappa/2$ on both walls then, as shown on the Fig. 4.6, the system behaves qualitatively like the symmetric system with homeotropic anchoring (Fig. 4.2(a)). By comparing the Q_{zz} profiles (Fig. 4.4(a) and Fig. 4.7(a)), the first thing we can notice is the fact that the Q_{zz} value increases with density in both case. There are, nevertheless, three main differences between the graphs. The first one is the location of the surface peaks. In the case where $k_s=0$, the first Q_{zz} peaks are situated at $|z - z_0| \sim 0$ whereas for $k_s=1.5$, the main peaks are situated at $|z - z_0| \sim \sigma_0$. The second difference is the periodicity of the peaks. Also, in the case of competing anchoring, the peaks are not as well distinguishable as those in the case with strong



(a) Q_{zz} profile



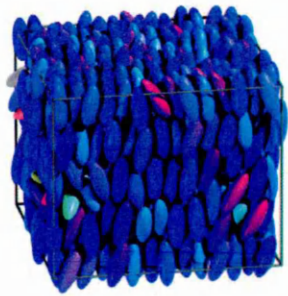
(b) Density profile

Figure 4.7: $Q_{zz}(z)$ and density profile of the symmetric system: $k_{st}=k_{sb}=1.5$

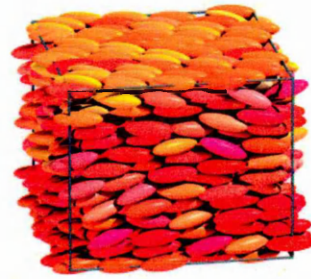
homeotropic anchoring. This can be explained if we look at the density profiles (Fig. 4.4(b) and Fig. 4.7(b)). These shows changes in both the locations and the numbers of peaks observed. Essentially, the surface peaks of the $k_s = \kappa/2$ system are shifted inwards, leading to a thinner LC film from which only three bulk peaks are apparent.

4.3.4 Other Systems: moderate planar and homeotropic anchoring

We have also run simulations with intermediate k_s values, corresponding to moderate homeotropic and planar anchoring. At first, we cannot really see a difference from the strongly anchored ones simply by comparing the snapshots (Fig. 4.2 and



(a) $k_{st}=k_{sb}=1$



(b) $k_{st}=k_{sb}=2$

Figure 4.8: Snapshots of symmetric systems

Fig. 4.8)

Moderate homeotropic anchoring

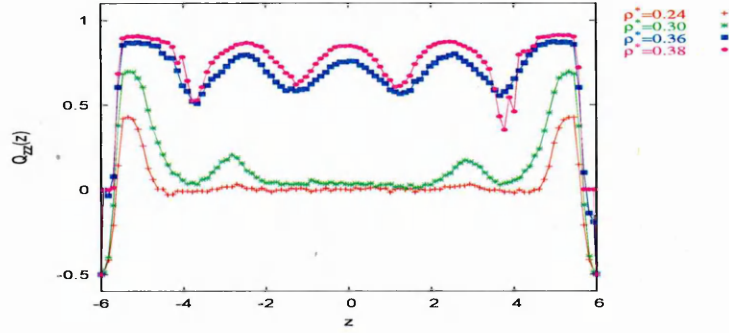
The graphs corresponding to the moderate homeotropic case are shown in Fig. 4.9. Once again, some differences can be spotted. Now, the first peaks are situated at $|z - z_0| \sim \sigma_0/2$. The periodicity of the peaks is greater than it was for $k_s=1.5$, although a total of five peaks is seen again.

Moderate planar anchoring

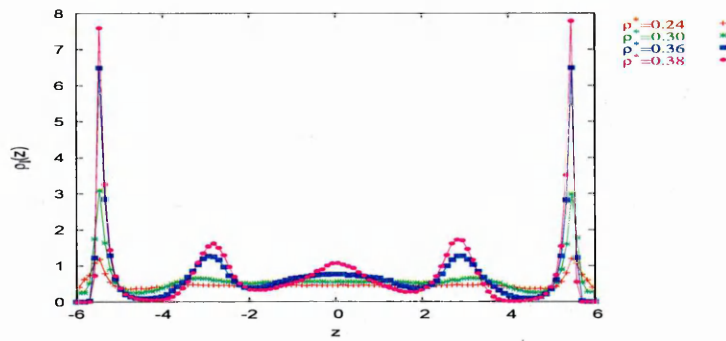
Looking at Fig. 4.5 and Fig. 4.10, we cannot see any difference between the typical profiles. For planar anchoring, the system profiles do not seem to be significantly influenced by changes in the value of k_s .

4.4 Hybrid anchored systems

We now go on to consider hybrid system, i.e., system where the nature of the opposite substrates is different. In our first hybrid system we impose strong homeotropic anchoring on one substrate and strong planar anchoring on the other. In the second and the third systems, conversely, we consider the behaviour when one substrate



(a) Q_{zz} profile



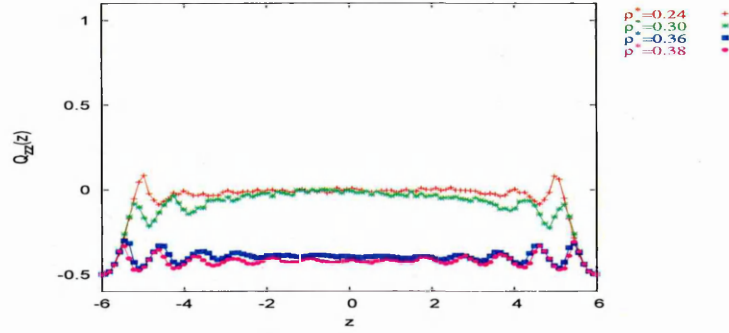
(b) Density profile

Figure 4.9: $Q_{zz}(z)$ and density profile of the symmetric system: $k_{st}=k_{sb}=1$

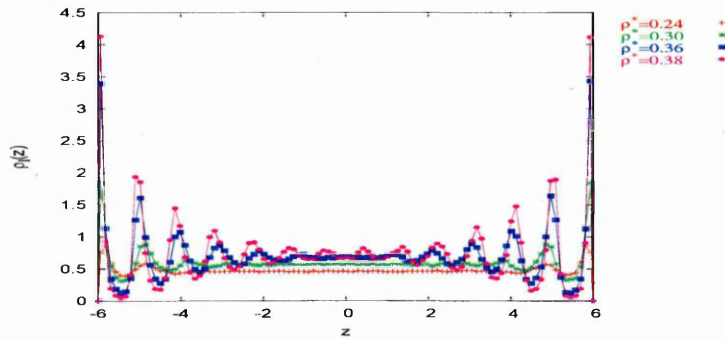
imposes specific molecular alignment (strong planar in one case, strong homeotropic in the other) whereas the other substrate, we just have competing anchoring. On increasing the density of these different systems, we obtain the three very different configurations shown in Fig. 4.11

4.4.1 $k_{st}=3; k_{sb}=0$

This hybrid system is the most extreme because of its strong planar anchoring at one substrate and strong homeotropic anchoring at the other. By increasing the density from the isotropic phase ($\rho^*=0.3$) to the nematic phase ($\rho^*=0.37$), we can notice, looking at the Q_{zz} profile (Fig. 4.12(a)) that planar and the homeotropic alignment grow at the walls well before combining with one another to form a bent director



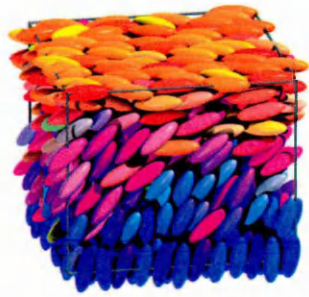
(a) Q_{zz} profile



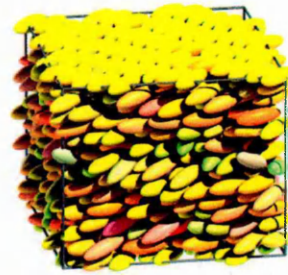
(b) Density profile

Figure 4.10: $Q_{zz}(z)$ and density profile of the symmetric system: $k_{st}=k_{sb}=2$

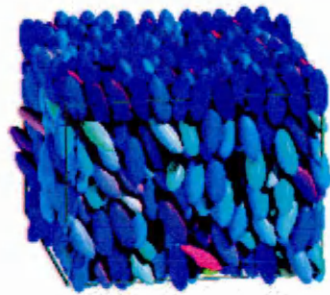
structure (Fig. 4.11(a)). Fig. 4.12(a) shows as well that, at the highest density, simulated, Q_{zz} becomes approximately linear in z away from the surfaces. The density profile remains approximately constant in this region. This behaviour has been reported by Cleaver and Teixeira [97] for $\kappa=5$ HGO particles. In their study, k_s was set at 5 on one surface and 1 on the other. The behaviour of hybrid systems has also been studied theoretically in [20]. The authors found that the behaviour of the hybrid system depends on a critical thickness d_c , defined as: $d_c \equiv K |1/W_H - 1/W_P|$, as well as the surface anchoring strength [129]. In [20], the authors reported that if the cell thickness is greater than this critical thickness, the LC should exhibit a bent-director configuration. For thinner cells, they predicted a uniform director aligning along the direction of the easy axis of the substrate with the stronger alignment.



(a) $k_{st}=3; k_{sb}=0$



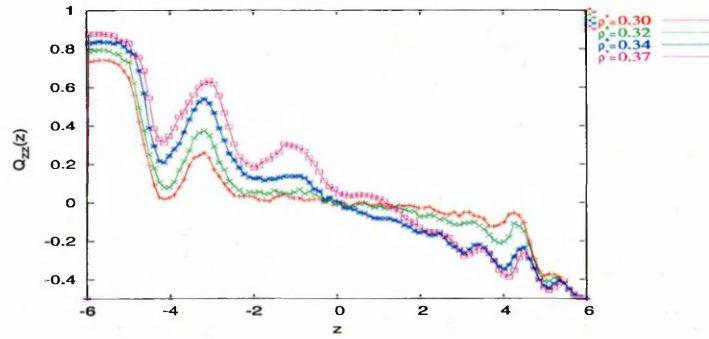
(b) $k_{st}=3; k_{sb}=1.5$



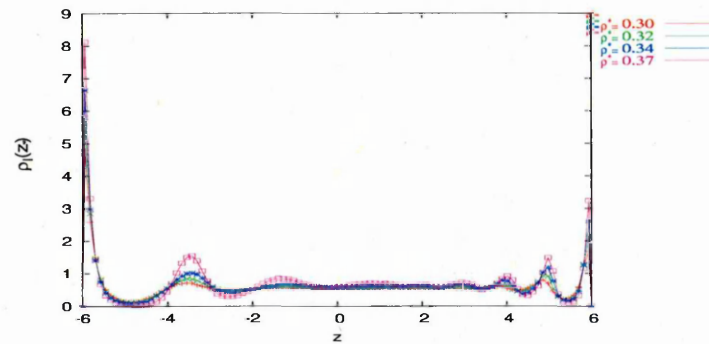
(c) $k_{st}=0; k_{sb}=1.5$

Figure 4.11: Snapshots of the hybrid systems

To understand how an hybrid cell behaves, it is useful to consider the different contributions to its free energy. It is known that the bigger the nematic order, the bigger the elastic resistance of the system to deformation of the director. We found that, depending on the thickness of the simulation box, this hybrid system can exhibit two different behaviours : a bent-director configuration or a cell where there is a discontinuity in the structural transition from homeotropic to planar (previous simulations using an identical cell thickness ($L_z=4\kappa$), but a different number of particles ($N=1000$) found this discontinuous behaviour [102]. It appears, then, that both structures are locally stable and that the arrangement adopted depends on details of the simulation series undertaken. A detailed comparison of the relative free energies of these structures for this parameter set is beyond the scope of this



(a) Q_{zz} profile



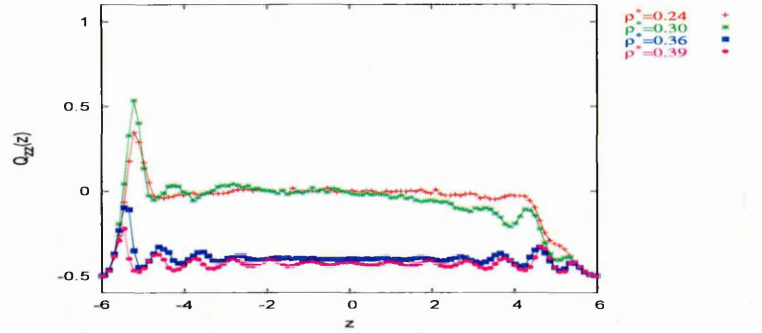
(b) Density profile

Figure 4.12: $Q_{zz}(z)$ and density profile of the hybrid system: $k_{st} = 3$; $k_{sb} = 0$

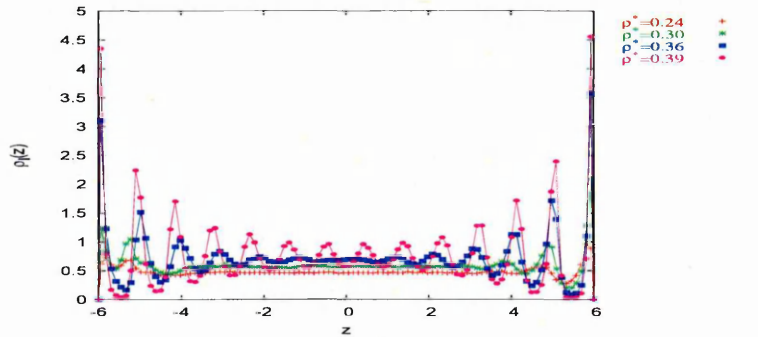
for this parameter set is beyond the scope of this thesis. Here, then, we simply note that both are consistent with the predictions of [102].

4.4.2 $k_{st} = 3$; $k_{sb} = 1.5$

In this system, $k_s = 3$ on the top substrate and 1.5 on the bottom substrate. Looking at the Fig. 4.13(a), we can see that the Q_{zz} profile at the lowest density (red line), is negative close to the upper substrate (this is where $k_s = 3$, so, we expect molecules to be parallel to the substrate) whereas at the bottom surface, the first peak of Q_{zz} is positive. On compressing gently the system to a density $\rho^* = 0.36$, the first Q_{zz} peak at the bottom surface shifts to negative values. Consequently, the lower wall acts like a substrate which promotes planar alignment. This is confirmed by the density



(a) Q_{zz} profile

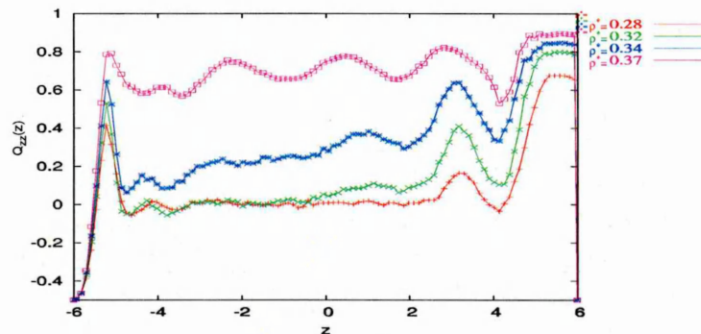


(b) Density profile

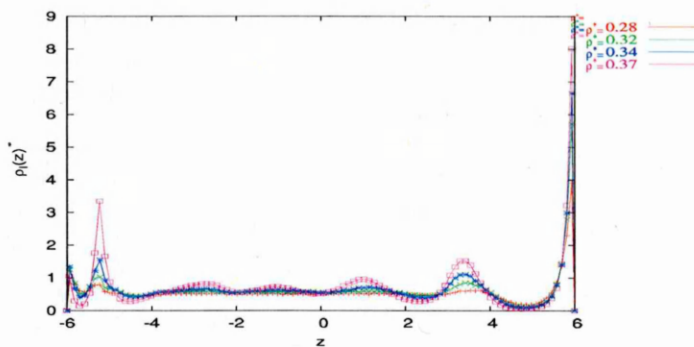
Figure 4.13: $Q_{zz}(z)$ and density profile of the hybrid system: $k_{st} = 3$; $k_{sb} = 1.5$

profile shown in Fig. 4.13(b). Here, at the higher density, there is a succession of peaks with a periodicity of about σ_0 . This behaviour can be easily explained by the fact that, in the case of a thin hybrid cell, the behaviour is determined by the anchoring strengths at the two surfaces. If at one surface the anchoring strength is high whilst that at the opposite surface is low, the director of the bulk nematic is dominated by the surface with the greatest anchoring strength. The bent director configuration has a high elastic distortion free energy and so is unstable with respect to the uniform planar structure. Even though the $k_s = 1.5$ bottom surface prefers homeotropic alignment, it has been shown by Barmes that k_s values only slightly larger than this yield stable planar alignment.

4.4.3 $k_{st}=0$; $k_{sb}=1.5$



(a) Q_{zz} profile

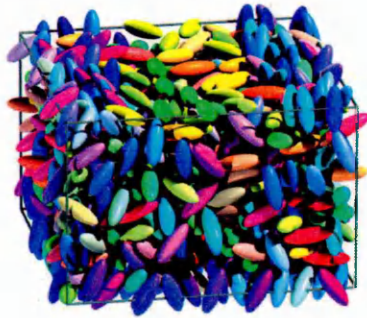


(b) Density profile

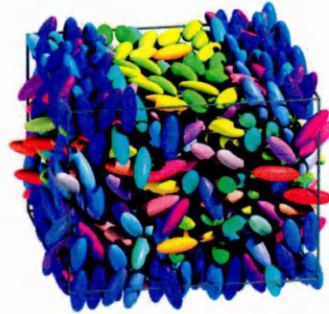
Figure 4.14: $Q_{zz}(z)$ and density profile of the hybrid system: $k_{st} = 0$; $k_{sb} = 1.5$

In this system, $k_s=0$ on the top substrate and $k_s=1.5$ on the bottom substrate. Looking at the Fig. 4.14(a), we can see that the Q_{zz} value, for the lowest density (red line), is now positive both close to the upper substrate (where $k_s=0$) and in the first peak of Q_{zz} at the bottom surface. On compressing gently the system to a density $\rho^*=0.37$, the Q_{zz} value goes positive across the whole of the simulation box. Even though the $k_s=1.5$ substrate is associated with its unusual alignment director here, the profiles obtained show significant z -dependence. Thus, it appears that, using substrates with the same anchoring director, but differing anchoring coefficients leads to a reduction in the structure of the resulting density profile.

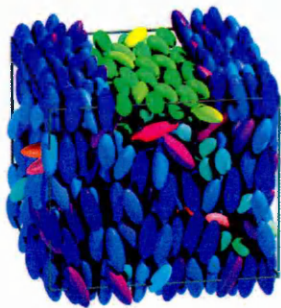
4.5 Systems with one striped substrate



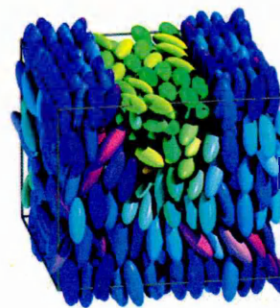
(a) $\rho^*=0.24$



(b) $\rho^*=0.32$



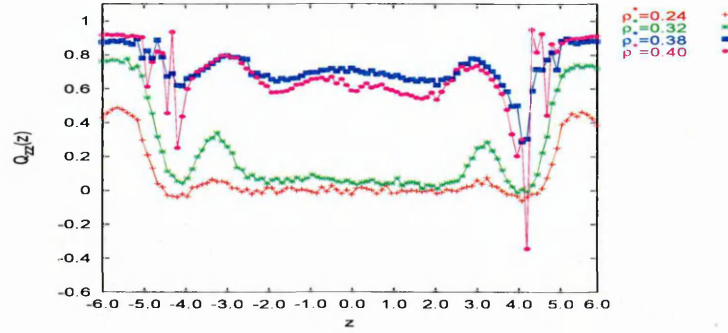
(c) $\rho^*=0.38$



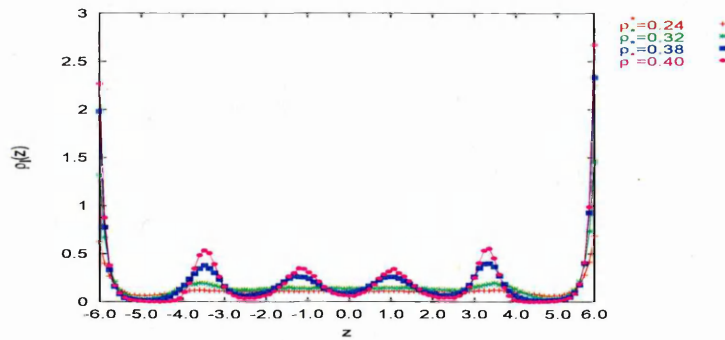
(d) $\rho^*=0.40$

Figure 4.15: Configuration snapshots from MC simulations of striped systems at four reduced densities. Particle colour is used to denote orientation (blue = along z , green=along x , red=along y).

In the previous sections, we have been considering unpatterned systems and we have established initial results for these systems. In this section, we now consider a system with one patterned substrate and one unpatterned substrate. The unpatterned substrate promotes homeotropic alignment whereas the patterned substrate is composed of identical width stripes alternatively favouring planar and homeotropic alignment. Here, we impose sharp transitions between the stripes, and the stripe boundaries run along the y -axis of the simulation box. Snapshots of



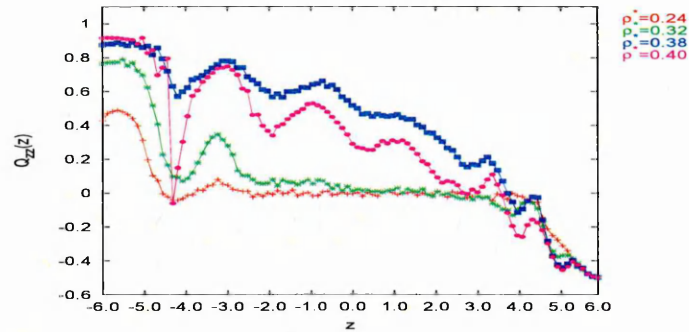
(a) Q_{zz} profile



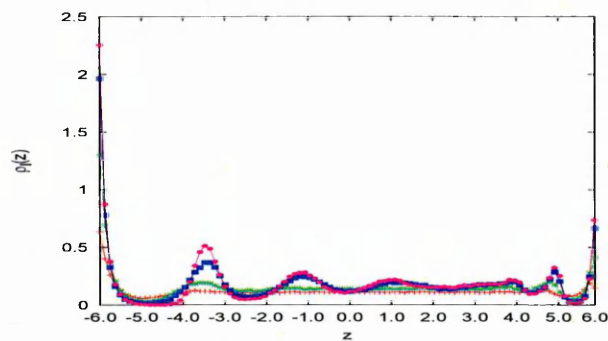
(b) Density profile

Figure 4.16: Nematic order parameter and density profile measured with respect to the substrate normal, $Q_{zz}(z)$ and $\rho^*(z)$ for striped system in the region where $k_s=0$ on both surfaces.

this system, at different reduced densities, can be seen in Fig. 4.15. At low density, $\rho^* < 0.33$, the bulk remained disordered. The pattern from the top surface is restricted to the immediate vicinity of the wall. Here, the molecules in direct contact with the top wall adopt the expected behaviour corresponding to the imposed k_s values. At the lowest density, we can see that the molecules adopt a homeotropic surface anchoring for the $k_s=0$ surface region and a planar surface anchoring on the remaining substrate area. For this 1D pattern, k_s depends only on x . For this system, k_s is fixed at 0 if $|x| \geq 0.25L_x$ and k_s is fixed at 3 otherwise. By moving randomly a particle, it is possible that the value of k_s changes. This is due to the



(a) Q_{zz} profile



(b) Density profile

Figure 4.17: Nematic order parameter and density profile measured with respect to the substrate normal, $Q_{zz}(z)$ and $\rho^*(z)$ for striped system in the region where $k_s=0$ on the bottom surface and $k_s=3$ on the top surface.

fact that, by translating a particle, it can cross the surface anchoring boundary. In the planar region, the molecules align along the stripes. As we increase the density to $\rho^*=0.38$, the central region of the bulk seems to form a homeotropic monodomain (see Fig. 4.15(c)) and only the region in direct contact with the planar alignment surface adopts a different behaviour. Rather surprisingly, as the density is increased to 0.4 (see Fig. 4.15(d)) the influence of the planar surface stripe appears to grow, the volume with planar character penetrating several particle-widths into the system. In order to examine what is really happening here in more detail, we have calculated density and order parameter profiles for this system. Figs. 4.16 and

4.17 show the Q_{zz} and ρ profiles corresponding to the two distinct regions delimited by the top surface pattern. In the homeotropic alignment region, one surprising feature is that for the stripe patterned system at $\rho^* = 0.4$, the Q_{zz} value attained in the central bulk region decreases with increase in density whereas (recall Fig. 4.3), for the unpatterned symmetric system, Q_{zz} increases monotonically with density. This can perhaps be explained by reference to the associated behaviour observed in the second region of the striped substrate system (see Fig. 4.17). In the “hybrid” region confined between a $k_s=0$ surface region at the bottom and a $k_s=3$ surface region at the top, increase in density leads to increasingly linear behaviour in the $Q_{zz}(z)$ profile linking the two substrates. This increased linearity in the Q_{zz} profile means that the system is adopting an uniform director bend. This system behaviour was noted in section 4.4.1 and in Cleaver and Teixeira’s study of hybrid aligned LC films [97]. To probe these observations more completely, we now make direct comparison between these striped system results and those obtained for the equivalent unpatterned substrate arrangements.

4.5.1 Comparison homeotropic region

In Fig. 4.18, we show the Q_{zz} profiles corresponding to the homeotropic region of the stripe patterned system and an unpatterned symmetric homeotropic system. These profiles are very similar, the I-N transition taking place at the same density for the two systems. The graph in Fig. 4.18(b) is perfectly symmetrical about $z=0$ because it corresponds to an unpatterned symmetric system. However, looking at Fig. 4.18(a), we can notice that the Q_{zz} value increases first close to the bottom surface and then close to the top surface. This is due to the top surface being patterned, and its planar region influencing the homeotropic one. This causes the Q_{zz} value to be slightly lower at the top surface, indicating a lower homeotropic anchoring strength due to the neighbouring planar alignment region. However, in the central part of the bulk, there is no difference in the Q_{zz} value. Thus, far from the substrate, the bulk central region is insensitive to the detail of the confining substrates.

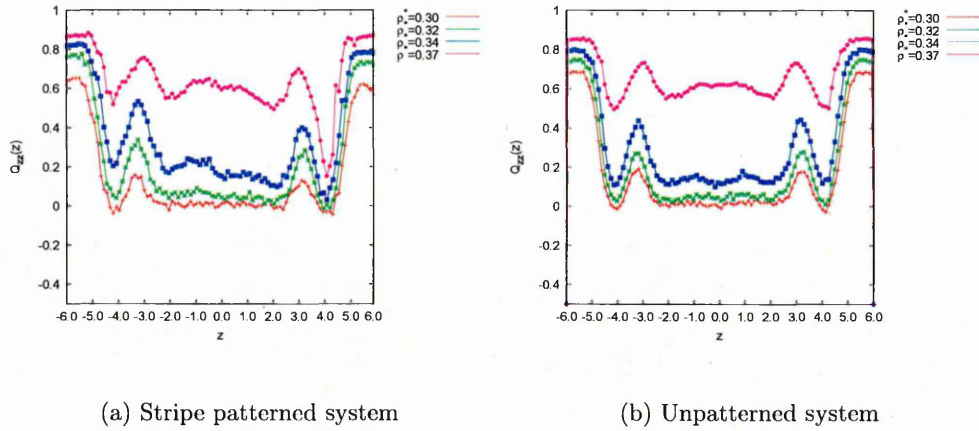


Figure 4.18: Homeotropic region. Comparison of the Q_{zz} profiles corresponding to the stripes pattern system and the unpatterned system at different reduced densities.

4.5.2 Comparison hybrid region

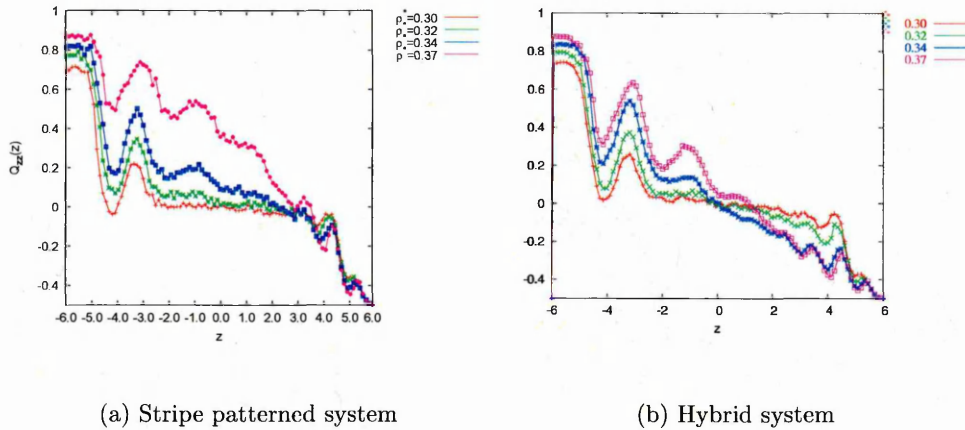


Figure 4.19: Hybrid region. Comparison of the Q_{zz} profiles corresponding to the stripes pattern system and the hybrid system at different reduced densities.

Fig. 4.19 shows the Q_{zz} profiles corresponding to the hybrid region of the stripe patterned system and to the unpatterned hybrid system studied in section 4.4.1. At high density ($\rho^* = 0.37$), the difference in profiles is more noticeable for the hybrid region than it was for the homeotropic region. For the unpatterned hybrid system $Q_{zz}(z)$ crosses 0 at $z=0$ (Fig. 4.19(b)). However, for the stripe patterned system,

the high density Q_{zz} profiles are shifted significantly to the upper surface. This suggests that the effective surface anchoring strength for the planar region of the upper surface is decreased due to its proximity to neighbour regions of opposite anchoring.

4.6 Conclusions

In this chapter we have presented representative results obtained from a set of increasingly complex confined LC film systems. From these, we have demonstrated that typical profiles (Q_{zz} and density) can be used to extract information on how each system behaves and how this varies with substrate conditions. We have used this approach to illustrate and explain the behaviour of three hybrid systems set up with different anchoring strength combinations at their surfaces. We concluded this chapter by showing the behaviour of a system with one striped substrate. This approach will be expanded considerably in the next chapter in which we will present a comprehensive study of systems with two striped substrates.

Chapter 5

Nematic liquid crystals on stripe patterned substrates

Chemical patterning of surfaces for LC alignment promises to deliver a number of significant advantages for device technology over existing non-patterned surfaces. Two of the main advantages are the improvement of optical performance and the widening of the viewing angles. An anchoring pattern can alternatively be written chemically using an appropriate combination of self-assembled-monolayers (SAMs). Patterned LC alignment raises various questions :

- How does the written pattern penetrate the liquid crystal (i.e. what is the z dependence) ?
- Can tilt be induced and controlled using patterning ?
- Can patterning give independent control over the two anchoring coefficients (polar and azimuthal) ?

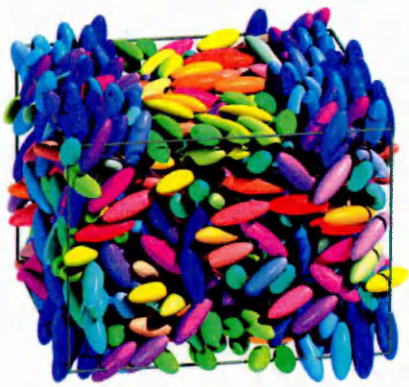
In 2005, Scharf *et al.* [130,131] discussed the alignment properties of nematic LCs on surfaces that contain homeotropic and planar alignment areas on the same substrate. The concept of simultaneous alignment of azimuthal and polar orientation of LCs by chemical nanopatterns has also been suggested experimentally [132–134]. Park *et al.* [130,131] showed that the polar orientation depends on the ratio of the homeotropic/planar surface potential areas, while the LC azimuthally orients along the direction of the stripes [135].

In this chapter, we concentrate on systems with stripe patterns on both of their substrates. First we will look at sharp transitions between the two surface areas, that is, substrates with discontinuous changes in their interaction potentials. In this, we will study the influence of different parameters on the systems, specifically the proportion of homeotropic and planar alignment regions on the substrates, the strengths of the homeotropic and planar alignment conditions and the thickness of the confined LC film. Then we will investigate the effect of smooth transitions and compare these results with the ones obtained for sharp pattern boundaries.

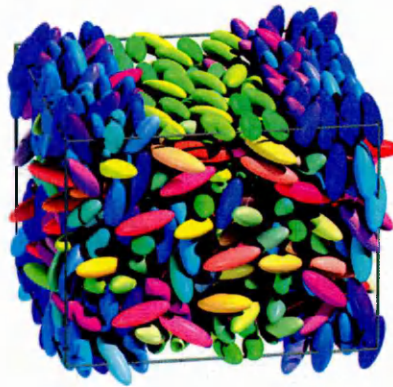
5.1 Initial system

We have studied a system of 864 molecules confined between two stripe patterned substrates. The substrates were separated by a distance $L_z = 4\kappa\sigma_0$. The molecules interacted with one another via the HGO potential and with the walls via the HNWI potential. Generally, on each substrate, k_s was set to a homeotropic-aligning value for half of its area and a planar value for the remainder (in the first simulation described below, the k_s values used were 0 and 3). For a more complete understanding of the variation of k_s across the system, please see Section 4.5. Here, sharp boundaries have been imposed between the different alignment regions, the stripe boundaries running parallel to the y -axis of the simulation box. The patterns on the top and bottom surfaces were kept in perfect registry with one another. As previously described, each system has been initialised at low density and gently compressed by decreasing the box dimensions L_x and L_y . At each density run lengths of 1 million MC sweeps (where one sweep represents one attempted move per particle) were performed, averages and profiles being accumulated for the final 500 000 sweeps.

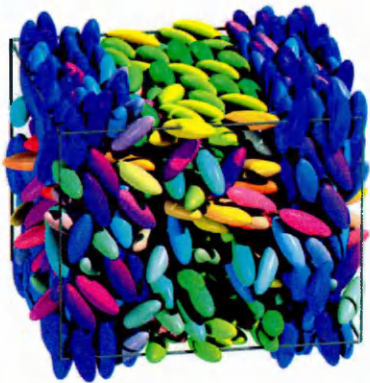
The outcomes of the first striped system simulated are summarised by the snapshots shown in Fig. 7.11. Several remarks emerge from these. At low density ($\rho^* = 0.3$), the central region of the film remains relatively disordered, but the near-surface regions adopt orientations consistent with their imposed k_s values (Fig. 5.1(a)). Even at the relatively low density of $\rho^* = 0.32$, the particles in the $k_s = 3$ stripe show a marked preference for lying parallel to the stripe boundaries (Fig. 5.1(b)).



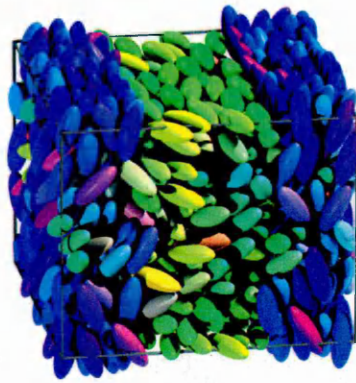
(a) $\rho^*=0.3$



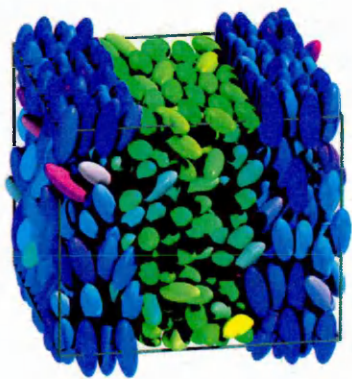
(b) $\rho^*=0.32$



(c) $\rho^*=0.34$



(d) $\rho^*=0.36$

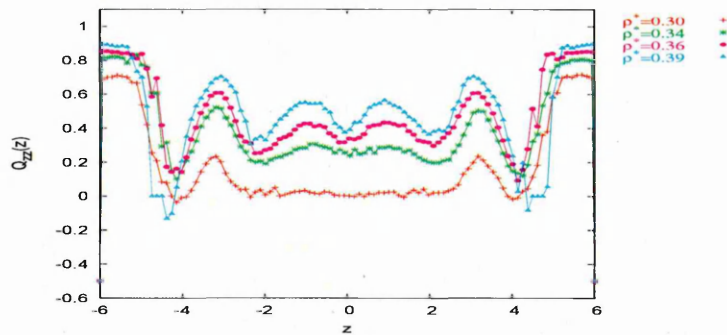


(e) $\rho^*=0.39$

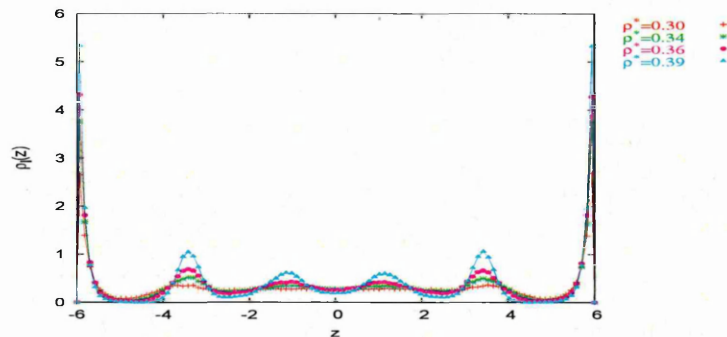
Figure 5.1: Snapshots of the stripe patterned system at different reduced densities.

With increase in density, the nematic phase appears to form between the $k_s=0$ surface regions (Fig. 5.1(c)) while the other part of the bulk region (confined between $k_s = 3$ region) remains relatively disordered. At the reduced density $\rho^* = 0.39$ (Fig. 5.1(e)), the orientations of the bulk regions are apparently the same as those of the molecules aligned at the substrate : the stripe pattern is, thus, written across the film.

To obtain more detailed information on this surface induced ordering, we consider the Q_{zz} profiles (Fig. 5.2(a) and Fig. 5.3(a)). These profiles show clear differences in the mid-film behaviours induced by the different substrate couplings. Looking



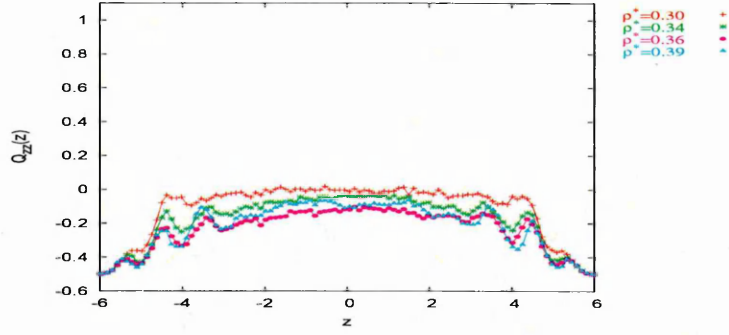
(a) Q_{zz} profile homeotropic region



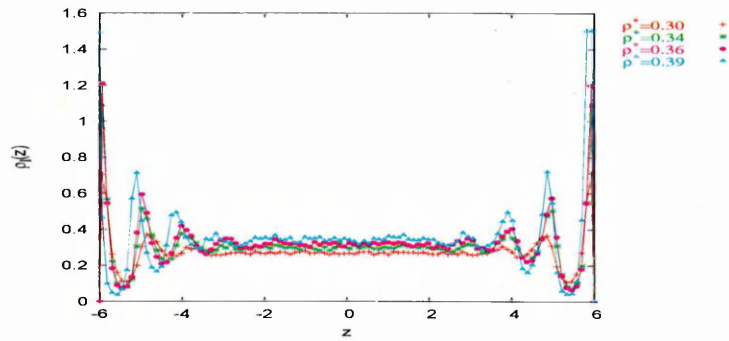
(b) $\rho_l(z)$ profile homeotropic region

Figure 5.2: Profiles corresponding to the homeotropic surface region.

at Fig. 5.2(a), the Q_{zz} profile of the LC confined between the $k_s=0$ substrate regions (homeotropic), we can see that, as the reduced density was increased, so



(a) Q_{zz} profile planar region



(b) $\rho_l(z)$ profile planar region

Figure 5.3: Profiles corresponding to the planar surface regions.

was the Q_{zz} value. With increasing the density, the bulk region confined between the two $k_s=0$ substrates, became more and more organised, with Q_{zz} behaviour consistent with the development of homeotropic anchoring. The behaviour of the remainder of the system (confined between the $k_s=3$ substrates), is not quite so straightforward. Fig. 5.3(a) shows that on increasing the reduced density, the Q_{zz} profile did not decrease as it did in the case of symmetric system with $k_s=3$ on both substrates (see Fig. 4.5(a)). Instead, the value of Q_{zz} stagnated at around -0.2. Rather than indicating a lack of orientational order, this behaviour of Q_{zz} suggests that the director tilts in this bulk region. Consequently, the behaviour of the bulk region confined between the two $k_s=3$ substrates is influenced by the bulk region confined between the two $k_s=0$ substrates. For this system, then, the influence of the $k_s=0$ substrates on the bulk behaviour appears to be greater than that of the

$k_s=3$ substrates. From this observation, one might infer that the homeotropic and the planar anchoring strengths might not be of comparable strength. The associated density profile depicted in Fig. 5.2(b) shows the formation of layers in the homeotropic region separated by a distance d : $2\sigma_0 \leq d \leq 2.5\sigma_0$. This distance nearly corresponds to the molecular length. If the system had been perfectly arranged in pseudo smectic layers, there would have been 3 peaks in the mid-film region and 2 peaks at the substrates. In this ideal case, the peaks would be separated by a distance $d=3\sigma_0$ (recall Fig. 4.4(a) for homeotropic anchored system). Fig. 5.3(b) shows that, in the “planar” region, the formation of layers is restricted to 3 monolayers at each substrate. This corresponds to the molecules forming a first layer at the substrate (the first peaks are situated at $|z - z_0| \sim 0$) and then developing other peaks with a periodicity of about σ_0 . In this region, then, it appears that the molecules are arranged side to side close to the substrates but that the positional structure is smeared out in the tilted central region.

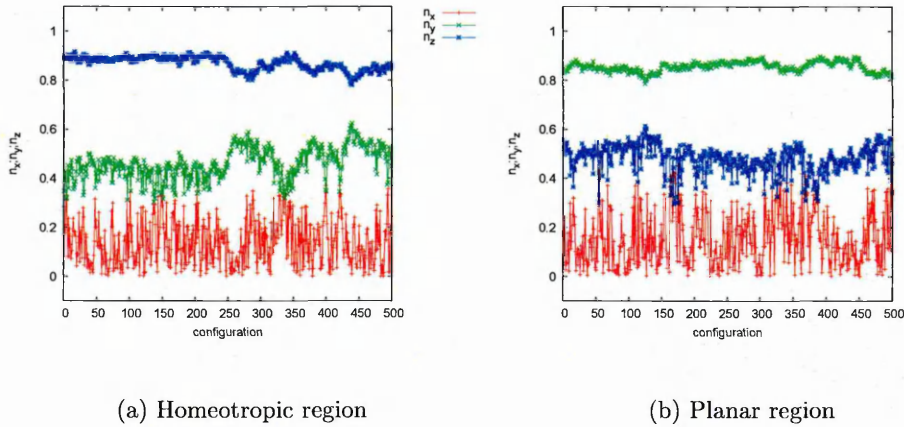


Figure 5.4: Director components for the $\rho^*=0.4$ run.

By looking at the components of the director, we can determine the orientation of the director and, thus, the angle formed between the box axes (x , y or z) and the director. n_x , n_y and n_z are the three components of the director. The angles θ_x , θ_y and θ_z formed between the box axes x , y or z and the director are then related to n_x , n_y and n_z by the inverse cosines :

$$\theta_i = \arccos(\langle n_i \rangle) \quad (5.1)$$

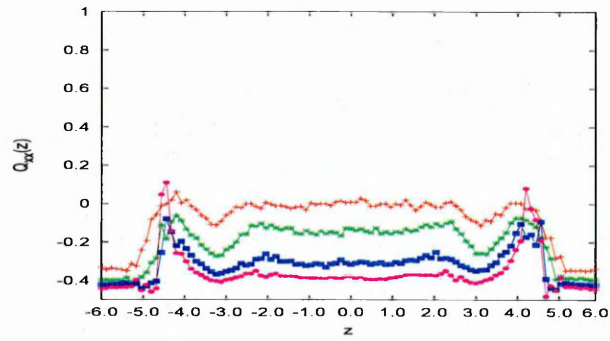
with $i=x, y$ or z .

Fig. 5.4(a) shows that for the bulk LC associated with the homeotropic alignment surface region, the largest director component is aligned along the z -axis, apparently, corresponding to homeotropic anchoring. In the other region, the largest component is aligned along the y -direction (Fig. 5.4(b)). To determine the tilt angles in the two regions, it is not ideal to calculate the two θ_z angles. Instead, we use the angle measured with respect to the largest component in each region because the n_z component in the $k_s=3$ surface region is noisy. From this, in the homeotropic region, we obtained an angle of $\theta_z=28.6$ degrees. In the planar region (Fig. 5.4(b)), where the director is pointing to the y axis, the angle $\theta_y=27.5$ degrees.

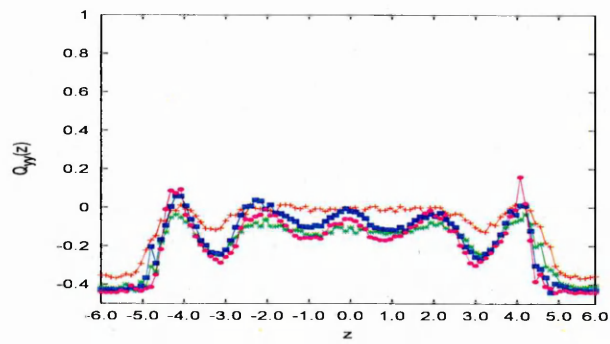
The director tilt angles determined in the previous paragraph indicate the inference drawn from the snapshots, that the film is split into homeotropic and planar regions, may not be fully correct. To probe this in more depth, we now look in more detail at the Q matrix data obtained in each patterning region and compare these with the equivalent data from symmetric confined systems.

5.1.1 Homeotropic confinement region

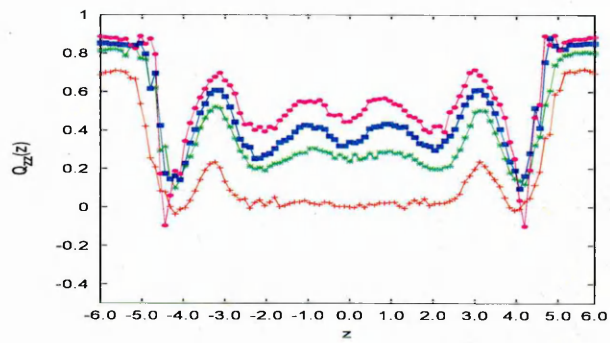
A more complete understanding of this system behaviour can be reached by looking at all three diagonal components of the director Q_{xx} , Q_{yy} and Q_{zz} (Fig. 5.6). At low density (isotropic phase), the diagonal component Q_{xx} is negative close to the wall ($\simeq -0.4$) and equal to zero in the bulk. On compression to nematic densities, the value of Q_{xx} decreases in the bulk ($Q_{xx}=-0.4$). This result indicates that the particles are perpendicular to the x -axis and so, parallel to the z -axis. For perfect homeotropic anchoring, Q_{zz} should tend to 1, Q_{xx} and Q_{yy} should tend to -0.5. The Q_{yy} diagonal component, at low density, is negative close to the wall. By increasing the density, peaks appear in the bulk region but the value of Q_{yy} stagnates at around -0.1. Fig. 5.5(c) shows that Q_{zz} , at low density, is zero in the bulk region but positive close to the wall, consistent with homeotropic order to the wall. On increasing the density, and entering the nematic phase, the Q_{zz} value increases and



(a) $Q_{xx}(z)$



(b) $Q_{yy}(z)$



(c) $Q_{zz}(z)$

Figure 5.5: Diagonal components of the order parameter tensor, homeotropic region.

the director in the bulk starts to align along the z -axis. With these three graphs, we can again conclude that the director in the bulk is nearly homeotropic but, because Q_{yy} value is not equal to -0.5, the director might be lying along the yz -plane.

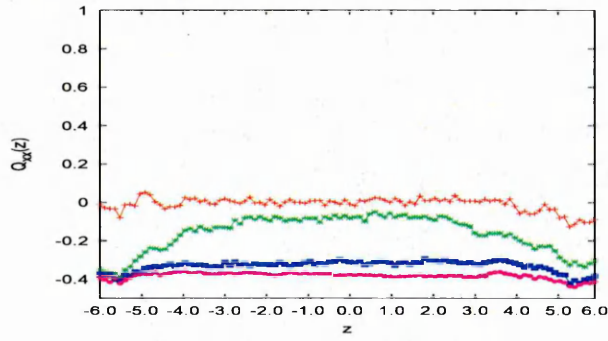
5.1.2 Planar confinement region

In the planar region, the behaviour of the three diagonal components is a bit different. Q_{xx} (Fig. 5.6(a)) at low density is zero everywhere. As the density increases, Q_{xx} becomes rapidly negative close to the wall and starts to become negative in the bulk region as well. At high density ($\rho^*=0.38$), Q_{xx} is about -0.4 everywhere. This behaviour of the Q_{xx} diagonal component shows that the molecules align perpendicular to x . In fact, the molecules align along the stripes. At low density, Q_{yy} (Fig. 5.6(b)) is positive close to the wall (~ 0.5) and zero in the bulk region. As the density increases, Q_{yy} increases close to the wall (~ 0.9) as well as in the bulk (~ 0.5). This high value of Q_{yy} arises because the molecules are parallel to the y -axis. This conclusion is confirmed by the behaviour of Q_{zz} (Fig. 5.6(c)) is negative close to the wall which indicates that the molecules are lying planar to the substrate. As the density increases, though, Q_{zz} becomes less negative, which means that the molecules are not strongly lying perpendicular to the z -axis. There are two ways to explain why $Q_{zz} \simeq -0.1$ in the bulk. Having a mix of homeotropic and planar anchoring in the central region of the film might explain this phenomenon because the Q_{zz} value is an average over all the particles in the mid-film. Another way to explain this is to suppose that the molecules in the mid-film are tilted.

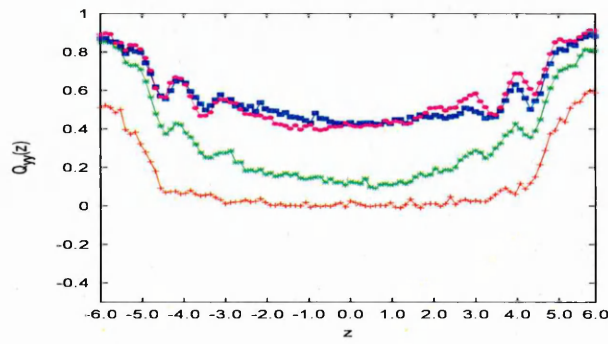
The off-diagonal components $Q_{xy}(z)$ and $Q_{xz}(z)$ vanish at all densities. In Fig. 5.7, we can see that the off-diagonal component $Q_{yz}(z)$ vanish for $\rho^* \leq 0.36$ in both regions. For ρ^* greater than 0.36, however $Q_{yz}(z)$ decreases and tends to -0.5. This result implies the presence of a splay/bend deformation in the structure (in the yz plane).

5.1.3 Preliminary conclusions

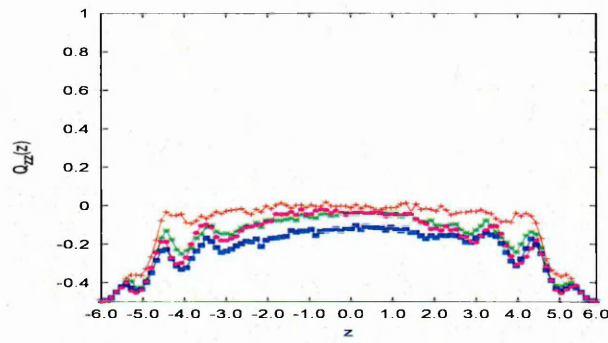
With the previous observations, we can make a set of conclusions concerning this initial stripe patterned substrates system. Here, we saw that the molecules align



(a) $Q_{xx}(z)$

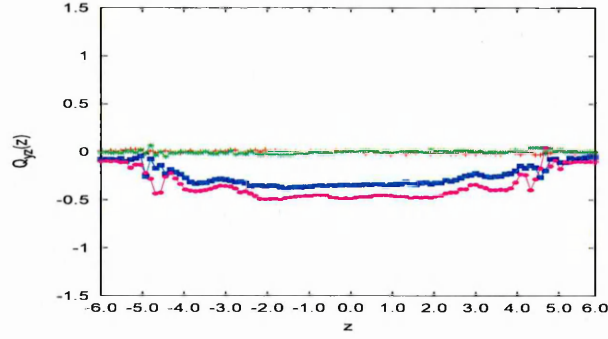


(b) $Q_{yy}(z)$

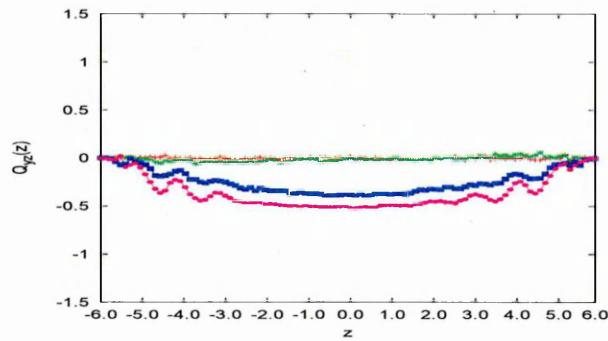


(c) $Q_{zz}(z)$

Figure 5.6: Diagonal components of the order parameter tensor, planar region.



(a)



(b)

Figure 5.7: Off diagonal component $Q_{yz}(z)$ of the order parameter tensor for a) Homeotropic region and b) planar region.

along the stripes (a well known property which was also demonstrated by our collaborators in Leeds : see section 2.7.3). Fig. 5.8 shows the azimuthal angle distribution obtained at the surface for a stripe patterned system for a reduced density of 0.39. The azimuthal angle is strongly parallel to the stripes at small angle $0 \leq \phi \leq 5^\circ$. The issue of polar anchoring is slightly more complex. At first sight, the surface patterns seemed to be written across the film but, as exposed in the analysis above, the bulk region confined between the $k_s=3$ surfaces actually shows a degree of tilt. To clarify this situation, we will, in the following sections, compare the profiles obtained for this striped system with those determined for $k_s=0$ and $k_s=3$ unpatterned surfaces.

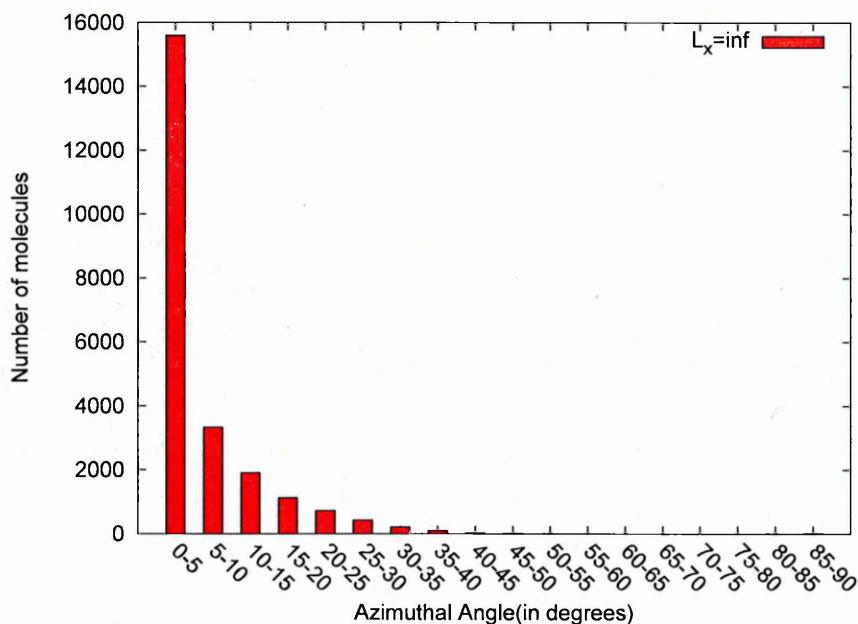
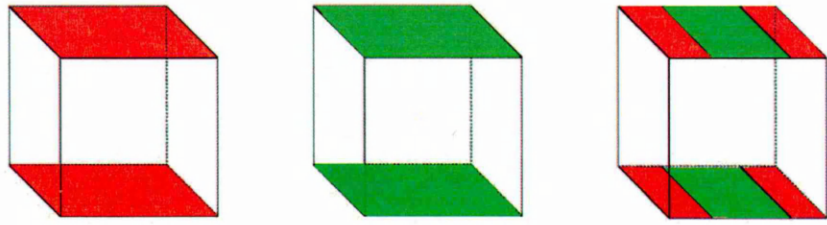


Figure 5.8: Histogram representing the repartition of the azimuthal angle in the planar surface region for the stripe patterned system with 50% H and 50% P on the surfaces. $\rho^*=0.39$

5.1.4 Comparison between the symmetric and the stripe patterned systems

Fig. 5.9 shows, in a very simple way, the representation of the different systems we shall now compare. The green regions represent regions where the molecules are lying parallel to the surface and the red regions, represent region where the molecules are in the plane of the surface. Initially here, we compare the Q_{zz} profiles of the homeotropic symmetric system and the Q_{zz} profile of the corresponding regions of the stripe patterned substrates system. By comparing these two systems, we can have a better idea of how the stripe patterned system is behaving. For clarity, only high density systems are represented in Fig. 5.10. This graph shows that the Q_{zz} value is consistently higher for the unpatterned system than the patterned one. This is due to the fact that the planar alignment of the molecules on the neighbouring substrate regions influences the behaviour of the “homeotropic” bulk and, as a consequence, the bulk director in the red region for the stripe patterned substrate is not truly perpendicular to the substrate.



(a) Homeotropic symmetric system (b) Planar symmetric system (c) Stripe patterned system

Figure 5.9: Schematic representations of different systems.

If we now compare the green regions (planar alignment on the surface) we can see, in Fig. 5.11, that the Q_{zz} value for the striped patterned system does not tend to -0.5 as it does for the symmetric system. Instead, the Q_{zz} value stagnates at around -0.1. We saw in section 5.1.2 that there is a splay/bend distortion in the structure which explains the behaviour of the Q_{zz} profile. However, looking back to Fig. 5.11, we can see that the system also loses a little of its positional order as well as having decreased Q_{zz} value in the bulk.

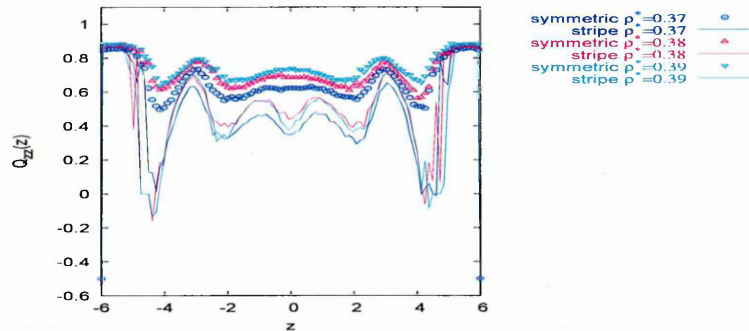


Figure 5.10: Q_{zz} profile corresponding to the homeotropic region of the stripe patterned substrate system and the homeotropic symmetric system.

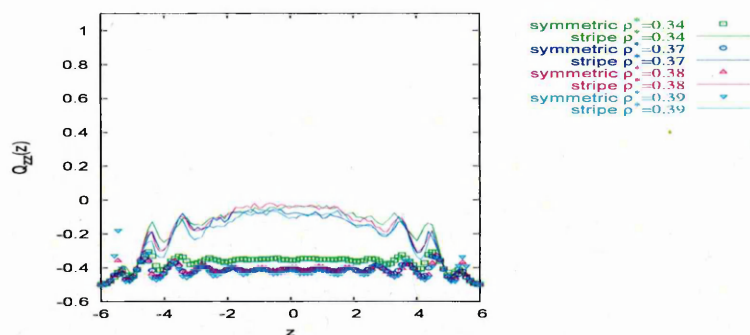


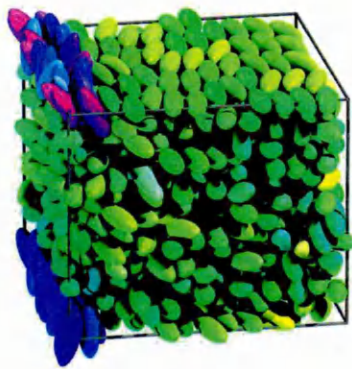
Figure 5.11: Q_{zz} profile corresponding to the planar region of the stripe patterned substrate system and the planar symmetric system.

5.1.5 Conclusion

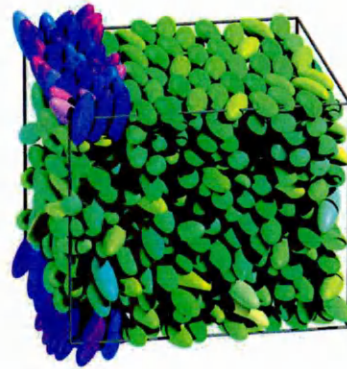
From this direct comparison, it is apparent that the green and the red regions have a non negligible impact, respectively on one another. For this initial system, it appears that the influence of the homeotropic surface region was greater than that of the planar. This is led to the bulk director adopting a spatial variation with small x component but changing y and z components. One can, alternatively, envisage possible stable structures in which a uniformly oriented bulk monodomain is the stable arrangement. To probe this further, we now study the behaviour of this sort of system as a function of the proportion of homeotropic and planar alignment of the molecules on the surfaces, the surface anchoring parameters used and the cell thickness. These influences will be exposed and discussed in detail in the coming sections.

5.2 Influence of the proportion %homeotropic %planar

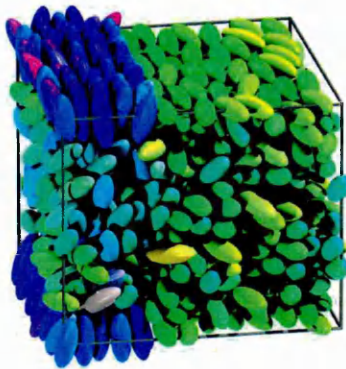
In this section, we want to study the influence of the proportion of the homeotropic and planar alignment regions on the substrate (H and P)(Table 5.1). To do this we consider systems otherwise identical to that used in the previous section. Full compression sequences were performed on all of these systems. Fig. 5.12 presents snapshots of the $\rho^*=0.4$ configurations obtained for the different systems studied



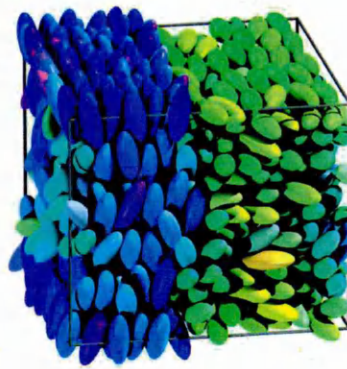
(a) 10% Homeotropic 90% Planar



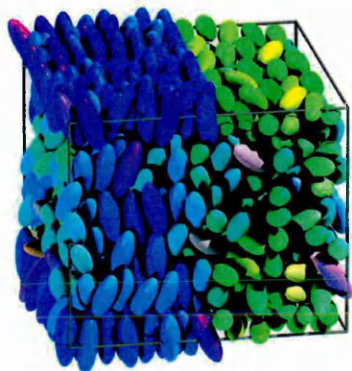
(b) 20% Homeotropic 80% Planar



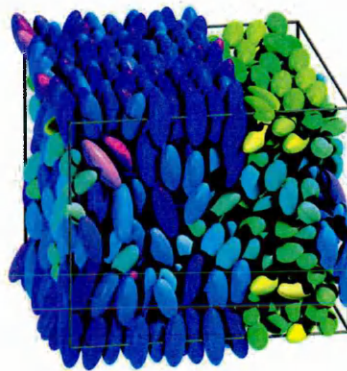
(c) 30% Homeotropic 70% Planar



(d) 40% Homeotropic 60% Planar

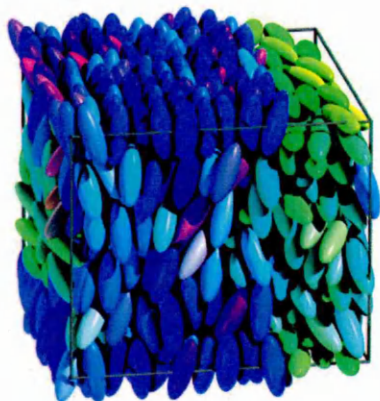


(e) 50% Homeotropic 50% Planar

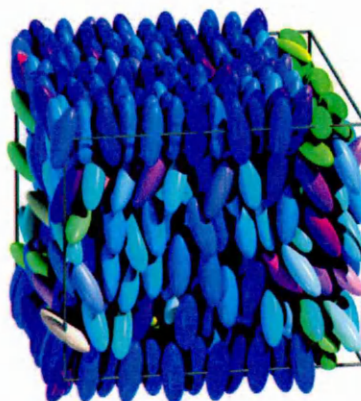


(f) 60% Homeotropic 40% Planar

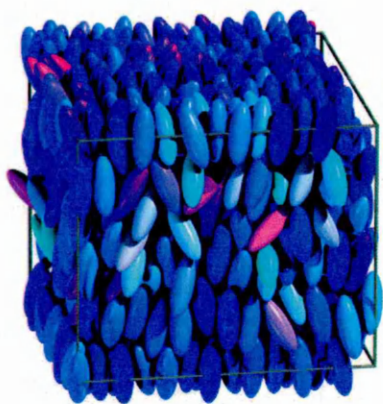
Figure 5.12: Snapshots of the stripe patterned system for different surface area ratios (homeotropic / planar). $\rho^*=0.4$



(g) 70% Homeotropic 30% Planar



(h) 80% Homeotropic 20% Planar



(i) 90% Homeotropic 10% Planar

Figure 5.12: (Continued)

here. These clearly indicate that, depending on the proportions of H and P on the surfaces, the whole system can indeed exhibit either a monodomain or an oscillatory two distinct domains arrangement. Fig. 5.13, Fig. 5.14 and Fig. 5.15 represent the n_y and n_z components of the director in each region of the studied systems. To aid reading of these graphs, n_x is not represented. Once again, analysis of these systems is clarified by discussing the similarities and the differences of the systems for the green and the red regions. First of all, we will look at what happens in the red region and the consequences of increasing the area of homeotropic alignment on the surfaces. We will then adopt the same approach regarding the green region.

homeotropic(%)	10	20	30	40	50	60	70	80	90
planar(%)	90	80	70	60	50	40	30	20	10

Table 5.1: Range of simulations

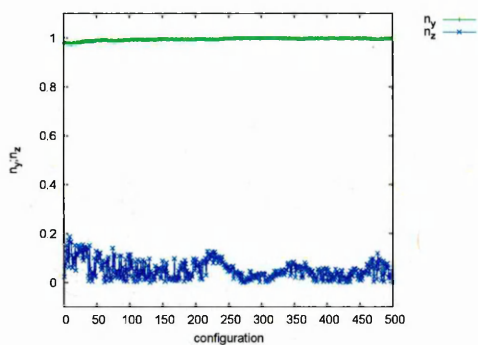
5.2.1 Homeotropic alignment region(H region)

If we look at the snapshots (Fig. 5.12), we can see that, for a proportion 10% H and 90% P (Fig. 5.12(a)), the system does not see the homeotropic part of the surface and seems to behave like an unpatterned system. This result is repeated for the 20% H and 80% P system (Fig. 5.12(b)). It appears, then, that this system does not see the homeotropic alignment on the substrate if the corresponding surface area is less than 30%. On the following snapshot (Fig. 5.12(c)), the system behaves differently. Here, the region confined between the $k_s=0$ surfaces does respond to the patterned substrate and the system can see the homeotropic alignment on the substrate. To check the validity of this assessment, we look at Fig. 5.13, which shows the n_y and n_z director components of these three first systems ($10\% \leq H \leq 30\%$). The graphs on the left hand side show the director components for the region of the bulk which is confined between the H surface regions, whereas the graphs on the right represent the director components in the remaining bulk. Figs. 5.13(a) and 5.13(c) confirm what was inferred from the snapshots for the 10% H and 20% H systems. The director for these two systems is aligned along the y -axis (i.e. along the stripes). Fig. 5.13(e) shows that the director in the red region is also largely aligned along the y -axis. However, here the n_y value is decreased

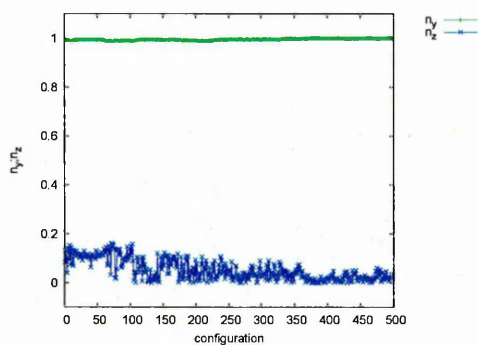
when compared with the planar region values in the 10 and 20% systems, which means that there is a non-trivial tilt angle between the director and the y -axis. So for this film thickness, 30% H on the substrates leads to the whole system being influenced by the homeotropic alignment regions of the surface. Put another way, for $H < 30\%$ of the surface area, the influence of the homeotropic region is too small to induce uniform homeotropic anchoring in the mid-film. For a proportion $H \geq 40\%$, the largest component of the director flips from the y -axis to the z -axis in the red region (Fig. 5.14(a)), which indicates that here, the influence of the homeotropic proportion at the substrate is sufficient to dominate the associated bulk behaviour. Increasing the proportion of homeotropic alignment on the surface leads to a slow growth in the n_z component in the H region, up to its limiting value of 1. As we increase the proportion of homeotropic alignment on the substrate, then, n_z increases (Figs. 5.14 and 5.15, graphs on the left) and correspondingly θ_z decreases i.e. the director becomes anchored perpendicular to the surface. The values of θ_y and θ_z corresponding to the homeotropic region are given in both Table 5.2 and Fig. 5.16. These indicate the full range of tilt angles accessed by these systems as a function of the homeotropic coverage. As was shown before in section 5.1.2, for the system with 50% H and 50% P, there is a periodic distortion in the structure. This distortion in the structure appears as well for other systems as we can see in Fig. 5.17. These graphs represent the off-diagonal component Q_{yz} of the order parameter tensor for different systems and show that for $(\%H \text{ or } \%P) \geq 30\%$, there is a bulk director tilt in the whole structure.

5.2.2 Planar alignment region(P region)

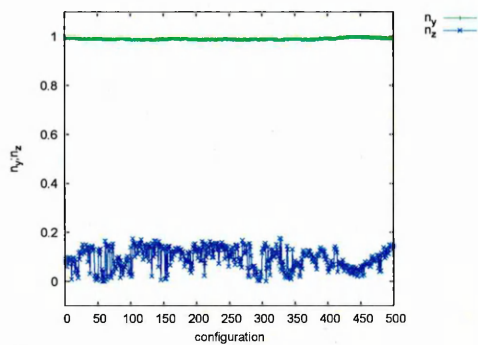
Looking at the snapshots represented in Figs. 5.12(h) and 5.12(i), we can see that at low planar surface coverage, the system is behaving as one with no pattern at the surfaces. Thus, as for the homeotropic case, when the proportion of planar alignment on the substrate less than 30%, the system is not able to see the pattern. This is confirmed by the graphs 5.15(d) and 5.15(f) where the bulk director confined between the $k_s=3$ substrates is aligning along the z -axis. As we increase the proportion of planar alignment on the substrates, we can see the same phenomenon as in the previous section. The bulk director here sweeps from the z -axis to the



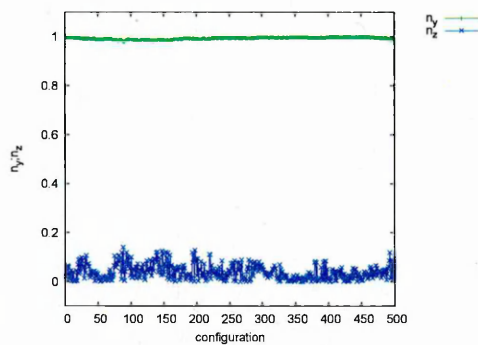
(a) Homeotropic surface region



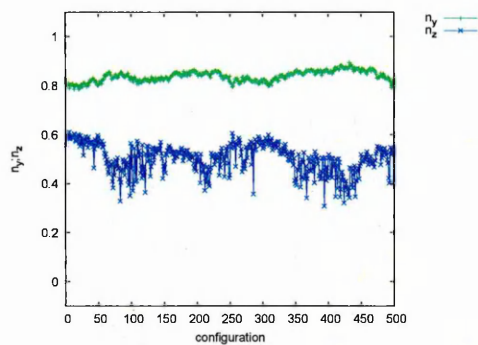
(b) Planar surface region



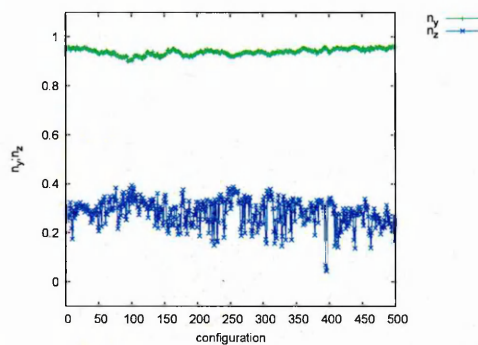
(c) Homeotropic surface region



(d) Planar surface region

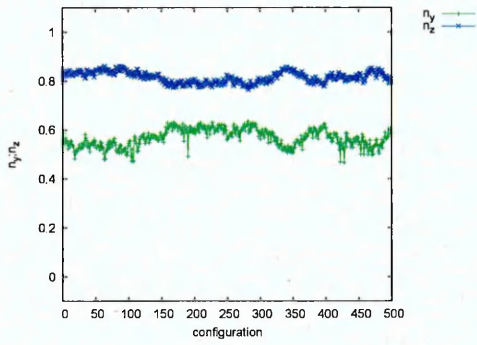


(e) Homeotropic surface region

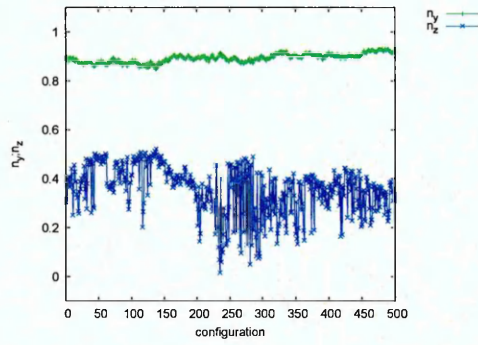


(f) Planar surface region

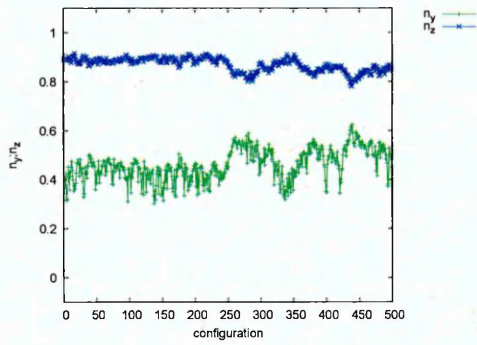
Figure 5.13: Components of the director at $\rho^*=0.4$ for the stripe patterned systems with different ratio surface area (%homeotropic /%planar). Top graphs :10%H 90%P, middle graphs :20%H 80%P, bottom graphs :30%H 70%P.



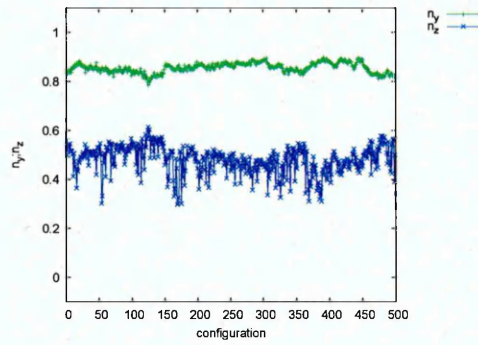
(a) Homeotropic surface region



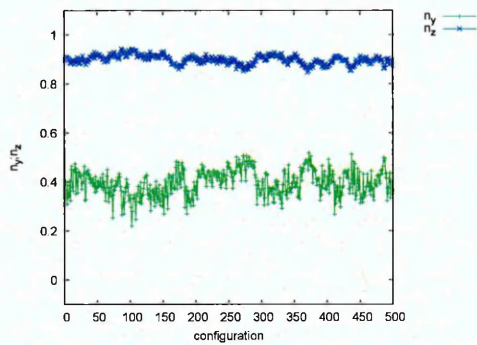
(b) Planar surface region



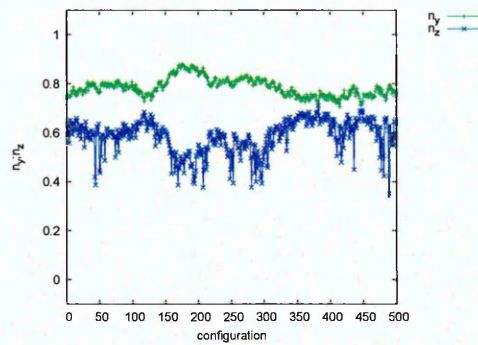
(c) Homeotropic surface region



(d) Planar surface region

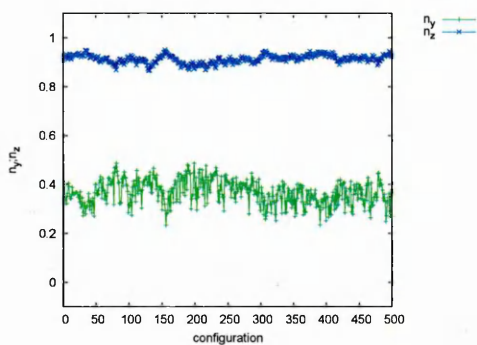


(e) Homeotropic surface region

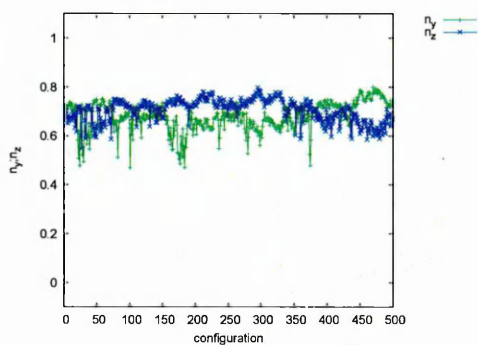


(f) Planar surface region

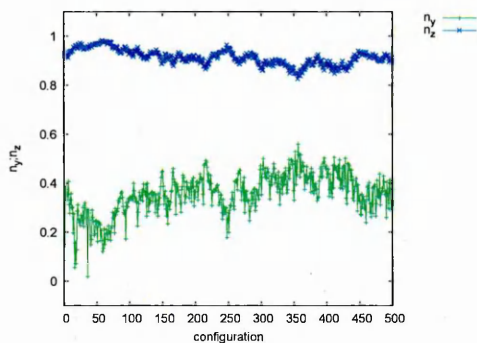
Figure 5.14: Components of the director at $\rho^*=0.4$ for the stripe patterned systems with different ratio surface area (%homeotropic /%planar). Top graphs :40%H 60%P, middle graphs :50%H 50%P, bottom graphs :60%H 40%P.



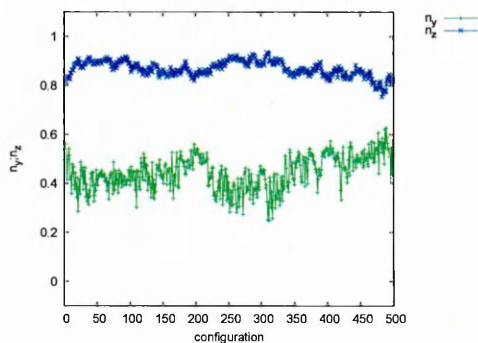
(a) Homeotropic surface region



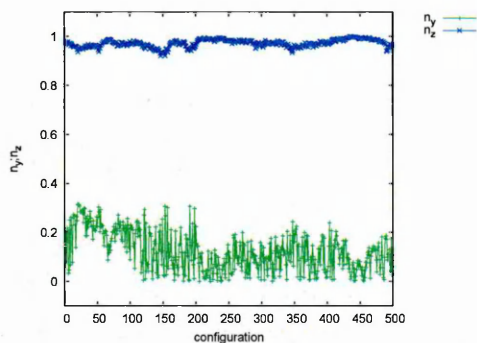
(b) Planar surface region



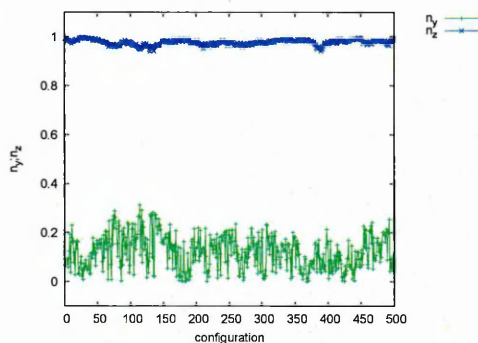
(c) Homeotropic surface region



(d) Planar surface region



(e) Homeotropic surface region



(f) Planar surface region

Figure 5.15: Components of the director at $\rho^*=0.4$ for the stripe patterned systems with different ratio surface area (%homeotropic /%planar). Top graphs :70%H 30%P, middle graphs :80%H 20%P, bottom graphs :90%H 10%P.

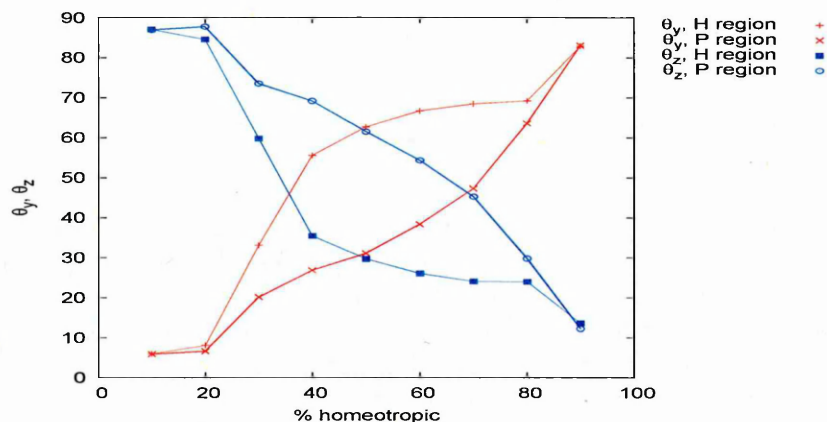


Figure 5.16: Comparison of θ_y and θ_z values in the two regions.

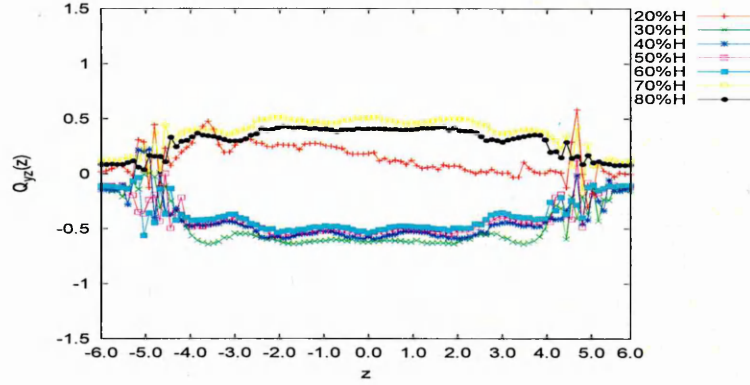
y -axis as % P increases. Fig. 5.15(b) shows that, for a proportion $P=30\%$, $n_y \simeq n_z$. This is actually confirmed in the table 5.2 where it is indicated that for a system with 30%P and 70%H, $\theta_y=47$ degrees and $\theta_z=45$ degrees. As we can see in Fig. 5.13 and Fig. 5.14, the bulk orients increasingly along the y -axis for a proportion $P>40\%$ of the substrate area. As we increase the proportion of planar alignment on the substrate, n_y increases (so, θ_y decreases) and the bulk director is getting more parallel to the surface.

5.2.3 Conclusion

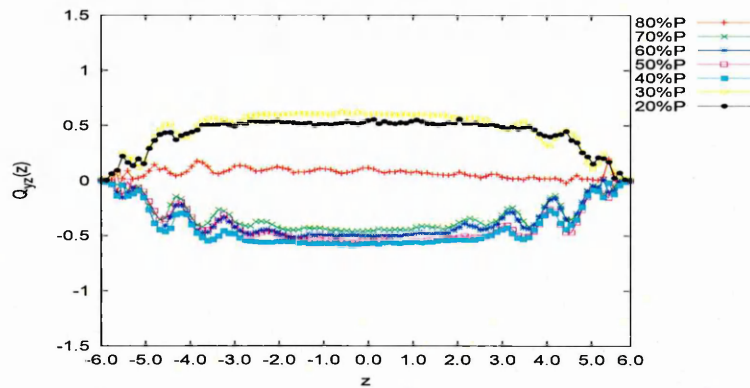
In this section, we have seen the importance of the proportion of the homeotropic and planar alignment regions on the substrate. If the proportion of one of the alignments is lower than 30%, the bulk behaves as if the substrate was unpatterned. By combining a mix of planar and homeotropic alignment regions on the substrate, however, it is possible to obtain a system which exhibits a monodomain or two distinct domains. This has been demonstrated at much larger lengthscales by Kondrat *et al.* [136]. They showed that, for finite anchoring, if one set of stripes (either homeotropic or homogeneous) is much narrower than the other, the nematic may adopt a spatially uniform configuration rather than a distorted configuration. A complete range of tilt angles can be obtained in the two-domain regions as shown in Table 5.2. Near the surface, the director field is distorted, but away from the surfaces, the nematic adopts a bulk orientation that depends on the relative sizes

	10% H; 90% P	20% H; 80% P	30% H; 70% P
H region	$\theta_y = 6$ $\theta_z = 87$	$\theta_y = 8$ $\theta_z = 85$	$\theta_y = 33$ $\theta_z = 60$
P region	$\theta_y = 6$ $\theta_z = 87$	$\theta_y = 7$ $\theta_z = 88$	$\theta_y = 20$ $\theta_z = 74$
	40% H; 60% P	50% H; 50% P	60% H; 40% P
H region	$\theta_y = 56$ $\theta_z = 35$	$\theta_y = 63$ $\theta_z = 30$	$\theta_y = 67$ $\theta_z = 26$
P region	$\theta_y = 27$ $\theta_z = 69$	$\theta_y = 31$ $\theta_z = 61$	$\theta_y = 38$ $\theta_z = 54$
	70% H; 30% P	80% H; 20% P	90% H; 10% P
H region	$\theta_y = 68$ $\theta_z = 24$	$\theta_y = 69$ $\theta_z = 24$	$\theta_y = 83$ $\theta_z = 14$
P region	$\theta_y = 47$ $\theta_z = 45$	$\theta_y = 64$ $\theta_z = 30$	$\theta_y = 83$ $\theta_z = 12$

Table 5.2: Tilt angle in degrees. System with different percentage of H and P on the substrates.



(a)



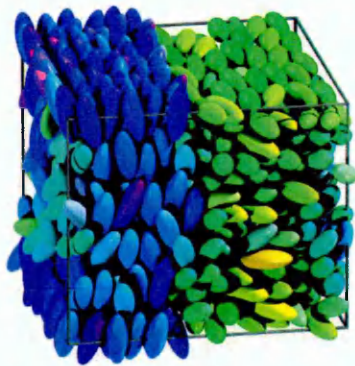
(b)

Figure 5.17: Off diagonal component $Q_{yz}(z)$ of the order parameter tensor for a) Homeotropic region and b) planar region for different %H and %P.

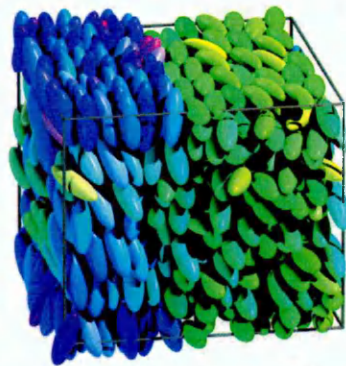
of homeotropic and homogeneous regions. It seems, therefore, possible to pattern a surface to promote any desired orientation in the bulk nematic because, looking at Fig. 5.16, the angle varies monotonically as we vary the stripe width.

5.3 Influence of the k_s values for a system with 40% H 60% P

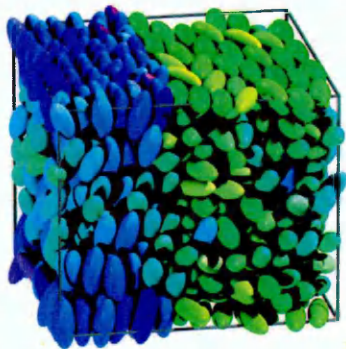
When $k_s=0$, the particle is able to vertically penetrate the wall by a distance maximum of $\frac{\kappa\sigma_0}{2}=1.5\sigma_0$. If we increase this value of k_s to 1, the particle is now able



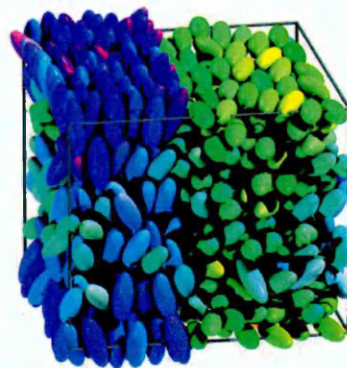
(a) $k_s=3$ $k_s=0$



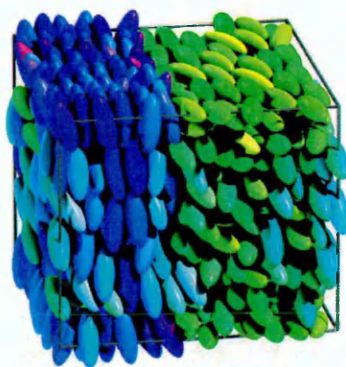
(b) $k_s=3$ $k_s=0.5$



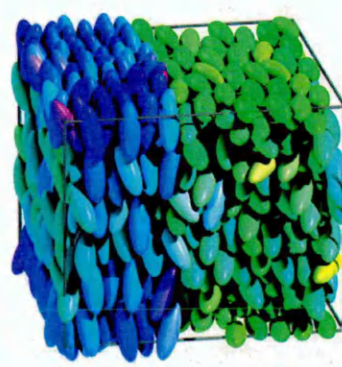
(c) $k_s=3$ $k_s=1$



(d) $k_s=2.5$ $k_s=0$

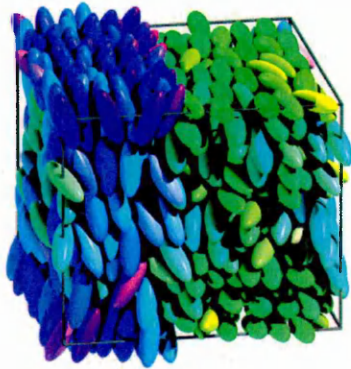


(e) $k_s=2.5$ $k_s=0.5$

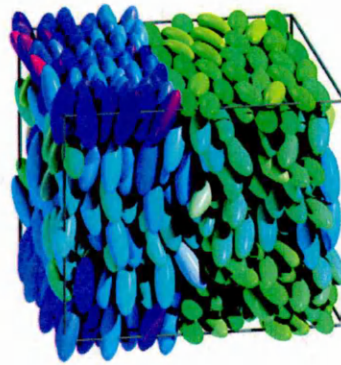


(f) $k_s=2.5$ $k_s=1$

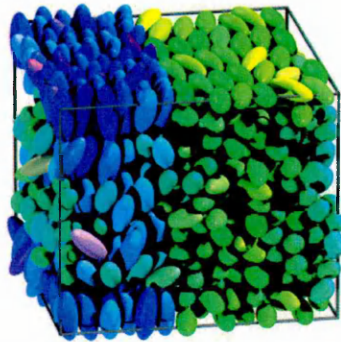
Figure 5.18: Snapshots of the stripe patterned system for a surface area ratio 40% homeotropic 60% planar and for different values of k_s at $\rho^*=0.4$.



(g) $k_s=2$ $k_s=0$



(h) $k_s=2$ $k_s=0.5$



(i) $k_s=2$ $k_s=1$

Figure 5.18: (Continued)

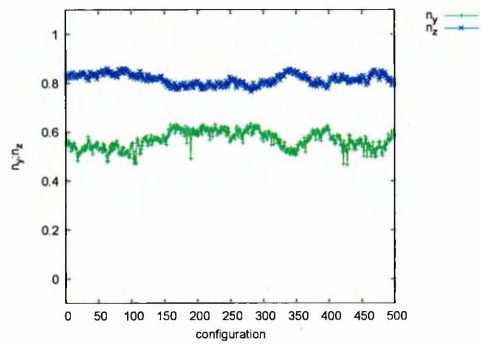
to penetrate the wall by a distance maximum of $\frac{(\kappa-k_s)\sigma_0}{2}=\sigma_0$. By increasing the k_s value while still keeping homeotropic alignment, the particles at the surface become able to explore tilted arrangements. For such particles, the anchoring at the substrate will then be not as strong as before, because they are more free regarding their polar angle. The polar angle θ corresponds to $(\pi/2) - \alpha$, α being the pretilt angle. Changing the k_s value, then, has a direct effect on the surface-region Q -tensor. If $k_s=3$, the molecules are not allowed to penetrate the wall vertically but they are allowed horizontally. If we decrease k_s from 3 to 2, the molecules are no longer required to lie flat against the substrate. They instead can show a small pretilt at the substrate as their extremities are now allowed to penetrate the walls. In this section, we want to investigate the influence of this increased orientational freedom on our systems. Table 5.3 shows the range of systems that have been considered for this.

H region	0	0	0	0.5	0.5	0.5	1	1	1
P region	3	2.5	2	3	2.5	2	3	2.5	2

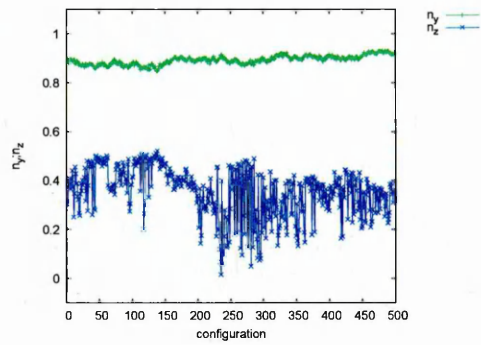
Table 5.3: Values of k_s used in new systems

Here, we present results for systems having 40% homeotropic and 60% planar alignment on the surface. If we first look at three different systems, all having the same planar alignment ($k_s=3$, which we can consider as strong planar anchoring at the surface) but having a different homeotropic alignment at the surface ($k_s=0, 0.5$ or 1), then it appears that the three systems behave differently. The snapshots corresponding to these systems are shown, respectively in Figs. 5.18(a) 5.18(b) and 5.18(c). From these snapshots, no differences are apparent. If, however, we look at the components of the director (Fig. 5.19), we see that slightly increasing the needle length k_s from 0 to 1, causes θ_y and θ_z to vary. We saw previously that if the planar alignment on the substrate is strong and if the homeotropic alignment on the remaining area is strong as well, the bulk director can oscillate between two different orientations, one domain with its main component along the y -axis and a second with its main component along the z -axis. On decreasing the strength of the homeotropic alignment regions, one could expect the influence of the planar surface regions to increase and, so, the anchoring angle (θ_z) in the bulk confined

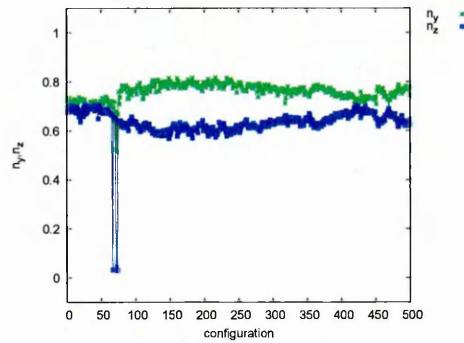
between the H regions to increase. Similarly, for the bulk region confined between the P regions, the anchoring angle (θ_y) would be expected to decrease due to the molecules lying increasingly parallel to the substrates. The average tilt angles in the two different regions of the system given in table 5.4, confirm this assessment. We can, alternatively, maintain strong homeotropic alignment and start to decrease the strength of the planar alignment region. For this, we set the k_s on the H region equal to 0 and vary the value of k_s on the remaining surface area from 3 to 2. Snapshots representing the high density configurations of these systems can be seen in Figs. 5.18(a), 5.18(d) and 5.18(g). The corresponding graphs representing the director components are respectively in Figs. 5.19(a) and 5.19(b), Figs. 5.20(a) and 5.20(b) and Figs. 5.21(a) and 5.21(b). The three sets of graphs are broadly similar, but a surprising trend is indicated by the average angles shown in Table 5.5. These show that reducing the planar anchoring leads to increased bulk alignment along the y -direction. The angular difference between the two domains also decreases. This result is in conflict with the intuitive argument which applied when the homeotropic region anchoring was weakened. Here, instead, it appears that the more pliant $k_s=2$ surface has a more far-reaching influence than the stiffer $k_s=3$ surface. This is presumably related to the tendency of the $k_s=2$ system to exhibit a more uniform configuration when compared with the more strongly differentiated domains seen in the $k_s=0$; $k_s=3$ system. The average tilt angles for the H and P domains for all of the k_s configurations considered here are shown in Table 5.6. All of these indicate that the systems split into two domains with different tilt angles. In Table 5.6, some values of θ_z are not communicated because the corresponding director component was too noisy (see Figs 5.19, 5.20 and 5.21). Table 5.6 shows, though, that the value of the tilt angle can vary significantly depending on the combination of k_s chosen. The angle data for these systems do not follow any simple trend; however, indicating either that these systems are prone to metastability or that there is a complex interplay between bulk and surface free energy terms in these thin film systems.



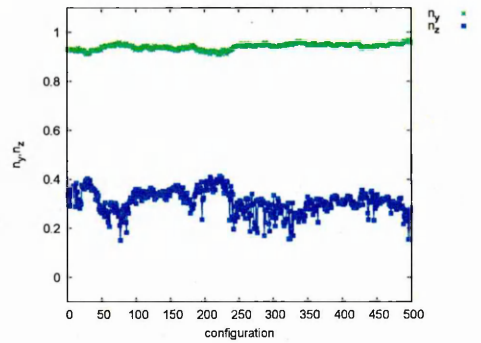
(a) H region



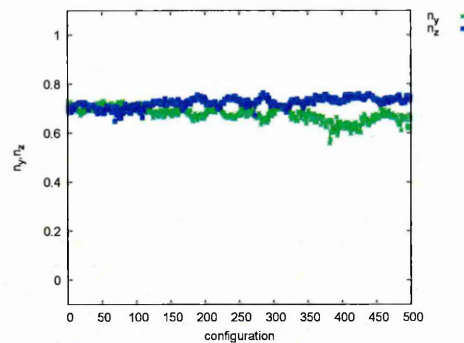
(b) P region



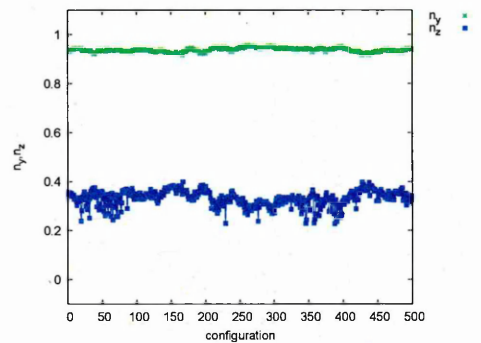
(c) H region



(d) P region

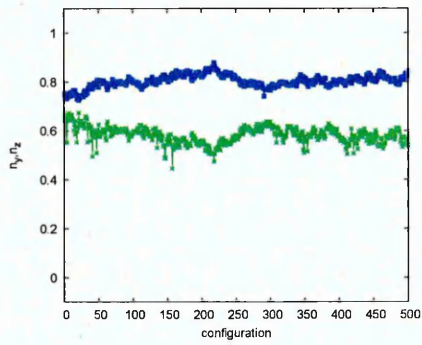


(e) H region

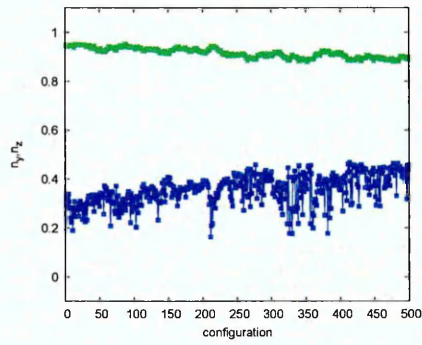


(f) P region

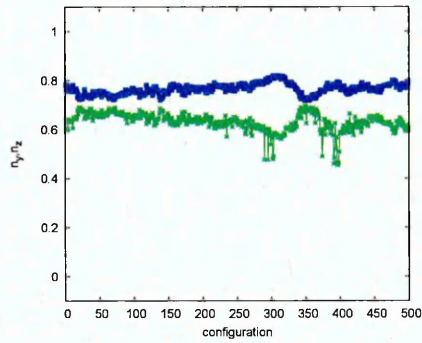
Figure 5.19: $L_z = 4\kappa\sigma_0$: Components of the director for the stripe patterned system; top graphs : $k_s=3$ $k_s=0$, middle graphs : $k_s=3$ $k_s=0.5$, bottom graphs : $k_s=3$ $k_s=1$. $\rho^*=0.4$



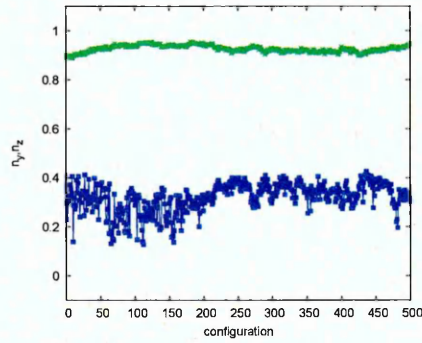
(a) H region



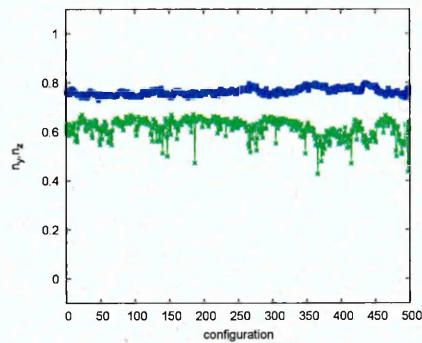
(b) P region



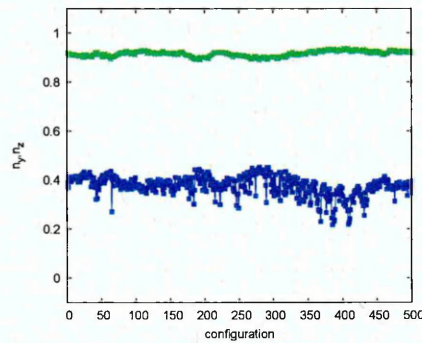
(c) H region



(d) P region

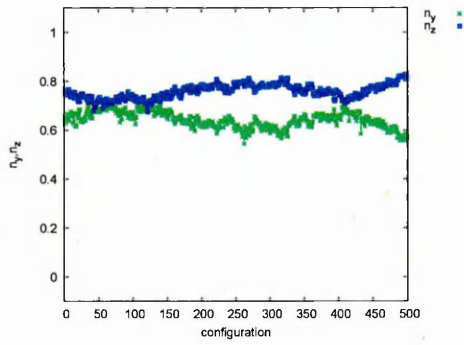


(e) H region

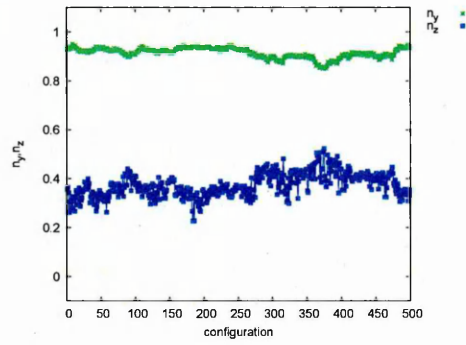


(f) P region

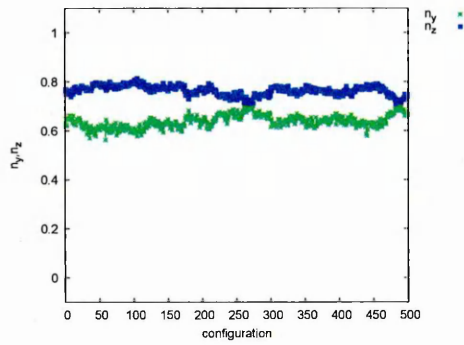
Figure 5.20: $L_z = 4\kappa\sigma_0$: Components of the director for the stripe patterned system; top graphs : $k_s=2.5$ $k_s=0$, middle graphs : $k_s=2.5$ $k_s=0.5$, bottom graphs : $k_s=2.5$ $k_s=1$. $\rho^*=0.4$



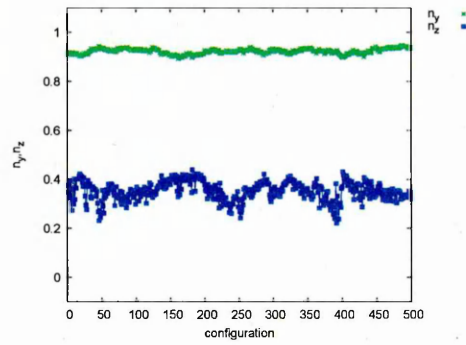
(a) H region



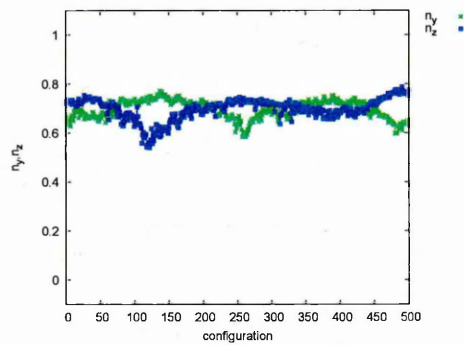
(b) P region



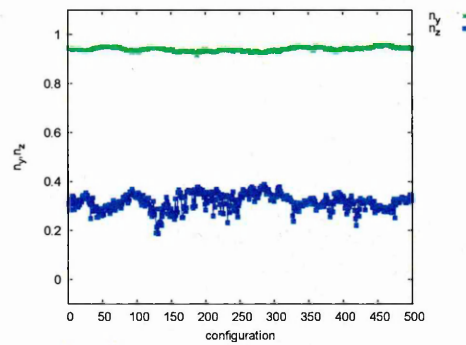
(c) H region



(d) P region



(e) H region



(f) P region

Figure 5.21: $L_z = 4\kappa\sigma_0$: Components of the director for the stripe patterned system; top graphs : $k_s=2$ $k_s=0$, middle graphs : $k_s=2$ $k_s=0.5$, bottom graphs : $k_s=2$ $k_s=1, \rho^*=0.4$

	$k_s=0;k_s=3$	$k_s=1;k_s=3$
H region	$\theta_z = 35$	$\theta_z = 44$
P region	$\theta_y = 27$	$\theta_y = 20$

Table 5.4: Tilt angle in degrees. System with 40% H 60% P with different k_s values.

	$k_s=0;k_s=3$	$k_s=0;k_s=2$
H region	$\theta_z = 35$	$\theta_z = 41$
P region	$\theta_y = 27$	$\theta_y = 24$

Table 5.5: Tilt angle in degrees. System with 40% H 60% P with different k_s values.

5.3.1 Conclusion

Here, we have shown that by keeping the homeotropic and planar proportions on the substrate fixed at 40% H and 60% P, and changing the surface interaction parameters, the system can exhibit a wide range of tilt angles. In the H region, the tilt angle can vary from 35° to 50°. In the P region, because the n_z component varies a lot, it is wiser to look at the θ_y value, which can vary from 20° to 27°. We have also seen that on increasing or decreasing the k_s value, the tilt angle does not always change monotonically. This limits the utility of generic simulation for predicting how best to control the angles by varying the local k_s values.

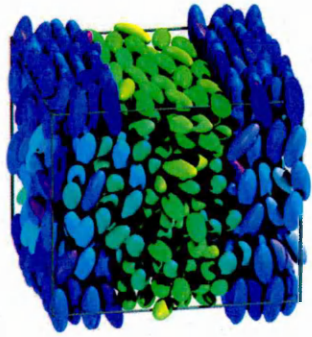
5.4 Influence of the thickness of the simulation box

In this section, we investigate the influence of the thickness of the cell. Here, the proportion of homeotropic and planar regions on the substrate have been fixed to 50%. At each density simulated, the surface areas of all systems were identical, with only the L_z values varying. Depending on the thickness of the box, the number of particles used was as indicated in table 5.7.

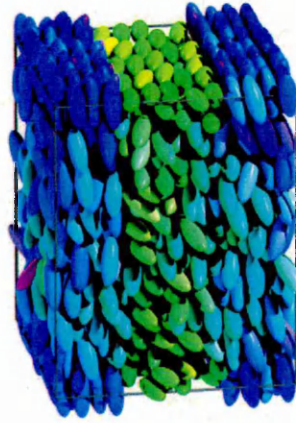
High density snapshots corresponding to these four systems are represented in Fig. 5.22. From these, we observe that, as the thickness was increased, the bulk tended increasingly to a monodomain arrangement rather than two distinct domains. To quantify this further, we once again divide the analysis into two parts : the bulk

	$k_s=0;k_s=3$	$k_s=0.5;k_s=3$	$k_s=1;k_s=3$
H region	$\theta_z = 35$	$\theta_z = 51$	$\theta_z = 44$
P region	$\theta_y = 27$	$\theta_y = 20$ $\theta_z = 72$	$\theta_y = 20$ $\theta_z = 71$
	$k_s=0;k_s=2.5$	$k_s=0.5;k_s=2.5$	$k_s=1;k_s=2.5$
H region	$\theta_z = 37$	$\theta_z = 40$	$\theta_z = 40.2$
P region	$\theta_y = 24$ $\theta_z = 69$	$\theta_y = 22$ $\theta_z = 71$	$\theta_y = 24$ $\theta_z = 68$
	$k_s=0;k_s=2$	$k_s=0.5;k_s=2$	$k_s=1;k_s=2$
H region	$\theta_z = 41$	$\theta_z = 40$	$\theta_z = 46$
P region	$\theta_y = 24$ $\theta_z = 68$	$\theta_y = 22$ $\theta_z = 71$	$\theta_y = 20$ $\theta_z = 72$
	$k_s=0;k_s=3$	$k_s=0;k_s=2.5$	$k_s=0;k_s=2$
H region	$\theta_z = 35$	$\theta_z = 37$	$\theta_z = 41$
P region	$\theta_y = 27$	$\theta_y = 24$ $\theta_z = 69$	$\theta_y = 24$ $\theta_z = 68$
	$k_s=0.5;k_s=3$	$k_s=0.5;k_s=2.5$	$k_s=0.5;k_s=2$
H region	$\theta_z = 51$	$\theta_z = 40$	$\theta_z = 40$
P region	$\theta_y = 18$ $\theta_z = 72$	$\theta_y = 22$ $\theta_z = 71$	$\theta_y = 23$ $\theta_z = 69$
	$k_s=1;k_s=3$	$k_s=1;k_s=2.5$	$k_s=1;k_s=2$
H region	$\theta_z = 44$	$\theta_z = 40$	$\theta_z = 46$
P region	$\theta_y = 20$ $\theta_z = 71$	$\theta_y = 24$ $\theta_z = 68$	$\theta_y = 20$ $\theta_z = 72$

Table 5.6: Tilt angle in degrees. System with 40% H 60% P with different k_s values.



(a) $L_z=4\kappa\sigma_0$



(b) $L_z=6\kappa\sigma_0$



(c) $L_z=7\kappa\sigma_0$



(d) $L_z=8\kappa\sigma_0$

Figure 5.22: Snapshots of the striped system for different L_z at $\rho^*=0.4$

L_z	$4\kappa\sigma_0$	$6\kappa\sigma_0$	$7\kappa\sigma_0$	$8\kappa\sigma_0$
N	864	1296	1512	1728

Table 5.7: Relation between the thickness of the simulation box and the number of particles.

confined between the H surface regions and that confined between the P surface regions.

5.4.1 Homeotropic surface region

Comparing the Q_{zz} profiles corresponding to the H region, shown in Figs. 5.24(a), 5.26(a) and 5.28(a), we see that increasing L_z generally leads to a decrease in Q_{zz} . Fig. 5.24(a) represents the Q_{zz} profiles for the stripe patterned system for $L_z=4\kappa\sigma_0$. It shows clear formation of layers at the surfaces and 4 peaks in the bulk region, lying more or less normal to the surfaces. At $\rho^*=0.39$, the average value of Q_{zz} in the bulk is about 0.5. The formation of layers is confirmed by the density profiles (Fig. 5.24(c)) which show that the layers are separated by a distance $d \simeq 2.5\sigma_0$. As the thickness of the box is increased to $L_z=6\kappa\sigma_0$, the peaks in the Q_{zz} profiles (Fig. 5.26(a)) appear damped near the centre of the film. The average value of Q_{zz} decreases to 0.4 at $\rho^*=0.4$. Looking at the corresponding density profile (Fig. 5.26(c)), we can see that there are now 7 discernable peaks in the bulk and 2 at the surfaces. The distance between the surface monolayer and the second layers is $d \simeq 3\sigma_0$ which correspond to the molecular length. The separation distance between the following layers is, however, decreased to $d \simeq 2\sigma_0$. The Q_{zz} profile shows a brutal decrease between the first and the second layers. This can be explained by the density profile which shows that, at this position, the local density is virtually 0. Increasing the film thickness further to $L_z=8\kappa\sigma_0$, the bulk seems to lose all positional layering order (Figs. 5.28(a) and 5.28(c)). At $\rho^*=0.39$, the latter shows 5 exponentially dumped peaks at each surface but no layers in the middle of the cell. The corresponding Q_{zz} profile (Fig. 5.28(a)), shows a clear I-N phase transition between densities $\rho^*=0.3$ and 0.34, the average value of Q_{zz} rising to about 0.5. However, with further increase in the reduced density to $\rho^*=0.36$, the Q_{zz} value decreases to an average value of 0.25 and stays at that value until $\rho^*=0.39$. Look-

ing at the director components corresponding to the three systems (Figs. 5.25(a), 5.27(a) and 5.29(a)), we can notice that in all cases the n_z component is the greatest. Nevertheless, as L_z is increased, n_z decreases, that is the molecules become increasingly parallel to the surfaces. Looking at Fig. 5.23, we can see that the variation of the tilt angle with L_z is quite linear in this region.

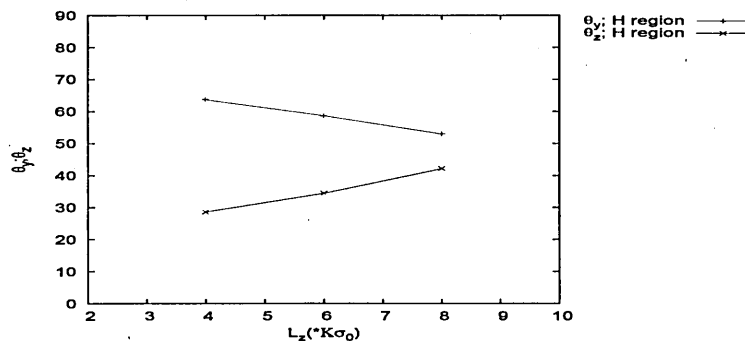
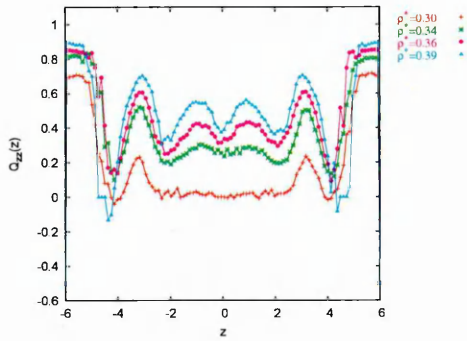


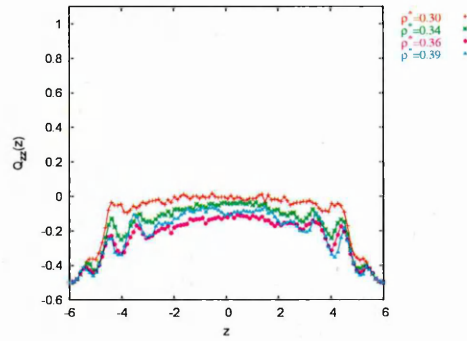
Figure 5.23: Variation of θ_y and θ_z in the H region

5.4.2 Planar surface region

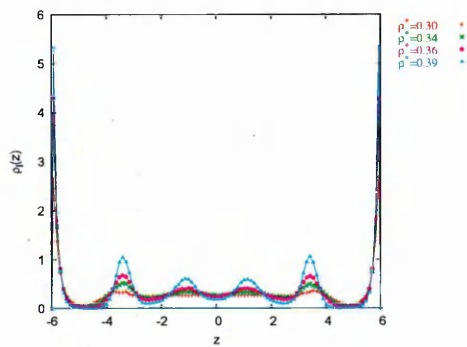
Looking at the Q_{zz} profile for the $L_z=4\kappa\sigma_0$ system (Fig. 5.24(b)), we can see that the average value of Q_{zz} in the bulk is about -0.1 at high reduced density. We know that for the unpatterned $k_s=3$ symmetric system, this value tends to -0.5. This deviation is, then, due to the influence of the homeotropic anchoring region, as noticed previously in this chapter. Unlike what was seen between the H surface areas, where we saw that the system was showing layering all the way to the centre of the cell, here, layers are restricted to the surface regions. On increasing the cell thickness to a value of $L_z=6\kappa\sigma_0$, we can see that the Q_{zz} value becomes more negative for a reduced density $\rho^*=0.34$. This is close to the behaviour of a $k_s=3$ system confined between unpatterned surfaces. However, as the reduced density increases further to $\rho^*=0.36$, Q_{zz} increases and equals 0.1, as the density of the system is increased to $\rho^*=0.39$. For the thickest film considered, the behaviour of the system is again different. The Q_{zz} profile in Fig. 5.28(b), shows that, as the density is increased from 0.3 to 0.34, Q_{zz} increases to 0.4. indeed, comparing the Q_{zz} profiles for the two regions here (Figs. 5.28(a) and 5.28(b)), we can see



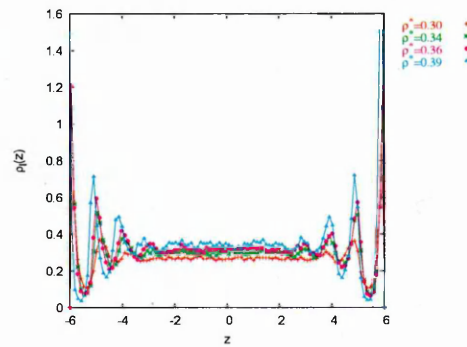
(a) Q_{zz} profile homeotropic region



(b) Q_{zz} profile planar region

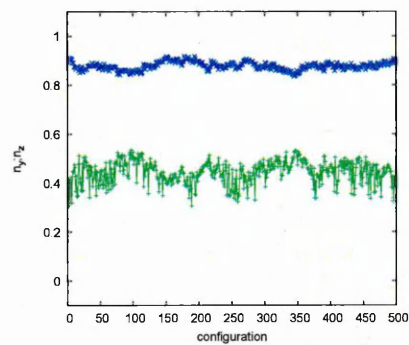


(c) $\rho_l(z)$ profile homeotropic region

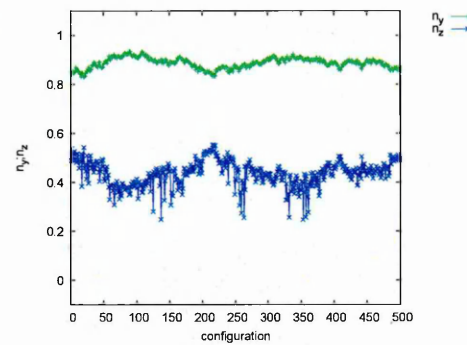


(d) $\rho_l(z)$ profile planar region

Figure 5.24: $L_z=4\kappa\sigma_0$: profiles corresponding to the two surface regions.

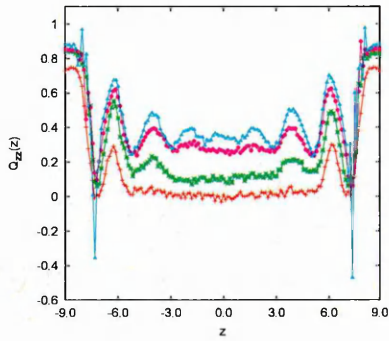


(a)

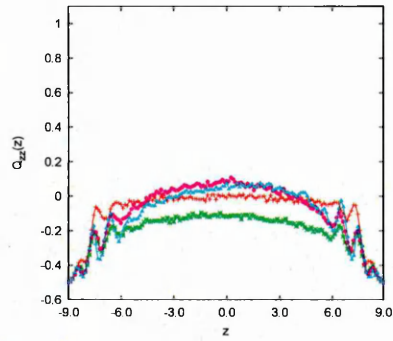


(b)

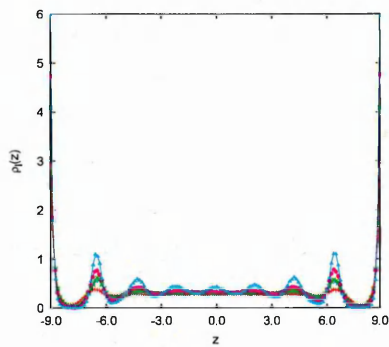
Figure 5.25: $L_z=4\kappa\sigma_0$: components of the director in the a)homeotropic region and b)planar region .



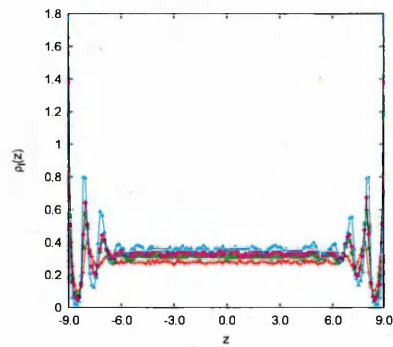
(a) Q_{zz} profile homeotropic region



(b) Q_{zz} profile planar region

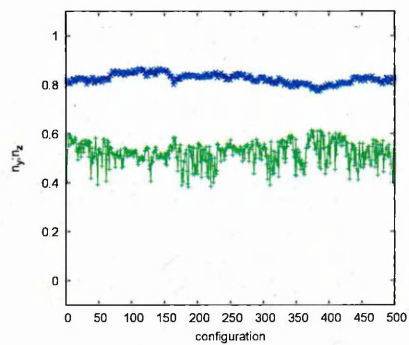


(c) $\rho_l(z)$ profile homeotropic region

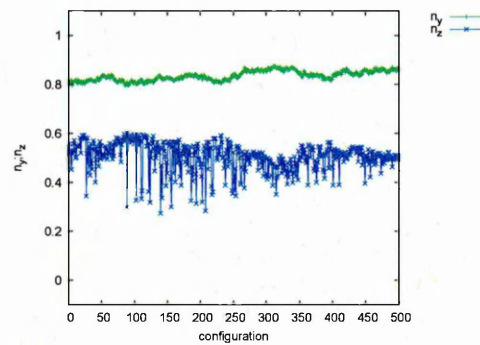


(d) $\rho_l(z)$ profile planar region

Figure 5.26: $L_z=6\kappa\sigma_0$: profiles corresponding to the two surface regions.

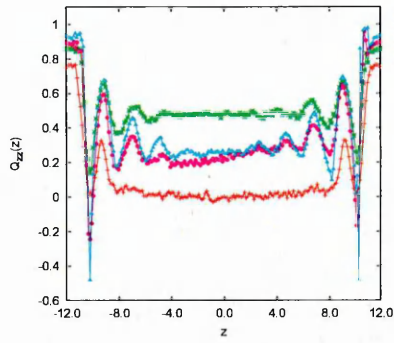


(a)

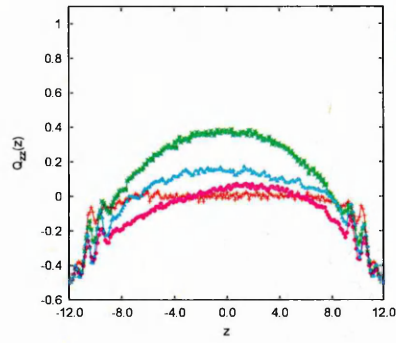


(b)

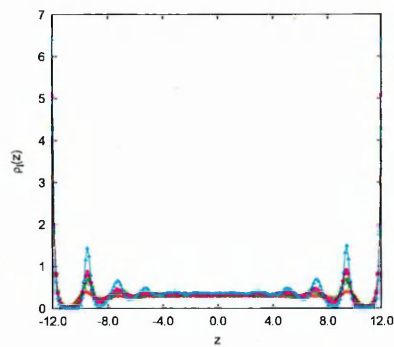
Figure 5.27: $L_z=6\kappa\sigma_0$: components of the director in the a)homeotropic region and b)planar region .



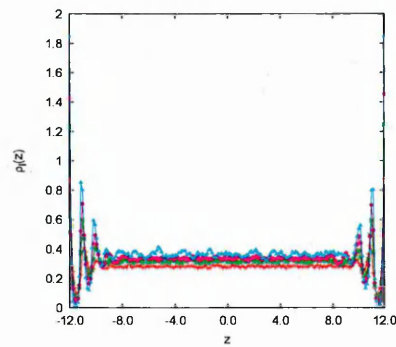
(a) Q_{zz} profile homeotropic region



(b) Q_{zz} profile planar region

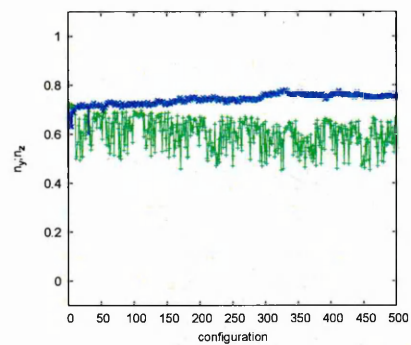


(c) $\rho_l(z)$ profile homeotropic region

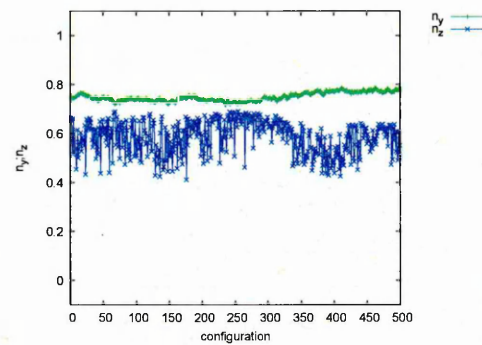


(d) $\rho_l(z)$ profile planar region

Figure 5.28: $L_z=8\kappa\sigma_0$: profiles corresponding to the two surface regions.



(a)



(b)

Figure 5.29: $L_z=8\kappa\sigma_0$: Components of the director in the a)homeotropic region and b)planar region .

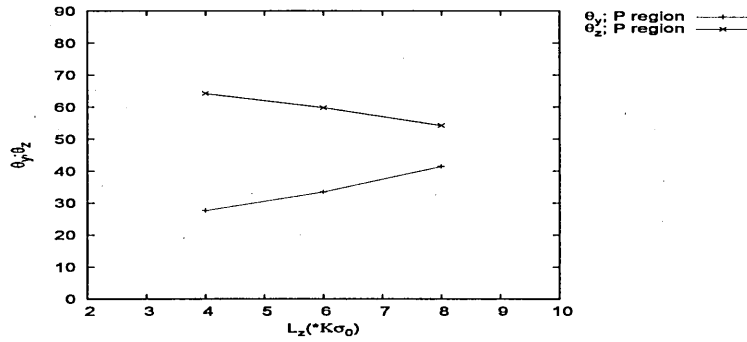


Figure 5.30: Variation of θ_y and θ_z in the P region

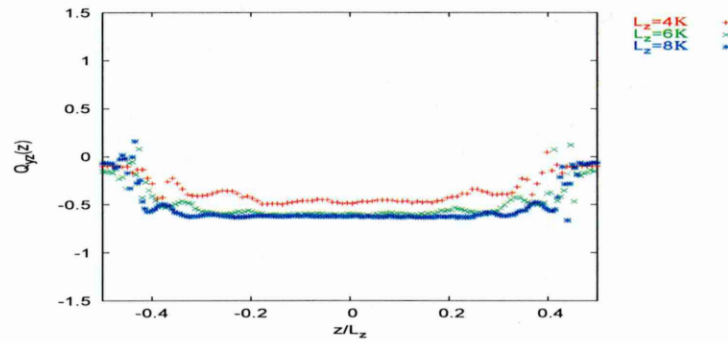
that the whole system is exhibiting homeotropic anchoring. So, at densities slightly higher than the I-N transition density, the $L_z=8\kappa\sigma_0$ system tends to exhibit an homeotropic anchoring. However, as the density increases to 0.39, the Q_{zz} value again decreases to reach 0.1. Fig. 5.31 shows the high density Q_{yz} profiles for the three film thickness. These show that, as the thickness is increased, the tilt in the cell increases and becomes very similar in the two regions (Fig. 5.30). This provides further evidence that as the thickness increases, the whole system tends to develop a tilted monodomain at high density.

5.4.3 Conclusion

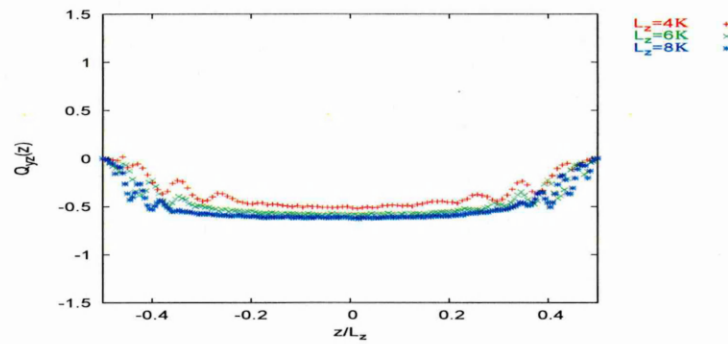
In this section, we have investigated the effect of changing the cell thickness. From this, we have seen that this parameter is very important. The high density tilt angles vary, in the two film regions, linearly with the L_z value. Also, as we increase the thickness of the box, these angles converge as the system tries to adopt a tilted monodomain behaviour. For the surface parameters and coverages considered here, the monodomain tilt angle resides in the range 40-50 degrees.

5.5 Influence of the k_s values for a system with 40% H 60% P, $L_z=8\kappa\sigma_0$

Here, we study a system of thickness $L_z=8\kappa\sigma_0$ and look at the influence of the k_s values imposed. Fig. 5.32 shows the high density snapshots obtained for a range of

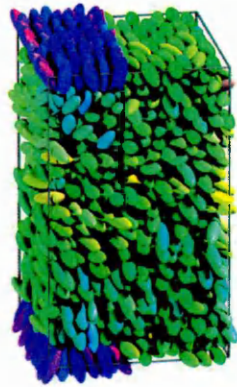


(a)



(b)

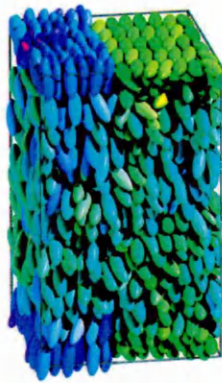
Figure 5.31: Q_{yz} profiles corresponding to the a)homeotropic region and b)planar region, depending on the thickness of the cell at $\rho^*=0.39$.



(a) $k_s=3$ $k_s=0$



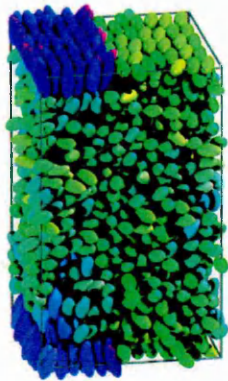
(b) $k_s=3$ $k_s=0.5$



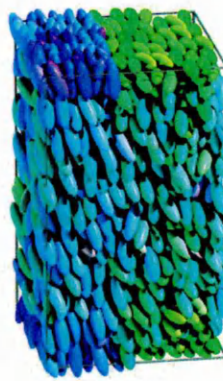
(c) $k_s=3$ $k_s=1$



(d) $k_s=2.5$ $k_s=0$

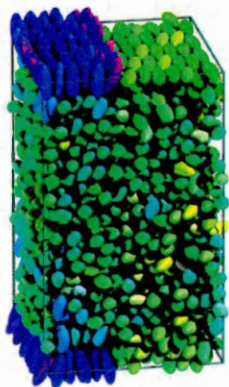


(e) $k_s=2.5$ $k_s=0.5$

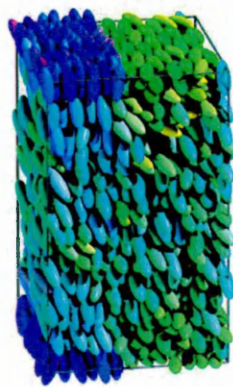


(f) $k_s=2.5$ $k_s=1$

Figure 5.32: Snapshots of the stripe patterned system for a surface area ratio 40% homeotropic 60% planar and for different values of k_s at $\rho^*=0.4$.



(g) $k_s=2$ $k_s=0$

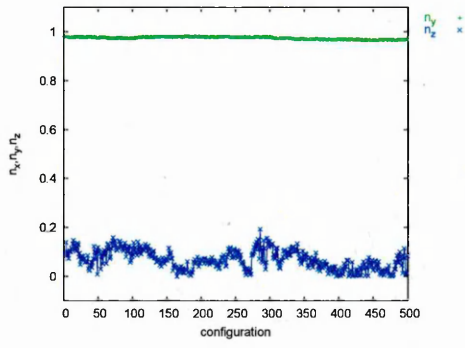


(h) $k_s=2$ $k_s=0.5$

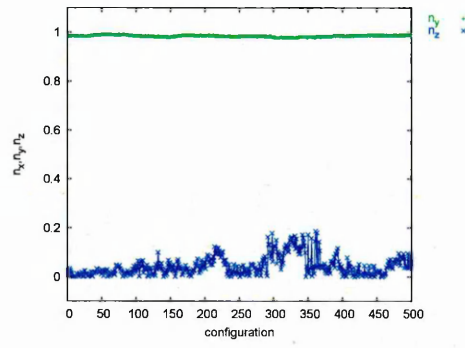


(i) $k_s=2$ $k_s=1$

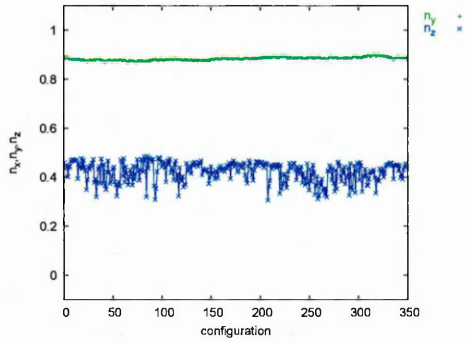
Figure 5.32: (Continued).



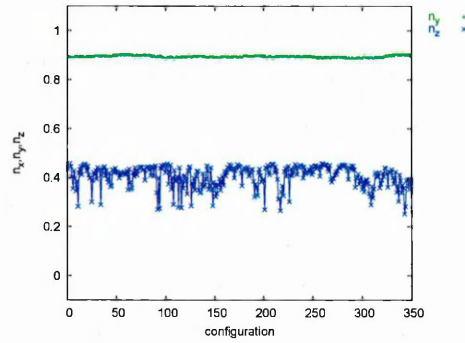
(a) H region



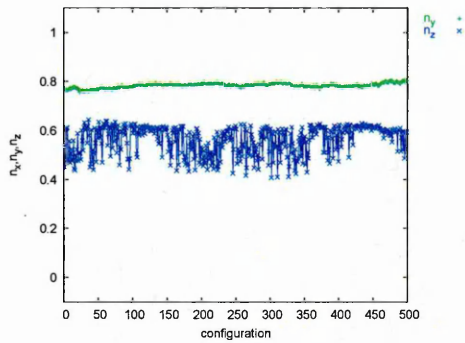
(b) P region



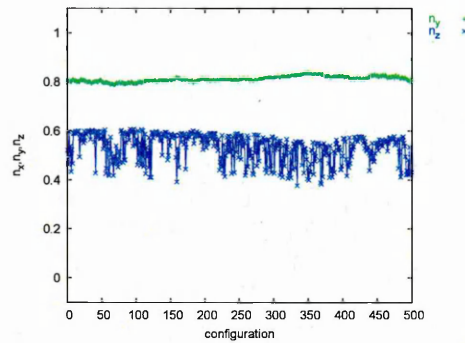
(c) H region



(d) P region

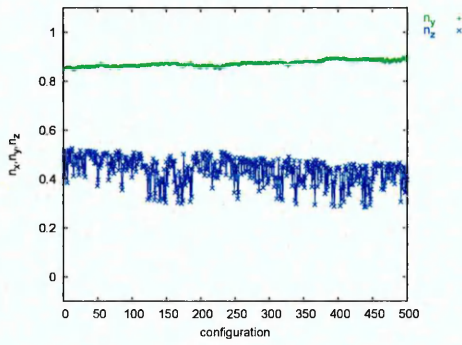


(e) H region

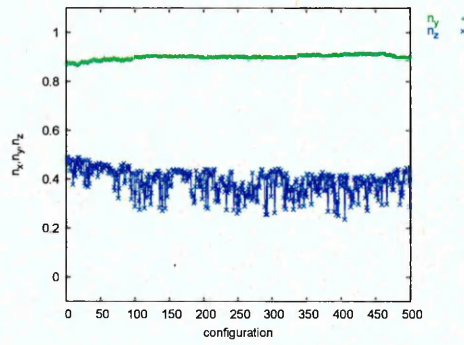


(f) P region

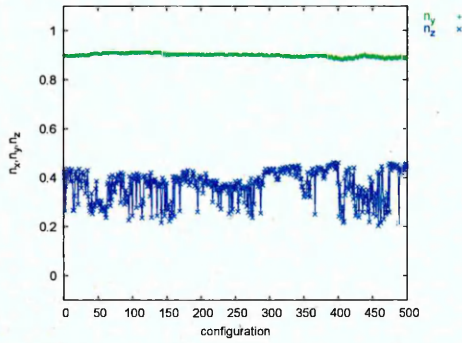
Figure 5.33: $L_z = 8\kappa\sigma_0$: Components of the director for the stripe patterned system at $\rho^*=0.4$; top graphs : $k_s=3$ $k_s=0$, middle graphs : $k_s=3$ $k_s=0.5$, bottom graphs : $k_s=3$ $k_s=1$.



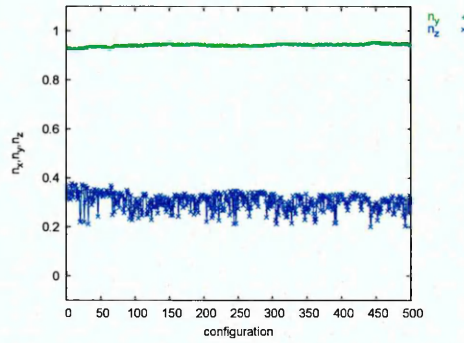
(a) H region



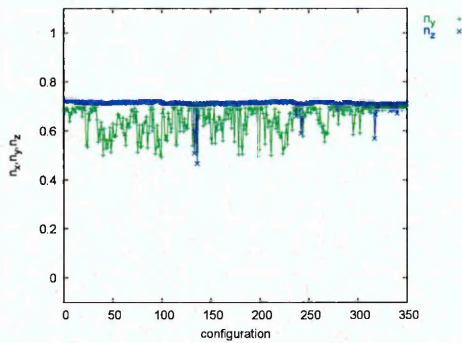
(b) P region



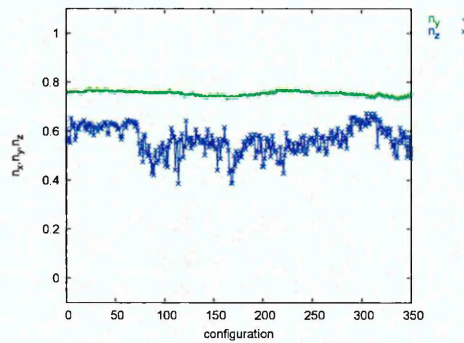
(c) H region



(d) P region

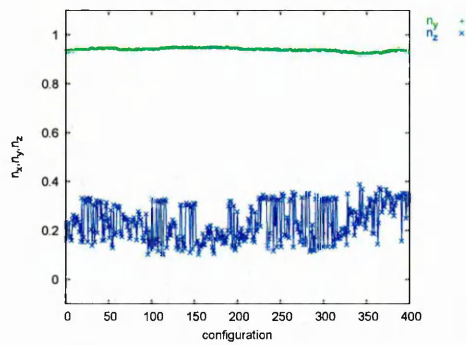


(e) H region

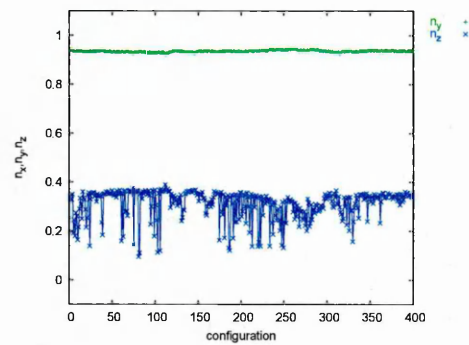


(f) P region

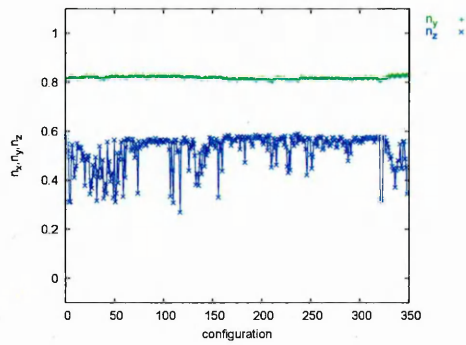
Figure 5.34: $L_z = 8\kappa\sigma_0$: Components of the director for the stripe patterned system at $\rho^*=0.4$; top graphs : $k_s=2.5$ $k_s=0$, middle graphs : $k_s=2.5$ $k_s=0.5$, bottom graphs : $k_s=2.5$ $k_s=1$.



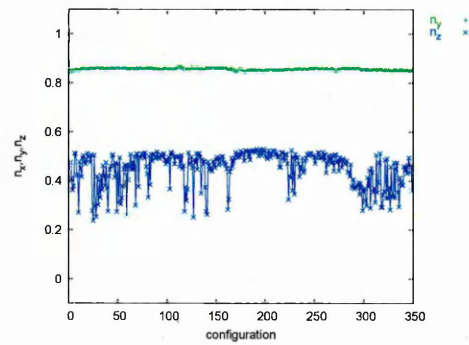
(a) H region



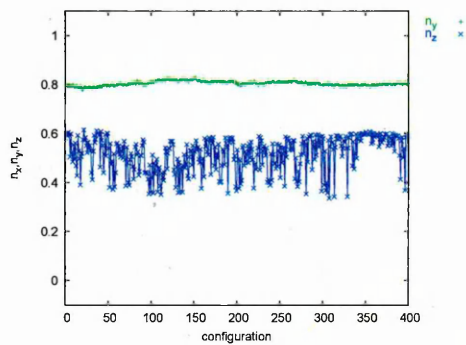
(b) P region



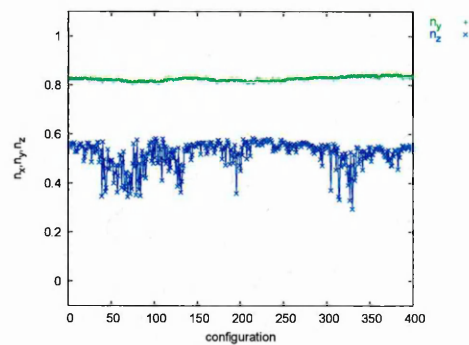
(c) H region



(d) P region



(e) H region



(f) P region

Figure 5.35: $L_z = 8\kappa\sigma_0$: Components of the director for the stripe patterned system at $\rho^*=0.4$; top graphs : $k_s=2$ $k_s=0$, middle graphs : $k_s=2$ $k_s=0.5$, bottom graphs : $k_s=2$ $k_s=1$.

such systems. From these, we can see that, for all values of k_s considered here, the systems exhibit a monodomain. This remark is not only founded on the appearance of the snapshots but also on the graphs of Figs. 5.33, 5.34 and 5.35, which show the corresponding variations of the n_y and n_z components of the director. All of these systems (except for that where $k_s=1$ set the homeotropic alignment and $k_s=2.5$ the planar alignment, Figs. 5.34(e) and 5.34(f)) exhibit a monodomain whose largest component aligns along the y -axis. Table 5.8 gives details of the various tilt angles measured for these systems. From these we can see that, once again, the tilt angles vary substantially with changing k_s but their variation is not always monotonic. Specifically, while there is a consistent link between the homeotropic region k_s value and θ_y , the link between the planar region k_s value and the bulk tilt angle appears more complex.

	$k_s=0;k_s=3$	$k_s=0.5;k_s=3$	$k_s=1;k_s=3$
H region	$\theta_y = 13$	$\theta_y = 28$	$\theta_y = 38$
P region	$\theta_y = 10$	$\theta_y = 27$	$\theta_y = 36$
	$k_s=0;k_s=2.5$	$k_s=0.5;k_s=2.5$	$k_s=1;k_s=2.5$
H region	$\theta_y = 29$	$\theta_y = 26$	$\theta_y = 49$
P region	$\theta_y = 26$	$\theta_y = 20$	$\theta_y = 41$
	$k_s=0;k_s=2$	$k_s=0.5;k_s=2$	$k_s=1;k_s=2$
H region	$\theta_y = 20$	$\theta_y = 35$	$\theta_y = 36$
P region	$\theta_y = 21$	$\theta_y = 31$	$\theta_y = 34$

Table 5.8: Tilt angle in degrees. System with 40% H 60% P, with different k_s values.

5.5.1 Conclusion

We have investigated, in this section, the influence of the k_s parameters on the tilt of thick monodomains films. From this, we have seen that changing these parameter values can produce bulk monodomain tilt angles in the range $10^\circ < \theta_y < 50^\circ$. This range is bigger than that observed in thinner $L_z=4\kappa\sigma_0$ systems. However, just as

for these thinner systems, the link between local k_s values and tilt angle is not always apparent.

5.6 Smooth transitions

Recent experimental work on the anchoring of LCs on a wettability gradient has been performed by Price and Schwartz [137]. In their work, they studied a hybrid aligned nematic LC cell where one of the surfaces was untreated and exhibited a homeotropic anchoring, and the second surface was degraded by exposure to UV radiation. The degraded surface was obtained by positioning a glass slide adjacent to a mercury pen lamp. The wettability gradient was then created by increasing the distance of the glass from the lamp. Because birefringence increases as the wettability increases, and because some previous work had shown that the director aligns parallel to a region of increasing birefringence, a transition from homeotropic anchoring to planar anchoring was found. The same year, Clare *et al.* [138] observed that, by creating surfaces with continuous gradient in chemical functionality, a full range of tilt angles of the LCs can be obtained. Finally, our collaborators in Leeds are able to generate gradient substrates properties through the use of photo-cleavable SAMs.

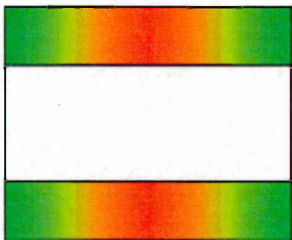


Figure 5.36: Schematic representation of a stripe patterned system with smooth transitions

In this section, we consider the behaviour of a stripe patterned system with smooth transitions between the homeotropic and planar substrate regions (see Fig. 5.36). This is achieved by imposing a gradient on the substrate, k_s becoming a function of x . Explicitly, we have imposed a linear profile of k_s , of the form $k_s = \left| \frac{\partial x}{L_x} \right|$. This result is a periodic substrates pattern, thanks to the periodic boundary con-

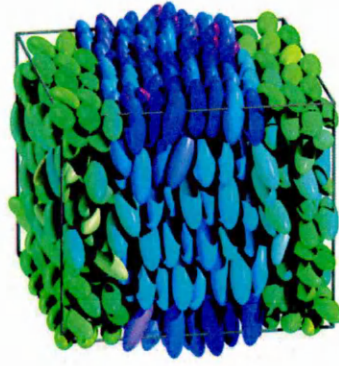


Figure 5.37: Stripe patterned system, smooth transitions at $\rho^*=0.4$

ditions. A snapshot of a high density configuration obtained with this system is shown in Fig. 5.37.

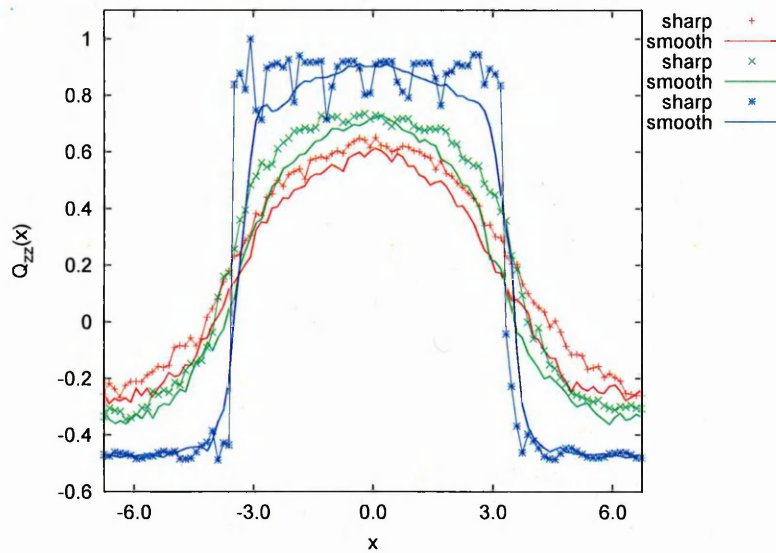
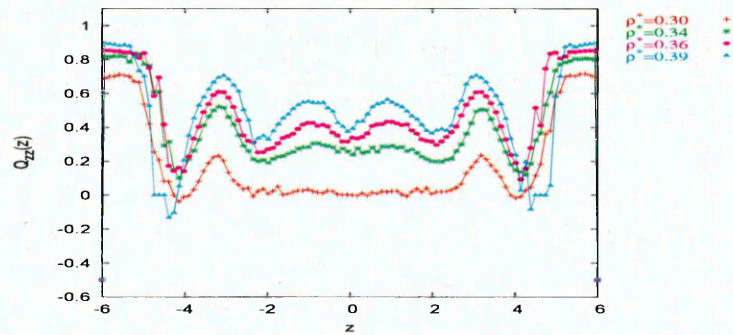
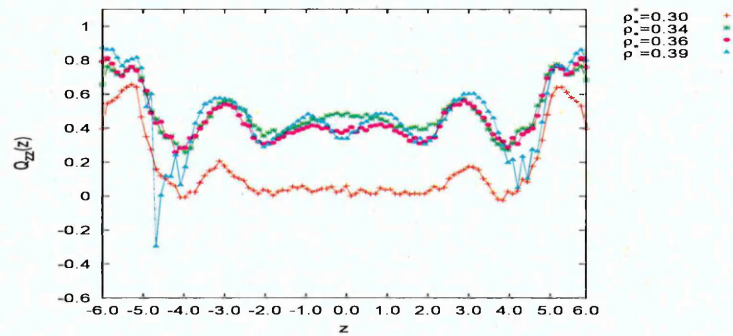


Figure 5.38: $Q_{zz}(x)$ profiles in different region of the systems (sharp and smooth transitions). Blue : $0 < |z| < 0.1L_z$; green : $0.2L_z < |z| < 0.3L_z$; red : $0.4L_z < |z| < 0.5L_z$.

In order to compare the structure of this system with that of an equivalent sharp transition film, we have determined a series of $Q_{zz}(x)$ profiles at different depths of the cell. Specifically, we measured such profiles close to the walls ($0.4L_z \leq |z| \leq$

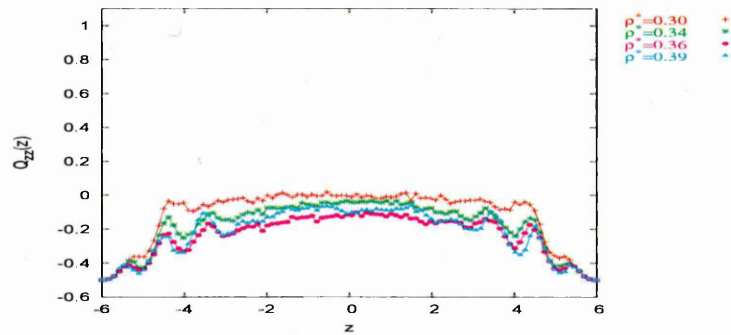


(a) Sharp transitions

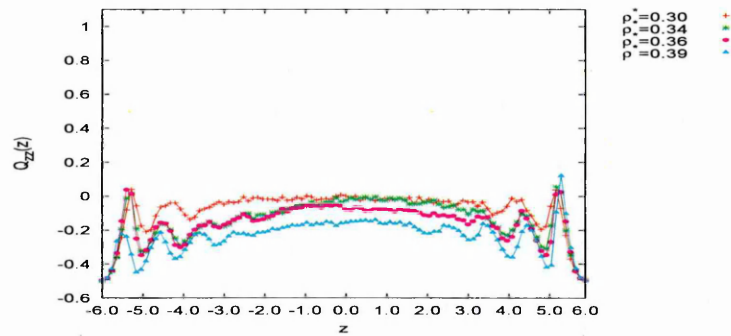


(b) Smooth transitions

Figure 5.39: Q_{zz} profiles corresponding to the stripe patterned systems, sharp and smooth transitions, H region.



(a) Sharp transitions



(b) Smooth transitions

Figure 5.40: Q_{zz} profiles corresponding to the stripe patterned systems, sharp and smooth transitions, P region.

$0.5L_z$), in the centre of the cell ($0 \leq |z| \leq 0.1L_z$) and in an intermediate region ($0.2L_z \leq |z| \leq 0.3L_z$) (see Fig. 5.38). The $Q_{zz}(x)$ profiles for smooth and sharp boundary systems are remarkably similar. Close to the surfaces, we can see that the transition from planar to homeotropic and from homeotropic to planar are obviously sharper for the system with sharp transitions (blue). However, the difference between these profiles is not that great given their fundamentally different substrates. In the intermediate region (green) and in the middle of the cell (red), the graphs corresponding to the two systems are even more similar, the homeotropic region Q_{zz} values being slightly higher for the system with sharp transitions. At first sight, then, the only substantive difference between the sharp and smooth patterned systems occurs in the immediate vicinity of the wall, the anchoring behaviour appearing insensitive to the molecular-level mechanism used to drive the transition from homeotropic alignment at the surfaces to planar. This assessment is confirmed by the associated $Q_{zz}(z)$ profiles represented in Figs. 5.39 and 5.40. We can see from these that both systems are equally well organised in the bulk, even down to the number of layers found. However, for the sharp transitions system, the average value of Q_{zz} in the bulk is about 0.6 at $\rho^*=0.39$ (see Fig. 5.39(a)) whereas for the smooth transition system, it is about 0.4-0.5 (see Fig. 5.39(b)).

5.6.1 Conclusion

We have investigated in this section the effect of the nature of the transition between the planar aligning and the homeotropic aligning surface regions. This has shown that the system behaviour is largely insensitive to the use of smooth rather than sharp substrate transitions. Thus, when linear variation in k_s is used, instead of a step change, the molecular alignment continues to exhibit a discontinuity between homeotropic and planar. In the bulk, the homeotropic anchoring seems to be stronger for sharp transition as the Q_{zz} value is greater for sharp transitions than for smooth transition. However, in the other bulk region, it seems that the planar anchoring is stronger for smooth transitions. This might be explained by the fact that using smooth transitions effectively introduces additional softness into the system, so reducing the influence of the homeotropic surface region on the bulk confined between the planar alignment surfaces. The main conclusion, here though,

is that even when the surface condition is continuous, any bulk tilt develops from a mix of planar and homeotropic surface particles; other pretilt angles do not appear to contribute.

5.7 Conclusions

In this chapter, we have presented a comprehensive set of simulation studies of stripe patterned systems. In these, we have investigated the impact of three different parameters : the relative stripe width, the k_s values used and the cell thickness. We have discovered that the relative stripe width is an important parameter in that it can be used to vary the anchoring tilt across the entire angular range. Importantly there appears to be a monotonic relationship between relative stripe width and bulk tilt angle.

Then, we have looked at the influence of the k_s values used in the system. This parameter was also found to lead to significant changes in the tilt angle. However, unlike the stripe width, the tilt angle does not always change monotonically with k_s . This more complex behaviour appears to derive from situations where the anchoring strengths at the surfaces are relatively weak, so allowing the system to be less constrained.

We have also looked at the influence of the cell thickness. The results here were not very surprising in that as the cell thickness is increased, for comparable stripe width and comparable anchoring strengths at the surface, the system tends to exhibit a 45° monodomain. When we investigated the effect of changing k_s values on thick film systems, we found that a good range of monodomain tilt angles could be obtained. This result supports the notion that, by combining different sets of parameters, a full range of tilt angles should be achievable for stripe patterned surfaces. At the end of this chapter, we looked briefly at the effect of imposing smooth transitions on the substrate conditions of these systems. The results in this section indicated a surprising degree of insensitivity of the anchoring behaviour observed to the molecular-level nature of the substrate patterning.

We conclude, therefore, that generic stripe patterning of homeotropic and planar substrate regions offers a viable route to achieving a full range of anchoring angles. For film thickness in excess of 8 molecular lengths, the bulk system behaviour is dominated by nematic monodomain arrangements, information on the substrate patterning being restricted to thin interfacial regions. For very thin films, however, differently oriented domains prove able to bridge the system at all nematic densities.

In the next chapter, we extend this stripe pattern work by considering LC films confined between substrates with 2D patterns, such as squares and rectangles. The aim here is to explore the viability of using this approach to modify the azimuthal anchoring properties of LC films.

Chapter 6

Nematic liquid crystals on rectangle patterned substrates

In the previous chapter, we investigated the influence of 1D patterns (stripes) on confined LCs. In this chapter, we extend this by considering systems involving 2D patterns (squares and rectangles). In the first section, we study nematic LCs on square patterned substrates, and consider both sharp and smooth pattern transitions. In the second section, we study systems confined between rectangle patterned substrates. Here we investigate the influence of different parameters on the systems : the value of the needle lengths k_s and the rectangle aspect ratio L_x/L_y .

6.1 Square patterned substrates

Here, we study a nematic LC on square patterned substrates. Square patterned substrates can be considered as a system with rectangle patterned substrate where $L_x=L_y$. In the first part of this section, we will consider a system where the transitions between the homeotropic and planar alignment regions are sharp. Then we will look at the same system with smooth transitions. Again, we study a system of 864 rod-shaped particles interacting with each other via the HGO potential (see Section 3.2.3). The molecules interact with the substrate through the HNW potential (see Section 4.2). The thickness of the simulation box is $L_z=4\kappa\sigma_0$. The pattern is straightforward to impose, the value of k_s , the needle length of a molecule, being dependent on the x and y coordinates of the molecule. We can write : $k_s(i)=f(x_i, y_i)$,

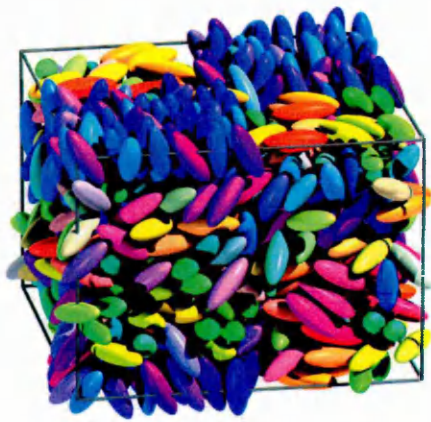
i being the index of the molecule.

6.1.1 Sharp transitions

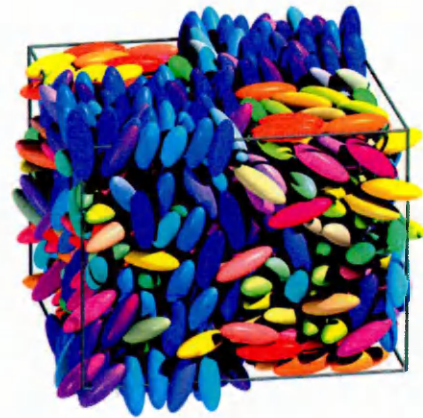
Fig. 6.1 shows a series of snapshots of a system confined between square patterned substrates at different reduced densities. Here, the k_s values used are 0 and 3. Looking at Fig. 6.1(e), we can see that at high density, the planar parts of the surface patterns are restricted to the immediate vicinity of the wall regions. Unlike the equivalent stripe patterned system, then, the planar parts of the pattern are not written across the LC film. In the planar region of the substrate, the molecules flip between the x and y orientations. This is apparent from Figs. 6.1(c), 6.1(d) and 6.1(e) which show that the molecules on the planar part of the substrate do not adopt a fixed orientation. Instead, the alignment in this surface region, between the x and y axes, is degenerate. With this pattern, then, it is not possible to fix or control the azimuthal angle (we saw in Chapter 5 that it is easy to control the azimuthal angle with stripe patterned substrate, because the molecules align along the stripes). At $\rho^*=0.37$, the system seems to exhibit an homeotropic anchoring (Fig. 6.1(c)). By increasing the density ($\rho^*=0.38$), the initial homeotropic anchoring appears to tilt (Fig. 6.1(d)) but if we carry on compressing gently to $\rho^*=0.40$, the bulk director realigns normal to the substrates (Fig. 6.1(e)).

Comparison between square patterned substrate systems and unpatterned systems

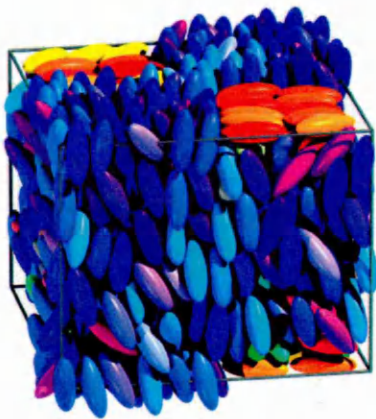
It is of interest here to compare, as we did in the previous chapter, the profiles corresponding to the red and to the green regions. The red region represents homeotropic surface alignment and the green region the planar surface alignment of the molecules. First of all, we will compare the behaviour of the bulk region confined between the red surface regions with the corresponding unpatterned symmetric system. Then, we will compare the behaviour of the bulk region confined between the green surface regions and the corresponding unpatterned symmetric system.



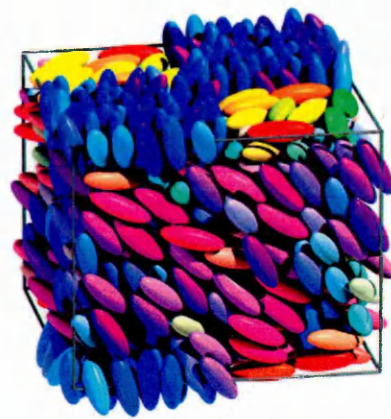
(a) $\rho^*=0.3$



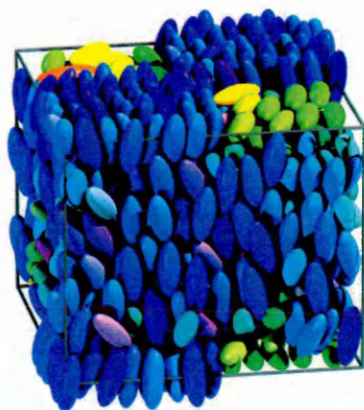
(b) $\rho^*=0.34$



(c) $\rho^*=0.37$



(d) $\rho^*=0.38$



(e) $\rho^*=0.40$

Figure 6.1: Snapshots of the square patterned system with sharp transitions between $k_s=0$ and $k_s=3$ regions for a series of different reduced densities.

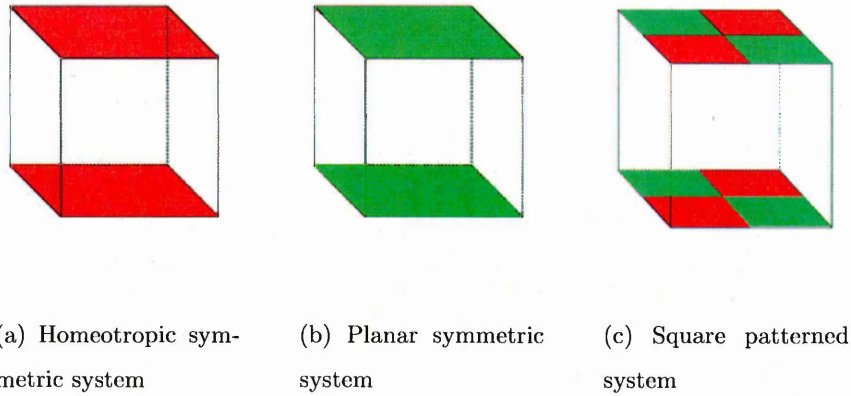
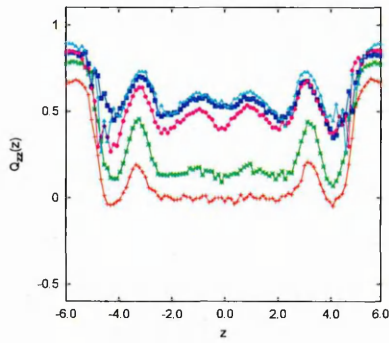


Figure 6.2: Schematic representations of different systems.

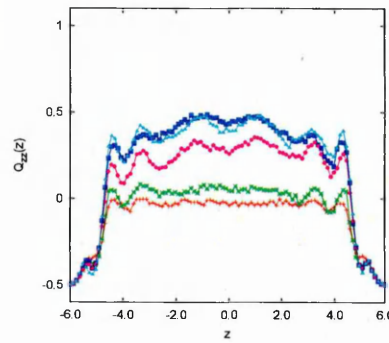
Red regions

Before comparing the behaviours of these two systems, we first analyse the behaviour of the LC film confined between the red substrate regions for the square patterned system. Fig. 6.3(a) shows the Q_{zz} profiles measured in this region. As the density is increased, the Q_{zz} value increases as well, showing the development of homeotropic anchoring in the bulk. As we increase the density to 0.37, the bulk Q_{zz} value reaches 0.60-0.65. As we carry on increasing the density to 0.38, however, the Q_{zz} value decreases to just below 0.5. Then, as the density reaches 0.4, the Q_{zz} increases again to $Q_{zz}=0.60-0.65$. This behaviour of the Q_{zz} profile confirms what we saw with the snapshots, the tilt apparent in the snapshots also being clear from the Q_{zz} profiles.

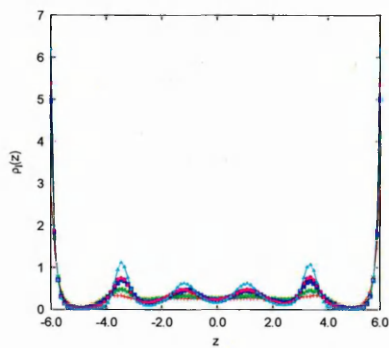
By way of comparison, Fig. 6.4 shows that for the equivalent symmetric, unpatterned system, increasing the density causes the Q_{zz} value to increase monotonically (dark blue line-pink line-light blue line). We saw, in Section 4.2 that, for short k_s , homeotropic anchoring is favoured and Q_{zz} tends to 1. The fact that Q_{zz} decreases at $\rho^* \simeq 0.37$ in the patterned system is, then, due to a tilt of the bulk director and this is a consequence of the pattern on the surface.



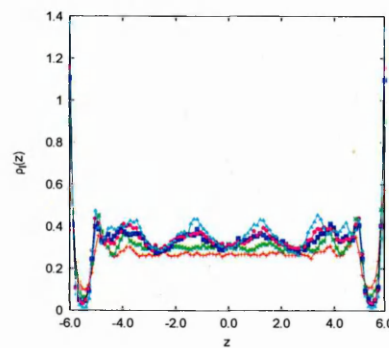
(a) Q_{zz} profile: H region



(b) Q_{zz} profile: P region



(c) Density profile: H region



(d) Density profile: P region

Figure 6.3: Q_{zz} and density profiles corresponding to the homeotropic and planar substrate regions of the $k_s=0$; $k_s=3$ square patterned system.

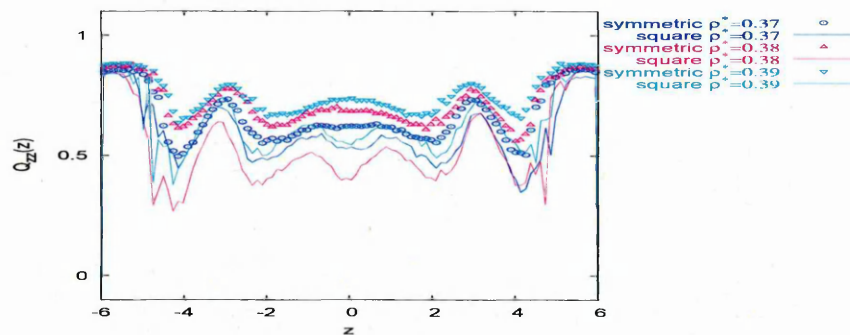


Figure 6.4: Comparison of the Q_{zz} profiles for the homeotropic regions.

Green region

Fig. 6.3(b) represents the Q_{zz} profile corresponding to the green region. We can see from this that, as we increase the density, the behaviour of Q_{zz} in this region of the

square patterned system is surprisingly similar to that seen in the red region. As we increase the density to 0.37, Q_{zz} increases. Then, as the density reaches the value of 0.38, Q_{zz} decreases before increasing again at a density of 0.4. This behaviour of the Q_{zz} profile confirms the observations and conclusions drawn from the snapshot sequence. The bulk confined between the green regions behaves very much like the material confined between the red regions. Only very close to the substrates is the planar nature of the green regions apparent from these Q_{zz} profiles.

An obvious difference between the behaviour of this square pattern system and the equivalent stripe patterned system is that the latter formed a 2 domain structure in which the surface pattern was written across the LC films. The loss of this bridging behaviour on moving away from striped systems appears, in fact, to be very general. We have observed monodomain configurations in virtually all of the wide variety of 2D patterned systems we have simulated in the course of this study.

To consider why this is the case, we consider a hypothetical planar aligned bridging domain, as shown schematically in Fig. 6.5. From this, it is apparent that such a domain would possess two distinct type of boundary with the neighbouring homeotropic material, one involving T configurations and another based on X configurations. Such an arrangement is clearly unstable since the surface tensions associated with these different interfaces could not, in general, be equal. This, we suggest, is why very few of our 2D-patterned systems exhibit bridging.

Conclusions

The $Q_{zz}(z)$ profiles obtained for square patterned systems are significantly different from those obtained from equivalent symmetric systems and striped systems. Rather than the bulk of the film adopting an orientation consistent with its bounding interface, then, for square patterned systems a monodomain structure is found for all systems. In the specific system considered here, this monodomain exhibits a density dependent tilt at most densities. Thus, even though the planar aligned material is restricted to the very thin near-substrate regions, the behaviour of the bulk director still reflects the patterned nature of the substrates.

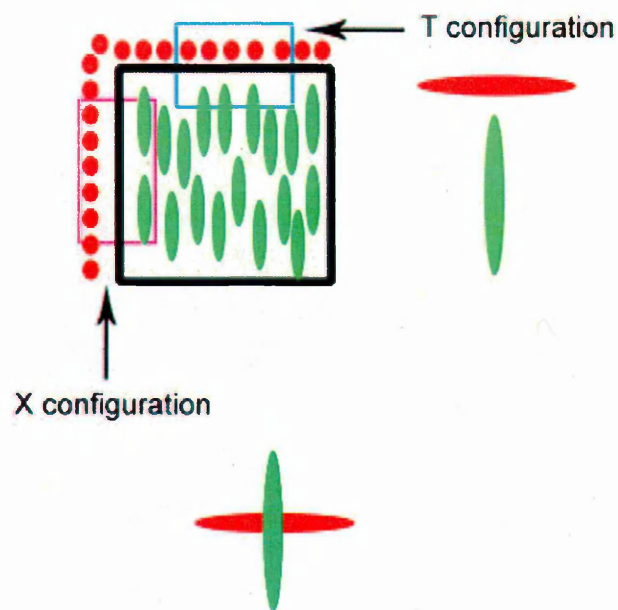


Figure 6.5: Schematic x-y plane slice through a hypothetical planar aligned bridging domain in a square patterned system.

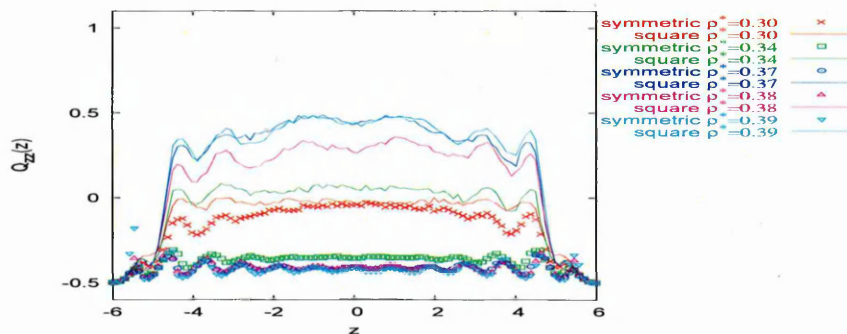


Figure 6.6: Comparison of the Q_{zz} profiles for the planar regions.

6.1.2 Azimuthal angle

In the previous section, we saw that it is not possible to control the azimuthal angle in the green region using a square surface pattern. We also said that the molecules on this green region flip between the x and y directions. This is confirmed by the histogram in Fig . 6.7 which shows a distribution of molecular azimuthal angles measured during the $\rho^*=0.37$ simulation. This histogram was generated from 500

stored configuration files and based on the orientations of particles within $1\sigma_0$ of the planar substrate regions. From this, it is apparent that the molecules at the surfaces are strongly disposed to adopting azimuthal angles ϕ of $0^\circ \leq \phi \leq 5^\circ$ or $85^\circ \leq \phi \leq 90^\circ$

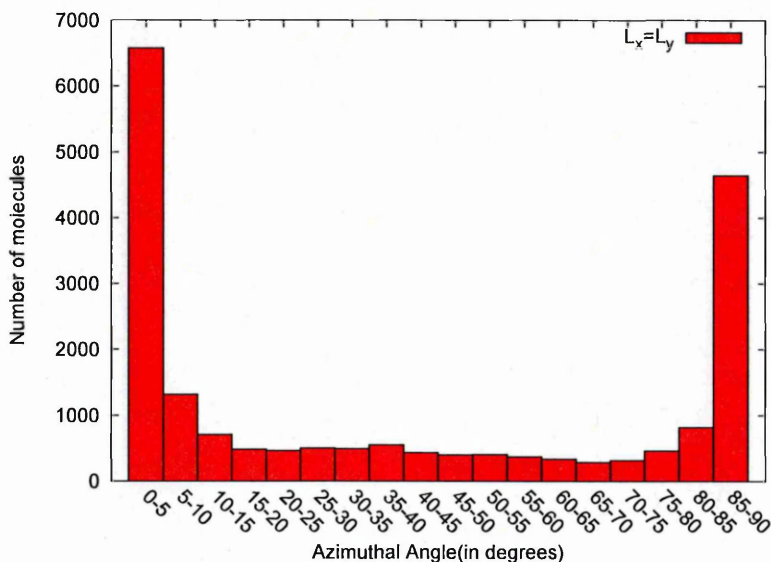


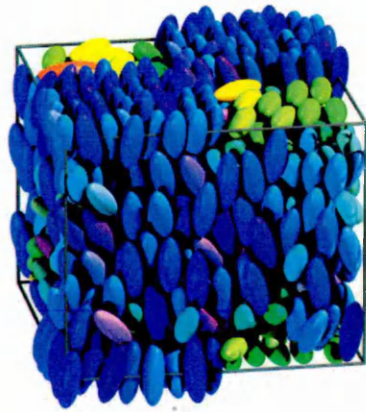
Figure 6.7: Histogram showing the azimuthal angle distribution of surface particles in the P region.

6.1.3 Smooth transitions

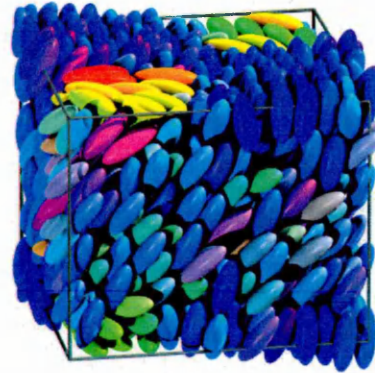
To complement the previous section, we have also studied a system similar to the previous one but with smooth transitions between the green and red regions. High density snapshots corresponding to these sharp and smooth transition systems are represented in Fig. 6.8. From these, it is apparent that a smooth transition system also exhibits tilted monodomain behaviour. To assess this more fully we now compare the red regions and the green regions separately.

Comparison of red regions

Fig. 6.9 shows the Q_{zz} profiles corresponding to the sharp and smooth transitions square patterned system. Even though not all densities are represented here, it is apparent that the I-N phase transitions happens at lower density for the smooth



(a) Sharp transitions



(b) Smooth transitions

Figure 6.8: Snapshots of the square patterned system for sharp and smooth transitions.

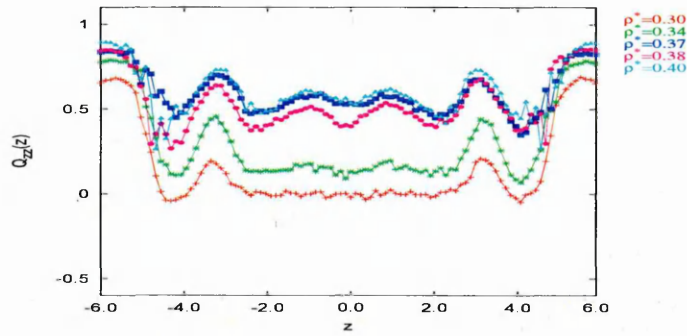
transitions system. Previous work on LC films confined between unpatterned surfaces observed delayed onset of nematic order at k_s values which gave bistable anchoring [102]. Thus, where planar and homeotropic surface domains compete, the films find it harder to form ordered monodomains. Here, then, we ascribe the change in I-N density to the fact that, for smooth transitions, the tilted monodomain arises naturally from the transition region rather than as a result of competition between two distinct substrate behaviours.

Comparison of green regions

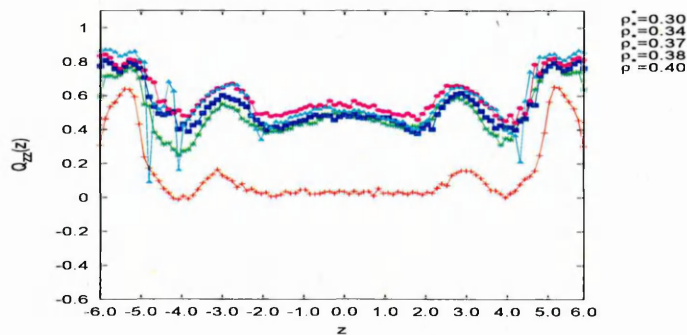
Regarding this region, we can notice that, if we look at the Q_{zz} profiles (see Fig. 6.10), here as well the I-N phase transition appears at a relatively lower density. The Q_{zz} value in the bulk is slightly lower for smooth transitions, which confirms that the bulk is tilted away from the normal to the substrate for smooth transitions. However, the difference in value is not very big.

6.1.4 Conclusion

In the first part of this chapter, we have been looking at square patterned substrates. With this type of 2D pattern, we found that the pattern is never written across the cell. For the k_s values considered here, the planar parts of the surface patterns



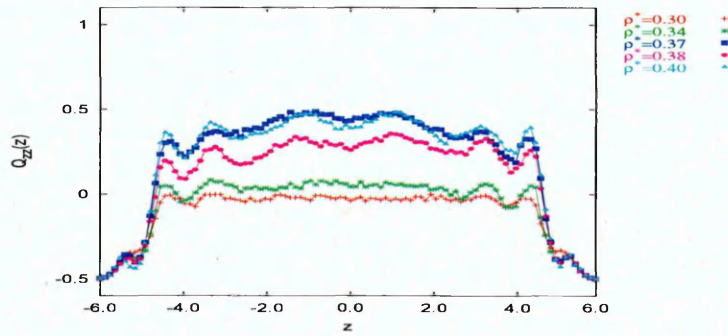
(a) Q_{zz} profile, sharp transitions



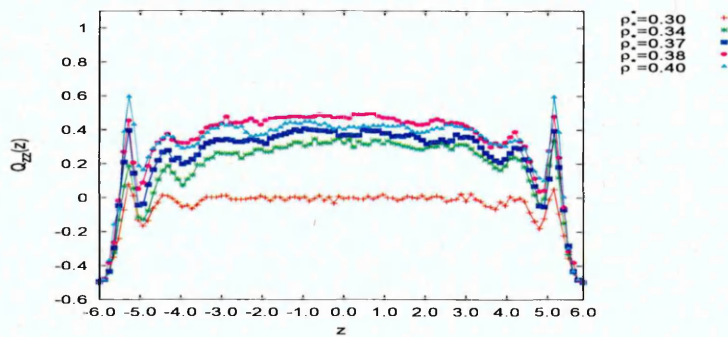
(b) Q_{zz} profile, smooth transitions

Figure 6.9: Q_{zz} profiles in the homeotropic region corresponding to the sharp and smooth transition square patterned systems.

are restricted to the immediate vicinity of the wall regions. The fact that different surface tensions applied to any associated domain walls can explain why there is no bridging. We also looked at the behaviour of the molecules on the planar part of the pattern to determine the azimuthal angle at the surface. This shows that the molecules are most likely to lie at 0° or 90° (i.e. along the edges of the surface pattern). Regular flipping between these states is observed within each simulation. Finally, we investigated the influence of smooth transition regions on the behaviour of square patterned systems and found that the major difference is the shift of the I-N phase transition to lower density. This appears related to the relative ease of monodomain formation in these systems. In the next section, we will expand our study to include rectangle patterns, by varying the ratio L_x/L_y which was equal to



(a) Q_{zz} profile, sharp transitions



(b) Q_{zz} profile, smooth transitions

Figure 6.10: Q_{zz} profiles in the planar region corresponding to the sharp and smooth transition square patterned systems.

1 in the case of square patterns.

6.2 Rectangle patterned substrates

In this section, we consider results from simulations performed on 864 molecules confined between rectangle patterned substrates. Again, the thickness of the simulation box is kept at $L_z=4\kappa\sigma_0$. In this section, we will investigate the influence of two parameters : the needle length k_s and the pattern ratio L_x/L_y .

6.2.1 Influence of the k_s values

Here, we concentrate on systems for which the ratio $L_x/L_y=3$, and investigate the effect of the needle length parameter on the systems. We have, first of all, studied a system with strong planar alignment regions ($k_s = 3$) and varied the homeotropic alignment strength on the remaining area ($0 \leq k_s \leq 1$). Then, we have considered the inverse case of a system with strong homeotropic alignment regions ($k_s=0$) and a range of planar alignment parameters ($2 \leq k_s \leq 3$) on the remaining area.

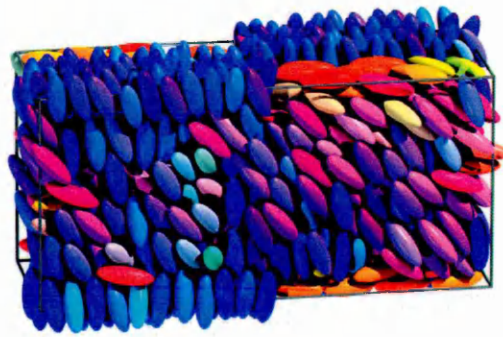
Strong planar alignment

We first used a combination of strong planar alignment of the molecules on the substrate ($k_s = 3$) with a strong homeotropic alignment ($k_s = 0$). Then, we slightly weakened the homeotropic alignment ($k_s = 0.5$) before going on to use a weak homeotropic alignment ($k_s = 1$). The high density snapshots corresponding to such systems are represented in Fig. 6.11. Looking at these snapshots, it is apparent that the molecules are aligning in the $x-z$ -plane (red, orange and yellow molecules). This is consistent with what we saw in the previous chapter, that the anchoring has a strong tendency to align along substrate stripes. It means, though, that for an edge ratio as low as 3, the rectangle patterned substrates are being seen by the system rather like well defined stripes. So, the first important remark is that we can control the azimuthal angle using relatively low aspect ratio rectangle patterns. The second noticeable thing from these snapshots is that the surface patterns are not written across the film. As with square patterns, this is presumably due to different surface tensions applying at the different faces of any domain boundaries. To see if there is much difference between these three systems, we have compared their Q_{zz} profiles (see Figs. 6.12). The main thing we can learn from these

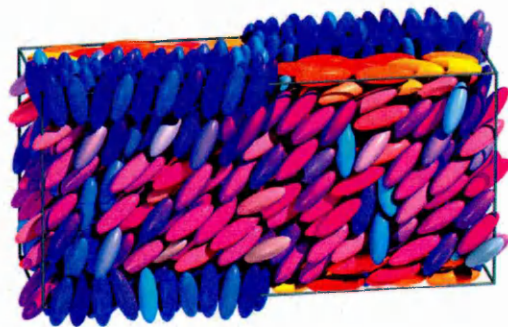
	$k_s=3;k_s=0$		$k_s=3;k_s = 0.5$		$k_s=3;k_s = 1$	
	$k_s=3$	$k_s = 0$	$k_s=3$	$k_s = 0.5$	$k_s = 3$	$k_s = 1$
$L_x/L_y = 3$	$\theta_z = 37$	$\theta_z = 31$	$\theta_z = 40$	$\theta_z = 33$	$\theta_z = 40$	$\theta_z = 34$

Table 6.1: Tilt angle in degrees in the two confined regions for $L_x/L_y = 3$, strong planar alignment

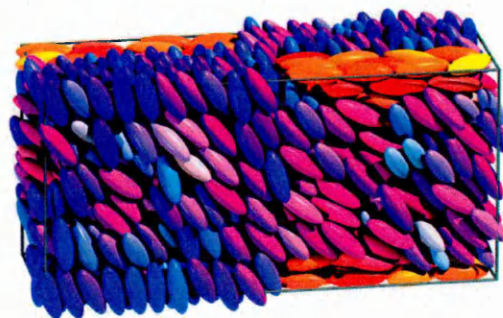
graphs is the fact that, in the homeotropic region, the Q_{zz} value is slightly greater



(a) $k_s=0; k_s=3$

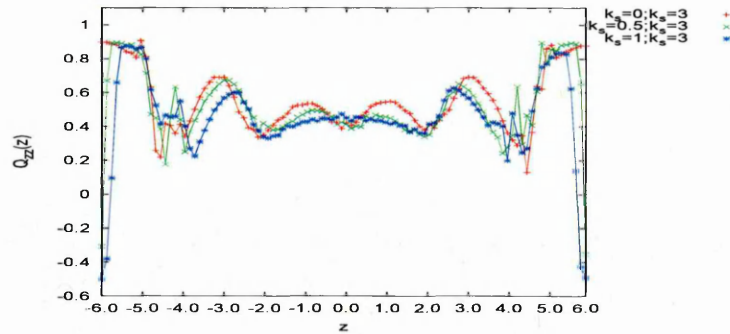


(b) $k_s=0.5; k_s=3$

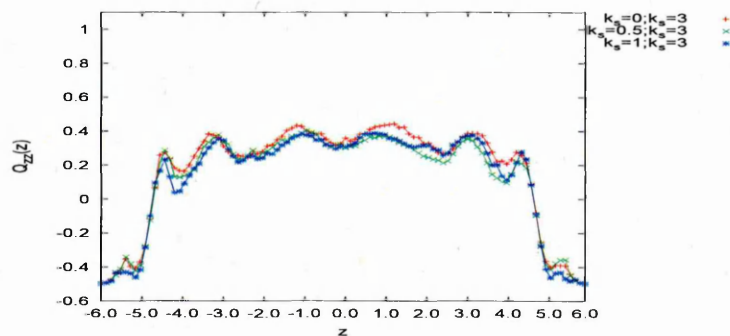


(c) $k_s=1; k_s=3$

Figure 6.11: Snapshots of the rectangle patterned system for different k_s values, strong planar anchoring. $\rho^*=0.4$.



(a) H region



(b) P region

Figure 6.12: influence of the k_s value on the Q_{zz} profiles.

for strong homeotropic anchoring at the surfaces (see Fig. 6.12(a)). The difference is not apparent though in the planar region (see Fig. 6.12(b)). Because the small differences in these graphs are not easy to pick out, we have also calculated the average bulk tilt angles. These are presented in table 6.1. These show that the system having strong planar and strong homeotropic anchoring at the surfaces ($k_s=0$ and $k_s=3$), exhibits two tilt angles θ_z which are close to each other, the difference being of 6° . As we decrease the strength of the homeotropic anchoring at the surface, we would expect the molecules in the bulk to align more parallel to the surfaces (so increasing θ_z). This trend in the tilt angle as a function of k_s is indeed observed, as shown in table 6.1 and the histograms of Fig. 6.13. The observed variation of θ_z with the homeotropic k_s value is very weak though. Thus, even when the homeotropic alignment on the substrate is weak ($k_s=1$), it still has

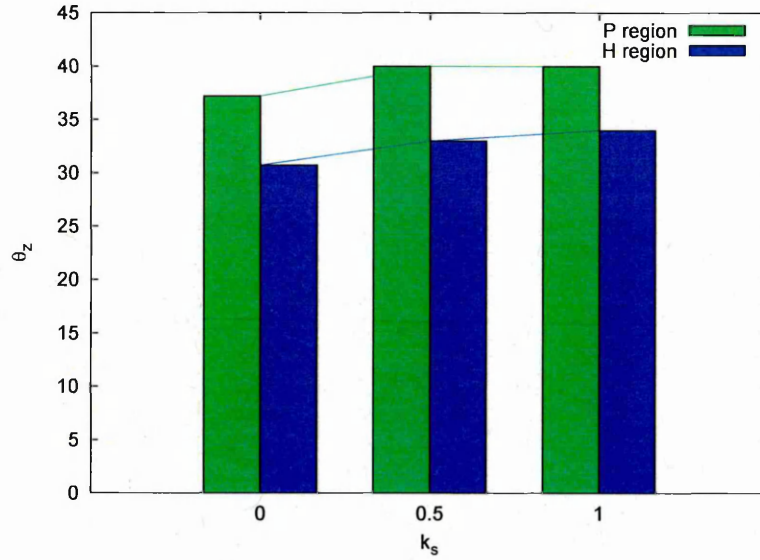


Figure 6.13: Evolution of θ_z in the two regions as the strength of the homeotropic anchoring at the surface is decreased.

a great influence on the whole system behaviour because the measured tilt angles are far from 90° .

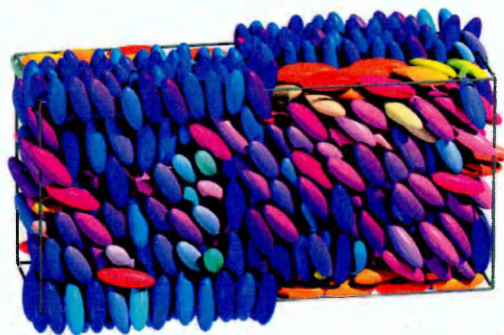
Strong homeotropic alignment

Here, we first consider the case of strong homeotropic anchoring regions at the surface ($k_s = 0$) combined with strong planar anchoring ($k_s = 3$) on the remaining area. Then, we slightly weaken the planar anchoring ($k_s = 2.5$) before using a weak

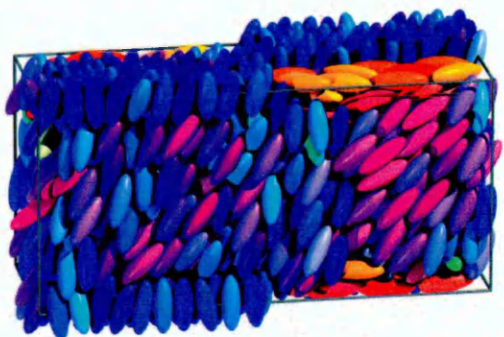
	$k_s=3; k_s = 0$		$k_s=2.5; k_s = 0$		$k_s=2; k_s = 0$	
	$k_s=3$	$k_s = 0$	$k_s=2.5$	$k_s = 0$	$k_s=2$	$k_s = 0$
$L_x/L_y=3$	$\theta_z=37$	$\theta_z=31$	$\theta_z=30$	$\theta_z=26$	$\theta_z=25$	$\theta_z=22$

Table 6.2: Tilt angle in degrees in the two confined regions for $L_x/L_y=3$, strong homeotropic alignment

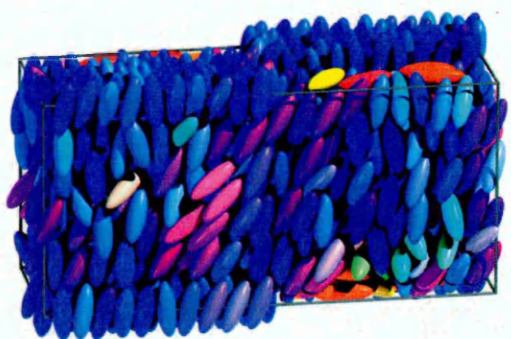
planar anchoring ($k_s = 2$). We saw, in the previous section, that for a combination of strong homeotropic and strong planar alignment on the substrates, the resultant tilt angles in the two regions are $30^\circ < \theta_z < 40^\circ$. If we look at the variation of the Q_{zz} profiles (see Fig. 6.15), we can see that as we decrease the planar anchoring



(a) $k_s=0$; $k_s=3$

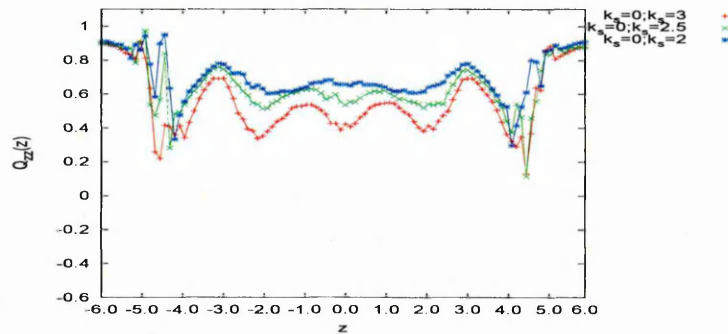


(b) $k_s=0$; $k_s=2.5$

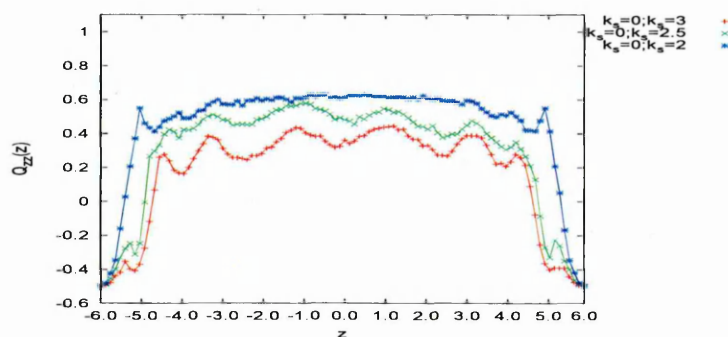


(c) $k_s=0$; $k_s=2$

Figure 6.14: Snapshots of the $L_x=3L_y$ rectangle patterned system, for different k_s values, strong homeotropic anchoring. $\rho^*=0.4$.



(a) H region



(b) P region

Figure 6.15: Influence of the k_s value on the Q_{zz} profiles.

strength, the Q_{zz} profiles increase in both regions. This means that the molecules are aligning increasingly perpendicular to the surfaces. This makes intuitive sense, since the relative influence of the homeotropic anchoring would be expected to grow in such a circumstances. This conclusion is confirmed by table 6.2 and Fig. 6.16, which present the tilt angles in the two regions as a function of the planar region needle length k_s . If we start to decrease the needle length in the planar surface region (to $k_s=2.5$), the tilt angles decrease in the two regions, going from $\theta_z=37^\circ$ to $\theta_z=30^\circ$ in the planar region and from $\theta_z=31^\circ$ to $\theta_z=26^\circ$ in the homeotropic region. As we carry on decreasing the value of k_s (to $k_s=2$), the tilt angle, once again decreases going from $\theta_z=30^\circ$ to $\theta_z=25^\circ$ in the planar region and from $\theta_z=26^\circ$ to $\theta_z=22^\circ$ in the homeotropic region.

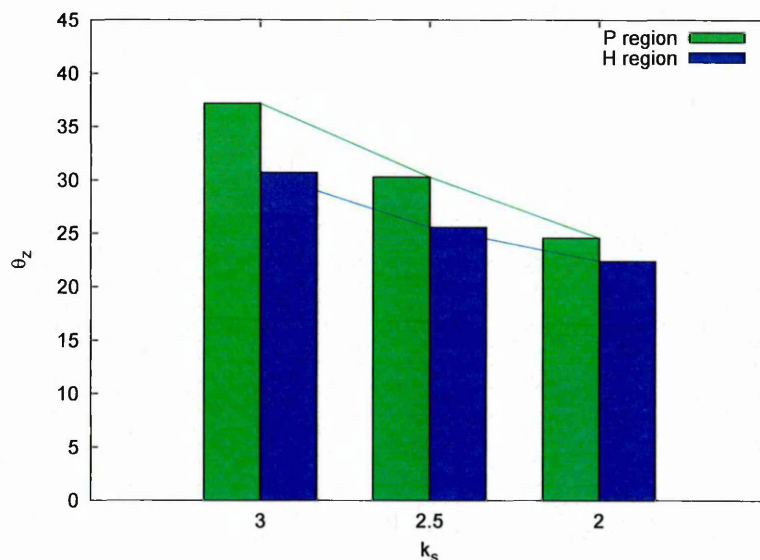
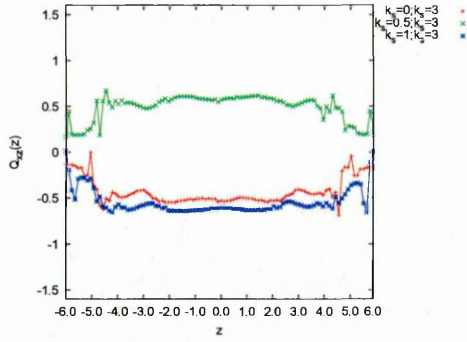


Figure 6.16: Evolution of θ_z in the two regions as the strength of the planar anchoring at the surface is decreased.

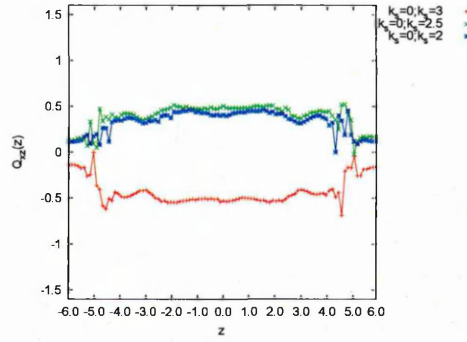
6.2.2 Conclusions

In this section, we have looked at the influence of the needle length on rectangle patterned systems. We have focused on two sets of systems. The first consisted of three systems having a strong planar anchoring regions and variable homeotropic strengths. We concluded that as the homeotropic anchoring is weakened, the influence of planar anchoring grows and the tilt angle increases. We saw as well that this type of pattern allows us to influence the azimuthal angle because the molecules clearly align in the x - z plane. This azimuthal coupling is apparent from the Q_{zz} profiles shown in Figs. 6.17(a) and 6.17(c). In the second part of this section, we have looked at the complementary set of systems where the homeotropic anchoring at the surface was held strong and the planar one was varied. Here, we saw that as the strength of the homeotropic anchoring was decreased, the influence of planar part of the substrate grew, so causing the tilt angles in the two regions of the system to increase. The Q_{xz} profiles corresponding to these systems are represented in Figs. 6.17(b) and 6.17(d).

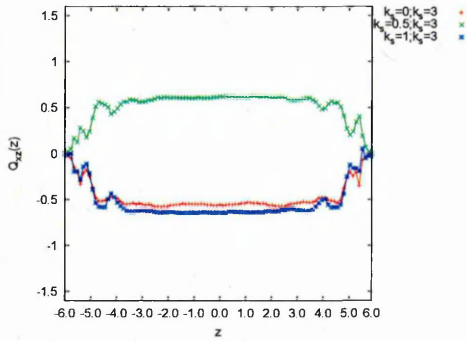
In addition to the results just presented, we have also looked at a number of related systems. Specifically, we have investigated the effect of the k_s parameter on systems



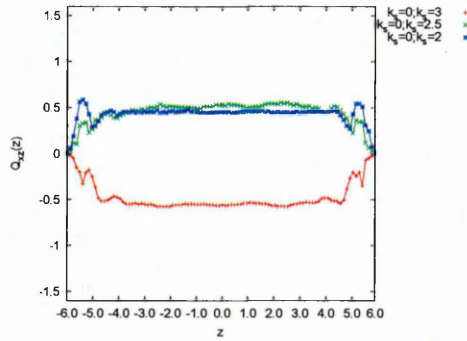
(a) H region, strong planar anchoring



(b) H region, strong homeotropic anchoring



(c) P region, strong planar anchoring

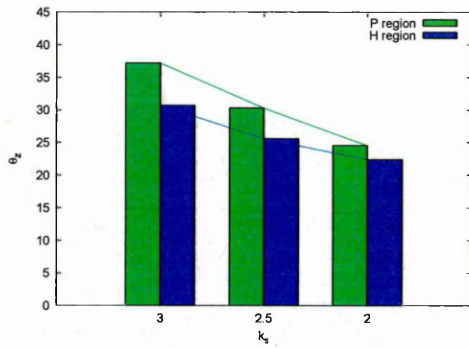


(d) P region, strong homeotropic anchoring

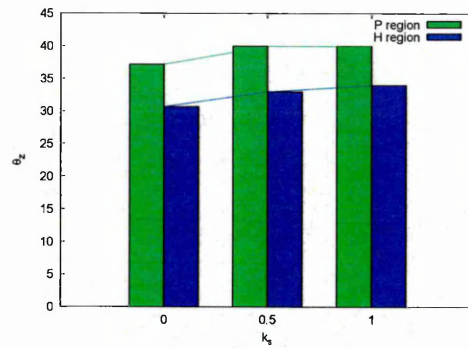
Figure 6.17: Influence of the k_s value on the Q_{xz} profiles

with fixed weak planar anchoring, weak homeotropic anchoring, moderate planar anchoring and moderate homeotropic anchoring at the surface. The variation of the tilt angles θ_z for each of these systems is given in Fig. 6.18. Here, we can notice that in all cases the variation of the tilt angles with k_s is monotonic and so, independent of the strength of the anchoring that is kept constant. We conclude, then, that using this type of pattern, allows us to control both the tilt angle and the azimuthal angle.

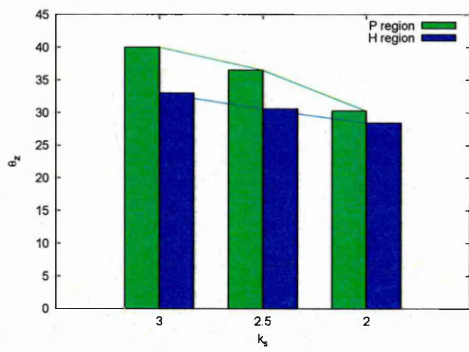
We have carried on the study of this class of system by varying the ratio L_x/L_y . In the next section, we will look at the influence of this ratio on the system behaviour. In the first part of this chapter, we have been looking at a systems where $L_x=L_y$.



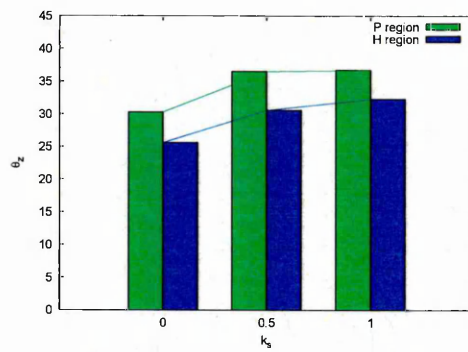
(a) $k_s=0$



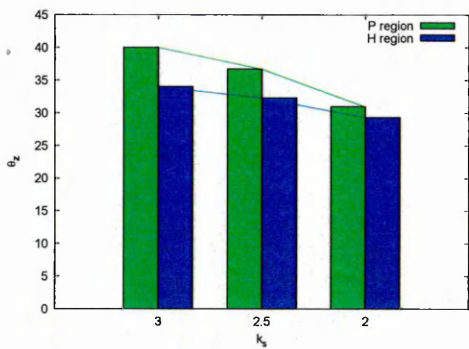
(b) $k_s=3$



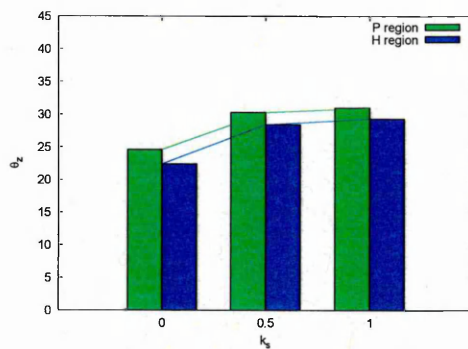
(c) $k_s=0.5$



(d) $k_s=2.5$



(e) $k_s=1$



(f) $k_s=2$

Figure 6.18: Evolution of the tilt angle as one k_s value is varied and the other is held fixed.

In this section, we have been looking at the influence of the needle length parameter on system for which the ratio L_x/L_y was equalled to 3. In the next section, we will be looking at the differences between systems for which the ratio can be equalled to 2 or 3.

6.2.3 Influence of the ratio L_x/L_y

Strong planar alignment

In section 6.2.1, we considered the behaviour of several $L_x/L_y=3$ systems. Here, we perform a similar assessment of a series of $L_x/L_y=2$ systems and then compare the two sets of results. Comparison high density snapshots are represented in Fig. 6.19. We note from these that, in all cases, the molecules adjacent to the planar part of the surface patterns align strongly along the x -axis. This indicates that control of the azimuthal angle with rectangle patterns is achievable even with $L_x/L_y \simeq 2$. The influence of the ratio L_x/L_y on the azimuthal angle will be investigated in more detail at the end of this section. Fig. 6.20 represents the high density Q_{zz} profiles of the $L_x/L_y=2$ systems with strong planar anchoring regions and varying homeotropic anchoring strength. These profiles are slightly more sensitive to the variation of the homeotropic surface anchoring for $L_x/L_y=2$ than they were for $L_x/L_y=3$. Specifically, the $L_x/L_y=2$ Q_{zz} profiles seem to be similar for $k_s=0$ and $k_s=0.5$, but very different for $k_s=1$. While for ratio=3, we had $0.4 < Q_{zz} < 0.5$, for ratio=2, $0.1 < Q_{zz} < 0.5$, the lowest Q_{zz} values corresponding to the systems with weakest homeotropic surface anchorings. This indicates that the influence of the strong planar anchoring regions on systems with weak homeotropic anchoring is greater if the ratio L_x/L_y is small. Fig. 6.21 represents the variation of the tilt angle θ_z as the strength of the homeotropic surface anchoring is decreased for the two system ratios. The θ_z value for the system where $L_x/L_y=2$ and $k_s=1$ on the homeotropic region is not communicated because the variation of the n_z component was too noisy and so, not usable. In this region, the molecules aligned primarily along the x -axis, and the corresponding angle is $\theta_x = 46.4^\circ$. However, we can see on Fig. 6.21(a) that, as the strength of the homeotropic anchoring at the surface is decreased, the tilt angle in the two regions of the cell increases which means that

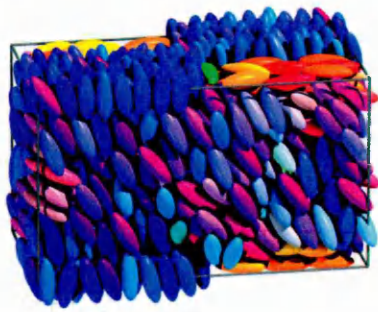
the molecules are lying more parallel to the surfaces. This behaviour is similar that observed for the $L_x/L_y=3$ system (see section 6.2.1 and Fig. 6.21(b)). The two sets of systems behave qualitatively identically. Now, though, we are in a position where we can compare quantitatively the systems. The tilt angles are grouped together in table 6.4. We can see from this that, as the ratio L_x/L_y is increased, the tilt angles in the two regions increase. In the case of strong planar anchoring at the surface, the tilt angles seem to vary monotonically with the value of the ratio L_x/L_y . Thus the system is sensitive only to both the size and shape of the surface pattern. The bigger the aspect ratio of the rectangle pattern, the greater the tilt angle. If we increase the ratio L_x/L_y to infinity (stripe patterned system), we know that depending on the stripe width, the pattern can sometimes be written across the film. For example, in the case of 50% homeotropic $k_s=0$ and 50% planar $k_s=3$ with a $L_z=4\kappa\sigma_0$ film, the pattern is written across the film. This gives very different tilt angles (Table 6.3). However, given the qualitative difference between 2 domains and 1 domain arrangements, it appears inappropriate to conclude much from these tilt angle changes.

	$k_s=3;k_s=0$	
	$k_s=3$	$k_s=0$
$L_x/L_y=2$	$\theta_z=35$	$\theta_z=29$
$L_x/L_y=3$	$\theta_z=37$	$\theta_z=31$
$L_x/L_y = \infty$	$\theta_z=61$	$\theta_z=30$

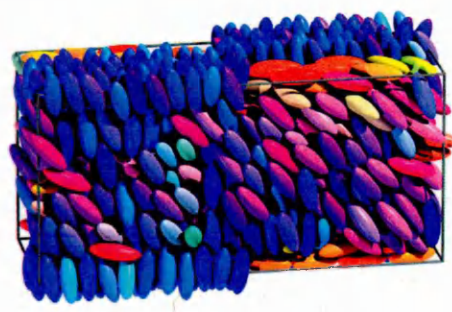
Table 6.3: Tilt angle depending on the ratio L_x/L_y , strong homeotropic and planar surface anchoring.

Strong homeotropic alignment

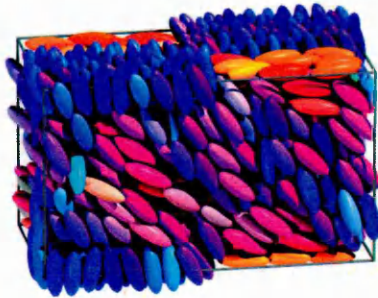
In this section, we consider the influence of the ratio L_x/L_y in the case of strong homeotropic surface anchoring and varying planar anchoring. The snapshots representing such systems are grouped together in Fig. 6.23. We can see from these that weakening the planar surface anchoring on the $L_x/L_y=2$ systems has an impact on the bulk behaviour. In Section 6.2.1, we investigated the effects of weakening the planar surface anchoring on $L_x/L_y=3$ systems. Fig. 6.22 shows the influence that



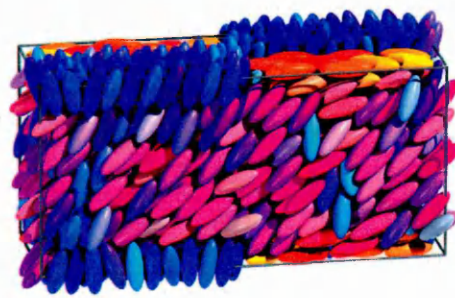
(a) $k_s=0; k_s=3$



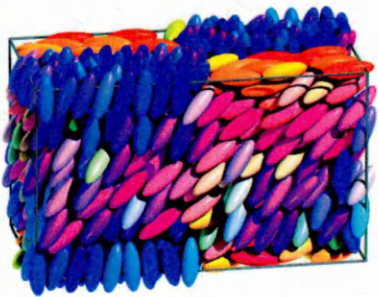
(b) $k_s=0; k_s=3$



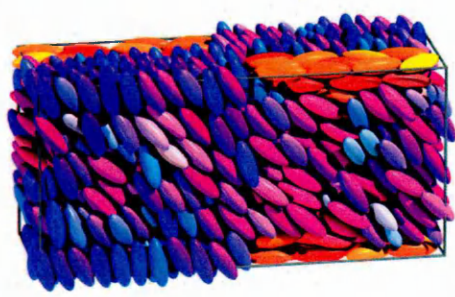
(c) $k_s=0.5; k_s=3$



(d) $k_s=0.5; k_s=3$

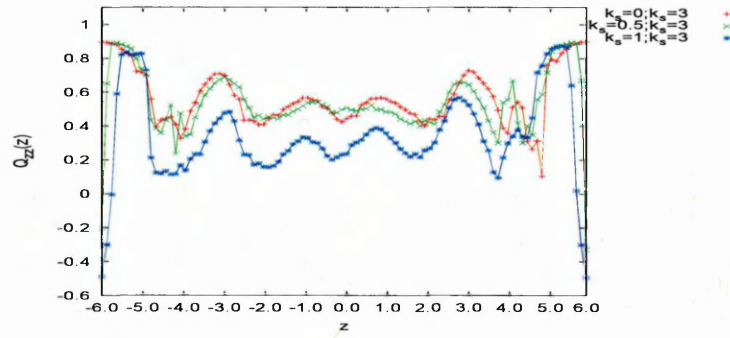


(e) $k_s=1; k_s=3$

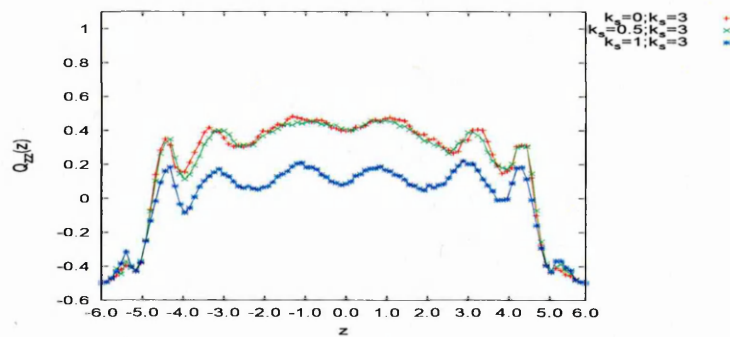


(f) $k_s=1; k_s=3$

Figure 6.19: Snapshots of systems with different homeotropic region k_s values. Snapshots on the left : $L_x=2L_y$ and snapshots on the right : $L_x=3L_y$. Strong planar anchoring.



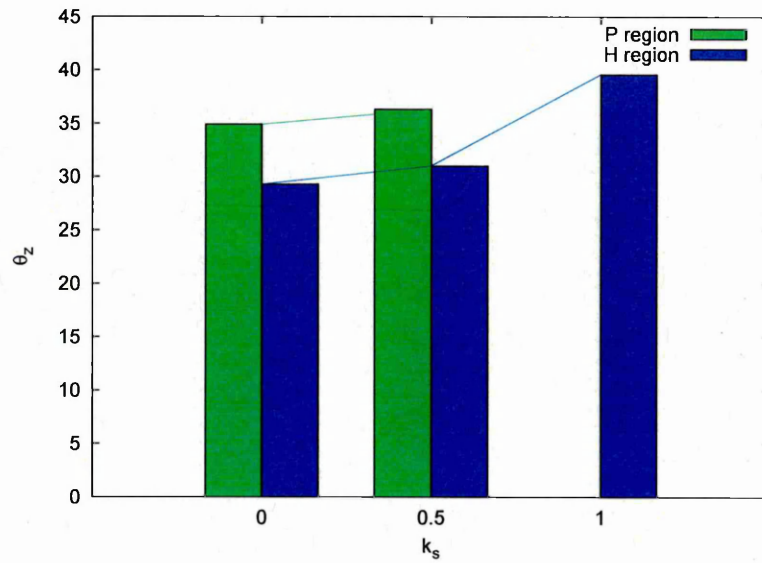
(a) H region



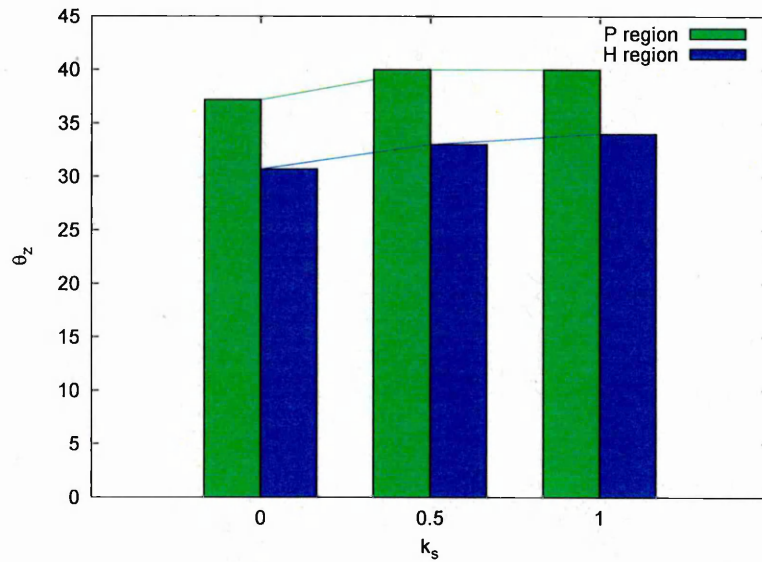
(b) P region

Figure 6.20: Influence of the k_s value on the Q_{zz} profiles of $L_x/L_y=2$ systems at $\rho^*=0.4$.

changing k_s in the planar part of the pattern has on the $L_x/L_y=2$ Q_{zz} profiles. The difference is noticeable this time as the Q_{zz} values are strongly influenced by k_s values. The Q_{zz} values in both regions increase as the planar surface anchoring strength decreases. This means that the molecules are lying increasingly normal to the surfaces, as confirmed by the data given in table 6.4. The evolution of the tilt angle is also represented in Fig. 6.24(a). If we now compare the results for $L_x/L_y=2$ and $L_x/L_y=3$ systems, we can notice, looking at table 6.4, that again, larger changes in tilt angle are apparent for the bigger pattern ratio system.



(a) $L_x/L_y=2$

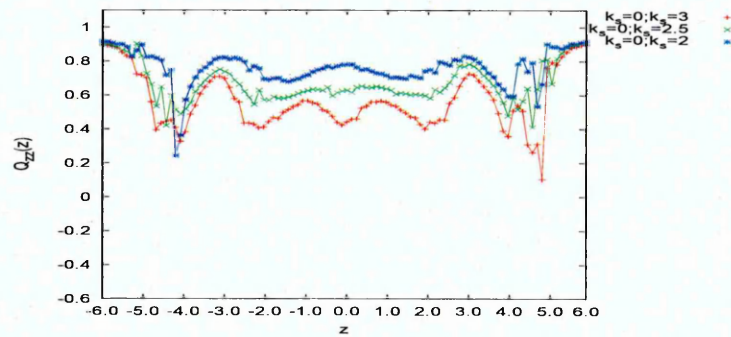


(b) $L_x/L_y=3$

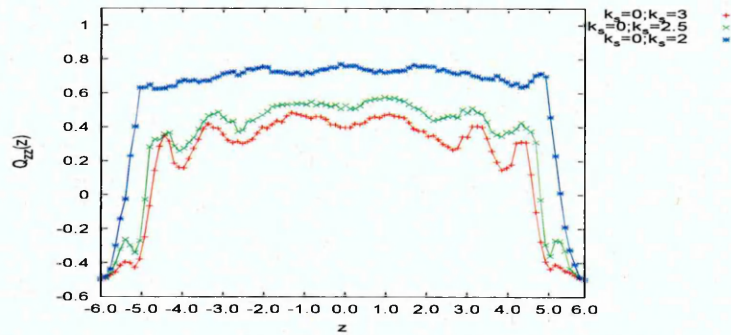
Figure 6.21: Evolution of the tilt angle as the homeotropic k_s and L_x/L_y vary, strong planar anchoring ($k_s=3$).

	$k_s=3;k_s=0$		$k_s=3;k_s=0.5$		$k_s=3;k_s=1$	
	$k_s=3$	$k_s=0$	$k_s=3$	$k_s=0.5$	$k_s=3$	$k_s=1$
$L_x/L_y=2$	$\theta_z=35$	$\theta_z=29$	$\theta_z=36$	$\theta_z=31$	$\theta_z=?$	$\theta_z=40$
$L_x/L_y=3$	$\theta_z=37$	$\theta_z=31$	$\theta_z=40$	$\theta_z=33$	$\theta_z=40$	$\theta_z=34$
	$k_s=3;k_s=0$		$k_s=2.5;k_s=0$		$k_s=2;k_s=0$	
	$k_s=3$	$k_s=0$	$k_s=2.5$	$k_s=0$	$k_s=2$	$k_s=0$
$L_x/L_y=2$	$\theta_z=35$	$\theta_z=29$	$\theta_z=29$	$\theta_z=24$	$\theta_z=15$	$\theta_z=15$
$L_x/L_y=3$	$\theta_z=37$	$\theta_z=31$	$\theta_z=30$	$\theta_z=26$	$\theta_z=25$	$\theta_z=22$

Table 6.4: Tilt angle depending on the ratio L_x/L_y



(a) H region

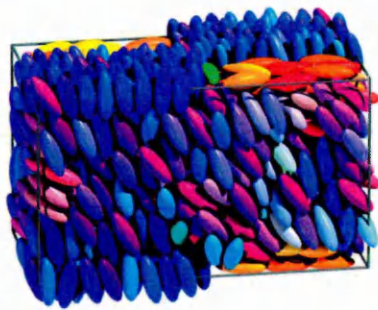


(b) P region

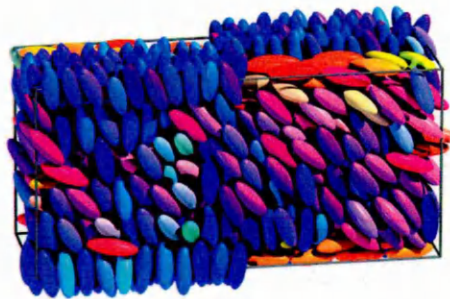
Figure 6.22: Influence of the k_s value on the Q_{zz} profiles.

Conclusions

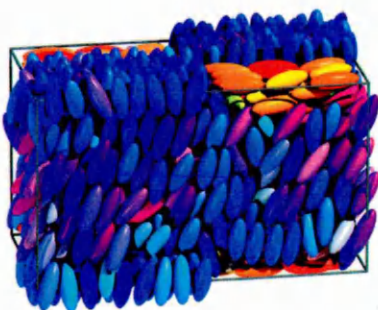
In this section, we have investigated the effects of changing the ratio L_x/L_y and the needle lengths. From this, we have observed that for a set of systems having



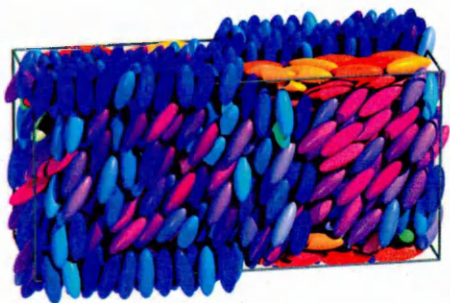
(a) $k_s=0; k_s=3$



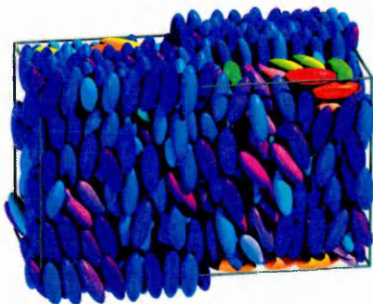
(b) $k_s=0; k_s=3$



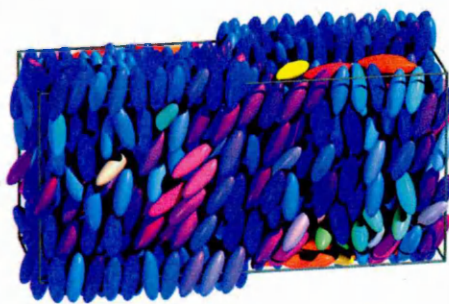
(c) $k_s=0; k_s=2.5$



(d) $k_s=0; k_s=2.5$

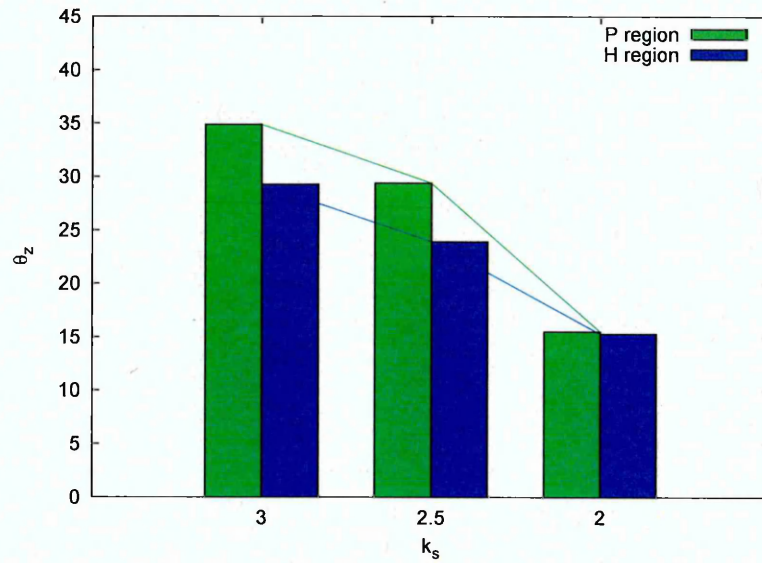


(e) $k_s=0; k_s=2$

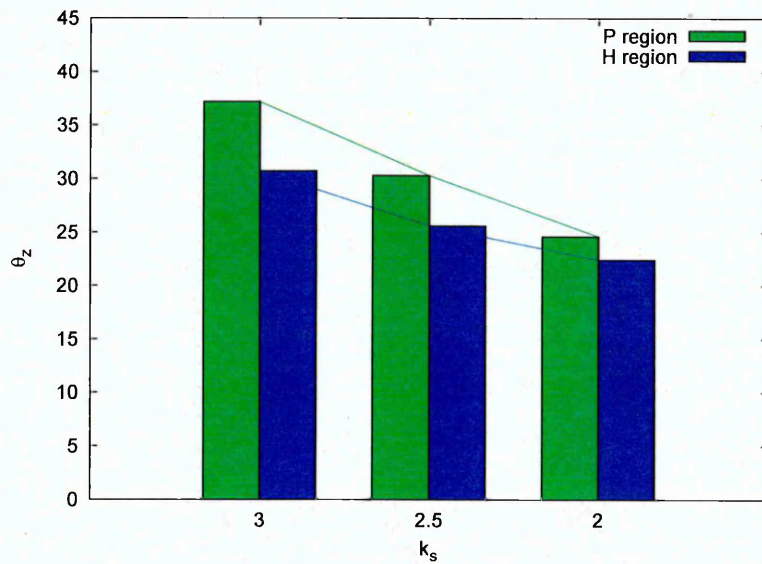


(f) $k_s=0; k_s=2$

Figure 6.23: Snapshots of system with different k_s . Snapshots on the right : $L_x=2L_y$ and snapshots on the left : $L_x=3L_y$. Strong homeotropic anchoring.

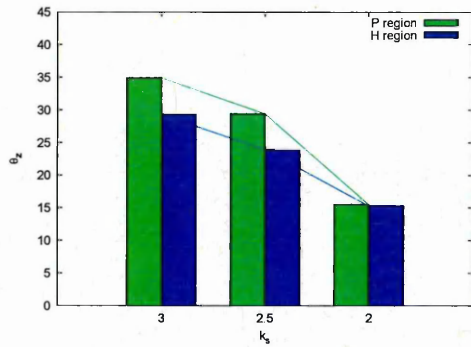


(a) $L_x/L_y=2$

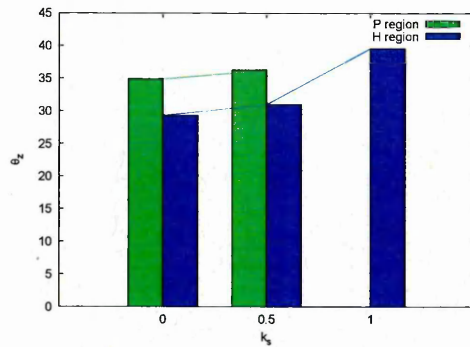


(b) $L_x/L_y=3$

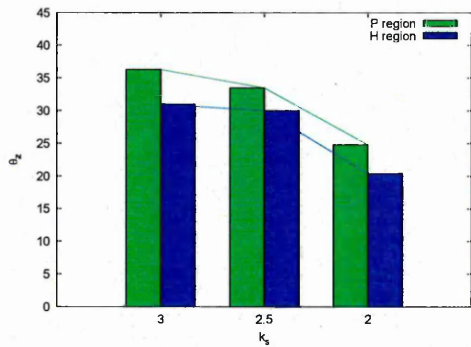
Figure 6.24: Evolution of the tilt angle as k_s and L_x/L_y varies, strong homeotropic anchoring.



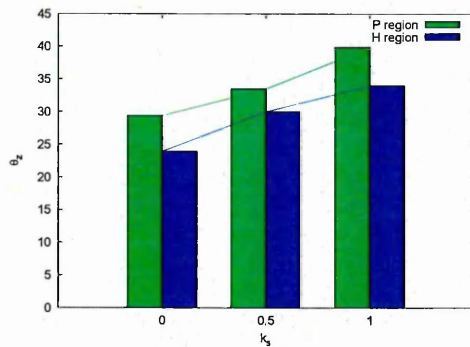
(a) $k_s=0$



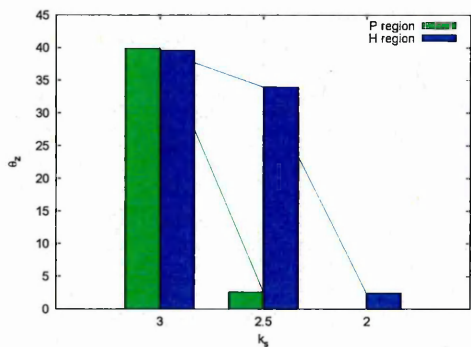
(b) $k_s=3$



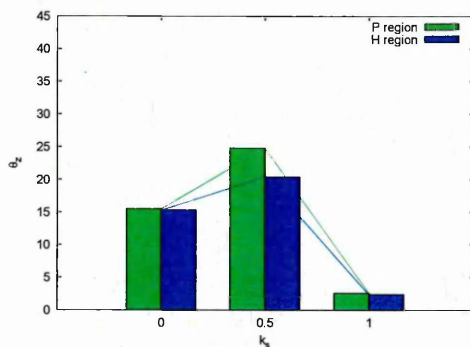
(c) $k_s=0.5$



(d) $k_s=2.5$



(e) $k_s=1$



(f) $k_s=2$

Figure 6.25: Evolution of the tilt angle for a full set of k_s combination for $L_x/L_y=2$ systems.

strong planar surface anchoring and decreasing homeotropic surface anchoring, the tilt angle θ_z in the two regions increases. As we increase the ratio L_x/L_y , this tilt angle increases even further.

For an equivalent set of systems with a strong homeotropic surface anchoring and a changing planar anchoring, the tilt angle in the two regions decreases as the planar anchoring is weakened. By increasing the ratio L_x/L_y , though, the tilt angle increases. In most cases, the tilt angle varies monotonically with the aspect ratio of the pattern and the needle length.

We have in fact investigated the effects of changing the needle length and the ratio L_x/L_y on a full array of systems. The full set of tilt angle results obtained from this is represented in Fig. 6.25. Looking at Fig. 6.25(f), we can see that the variation of the tilt angle is not monotonic all the time. It would therefore be interesting to study systems with varying needle length with a pattern ratio $L_x/L_y=4$ to examine this tilt angle behaviour more fully.

Azimuthal angle

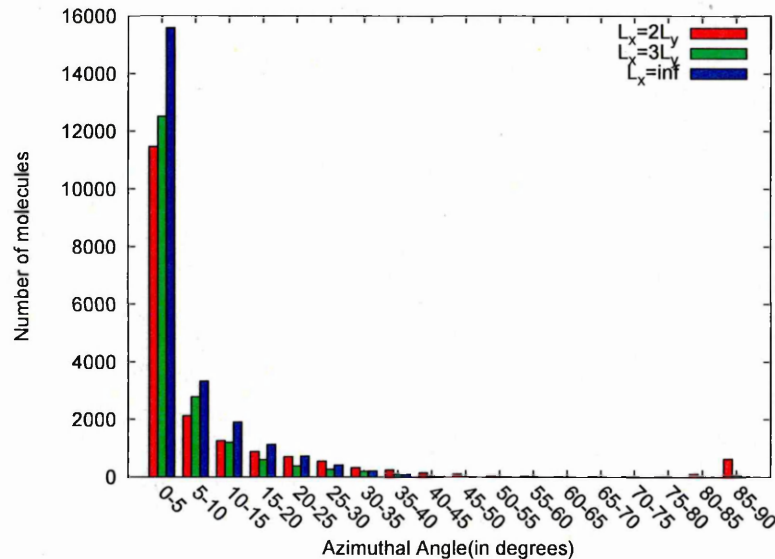


Figure 6.26: Influence of the pattern size on the azimuthal angle.

Before concluding, we investigate the effect that varying the ratio L_x/L_y has on the azimuthal angle. In section 6.1, we saw that the azimuthal angle cannot be

effectively controllable using square patterned substrates. In this section, though, we saw that the molecules tend to align along the x -axis, which suggests that it is possible to control the azimuthal angle using rectangle patterns. The question is how does the ratio L_x/L_y affect the azimuthal values adopted. Fig. 6.26 shows the influence of the ratio L_x/L_y on the distribution of azimuthal angles. We can see from this that as we increase the ratio L_x/L_y , more and more particles align along the stripe with an azimuthal angle lower than 5° . Increasing the ratio, then, does impose an increasing constraint on the azimuthal angle. If we keep increasing this ratio to ∞ (stripe patterned systems), we can notice (see Fig. 6.26) that this limiting behaviour appears to be a natural extension of what is seen at finite L_x/L_y . Importantly, these changes to the azimuthal orientation distribution represent an increase in the azimuthal anchoring coefficient.

6.3 Conclusions

In this chapter, we have investigated the effects of 2D patterns. First of all, we have studied square patterned systems. We noticed that, using this kind of pattern, we are not able to control the azimuthal angle. We have also found that qualitatively similar behaviour is obtained with smooth or sharp transition systems. In all cases, tilted monodomains proved the dominant bulk behaviour. We then went on to consider rectangle patterned systems and looked at the influence of different parameters : the needle lengths and the pattern ratio L_x/L_y . We saw from this that both parameters have an impact on the system. The tilt angle varies monotonically with the ratio L_x/L_y , and in all but one case, with the needle length. Finally, we looked at the behaviour of the azimuthal angle and found that the greater the ratio L_x/L_y , the stronger the azimuthal anchoring strength.

Chapter 7

Conclusions and future work

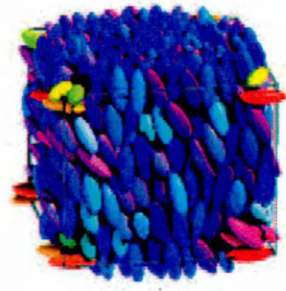
In this thesis, the study of nematic LC films confined between patterned substrates has been addressed. The main direction of this work has focussed on the possibility of controlling the azimuthal and polar anchoring angles using patterning. Here, the main conclusions that have been drawn from this study are summarised and various avenues for future work are discussed. Prior to that, highlights from some other research directions that were initiated but not fully investigated, are briefly presented.

7.1 Other directions

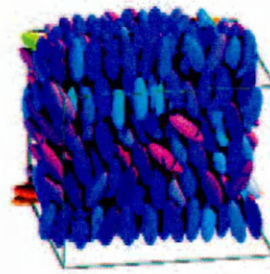
Our study of LCs confined between patterned substrates has not been limited to stripe and rectangle patterns. In fact, we considered a number of other patternings, including circles, out of phase stripes, out of phase squares and stripe patterned substrates rotated by 90 degrees with respect to each other.

7.1.1 Circle patterns

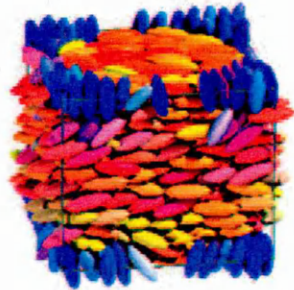
When we started to investigate the effect of patterned substrates on nematic LC films, we first looked at circle patterns. The reason we started with this pattern is simply because our collaborators were interested in it. In this, we investigated the effects of both the circle diameter D and the film thickness L_z . We found that, depending on these two parameters, the pattern can sometimes be written across the film. We found, for $L_z=4\kappa\sigma_0$, that the behaviour of the film depends on D . If



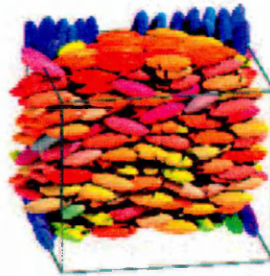
(a)



(b)

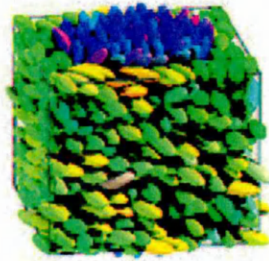


(c)

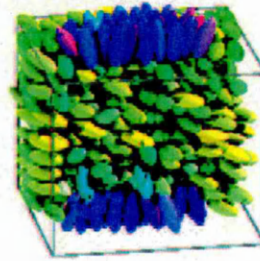


(d)

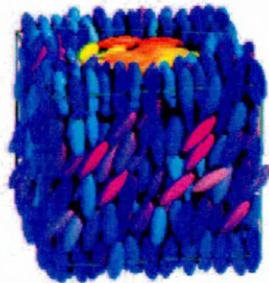
Figure 7.1: Snapshot corresponding to circle patterned substrate systems. $L_z = 4\kappa\sigma_0$, $D=L_x$, $\rho^*=0.4$, $k_s=0$ and 3. a) and c) show full snapshots, b) and d) show slices through systems midplane.



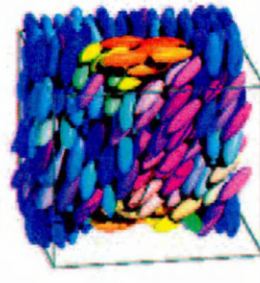
(a) Top surface



(b) Bottom surface



(c) Top surface



(d) Bottom surface

Figure 7.2: Snapshot corresponding to circle patterned substrate systems. $L_z = 4\kappa\sigma_0$, $D = \frac{2L_x}{3}$, $\rho^* = 0.4$, $k_s = 0$ and 3. a) and c) show full snapshots, b) and d) show slices through systems midplane.

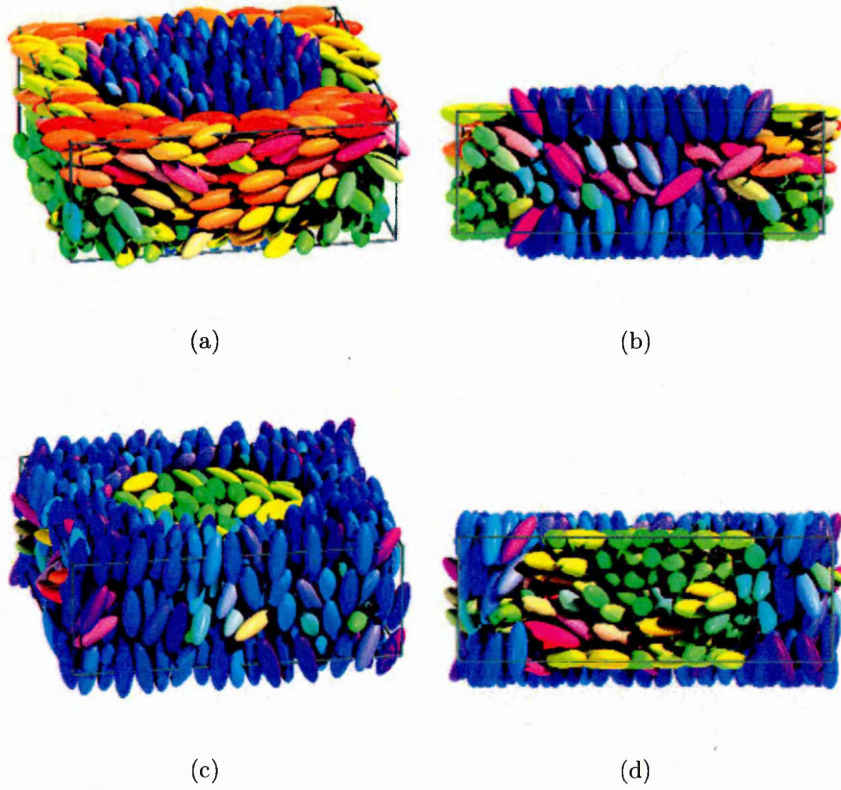


Figure 7.3: Snapshot corresponding to circle patterned substrate systems. $L_z = 2\kappa\sigma_0$, $D = \frac{2L_y}{3}$, $\rho^* = 0.4$, $k_s = 0$ and 3. a) and c) show full snapshots, b) and d) show slices through systems midplane.

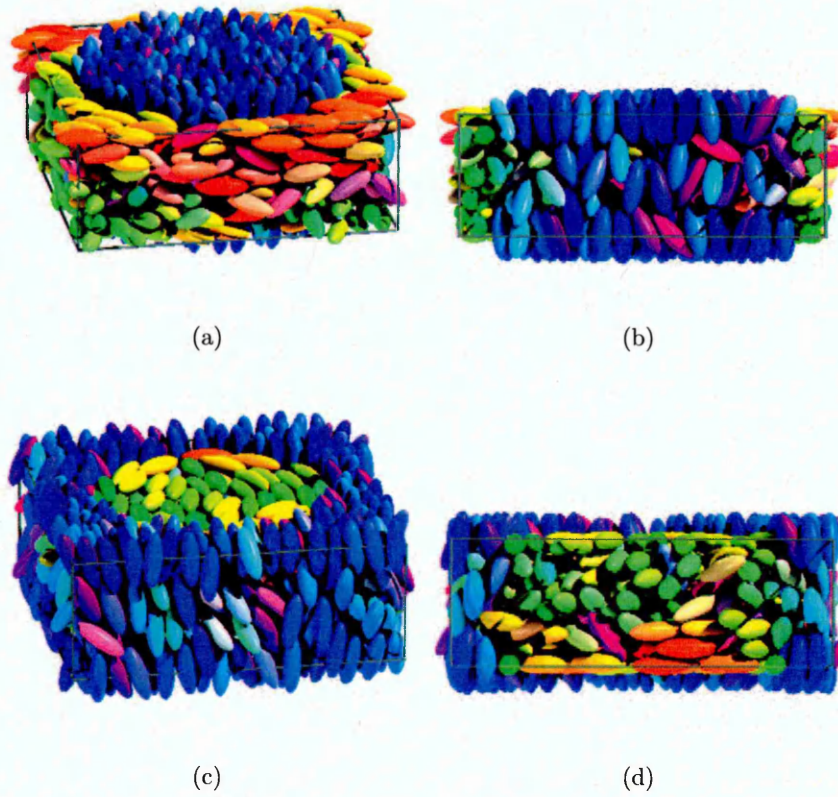


Figure 7.4: Snapshot corresponding to circle patterned substrate systems. $L_z = 2\kappa\sigma_0$, $D = \frac{4L_y}{5}$, $\rho^* = 0.4$, $k_s = 0$ and 3. a) and c) show full snapshots, b) and d) show slices through systems midplane.

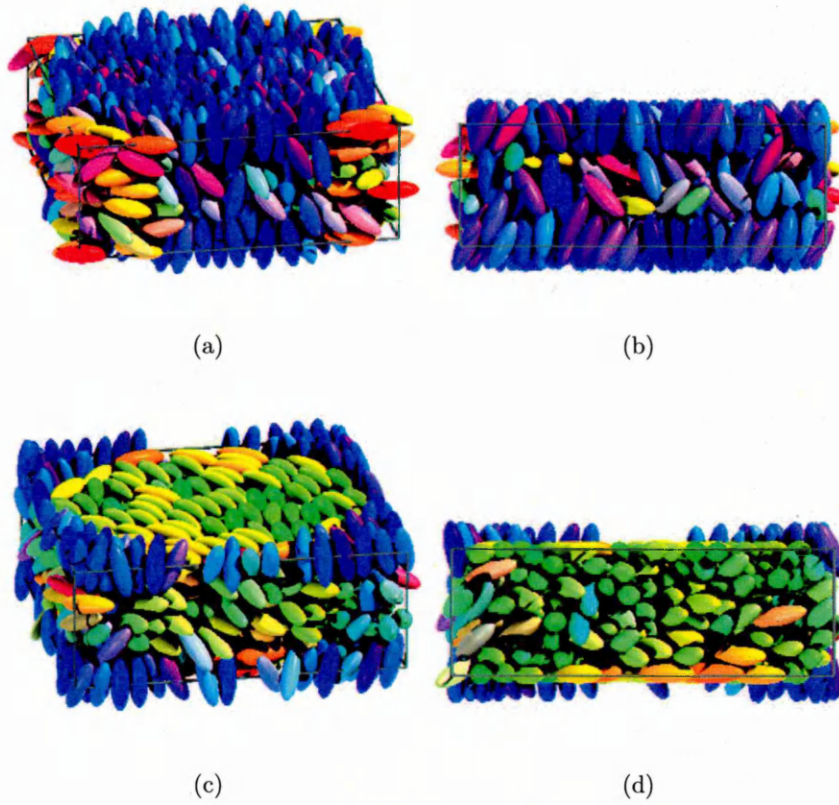


Figure 7.5: Snapshot corresponding to circle patterned substrate systems. $L_z = 2\kappa\sigma_0$, $D=L_y$, $\rho^*=0.4$, $k_s=0$ and 3. a) and c) show full snapshots, b) and d) show slices through systems midplane.

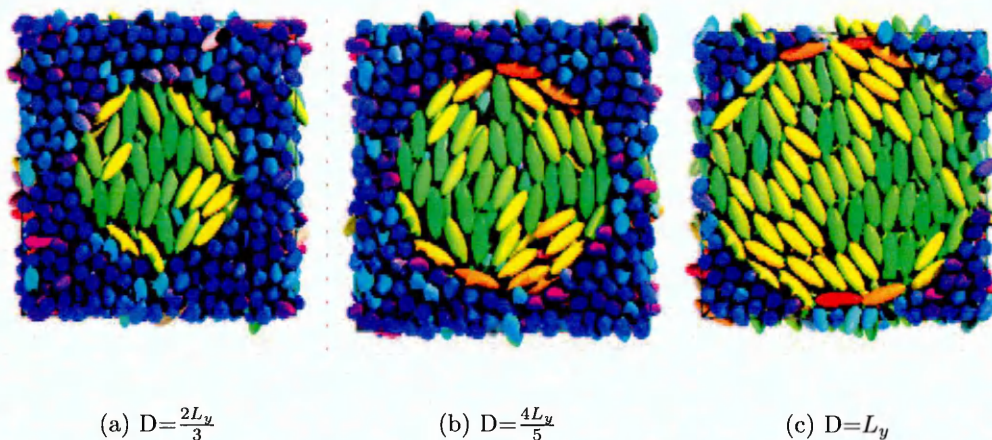
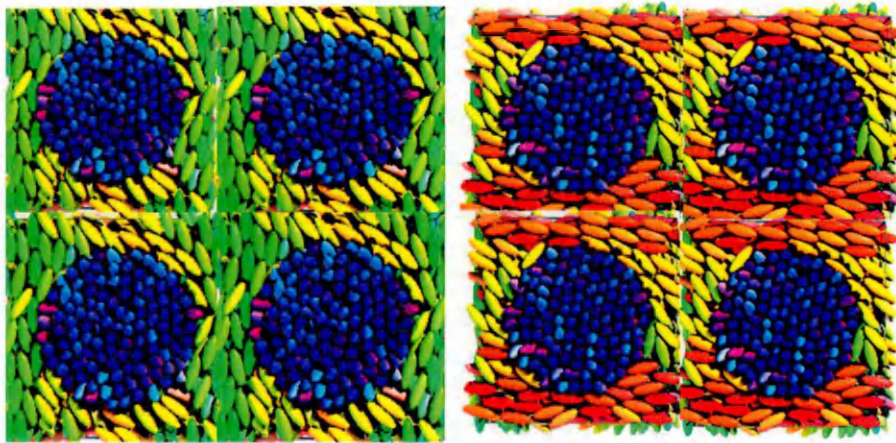


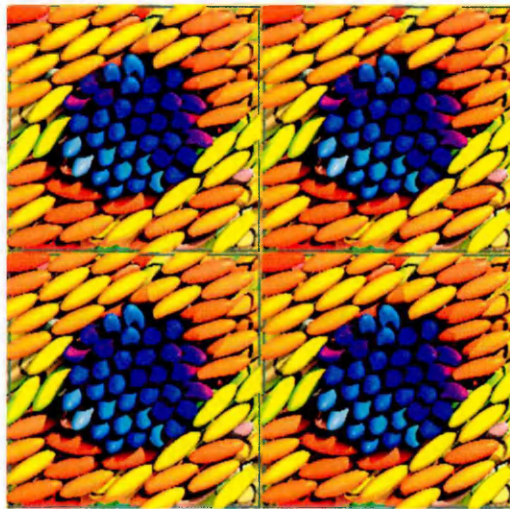
Figure 7.6: Top surface of these $L_z = 2\kappa\sigma_0$ system with different values of D

$D < L_y$, the circle anchoring pattern is not written across the film (see Figs. 7.1 and 7.2) whereas if $D = L_y$, the circle anchoring dominates the border anchoring. We carried on the study on thinner films ($L_z < 3\kappa\sigma_0$) and investigated the influence of changing D . Here we looked at three different values of D : $D = \frac{2L_y}{3}$ (see Fig. 7.3), $D = \frac{4L_y}{5}$ (see Fig. 7.4) and $D = L_y$ (see Fig. 7.5). Looking at these figures, it appears that, whatever the circle diameter, the circle and the border are both written across the film. In the case where the circle is composed of molecules lying flat against the surface, the value of the diameter has an impact on the stability of the circle. This is because for $D \leq \frac{2L_y}{3}$, the molecules do not form a tangential boundary region around the full circle pattern as they do for greater values of D (see Fig. 7.6). In the case of circle patterned surfaces, with $D \geq \frac{2L_y}{3}$ bridging is still seen due to the fact that, here, there is only one surface tension involved (in opposition to the square and rectangle patterns where two surface tensions are applied). We also found that, depending on the surface area ratio (circle/outside region), the molecules in the outside regions can align along the diagonal, (i.e at 45 degrees), or along the x or y axes, if the circle is composed of molecules normal to the surface. From this, it appears that the surface area ratio could offer a route to controlling the azimuthal angle. In the case of circle patterned surfaces, the bridging is still seen due to the fact that, here, there is only one surface tension involved (in opposition to the square and rectangle patterns where two surface tensions are applied).



(a) Top surface

(b) Bottom surface



(c) Top surface

Figure 7.7: The top figures correspond to a circle patterned system with $D=L_x/2$. The bottom figure corresponds to a circle patterned system for $D=2L_x/3$. $L_z = 4\kappa\sigma_0$. In all cases, mosaic images of four simulation box replicas are used to accentuate the different planar region alignments.

7.1.2 Striped substrates : out of phase

We have also investigated the effect of shifting the relative position of the stripes in the systems of the type studied in Chapter 5 (see Fig. 7.8). This effect was studied for a range of film thicknesses (see Fig. 7.9). It is noticeable, looking at the high density snapshot configurations from these simulations that, for a film thickness greater than $7\kappa\sigma_0$, the effect of shifting these stripes with respect to one another is immaterial. For these thickness films, the bulk adopts, a tilted monodomain and no domain bridging is observed. This result is very important in the sense that, it is very difficult to perfectly align two patterned substrates experimentally. The thinner systems with shifted stripe patterns exhibit clear diagonal domain arrangements which tended to fluctuate significantly during simulations. These represent a means of potentially coupling the striped surfaces via LC domains, but appear to be of limited practical application due to the very thin films required to maintain these bridging domains.

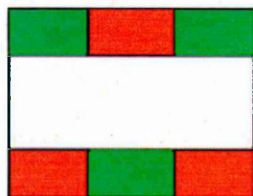
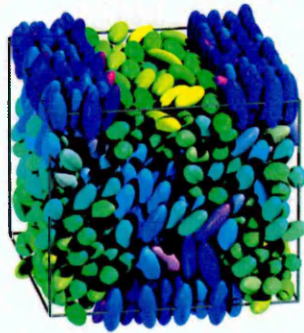


Figure 7.8: Schematic representation of stripe patterned system where the stripes are shifted with respect to each other

7.1.3 Striped substrates rotated at 90 degrees to each other

The schematic representation in Fig . 7.10 is a prediction about the behaviour of an LC confined by orthogonal striped substrates. This schematic representation clearly shows four regions in each of which the LC is predicted to adopt a different behaviour.

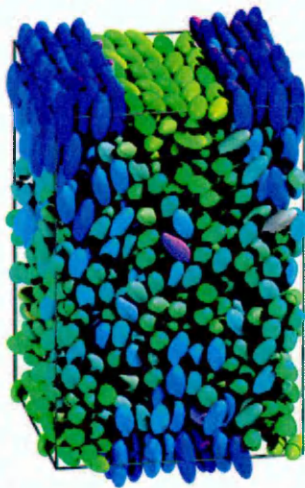
The green region is a region where the LC is confined between two homeotropic alignment regions. In this region, the LC would be expected to adopt an homeotropic anchoring in the bulk region. This is actually confirmed by simulation (see Fig . 7.11(a)).



(a) $L_z=4\kappa\sigma_0$



(b) $L_z=6\kappa\sigma_0$



(c) $L_z=7\kappa\sigma_0$



(d) $L_z=8\kappa\sigma_0$

Figure 7.9: Snapshots of the striped systems for different L_z at $\rho^*=0.4$. The stripes are shifted with respect to one another to be perfectly out of phase.

The orange and the blue regions in Fig. 7.10 shows that the LC confined between homeotropic and planar alignment regions will exhibit a splay. The snapshot in Fig. 7.11(b) shows the splay in the structure in the orange region. We can clearly notice that the molecules at the surface are mainly blue (blue corresponds to a normal alignment of the molecules on the substrate) and mainly red at the bottom surface (red corresponds to a planar alignment of the molecules along the x-axis). In between, they adopt intermediate colours corresponding to alignment in the xz plane. The snapshot in Fig. 7.11(d) shows the splay in the structure in the blue region. Here, the molecules at the surface are mainly green (green corresponds to a planar alignment of the molecules on the substrate along the y-axis) and they are mainly blue at the bottom surface. In between, they adopt a light blue colour which corresponds to molecules aligning in the yz plane.

Finally, Fig. 7.11(c) corresponds to a region where the LC adopts a twist configuration (red region on Fig. 7.10). The molecules are planar to the substrates in this region (green molecules at the top surface corresponding to molecules aligning along the y axis and red molecules at the bottom surface corresponding to molecules aligning along the x axis). The change in colour clearly indicates this twist, from green to light blue, followed by pink-purple and finally red.

What was surprising with this system was the fact that, even though the scale of the patterning was very small, the LCs clearly adopted the different four distinct configurations illustrated in Fig. 7.10. Given what we learnt about the incompatibility of 2D pattern bridging in Chapter 6, it could be interesting to interrogate this twisted system, particularly to determine how the very complex structure just described relates to the twisted monodomain arrangement that might otherwise be expected.

7.2 Conclusions

The study of confined hard particle (HGO) liquid crystalline systems has been addressed in Chapters 4, 5 and 6. In Chapter 4, we investigated surface induced structural changes in symmetric anchored systems using the Hard Needle Wall (HNW) potential. Here, we showed that the HNW potential can induce planar

and homeotropic anchoring for respectively long and short needle lengths k_s . In this chapter, using the HNW as a surface potential, we created a number of hybrid anchored slabs. One of these was the most extreme hybrid system, having strong planar anchored molecules at one substrate and strong homeotropic anchored molecules on the opposite substrate. We looked at two other hybrid systems where strong homeotropic and planar alignment was imposed on the top surface and competing anchoring on the other. We found for these systems that, the bottom surface adopted the behaviour promoted by the top one. We concluded this chapter with a first attempt to simulate system having a patterned substrate.

Chapter 5 addressed the study of stripe patterned systems. Here, we investigated the influence of three parameters : the stripe width, the k_s value and the thickness of the film. We found that the stripe width is a very convenient parameter for controlling the bulk tilt angle. The tilt angle varies monotonically with the stripe width. We then looked at the surface interaction parameter and realised that, even if the tilt angle varies as k_s varies, there is not a monotonic relationship between the two. Finally, we found that, by increasing the film thickness, the bulk tends to exhibit a tilted monodomain. This study on stripe patterned system achieved one of our aims which was to be able to induce and control the tilt angle. We can conclude from this chapter that, by changing the stripe width as well as the surface interaction parameter, patterning appears able to induce any desired tilt angle.

In Chapter 6, we extended our study onto nematic LC confined by 2D patterned substrates. We investigated, by looking at rectangle patterns, what were the influence of the shape of the pattern (by changing the L_x/L_y ratio) and the influence of surface interaction parameter. We saw that both parameters have an impact on the system. The tilt angle varies monotonically with the ratio L_x/L_y . Regarding the needle length, we noticed that, except for one system, the tilt angle varies monotonically. Finally, we looked at the azimuthal angle and found that the ratio L_x/L_y offers control over the azimuthal anchoring coefficient.

Finally, it is appropriate to conclude by relating our work with the work that

our collaborators have been undertaking. We found, by comparing our results that our conclusions on stripe patterned systems agree very closely with experimental observations. However, regarding the rectangle patterned systems, we did not agree with our collaborators existing results. Fig . 7.12 shows a nematic LC in contact with rectangle patterned substrate and Table 7.1 presents different azimuthal angles obtained experimentally from a range of rectangle shape. For the pattern sizes currently accessed by the Leeds group, it is apparent that the long edges of the rectangles do not dominate azimuthal anchoring as well as they do in our simulations. This is presumably related to the very different lengthscales involved. Nevertheless, efforts are ongoing at Leeds to extend their rectangle systems further in search of our predicted behaviour.

B (μm)	Azimuthal angle (degrees)
10	45 ± 1
12	50 ± 1
14	69 ± 2
16	65 ± 3
18	63 ± 3
20	68 ± 3

Table 7.1: Azimuthal angles obtained by our collaborators in Leeds for different values of B. A= $10\mu\text{m}$

7.3 Future work

The work performed in this thesis has led us to understand the different possibilities of using patterning to control the polar and azimuthal anchoring. Much of the work on the stripe patterned substrate has been done. However, a more detailed analysis of the influence of the surface interaction parameter k_s on the system should be done. The work that will follow might also consider alternative new patterned surfaces. An ellipsoid patterned substrate for example might offer an interesting approach to control the azimuthal angle. Also, the use of molecular dynamics (MD) method

would provide interesting results by giving access to the true dynamics of the model systems. It should also be interesting to use MD to simulate bigger systems. The work presented in this thesis represents a step along the path towards providing more efficient display cells. Also, it would probably be reasonable to argue that future modelling could concentrate on lengthscales that differ from the one we have used. For example, more atomistic models could, perhaps, be used to try to explain how /why it is that different SAMs induce different alignments (or why sometimes the same SAM induces different alignments on different members of the nCB family (see Fig. 7.13.) Alternatively, looking the other way, more mesoscopic modelling (Lattice Boltzmann) might be useful in explaining why sometimes our predictions do not match up with experiment.

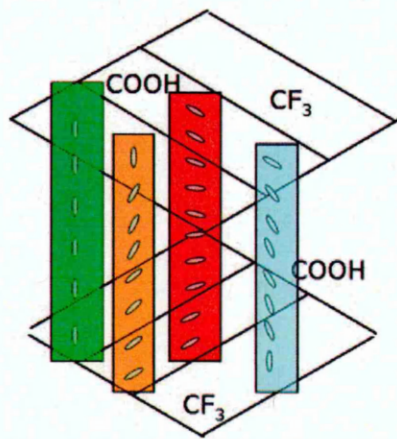
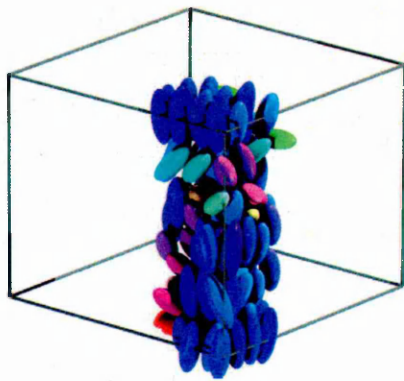
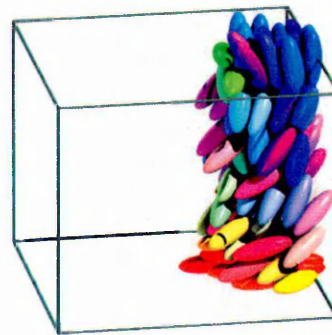


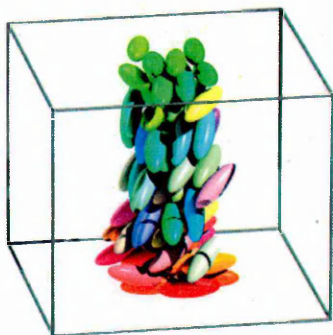
Figure 7.10: System of stripe patterned substrate, rotated by 90 degree with respect to each other



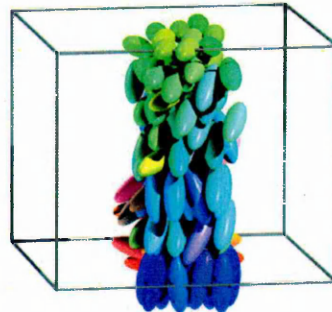
(a) green region



(b) orange region



(c) red region



(d) blue region

Figure 7.11: Snapshots of different regions from simulation of LC confined between orthogonally oriented stripe surfaces. $\rho^*=0.4$.

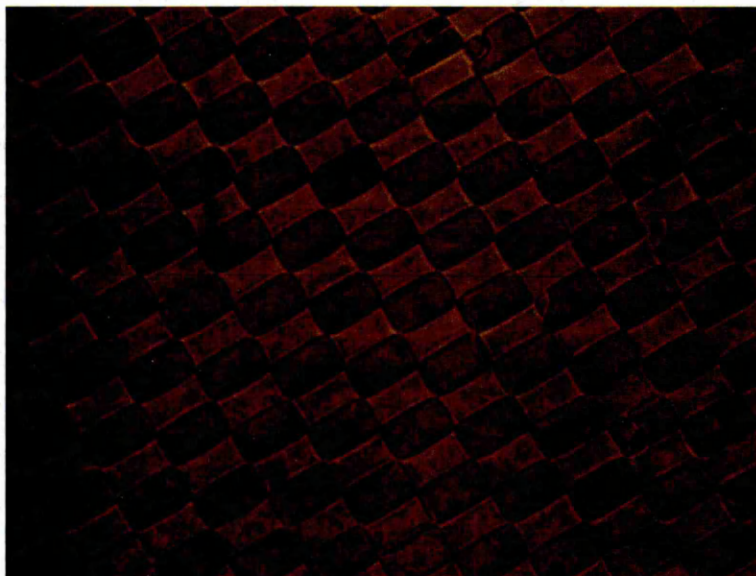


Figure 7.12: Nematic LC aligned on $10\mu\text{m}$ by $20\mu\text{m}$ squares. Image produced by Jonathan Bramble in Leeds

Sam/LC	5CB	6CB	7CB	8CB	9CB
CF_3	Transition				
CH_3				Transition	
COOH					

Figure 7.13: Surface orientation on nCB series with functionalised SAMs. Image done by Jonathan Bramble in Leeds

References

- [1] O. Lehmann. Uber fließende krystalle. *Zeitschrift fr Physikalische Chemie*, 4:462–472, 1889.
- [2] G. W. Gray and P. A. Winsor. *Liquid crystals plastic crystals. Volume 1*. Ellis Horwood, 1974.
- [3] G. Friedel. Les etats mesomorphes de la matiere. *Annales de physique*, 18:273, 1922.
- [4] P. J. Collings. *Liquid Crystals : Nature's delicate phase of matter*. Adam Hilger, 1990.
- [5] P. G. de Gennes. *The physics of liquid crystals*. Clarendon Press, 1974.
- [6] P. J. Collings and M. Hird. *Introduction to liquid crystals : Chemistry and physics*. CRC Press, 1997.
- [7] The Barrett Research Group. Introduction to liquid crystals. Website, Accessed 28/05/08. <http://www.barrett-group.mcgill.ca/teaching/liquidcrystal/LC01.htm>.
- [8] Welcome to polymers and liquid crystals. Website, Accessed 28/05/08. <http://plc.cwru.edu/tutorial/enhanced/files/textbook.htm>.
- [9] G. Vertogen and W. H. de Jeu. *Thermotropic liquid crystals, fundamentals*. Springer-Verlag, 1988.
- [10] S. Kumar. *Liquid crystals: Experimental study of physical properties and phase transitions*. Cambridge University Press, 2001.

- [11] World Technology(WTEC). Twisted nematic LCDs. Website, Accessed 28/05/08. <http://www.wtec.org/loyola/dsplyjp/c4s3.htm>.
- [12] Magic Media. Saint-Gobain Glass. Website, Accessed 28/05/08. <http://www.sggprivalite.com>.
- [13] B. Jérôme. Surface effects and anchoring in liquid crystals. *Reports on Progress in Physics*, 54:391–451, 1991.
- [14] M. Nishikawa. Design of polyimides for liquid crystal alignment films. *Polymers for Advanced Technologies*, 11:404–412, 2000.
- [15] D. S. Seo. Influence of the washing process on the aligning capability of a nematic liquid crystal on polymer surfaces. *Liquid Crystals*, 27:789–793, 2000.
- [16] J. Stohr and M. G. Samant. Liquid crystal alignment by rubbed polymer surfaces: a microscopic bond orientation model. *Journal of Electron Spectroscopy and related phenomena*, 98-99:189–207, 1999.
- [17] D. M. Walba, C. A. Liberko, R. Shao, and N. A. Clark. Smectic liquid crystal alignment using mechanically rubbed n-octadecylsiloxane self-assembled monolayers. *Liquid Crystals*, 29:1015–1024, 2002.
- [18] D. S. Seo, M. Nishikawa, and S. Kobayashi. Preliminary communication : Generation of high pretilt angles of nematic liquid crystal (5cb) on rubbed organic solvent soluble polyimide surfaces with helical; backbone structure and trifluoromethyl moities. *Liquid Crystals*, 22:515–517, 1997.
- [19] M. O’Neill and S. M. Kelly. Photoinduced surface alignment for liquid crystal displays. *Journal of Physics D: Applied Physics*, 33:67–84, 2000.
- [20] Th. Rasing and I. Muševič. *Surfaces and interfaces of liquid crystals*. Springer, 2004.
- [21] M. Nishikawa, J. L. West, and Y. Reznikov. Effect of chemical structures of polyimides on photosensitivity of liquid crystal alignment using a polarized uv exposure. *Liquid Crystals*, 26:575–580, 1999.

- [22] A. Pockels. Surface tension. *Nature*, 43:437, 1891.
- [23] KSV Instruments LTD. Introduction to Langmuir and Langmuir-Blodgett Films. Website, Accessed 28/05/08. <http://www.ksvltd.fi/Literature/Application>
- [24] K. Blodgett. Film built by depositing successive monomolecular layers on a solid surface. *Journal of the American Chemical Society*, 57:1007–1022, 1935.
- [25] J. Bramble. Liquid crystal alignment on patterned self assembled monolayers. Technical report, University of Leeds, 2005.
- [26] R. K. Smith, P. A. Lewis, and P. S. Weiss. Patterning self-assembled monolayers. *Progress in surface science*, 75:1–68, 2004.
- [27] R. A. Drawhorn and N. L. Abbott. Anchoring of nematic liquid crystals on self-assembled monolayers formed from alkanethiols on semitransparent films of gold. *Journal Of Physical Chemistry*, 99:16511–16515, 1995.
- [28] S. D. Evans, H. Allinson, N. Boden, and J. R. Henderson. Surface-field induced organisation at solid/fluid interfaces. *Faraday Discussions*, 104:37–48, 1996.
- [29] V. K. Gupta and N. L. Abbott. Uniform anchoring of nematic liquid crystals on self-assembled monolayers formed from alkanethiols on obliquely deposited films of gold. *Langmuir*, 12:2587–2593, 1996.
- [30] B. Alkhairalla, H. Allinson, N. Boden, S. D. Evans, and J. R. Henderson. Anchoring and orientational wetting of nematic liquid crystals on self assembled monolayer substrates: An evanescent wave ellipsometric study. *Physical Review E*, 59:3033–3039, 1999.
- [31] S. Kumar and G. M. Whitesides. Features of gold having micrometer to centimeter dimensions can be formed through a combination of stamping with an elastomeric stamp and an alkanethiol "ink" followed by chemical etching. *Applied Physics Letters*, 63:2002–2004, 1993.
- [32] Y. Xia and G. M. Whitesides. Soft lithography. *Angewandte Chemie International Edition*, 37:550–575, 1998.

- [33] B. Michel *et al.*. Printing meets lithography: Soft approaches to high-resolution printing. *IBM Journal of Research and Development*, 45:697–719, 2001.
- [34] S. Kumar, J. H. Kim, and Y. Shi. What aligns liquid crystals on solid substrates? The role of surface roughness anisotropy. *Physical Review E*, 94:077803, 2005.
- [35] J. C. Jones, S. Beldon, E. Wood, P. Brett, M. Francis, and M. Goulding. Low voltage zenithal bistable devices with wide operating windows. *SID Symposium Digest of Technical Papers*, 34:954, 2003.
- [36] J. H. Kim, M. Yoneya, J. Yamamoto, and H. Yokoyama. Surface alignment bistability of nematic liquid crystals by orientationally frustrated surface patterns. *Applied Physics Letters*, 78:3055–3057, 2001.
- [37] M. Yoneya, J. H. Kim, and H. Yokoyama. Simple model for patterned bidirectional anchoring of nematic liquid crystal and its bistability. *Applied Physics Letters*, 80:374–376, 2002.
- [38] J. H. Kim, M. Yoneya, and H. Yokoyama. High resolution bistable nematic liquid crystal device realized on orientational surface patterns. *Applied Physics Letters*, 83, 2003.
- [39] F. K. Lee, B. Zhang, and P. Sheng. Continuous liquid crystal pretilt control through textured substrate. *Applied Physics Letters*, 85:5556–5558, 2004.
- [40] I. H. Bechtold and E. A. Oliveira. Liquid crystal alignment on isotropic submicro-textured surfaces of homeotropic-planar states. *Liquid Crystals*, 32:343–347, 2005.
- [41] R. James, F. A. Fernandez, and S. E. Day. Modelling of high resolution phase spacial light modulators. *Molecular Crystals and Liquid Crystals*, 422:209–217, 2004.
- [42] R. James, M. C. Gardner, F. A. Fernandez, and S. E. Day. 3d modelling of high resolution devices. *Molecular Crystals and Liquid Crystals*, 450:105–118, 2006.

- [43] N. Metropolis, A. W. Rosenbluth, M. N. Rosenbluth, A. H. Teller, and E. Teller. Equation of state calculations by fast computing machines. *The Journal of Chemical Physics*, 21:1087–1092, 1953.
- [44] M. P. Allen and D. J. Tildesley. *Computer simulation of liquids*. Oxford U.P., 1997.
- [45] D. Frenkel and B. Smit. *Understanding molecular simulation from algorithms to applications*. Academic Press, 2002.
- [46] P. A. Lebwohl and G. Lasher. Nematic liquid crystal order—a Monte Carlo calculation. *Physical review A*, 6:426–429, 1972.
- [47] U. Fabbri and C. Zannoni. A Monte Carlo investigation of the Lebwohl-Lasher lattice model in the vicinity of its orientational phase transition. *Molecular Physics*, 58:763–788, 1986.
- [48] F. Biscarini, C. Chiccoli, P. Pasini, F. Semeria, and C. Zannoni. Phase diagram and orientational order in a biaxial lattice model : a Monte Carlo study. *Physical Review Letters*, 75:1803–1806, 1995.
- [49] H. Jang and M. J. Grimson. Surface-induced ordering in thin uniaxial liquid crystal films. *Physical review E*, 61:511–518, 2000.
- [50] L. Onsager. The effects of shape on the interaction of colloidal particles. *Annals New York Academy of Sciences*, 51:627, 1949.
- [51] T. Boublik and I. Nezbeda. P-v-t behaviour of hard body fluids. theory and experiment. *Collection Czechoslovak Chem. Commun.*, 51:2301–2417, 1986.
- [52] J. Vieillard-Baron. Phase transition of the classical hard-ellipse system. *Journal of Chemical Physics*, 56:4729, 1972.
- [53] J. W. Perram, M. S. Wertheim, J. L. Lebowitz, and G. O. Williams. Monte-carlo simulation of hard spheroids. *Chemical Physics Letters*, 105:277, 1984.
- [54] J. W. Perram and M. S. Wertheim. Statistical mechanics of hard ellipsoids 1. overlap algorithm and the contact function. *Journal of Computational Physics*, 58:409, 1985.

- [55] D. Frenkel, B. M. Mulder, and J. P. McTague. Phase diagram of a system of hard ellipsoids. *Physical Review Letters*, 52:287, 1984.
- [56] D. Frenkel and B. M. Mulder. The hard ellipsoid of revolution fluid i. monte carlo simulations. *Molecular Physics*, 55:1171, 1985.
- [57] M. P. Allen and D. Frenkel. Observation of dynamical precursors of the isotropic-nematic transition by computer simulation. *Physical Review Letters*, 58:1748–1750, 1987.
- [58] M. P. Allen and D. Frenkel. Calculation of liquid-crystal Frank constants by computer simulation. *Physical Review A*, 37:1813–1816, 1988.
- [59] M. P. Allen and M. R. Wilson. Computer simulation of liquid crystals. *Journal of computer-aided molecular design*, 3(4):335–353, 1989.
- [60] J. Vieillard-Baron. The equation of state of a system of hard spherocylinders. *Molecular Physics*, 28:809, 1974.
- [61] A. Stroobants, H. N. W. Lekkerkerker, and D. Frenkel. Evidence for smectic order in a fluid of hard parallel spherocylinders. *Physical Review Letters*, 57:1452–1455, 1986.
- [62] A. Stroobants, H. N. W. Lekkerkerker, and D. Frenkel. Evidence for one-, two-, and three dimensional order in a system of hard parallel spherocylinders. *Physical Review A*, 36:2929–2945, 1987.
- [63] D. Frenkel. Onsager’s spherocylinders revisited. *Journal of physical chemistry*, 91:4912–4916, 1987.
- [64] D. Frenkel. Structure of hard-core models for liquid crystals. *Journal of physical chemistry*, 92:3280–3284, 1988.
- [65] J. A. C. Veerman and D. Frenkel. Phase diagram of a system of hard spherocylinders by computer simulation. *Physical review A*, 41:3237, 1990.
- [66] S. C. McGrother, D. C. Williamson, and G. Jackson. A re-examination of the phase diagram of hard spherocylinders. *Journal of chemical physics*, 104:6757, 1996.

- [67] P. Padilla and E. Velasco. The isotropic-nematic transition for the hard gaussian overlap fluid: Testing the decoupling approximation. *The Journal of Chemical Physics*, 106:10299, 1997.
- [68] E. de Miguel and E. Martín del Río. The isotropic-nematic transition in hard gaussian overlap fluid. *Journal of Chemical Physics*, 115:9072–9083, 2001.
- [69] M. Rigby. Hard gaussian overlap fluid. *Molecular Physics*, 68:687–697, 1989.
- [70] L. Verlet. Computer "experiments" on classical fluids 1. thermodynamical properties of lennard-jones molecules. *Physical Review*, 159:98, 1967.
- [71] B. J. Berne and P. Pechukas. Gaussian model potentials for molecular interactions. *Journal of Chemical Physics*, 56:4213–4216, 1972.
- [72] D. J. Adams, G. R. Luckhurst, and R. W. Phippen. Computer simulation studies of anisotropic systems. XVII. the Gay-Berne model nematogen. *Molecular Physics*, 61:1575, 1987.
- [73] J. G. Gay and B. J. Berne. Modification of the overlap potential to mimic a linear site-site potential. *Journal of Chemical Physics*, 74:3316–3319, 1981.
- [74] J. T. Brown, M. P. Allen, E. Martín del Río, and E. de Miguel. Effects of elongation on the phase behaviour of the Gay-Berne fluid. *Physical Review E*, 57:6685, 1998.
- [75] E. de Miguel, L. F. Rull, M. K. Chalam, and K. E. Gubbins. Liquid-vapour coexistence of the Gay-Berne fluid by Gibbs-ensemble simulation. *Molecular Physics*, 71:1223–1231, 1990.
- [76] E. de Miguel, E. M. E. Martín del Río, J. T. Brown, and M. P. Allen. Effect of the attractive interactions on the phase behavior of the gayberne liquid crystal model. *Journal of Chemical Physics*, Volume 105(Issue 10):4234–4249, 1996.
- [77] M. P. Allen, J. T. Brown, and M. A. Warren. Computer simulation of liquid crystals. *Journal of Physics: Condensed Matter*, 8:9433–9437, 1996.
- [78] D. J. Earl, J. Ilnytskyi, and M. R. Wilson. Computer simulation of soft repulsive spherocylinders. *Molecular physics*, 85:1719–1726, 2001.

- [79] M. R. Wilson and M. P. Allen. Computer simulations of mesogenic molecules using realistic atom-atom potentials. *Molecular Crystals and Liquid Crystals*, 198:465–477, 1991.
- [80] S. J. Picken, W. F. Van Gunsteren, P. Th Van Duijnen, and W. H. De Jeu. A molecular dynamics study of the nematic phase of 4-n-pentyl-4'-cyanobiphenyl. *Liquid Crystals*, 6(3):357–371, 1989.
- [81] C. W. Cross and B. M. Fung. A simplified approach to molecular dynamics simulations of liquid crystals with atom-atom potentials. *Journal of Chemical Physics*, 101(8):6839–6848, 1994.
- [82] A. V. Komolkin, A. Laaksonen, and A. Maliniak. Molecular dynamics simulation of a nematic liquid crystal. *Journal of Chemical Physics*, 101(5):4103–4116, 1994.
- [83] M. J. Cook and M. R. Wilson. The first thousand-molecule simulation of a mesogen at the fully atomistic level. *Molecular crystals and Liquid crystals*, 363:181–193, 2001.
- [84] R. Berardi, L. Muccioli, and C. Zannoni. Can nematic transition be predicted by atomistic simulations? A computational study of the odd-even effect. *ChemPhysChem*, 5:104–111, 2004.
- [85] M. R. Wilson. Progress in computer simulations of liquid crystals. *International Reviews in Physical Chemistry*, 24:421–455, 2005.
- [86] A. Poniewierski and R. Holyst. Nematic alignment at a solid substrate: the model of hard spherocylinders near a hard wall. *Physical Review A*, 38:3721, 1988.
- [87] A. Poniewierski. Ordering of hard needles at a hard wall. *Physical Review E*, 47:3396–3403, 1993.
- [88] Y. Mao, P. Bladon, H. N. W. Lekkerkerker, and M. E. Cates. Density profiles and thermodynamics of rod-like particles between parallel walls. *Molecular Physics*, 92:151–159, 1997.

- [89] M. A. Bates and D. Frenkel. Phase behaviour of two-dimensional fluids. *Journal of chemical physics*, 112:10034–10041, 2000.
- [90] M. P. Allen. Molecular simulation and theory of liquid crystal surface anchoring. *Molecular physics*, 96:1391–1397, 1999.
- [91] M. P. Allen. Long-range behaviour in liquid crystals by computer simulation. *Journal of Molecular Liquids*, 85:161–171, 2000.
- [92] D. Andrienko, G. Germano, and M. P. Allen. Liquid crystal director fluctuations and surface anchoring by molecular simulation. *Physical Review E*, 62:6688–6693, 2000.
- [93] R. van Roij, M. Dijkstra, and R. Evans. Orientational wetting and capillary nematization of hard-rod fluids. *Europhysics letters*, 49:350, 2000.
- [94] R. van Roij, M. Dijkstra, and R. Evans. Interfaces, wetting, and capillary nematization of a hard-rod fluid: theory for the Zwanzig model. *Journal of chemical physics*, 113:7689–7701, 2000.
- [95] M. Dijkstra, R. van Roij, and R. Evans. Wetting and capillary nematization of a hard-rod fluid : a simulation study. *Physical review E*, 63:051703–1–051703–7, 2001.
- [96] A. Chrzanowska, P. I. C. Teixeira, H. Ehrentraut, and D. J. Cleaver. Ordering of hard particles between hard walls. *Journal of Physics: Condensed Matter*, 13:4715–4726, 2001.
- [97] D. J. Cleaver and P. I. C. Teixeira. Discontinuous structural transition in a thin hybrid liquid crystal film. *Chemical Physics Letters*, 338:1, 2001.
- [98] M. T. Downton and M. P. Allen. Computer simulation of liquid crystal surface modification. *Europhysics letters*, 65:48, 2004.
- [99] H. Lange and F. Schmid. Surface anchoring on liquid crystalline polymer brushes. *Computer Physics communications*, 147:276, 2002.
- [100] H. Lange and F. Schmid. An anchoring transition at surfaces with grafted liquid-crystalline chain molecules. *European Physical Journal E*, 7:175, 2002.

- [101] M. T. Downton and S. Hanna. Atomistic modelling of liquid-crystal surface modification. *Europhysics Letters*, 74:69, 2006.
- [102] F. Barmes. Phd thesis : Computer simulation of confined and flexoelectric liquid crystalline systems. Sheffield Hallam University, 2003.
- [103] F. Barmes and D. J. Cleaver. Computer simulation of a liquid-crystal anchoring transition. *Phys.Rev.E*, 69(6 Pt 1):061705, 2004.
- [104] Z. Zhang, A. Chakrabarti, O. G. Mouritsen, and M. J. Zuckermann. Substrate-induced bulk alignment of liquid crystals. *Physical Review E*, 53:2461–2465, 1996.
- [105] J. Stelzer, L. Longa, and H. R. Trebin. Homeotropic surface anchoring of a Gay-Berne nematic liquid crystal. *Physical review E*, 55:7085–7089, 1997.
- [106] J. Stelzer, P. Galatola, G. Barbero, and L. Longa. Molecular dynamics simulations of surface-induced ordering in a nematic liquid crystal. *Physical review E*, 55:477–480, 1997.
- [107] J. Stelzer, P. Galatola, G. Barbero, and L. Longa. Surface-induced order parameter profiles in a nematic liquid crystal from molecular dynamics simulations. *Molecular crystals and liquid crystals*, 299:61–64, 1997.
- [108] G. D. Wall and D. J. Cleaver. Computer simulation studies of confined liquid-crystal films. *Physical Review E*, 56:4306–4312, 1997.
- [109] V. Palermo, F. Biscarini, and C. Zannoni. Abrupt orientational changes for liquid crystals adsorbed on a graphite surface. *Physical review E*, 57:2519–2522, 1998.
- [110] T. Gruhn and M. Schoen. Grand canonical ensemble Monte Carlo simulations of confined “nematic” Gay-Berne films. *Thin solid films*, 330:46–58, 1998.
- [111] T. Gruhn and M. Schoen. A grand canonical ensemble Monte Carlo study of confined planar and homeotropically anchored Gay-Berne films. *Molecular physics*, 93:681–692, 1998.

- [112] R. Latham and D. J. Cleaver. Substrate induced demixing in a confined liquid crystal film. *Chemical physics letter*, 330:7–14, 2000.
- [113] R. E. Webster, N. J. Mottram, and D. J. Cleaver. Molecular simulation of chevrons in confined smectic liquid crystals. *Physical Review E*, 68:021706–1–021706–9, 2003.
- [114] H. Steuer, S. Hess, and M. Schoen. Phase behavior of liquid crystals confined by smooth walls. *Physical Review E*, 69:031708–1–031708–9, 2004.
- [115] D. L. Cheung and F. Schmid. Monte carlo simulations of liquid crystals near rough walls. *Journal of Chemical Physics*, 122:074902, 2005.
- [116] D. L. Cheung and F. Schmid. Isotropic-nematic transition in liquid crystals confined between rough walls. *Chemical physic letters*, 418:392–396, 2006.
- [117] K. Kiyohara, K. Asaka, H. Monobe, N. Terasawa, and Y. Shimizu. Surface anchoring of rod-like molecules on corrugated substrates. *Journal of Chemical Physics*, 124:034704–1–034704–11, 2006.
- [118] D. J. Cleaver and D. J. Tildesley. Computer modelling of the structure of 4-n-octyl-4'-cyanobiphenyl adsorbed on graphite. *Molecular physics*, 81:781–799, 1994.
- [119] M. Yoneya and Y. Iwakabe. Molecular dynamics simulations of liquid crystal molecules adsorbed on graphite. *Liquid crystals*, 18:45–49, 1995.
- [120] M. Yoneya and Y. Iwakabe. Molecular dynamics simulations of liquid crystals molecules on a polyimide monolayer. *Liquid crystals*, 21:347–359, 1996.
- [121] D. J. Cleaver, M. J. Callaway, T. Forester, W. Smith, and D. J. Tildesley. Computer modelling of the 4-n-alkyl-4'-cyanobiphenyls adsorbed on graphite: energy minimizations and molecular dynamics of periodic systems. *Molecular Physics*, 86(4):613–636, 1995.
- [122] D. R. Binger and S. Hanna. Computer simulation of interaction between liquid crystal molecules and polymer surfaces. i. alignment of nematic and smectic a phases. *Liquid crystals*, 26:1205–1224, 1999.

- [123] D. R. Binger and S. Hanna. Computer simulation of interaction between liquid crystal molecules and polymer surfaces. ii. alignment of smectic C-forming mesogens. *Liquid crystals*, 27:89–102, 2000.
- [124] D. R. Binger and S. Hanna. Computer simulation of interaction between liquid crystal molecules and polymer surfaces. iii. use of pseudopotentials to represent the surface. *Liquid crystals*, 28:1215–1234, 2001.
- [125] A. J. McDonald and S. Hanna. Atomistic computer simulations of terraced wetting of 8CB molecules at crystal surfaces. *Molecular crystal and Liquid crystals*, 413:135–144, 2004.
- [126] A. J. McDonald and S. Hanna. Computer simulations of wetting of solid surfaces by liquid crystals. *Physical Review E*, 75:041703, 2007.
- [127] A. Poniewierski and A. Samborski. Anchoring of nematic liquid crystals at a solid substrate. *Physical Review E*, 53:2436–2443, 1996.
- [128] B. Jérôme. Interfacial structural transitions in nematic liquid crystals. *Journal of Physics: Condensed Matter*, 6:A269–A273, 1994.
- [129] H. G. Galabova, N. Kothekar, and D. W. Allender. Stable configurations in hybrid nematic cells in relation to thickness and surface order. *Liquid Crystal*, 23:803–811, 1997.
- [130] S. Park, C. Padeste, H. Schiff, J. Gobrecht, and T. Scharf. Chemical nanopatterns via nanoprnt lithography for simultaneous control over azimuthal and polar alignment of liquid crystals. *Advanced Materials*, 17:1398–1401, 2005.
- [131] T. Scharf, S. Park, C. Padeste, H. Schiff, N. Basturk, and J. Grupp. Liquid crystal alignment on chemical nanopatterns: control over azimuthal and polar alignment. *Molecular Crystals and Liquid Crystals*, 438:55/[1619]–65/[1629], 2005.
- [132] D. W. Berreman. Solid surface shape and the alignment of an adjacent nematic liquid crystal. *Physical review letters*, 28:1683–1686, 1972.

- [133] T. Z. Qian and P. Sheng. Orientational states and phase transitions induced by microtextured substrates. *Physical Review E*, 55(6):7111–7120, 1997.
- [134] T. Z. Qian and P. Sheng. Liquid-crystal phase transitions induced by microtextured substrates. *Physical Review Letters*, 77(22):4564–4567, 1996.
- [135] B. Lee and N. A. Clark. Alignment of liquid crystals with patterned isotropic surfaces. *Science*, 291:2576, 2001.
- [136] S. Kondrat, A. Poniewierski, and L. Harnau. Orientational phase transition and the solvation force in a nematic liquid crystal confined between inhomogeneous substrates. *The European Physical Journal E*, 10(2):163–170, 2003.
- [137] A. D. Price and D. K. Schwartz. Anchoring of a nematic liquid crystal on a wettability gradient. *Langmuir*, 22:9753–9759, 2006.
- [138] B. H. Clare, K. Efimenko, D. A. Fischer, J. Genzer, and N. L. Abbott. Orientations of liquid crystals in contact with surfaces that present continuous gradients of chemical functionality. *Chem. Mater.*, 18:2357–2363, 2006.